10 July 2009 | $10

Science

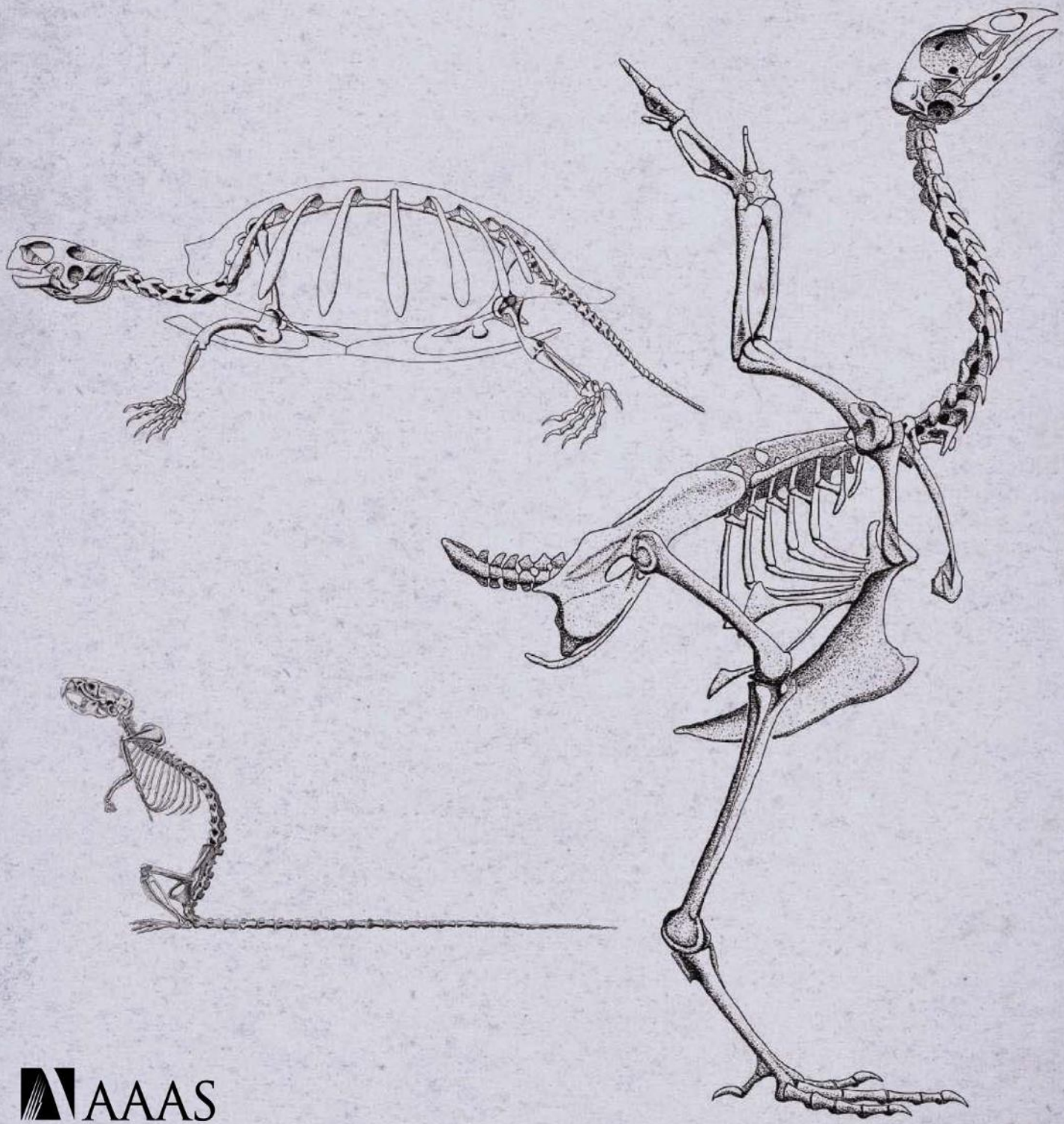

AAAS

Submission deadline August 1

"It's truly exhilarating to be recognized for your hard work. This prize will motivate young generations of scientists and encourage new discoveries."

Dr. Christine Jacobs-Wagner
Grand Prize winner 1997

The GE & Science Prize for Young Life Scientists. Rewarding brilliance since 1995.

Imagine standing on the podium at the Grand Hotel in Stockholm, making your acceptance speech. Imagine joining the ranks of those published in Science magazine and having your essay on your work in molecular biology read by your peers around the world. Imagine taking part in a seminar with the other Prize winners and Nobel Prize laureates and discussing your work with leaders in the field. Imagine what you could do with the US$25,000 prize money. Imagine this brilliant start to your career and where it could lead you. Now stop imagining, and make it a reality.

Dr. Christine Jacobs-Wagner did just that. In 1997, she entered in the GE & Science Prize for Young Life Scientists and won the grand prize. So why not you? If you are one of those who were awarded a Ph.D in 2008, then submit your 1000-word essay by August 1, 2009. Your brilliant idea could well be on its way to building a better reality, for you and for those around you.

All the information you need awaits you at: www.gelifesciences.com/science

GE & Science Prize for Young Life Scientists

For the purpose of this prize, molecular biology is defined as "that part of biology which attempts to interpret biological events in terms of the physico-chemical properties of molecules in a cell".

(McGraw-Hill Dictionary of Scientific and Technical Terms, 4th Edition).

imagination at work

Science AAAS

cell sciences®

www.CytokineCenter.com

www.cellsciences.com

Cytokine Center

Browse our web site with over 1300 proteins, including recombinant cytokines, growth factors, chemokines and neurotrophins. Daily shipping and competitive pricing are offered. Bulk quantities of many proteins available.

PROTEINS

4-1BBL
4-1BB Receptor
6 Ckine
ACAD8
ACAT2
gAcrp30/Adipolean
Activin A
Activin B
ACY1
ADAT1
Adiponectin
ADRP
AITRL
Akt1
Alpha-Feto Protein (AFP)
Alpha-Galactosidase A
Angiopoietin-1 (Ang-1)
Angiopoietin-2 (Ang-2)
Angiostatin K1-3
Annexin-V
apo-SAA
Apoliprotein A-1
Apoliprotein E2
Apoliprotein E3
Apoliprotein E4
APRIL
Artemin
ATF2
Aurora A
Aurora B
BAFF
BAFF Receptor
BCA-1 / BLC / CXCL13
BCMA
BD-1
BD-2
BD-3
BDNF
Betacellulin
Bivalirudin
BMP-2
BMP-4
BMP-6
BMP-7
BMP-13
sBMPR-1A
Brain Natriuretic Protein
BRAK
Breast Tumor Antigen
C5a
C5L2 Peptide
C-10
C-Reactive Protein
C-Src
Calbindin D-9K
Calbindin D-28K
Calbindin D-29K
Calmodulin
Calcitonin Acetate
Carbonic Anhydrase III
Carcino-embryonic Antigen
Cardiotrophin-1
Caspase-3
Caspase-6
CD4
CD14
CD22
CD40 Ligand / TRAP
CD95 / sFas Ligand
CD105 / Endoglin
CHIPS
CNTF
Collagen
CREB
CTACK / CCL27
CTGF
CTGFL / WISP-2
CTLA-4 / Fc
CXCL16
CYR61
Cytokeratin 8
DEP-1
Desmopressin
Disulfide Oxidoreductase
E-selectin
ECGF
EGF
Elafin / SKALP
EMAP-II
ENA-78 / CXCL5
Endostatin
Enteropeptidase
Eotaxin / CCL11
Eotaxin-2
Eotaxin-3 (TSC)
EPHB2
EPHB4
Epigen
Epiregulin
Eptifbatide
Erk-2
Erythropoietin (EPO)
Exodus-2
Fas Ligand
Fas Receptor
FGF-1 (acidic)
FGF-2 (basic)
FGF-4
FGF-5
FGF-6
FGF-7 / KGF
FGF-8
FGF-9
FGF-10
FGF-16
FGF-17
FGF-18
FGF-19
FGF-20
sFGFR-1 (IIIc) / Fc Chimera
sFGFR-2 (IIIc) / Fc Chimera
sFGFR-3 / Fc Chimera
sFGFR-4 / Fc Chimera
sFlt-1 (native)
sFlt-1 (D3)
sFlt-1 (D4)
sFlt-1 (D5)
sFlt-1 (D7)
Flt3-Ligand
sFlt-4
sFlt-4 / Fc Chimera
Follistatin
FSH
Fractalkine / CX3C
G-CSF
α-Galactosidase A
Galectin-1
Galectin-3
Gastrointestinal CA
GCP-2
GDF-3
GDF-9
GDF-11
GDNF
GLP-1
Glucagon
GM-CSF
Goserelin
GPBB
Granzyme B
GROα
GROβ
GROγ
GRO/MGSA
Growth Hormone
Growth Hormone BP
GST-p21/WAF-1
HB-EGF
HCC-1
HGF
Histdyl-tRNA synthetase
Histrelin
HRG1-β1
I-309
I-TAC
IFN-α
IFN-α A
IFN-α 2a
IFN-α 2b
IFN-β
IFN-γ
IFN-Omega
IGF-I
IGF-II
proIGF-II
IGFBP-1
IGFBP-2
IGFBP-3
IGFBP-4
IGFBP-5
IGFBP-6
IGFBP-7
IL-1α
IL-1β
IL-2
IL-3
IL-4
sIL-4 Receptor
IL-5
IL-6
sIL-6 Receptor
IL-7
IL-8 (72 a.a.)
IL-8 (77 a.a.)
IL-9
IL-10
IL-11
IL-12
IL-13
IL-13 analog
IL-15
IL-16 (121 a.a.)
IL-16 (130 a.a.)
IL-17
IL-17B
IL-17D
IL-17E
IL-17F
IL-19
IL-20
IL-21
IL-22
IL-31
Insulin
IP-10
JE
JNK2a1
JNK2a2
KC / CXCL1
KGF
L-asparaginase
LAG-1
LALF Peptide
LAR-PTP
LBP
LC-1
LD-78β
LDH
LEC / NCC-4
Leptin
LIGHT
LIX
LKM
LL-37
Lungkine / CXCL15
Lymphotactin
sLYVE-1
M-CSF
MCP-1 (MCAF)
MCP-2
MCP-3
MCP-4
MCP-5
MDC (67 a.a.)
MDC (69 a.a.)
MDH
MEC
Mek-1
MIA
Midkine
MIG / CXCL9
MIP-1α / CCL3
MIP-1β / CCL4
MIP-3 / CCL23
MIP-3α / CCL20
MIP-3β / CCL19
MIP-4 (PARC) / CCL18
MIP-5 / CCL15
MMP-3
MMP-7
MMP-13
Myostatin
Nanog
NAP-2
Neurturin
NFAT-1
β-NGF
NOGGIN
NOV
NP-1
NT-1/BCSF-3
NT-3
NT-4
Ocreotide
Oncostatin M
Osteoprotegerin (OPG)
OTOR
Oxytocin
p38-α
PAI-1
Parathyroid Hormone
PDGF-AA
PDGF-AB
PDGF-BB
PDGF-CC
Persephin
PF-4
PIGF-1
PIGF-2
PKA α-subunit
PKC-α
PKC-γ
Pleiotrophin
PLGF-1
Polymyxin B (PMB)
PRAS40
PRL-1
PRL-2
PRL-3
Prokineticin-2
Prolactin
Protirelin
PTHrP
PTP1B
PTP-IA2
PTP-MEG2
PTP-PEST
sRANK
sRANKL
RANTES
RELM-α
RELM-β
Resistin
RPTPβ
RPTPγ
RPTPμ
SCF
SCGF-α
SCGF-β
SDF-1α
SDF-1β
Secretin
SF20
SHP-2
STAT1
c-Src
TACI
TARC
TC-PTP
TECK
TFF2
TGF-α
TGF-β1
TGF-β2
TGF-β3
Thymosin α1
sTIE-1/Fc Chimera
sTIE-2/Fc Chimera
TL-1A
TNF-α
TNF-β
sTNF-receptor Type I
sTNF-receptor Type II
TPO
sTRAIL R-1 (DR4)
sTRAIL R-2 (DR5)
TRAIL/Apo2L
TSG
TSH
TSLP
TWEAK
TWEAK Receptor
Urokinase
EG-VEGF
VEGF121
VEGF145
VEGF165
VEGF-C
VEGF-C I125
VEGF-E
HB-VEGF-E
sVEGFR-1
sVEGFR-2
sVEGFR-3
Visfatin
WISP-1
WISP-2
WISP-3
WNT-1

480 Neponset Street, Building 12A, Canton, MA 02021 • TEL (781) 828-0610 • EMAIL info@cellsciences.com

CALL TOLL FREE (888) 769-1246 • FAX (781) 828-0542 • VISIT www.cellsciences.com

Biacore systems

from inspiration ...to publication

Highest quality, information-rich interaction data from Biacore™ systems deepen your understanding of molecular mechanisms and interaction pathways and enable you to add function to structure.

Select the perfect solution for your application and draw conclusions with confidence – from the company that continues to set the standard for label-free protein interaction analysis.

For further information or register to have one of our scientific experts contact you, please visit **www.gelifesciences.com/biacore-science**

Biacore T100
unmatched performance

Biacore X100
ready to run research system

Biacore Flexchip
array-based comparative profiling

imagination at work

CONTENTS continued **>>**

page 136

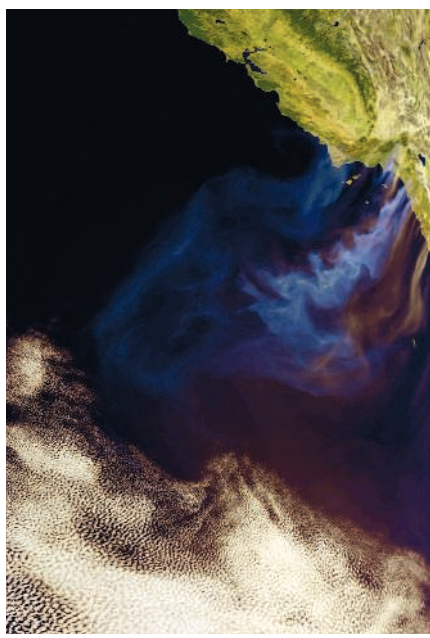

pages 153 & 187

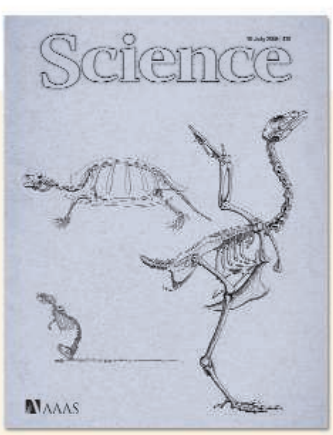

COVER

Skeletons of turtle, chicken, and mouse. The turtle body plan is unusual in that the ribs are transformed into a carapace, and the scapula, situated outside the ribs in other animals, is found inside the carapace. A report on page 193 explains the evolutionary origin of this inside-out skeletal morphology.

Drawings: Hiroshi Nagashima

DEPARTMENTS

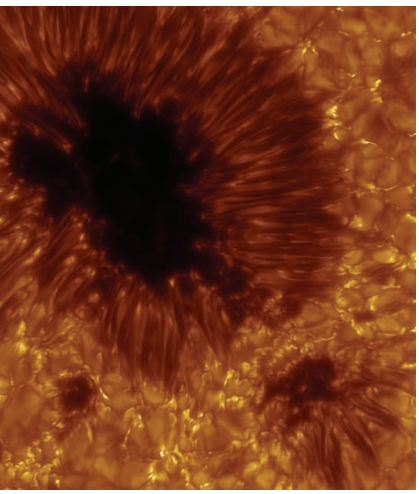

pages 155 & 171

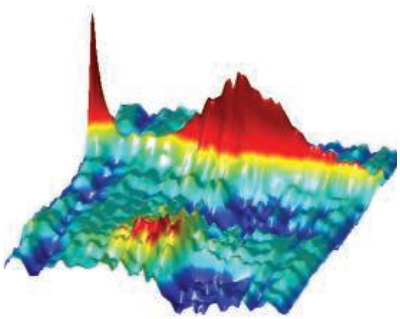

page 181

page 201

RESEARCH ARTICLE

REPORTS

Published by AAAS

SCIENCEONLINE

SCIENCEXPRESS
www.sciencexpress.org

Pre-Target Axon Sorting Establishes the Neural Map Topography
T. Imai et al.

The mouse olfactory topographic neural map is self-organized by interactions between axons, not directed by the target.
10.1126/science.1173596

Dependence of Mouse Embryonic Stem Cells on Threonine Catabolism
J. Wang et al.

Mouse embryonic stem cells exist in a high-flux metabolic state comparable to that of rapidly dividing bacteria.
10.1126/science.1173288

Flexible Learning of Multiple Speech Structures in Bilingual Infants
Á. M. Kovács and J. Mehler

Exposure to two languages facilitates the development of a more flexible associative learning capacity.
10.1126/science.1173947

Positive Selection of Tyrosine Loss in Metazoan Evolution
C. S. H. Tan et al.

Evolution of tyrosine phosphorylation as a signaling mechanism may have coincided with loss of tyrosine residues to avoid noise.
10.1126/science.1174301

The Formation of Population III Binaries from Cosmological Initial Conditions
M. J. Turk et al.

Simulations show that binary systems are likely to exist among the first generation of stars.
10.1126/science.1173540

TECHNICALCOMMENTS

Comment on "DNA from Pre-Clovis Human Coprolites in Oregon, North America"
H. Poinar et al.

full text at www.sciencemag.org/cgi/content/full/325/5937/148-a

Response to Comment by Poinar *et al.* on "DNA from Pre-Clovis Human Coprolites in Oregon, North America"
M. T. P. Gilbert et al.

full text at www.sciencemag.org/cgi/content/full/325/5937/148-b

Comment on "DNA from Pre-Clovis Human Coprolites in Oregon, North America"
P. Goldberg et al.

full text at www.sciencemag.org/cgi/content/full/325/5937/148-c

Response to Comment by Goldberg *et al.* on "DNA from Pre-Clovis Human Coprolites in Oregon, North America"
M. Rasmussen et al.

full text at www.sciencemag.org/cgi/content/full/325/5937/148-d

SCIENCENOW
www.sciencenow.org
Highlights From Our Daily News Coverage

Social Security Numbers Are Easy to Guess
Numbers can be predicted with public data, triggering fears of identity theft.

New Fossil Primate Challenges 'Missing Link' Ida
Researchers propose that it was Asian, not European or African, primates that gave rise to monkeys, apes, and humans.

Finally, an Average Black Hole
Astronomers may have discovered a black hole that's neither small nor gigantic.

SCIENCESIGNALING
www.sciencesignaling.org
The Signal Transduction Knowledge Environment

RESEARCH ARTICLE: Oxygen-Regulated β_2-Adrenergic Receptor Hydroxylation by EGLN3 and Ubiquitylation by pVHL
L. Xie et al.

Hypoxia reduces proline hydroxylation and ubiquitylation of a G protein–coupled receptor, preventing down-regulation.

PERSPECTIVE: Caspase-8 for Outer Harmony
G. Sollberger and H.-D. Beer

Ablation of caspase-8 in keratinocytes activates proliferative and inflammatory responses in the epidermis.

NETWATCH: The Gene Ontology
This project develops species-independent classifiers for describing gene products; in Bioinformatics Resources.

NETWATCH: Prosite
Identify and explore protein domains; in Protein Databases.

SCIENCECAREERS
www.sciencecareers.org/career_magazine
Free Career Resources for Scientists

Basic Scientists in the Clinic
B. Vastag

Scientists now have more opportunities to interact with patients.

From Research to the World of Diplomacy
E. Pain

Nicola Sasanelli left electronic engineering in Italy to become a special envoy.

Science Careers Blog
Science *Careers Staff*

Get frequent updates with advice, opinion, news, and funding opportunities.

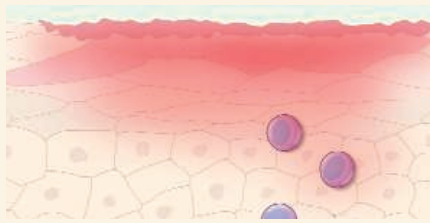

SCIENCESIGNALING
Skin inflammation.

SCIENCECAREERS
Researchers interact with patients.

CREDITS: (*SCIENCE SIGNALING*) PRESTON HUEY; (*SCIENCE CAREERS*) COMSTOCK MEDICAL

SCIENCEPODCAST
www.sciencemag.org/multimedia/podcast
Free Weekly Show

Download the 10 July *Science* Podcast to hear about swine as a host for *Reston ebolavirus*, nuclear waste management in the U.S., the art and science of hominin reconstruction, and more.

ORIGINSBLOG
blogs.sciencemag.org/origins
A History of Beginnings

SCIENCEINSIDER
blogs.sciencemag.org/scienceinsider
Science Policy News and Analysis

QUARTERLY AUTHOR INDEX
www.sciencemag.org/feature/data/aindex.dtl

SCIENCE (ISSN 0036-8075) is published weekly on Friday, except the last week in December, by the American Association for the Advancement of Science, 1200 New York Avenue, NW, Washington, DC 20005. Periodicals Mail postage (publication No. 484460) paid at Washington, DC, and additional mailing offices. The title SCIENCE is a registered trademark of the AAAS. Domestic individual membership and subscription (51 issues): $146 ($74 allocated to subscription). Domestic institutional subscription (51 issues): $835; Foreign postage extra: Mexico, Caribbean (surface mail) $55; other countries (air assist delivery) $85. First class, airmail, student, and emeritus rates on request. Canadian rates with GST available upon request, GST #1254 88122. Publications Mail Agreement Number 1069624. **Printed in the U.S.A.**

Change of address: Allow 4 weeks, giving old and new addresses and 8-digit account number. **Postmaster:** Send change of address to AAAS, P.O. Box 96178, Washington, DC 20090–6178. **Single-copy sales:** $10.00 current issue, $15.00 back issue prepaid includes surface postage; bulk rates on request. **Authorization to photocopy** material for internal or personal use under circumstances not falling within the fair use provisions of the Copyright Act is granted by AAAS to libraries and other users registered with the Copyright Clearance Center (CCC) Transactional Reporting Service, provided that $20.00 per article is paid directly to CCC, 222 Rosewood Drive, Danvers, MA 01923. The identification code for *Science* is 0036-8075. *Science* is indexed in the *Reader's Guide to Periodical Literature* and in several specialized indexes.

AAAS
ADVANCING SCIENCE, SERVING SOCIETY

Eppendorf Consumables – it's your sample

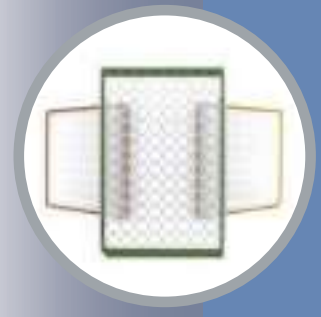

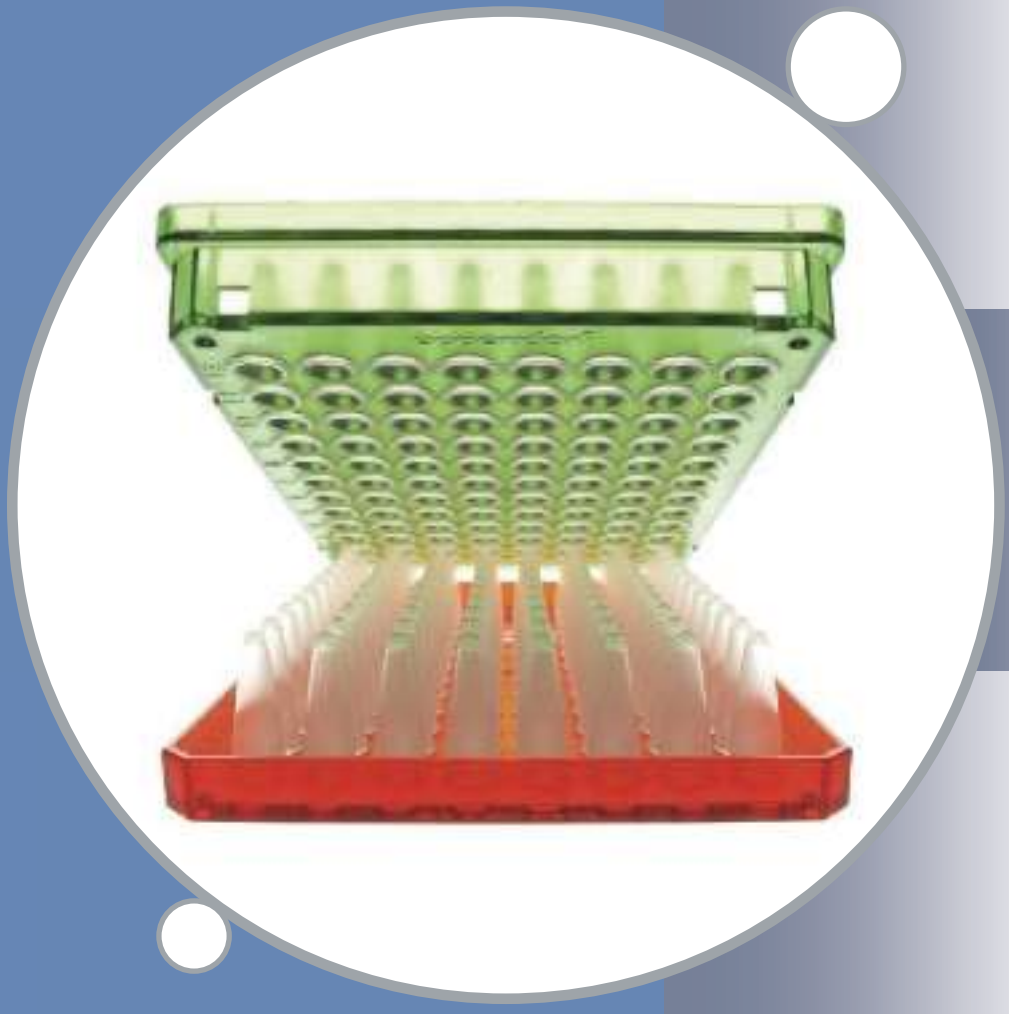

Make the best of it!

Top quality for your sample.

Each of your valuable samples deserves the best treatment. See for yourself how the eppendorf Plate® will save time and reduce costs.

Sample loss in plates can be time consuming and expensive. Therefore, the close environment of each sample should be adapted to its specific quality and purity needs. This can involve a specific purity level or the absence of certain substances, but also stability, reliability, or geometry. The eppendorf Plate® is designed to cover all of the specific needs of your samples!

Eppendorf twin.tec PCR plates*

- Rigid skirt for barcodes and automated handling
- Raised rims for effective sealing
- "skirted" (stackable) and "semi-skirted" plates
- Optimal heat transfer due to reduced wall thickness
- Autoclavable (121 °C, 20 min.)

* Eppendorf owns protective rights under European Patent EP 1 161 994 and US patents US 7,347,977 and US 6,340,589

Learn more about Eppendorf consumables:
www.eppendorf.com/consumables

eppendorf

In touch with life

Your local distributor www.eppendorf.com/worldwide · **Application Support** E-Mail: support@eppendorf.com
Eppendorf AG · Hamburg · Germany · Tel: +49 40 538 01-0 · Eppendorf North America, Inc. · USA · Tel.: +1 800 645 3050

EDITED BY STELLA HURTLEY

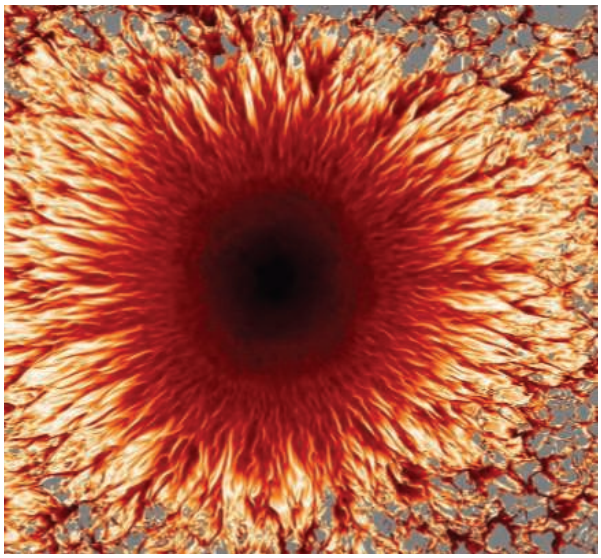

<< Sunspots Before Your Eyes

Sunspots have a dark central region, the umbra, surrounded by a region of lighter radial filaments, the penumbra, along which there are outward horizontal mass flows that are still not fully understood despite their discovery 100 years ago. Now **Rempel *et al.*** (p. 171, published online 18 June; see the Perspective by **Scharmer**) present comprehensive numerical simulations of a pair of sunspots that show the development of an outer penumbra with systematic radial outflows along channels of nearly horizontal magnetic field in regions where the average field inclination is greater than 45 degrees. The outflows result from rising hot plasma that turns over and is guided outward by the strong and inclined magnetic field. The simulations reproduce observed properties throughout the entire penumbra and show that the penumbral structure and outflows in sunspots can be understood in terms of convective flow in a magnetic field with varying inclination.

Cooling Down

Some aerosols, such as sulfates, reflect solar radiation and have a cooling effect on climate, while others, such as black carbon, have a warming effect because they absorb solar radiation. The preponderance of reflective aerosols causes the net effect to be one of cooling, but the amount of cooling is uncertain, owing to a large difference in estimates of the effect of aerosols in global aerosol models compared with estimates based on observations. **Myhre** (p. 187, published online 18 June; see the Perspective by **Quaas**) uses a combination of observational data and modeling to reconcile the two approaches, drawing particular attention to relative increases in the aerosol fraction of black carbon. Taken together, the results suggest a best estimate of the cooling effect of aerosols that is 60% of previous reports.

Starved to Life?

Caloric restriction—reducing the calories ingested by around 30% of that of a normal, fit individual—leads to substantial increases in life span in experimental animals. In an extensive study of caloric restriction in primates, **Colman *et al.*** (p. 201) report that rhesus monkeys, which were subjected to caloric restriction as adults and followed for the last 20 years, show decreased mortality and delayed onset of age-related diseases when compared to normally fed control animals. If compliance with such a diet were not so difficult, many humans would be strongly tempted to enjoy the decreased incidence of brain degeneration, cardiovascular disease, diabetes, and cancer apparent in this population of monkeys.

CREDITS (TOP TO BOTTOM): REMPEL *ET AL.*; BARRETTE *ET AL.*

Neurogenesis and Spatial Memory

The dentate gyrus of the hippocampus is one of two sites in the brain where new neurons are produced throughout life. Adult-born neurons integrate into the dentate gyrus circuitry and are thought to play a role in learning and memory. However, their contribution to hippocampal function remains unclear. **Clelland *et al.*** (p. 210) disrupted neurogenesis in mice and used two behavioral tasks to test for impairment in the formation of uncorrelated episodic memory representations. In one task, two arms were presented and the mice were rewarded for choosing the most recently visited arm in an earlier sequence; in the second task, animals were rewarded for choosing a certain location on a touch screen. Ablation of neurogenesis affected discrimination performance in both tasks but only when the arms or screen locations were close to one another. Neurogenesis is thus necessary for spatial pattern separation in the dentate gyrus.

Parkfield Tremors

Parkfield, California, sits on the San Andreas Fault near the end of a major historic rupture in 1857. Recent monitoring has resolved a change in the seismic tremor—small repeating earthquakes that have been occurring in certain parts of the fault. **Nadeau and Guilhem** (p. 191) now show that the tremors increased and periodic episodes began around the time of two moderate nearby earthquakes 4 years ago. Surprisingly, the tremor episodes have persisted, rather than decaying after the quakes, which may imply that there has been a step change in the state of stress on this part of the San Andreas Fault.

Not Reston at All

Reston ebolavirus is named, mistakenly perhaps, for Reston, Virginia, where it was discovered in the 1970s in imported macaques. After some alarm it was found not to be virulent in humans, uniquely among the ebola viruses, which are characteristically fatal causing a horrific spectrum of symptoms. Using a panviral detection assay, *Reston ebolavirus* has been rediscovered by **Barrette *et al.*** (p. 204) in domesticated pigs in the Philippines in association with other viruses that cause respiratory illness. The strains involved are closely related to the original macaque strain and, given how little variance there is among the viruses, it appears that it is freely circulating between these species possibly, like several other zoonotic viruses, having a reservoir in bats. Serological assays indicated that farm workers have become infected, although no obvious symptoms of human disease have been reported.

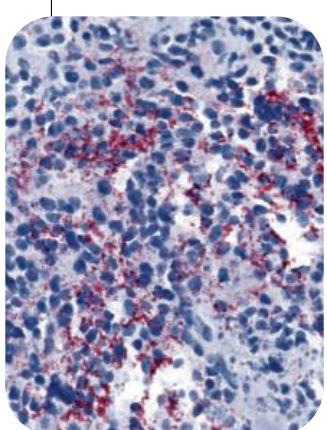

Published by AAAS

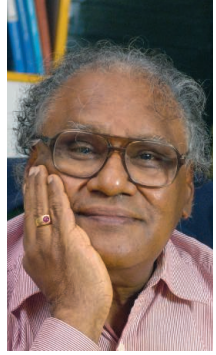

Science in the Future of India

C. N. R. Rao is a National Research Professor at the Jawaharlal Nehru Centre for Advanced Scientific Research in Bangalore, India, and has been chair of the Science Advisory Council to the Prime Minister of India. E-mail: cnrrao@jncasr.ac.in

INDIA HAS VOTED FOR SCIENCE. IN MAY, HALF A BILLION PEOPLE CAST THEIR BALLOTS, AND THEY decisively favored spurring the development of the world's second most populous nation. The reelected Prime Minister Manmohan Singh and his new coalition government have made a commitment to reduce poverty and disease, create employment, and stimulate rural and industrial development. Attaining these goals will require substantial new investments in science and technology (S&T) plus much greater investments in human capital.

Since achieving freedom in 1947, India has established many institutions devoted to science and higher education. Most notably, five Indian Institutes of Technology (IITs) were established between 1951 and 1963, and by 2008 there were 13 IITs: national degree-granting institutions devoted to the training of high-quality engineers and scientists. Despite the gap in infrastructure between advanced countries and India, there have been critical successes in areas such as space, atomic energy, and agriculture. In fundamental research too, India has made progress. Because of the innumerable demands on the economy, however, the higher-education sector has not received adequate support. Part of the reason for the decline in India's university science education system in the past decades has been the preferential funding for R&D activities in national research laboratories.

Prime Minister Singh has recently announced an increase in government investment in S&T from the present 1% of gross domestic product (GDP) to 2% of GDP over the next year or two, an increase of unprecedented magnitude. The contribution of industry has also increased significantly in the past few years, now amounting to approximately 20% of the nation's total investment in science R&D. And the government has begun appropriate administrative reforms as well. For example, two new government departments dealing with Earth system science and health research have been created. In addition, the Indian parliament has approved creating a National Science and Engineering Research Board, an entity somewhat similar to the U.S. National Science Foundation (NSF), that will be responsible for funding scientific research. It will provide competitive grants and establish new facilities in priority areas. Like NSF, the board will also produce annual "science indicators": detailed analyses for measuring progress in S&T from year to year.

This is all good news. But the human resources essential for supporting an expanded S&T agenda are lacking. Young graduates today are readily attracted to professions other than those related to science and engineering; thus, banking, business, and information technology have become immensely popular. India must now focus on creating a large body of outstanding young people interested in taking up professions in science and engineering. To improve the quality of the university education system, new support is being provided. For example, five new Indian Institutes of Science Education and Research have been established in the past 3 years. Admitting undergraduates on the basis of competitive examinations (as do the IITs), these new national institutes will encourage bright young students to pursue science as a career, at both the undergraduate and Ph.D. levels. In addition, to meet the demand for top-class engineering graduates nationally and internationally, the country will increase the total number of IITs to 15.

Sixty percent of the Indian population is below the age of 25, and most reside in villages. This untapped talent represents a great potential asset. Around 600,000 scholarships are now available each year for talented school students from these areas, with an emphasis on those living in poverty. One million science awards are being given to students to promote interest in science, and 10,000 scholarships are available to support students who wish to pursue education beyond high school. In addition, the new government has already initiated important structural reforms in the education sector.

India's citizens have risen to the occasion with their vote. The tasks and challenges for the new government are clear but daunting: It must now satisfy the aspirations of a billion people.

– C. N. R. Rao

10.1126/science.1177202

CREDITS: (LEFT) JERRY COOKE/CORBIS; (RIGHT) THE JAWAHARLAL NEHRU CENTRE FOR ADVANCED SCIENTIFIC RESEARCH

EDITED BY GILBERT CHIN AND JAKE YESTON

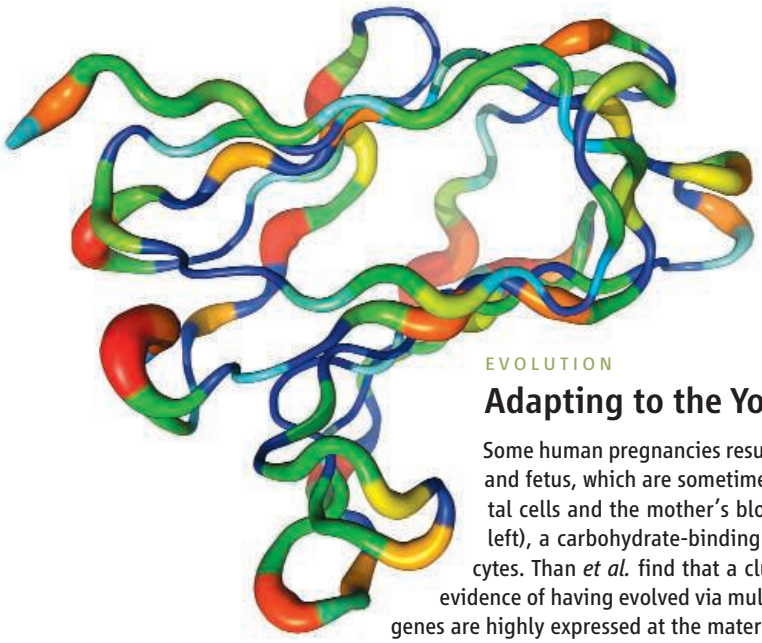

EVOLUTION

Adapting to the Young

Some human pregnancies result in deleterious immune interactions between the mother and fetus, which are sometimes attributed to genetic incompatibilities between placental cells and the mother's blood. One such interaction is mediated by galectin (above left), a carbohydrate-binding protein that recognizes cell surface molecules on leukocytes. Than *et al.* find that a cluster of galectin genes on human chromosome 19 shows evidence of having evolved via multiple duplications and rearrangements, and three of these genes are highly expressed at the maternal-fetal interface. This cluster of galectins is present and expressed in the great apes, and in Old World and New World monkeys, but is not found in prosimians (lemurs) or nonprimates. Furthermore, lineage-specific loss and gain of specific gene copies were identified within the monkey and ape clusters, and functional data indicate that differential sugar binding has evolved within the gene cluster. Overall, these findings suggest that the evolution of the long gestational period of humans may have been accompanied by changes in genes involved in maternal-fetal tolerance. — LMZ

Proc. Natl. Acad. Sci. U.S.A. **106**, 9731 (2009).

CELL BIOLOGY

Energy Makers

Mitochondria are the powerplants of most eukaryotic cells; they generate ATP by oxidative phosphorylation, a process mediated by membrane-bound protein complexes. Some of the subunits of these complexes are encoded in the mitochondrial genome, along with a set of transfer RNA (tRNA) genes. The protein mTERF1 is a mitochondrial transcription termination factor, and a mutation in a mitochondrial tRNA (Leu) gene reduces mTERF1 binding to mitochondrial DNA (mtDNA), leading to encephalomyopathy. Wenz *et al.* show that mTERF2 regulates oxidative phosphorylation by modulating mitochondrial transcription. Knocking out mTERF2 in mice produced memory mistakes and muscle weakness; these two tissues rely on mitochondrial ATP. Cells from these mice expressed lower levels of oxidative phosphorylation–related proteins and also exhibited decreased mitochondrial transcription. mTERF2 binds to mtDNA as well as other mTERF proteins, suggesting a direct role for it in transcriptional regulation. — HP

Cell Metab. **9**, 499 (2009).

CHEMISTRY

Gold Needles in a Haystack

Noble metals such as platinum and gold dispersed on oxide supports are widely used as catalysts, and structural characterization of their morphology is crucial to obtaining mechanistic insight. Electron tomography through adapted scanning transmission electron microscopy has yielded three-dimensional images, but the technique relies on contrasting heavy and light elements (so-called *Z*-contrast, where *Z* is the atomic number), and so has largely been applied to systems with light supports. González *et al.* now extend this method to a system with a much smaller atomic number difference, specifically gold particles supported on a ceria-based mixed oxide, a catalyst that may find application in the production of hydrogen for fuel cells. After either oxidative or reductive treatment of the as-prepared catalyst, electron tomography revealed the presence of gold particles that were 1 to 3 nm in diameter. The data showed that the support (blue) consisted mainly of octahedral crystallites joined together through numerous nanocrystal boundaries. The particles (yellow) were concentrated at oxide nanocrystal boundaries or stepped sites of the support. — JFU

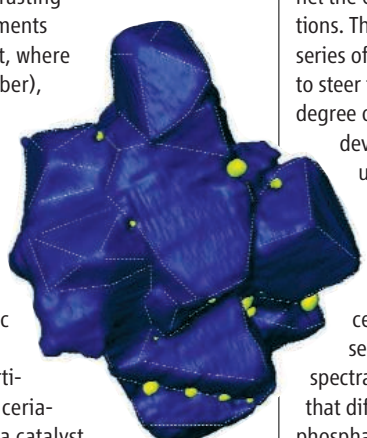

Angew. Chem. Int. Ed. **48**, 10.1002/anie.200901308 (2009).

CHEMISTRY

Spectral Steering

When a molecule absorbs light, its electrons channel the energy into rearranging their relative positions. The process often entails a rather complex series of subtle movements, and researchers yearn to steer the trajectory with an ever increasing degree of external control. To this end, they have developed sophisticated techniques to modulate the spectral phases and amplitudes of the illuminating pulse, which in turn guide the excitation pathway. Roth *et al.* show that such coherent control methodology can induce distinct fluorescence behavior in two compounds that possess nearly identical electronic absorption spectra. The molecules in question were flavins that differed by the presence or absence of a phosphate group on a side chain appended to the central aromatic chromophore. The authors applied two sequential excitations, a leading ultraviolet pulse that induced fluorescence and a trailing infrared pulse that quenched it; they then used feedback to discover ultraviolet pulse shapes that either maximized or minimized the depletion ratio of the phosphate-bound to phosphate-free flavin emission. The optimal pulses achieved nearly 30% differentiation in either direction, an effect the authors attribute to the sensitive manipulation of low-frequency vibrational modes along the side chain. — JSY

Phys. Rev. Lett. **102**, 253001 (2009).

CREDITS (TOP TO BOTTOM): THAN *ET AL., PROC. NATL. ACAD. SCI. U.S.A.* **106**, 9731 (2009); GONZÁLEZ *ET AL., ANGEW. CHEM. INT. ED.* **48**, 10.1002/ANIE.200901308 (2009)

Published by AAAS

www.sciencemag.org

Science

1200 New York Avenue, NW
Washington, DC 20005
Editorial: 202-326-6550, FAX 202-289-7562
News: 202-326-6581, FAX 202-371-9227
Bateman House, 82-88 Hills Road
Cambridge, UK CB2 1LQ
+44 (0) 1223 326500, FAX +44 (0) 1223 326501

Subscription Services For change of address, missing issues, new orders and renewals, and payment questions: 866-434-AAAS (2227) or 202-326-6417, FAX 202-842-1065. Mailing addresses: AAAS, P.O. Box 96178, Washington, DC 20090-6178 or AAAS Member Services, 1200 New York Avenue, NW, Washington, DC 20005

Institutional Site Licenses please call 202-326-6755 for any questions or information

Reprints: Author Inquiries 800-635-7181
Commercial Inquiries 803-359-4578

Permissions 202-326-7074, FAX 202-682-0816

Member Benefits AAAS/Barnes&Noble.com bookstore www.aaas.org/bn; AAAS Online Store www.apisource.com/aaas/ code MKB6; AAAS Travels: Betchart Expeditions 800-252-4910; Apple Store www.wapple/eppstore/aaas; Bank of America MasterCard 1-800-833-6262 priority code FAA3YU; Cold Spring Harbor Laboratory Press Publications www.cshlpress.com/affiliates/aaas.htm; GEICO Auto Insurance www.geico.com/landingpage/go51.htm?logo=17624; Hertz 800-654-2200 CDP#343457; Office Depot https://bsd.officedepot.com/portalLogin.do; Seabury & Smith Life Insurance 800-424-9883; Subaru VIP Program 202-326-6417; VIP Moving Services www.vipmayflower.com/domestic/index.html; Other Benefits: AAAS Member Services 202-326-6417 or www.aaasmember.org.

science_editors@aaas.org	(for general editorial queries)
science_letters@aaas.org	(for queries about letters)
science_reviews@aaas.org	(for returning manuscript reviews)
science_bookrevs@aaas.org	(for book review queries)

Published by the American Association for the Advancement of Science (AAAS), *Science* serves its readers as a forum for the presentation and discussion of important issues related to the advancement of science, including the presentation of minority or conflicting points of view, rather than by publishing only material on which a consensus has been reached. Accordingly, all articles published in *Science*—including editorials, news and comment, and book reviews—are signed and reflect the individual views of the authors and not official points of view adopted by AAAS or the institutions with which the authors are affiliated.

AAAS was founded in 1848 and incorporated in 1874. Its mission is to advance science, engineering, and innovation throughout the world for the benefit of all people. The goals of the association are to: enhance communication among scientists, engineers, and the public; promote and defend the integrity of science and its use; strengthen support for the science and technology enterprise; provide a voice for science on societal issues; promote the responsible use of science in public policy; strengthen and diversify the science and technology workforce; foster education in science and technology for everyone; increase public engagement with science and technology; and advance international cooperation in science.

Information for Authors
See pages 807 and 808 of the 6 February 2009 issue or access www.sciencemag.org/about/authors

EDITOR-IN-CHIEF **Bruce Alberts**
EXECUTIVE EDITOR **Monica M. Bradford** NEWS EDITOR **Colin Norman**
MANAGING EDITOR, RESEARCH JOURNALS **Katrina L. Kelner**
DEPUTY EDITORS **R. Brooks Hanson, Barbara R. Jasny, Andrew M. Sugden**

Editorial senior editor/commentary Lisa D. Chong, Brad Wible; **senior editors** Gilbert J. Chin, Pamela J. Hines, Paula A. Kiberstis (Boston), Marc S. Lavine (Toronto), Beverly A. Purnell, L. Bryan Ray, Guy Riddihough, H. Jesse Smith, Phillip D. Szuromi (Tennessee), Valda Vinson, Jake S. Yeston; **associate editors** Kristen L. Mueller, Nicholas S. Wigginton, Laura M. Zahn; **online editor** Stewart Wills; **associate online editors** Robert Frederick, Tara S. Marathe; **web content developer** Martyn Green; **book review editor** Sherman J. Suter; **associate letters editor** Jennifer Sills; **editorial manager** Cara Tate; **senior copy editors** Jeffrey E. Cook, Cynthia Howe, Harry Jach, Barbara P. Ordway, Trista Wagoner; **copy editors** Chris Filiatreau, Lauren Kmec; **editorial coordinators** Carolyn Kyle, Beverly Shields; **publications assistants** Ramatoulaye Diop, Carlos L. Durham, Joi S. Granger, Jeffrey Hearn, Lisa Johnson, Scott Miller, Jerry Richardson, Jennifer A. Seibert, Brian White, Anita Wynn; **editorial assistants** Emily Guise, Michael Hicks, Patricia M. Moore; **executive assistant** Sylvia S. Kihara; **administrative support** Maryrose Madrid

News deputy news editors Robert Coontz, Eliot Marshall, Jeffrey Mervis, Leslie Roberts; Contributing Editors Elizabeth Culotta, Polly Shulman; **news writers** Yudhijit Bhattacharjee, Adrian Cho, Jennifer Couzin, David Grimm, Constance Holden, Jocelyn Kaiser, Richard A. Kerr, Eli Kintisch, Andrew Lawler (New England), Greg Miller, Elizabeth Pennisi, Robert F. Service (Pacific NW), Erik Stokstad; **interns** Michael Torrice, Brittany Johnson, Preyanka Makadia; **contributing correspondents** Dan Charles, Jon Cohen (San Diego, CA), Daniel Ferber, Ann Gibbons, Robert Koenig, Mitch Leslie, Charles C. Mann, Virginia Morell, Evelyn Strauss, Gary Taubes; **copy editors** Linda B. Felaco, Melvin Gatling, Melissa Raimondi; **administrative support** Scherraine Mack, Fannie Groom; **bureaus** New England: 207-549-7755, San Diego, CA: 760-942-3252, FAX 760-942-4979, Pacific Northwest: 503-963-1940

Production director James Landry; **senior manager** Wendy K. Shank; **assistant manager** Rebecca Doshi; **senior specialists** Steve Forrester, Chris Redwood; **specialist** Anthony Rosen; **Preflight director** David M. Tompkins; **manager** Marcus Spiegler; **specialist** Jason Hillman

Art director Yael Kats; **associate art director** Laura Creveling; **senior illustrators** Chris Bickel, Katharine Sutliff; **illustrator** Yana Greenman; **senior art associates** Holly Bishop, Preston Huey, Nayomi Kevitiyagala; **art associates** Jessica Newfield, Matthew Twombly; **photo editor** Leslie Blizard

***Science* International**

Europe (science@science-int.co.uk) **editorial: international managing editor** Andrew M. Sugden; **senior editor/commentary** Julia Fahrenkamp-Uppenbrink; **senior editors** Caroline Ash, Stella M. Hurtley, Ian S. Osborne, Peter Stern; **associate editor** Maria Cruz; **locum editor** Helen Pickersgill; **editorial support** Deborah Dennison, Rachel Roberts, Alice Whaley; **administrative support** John Cannell, Janet Clements, Louise Moore; **news: europe news editor** John Travis; **deputy news editor** Daniel Clery; **contributing correspondents** Michael Balter (Paris), John Bohannon (Vienna), Martin Enserink (Amsterdam and Paris), Gretchen Vogel (Berlin); **intern** Claire Thomas

Asia Japan Office: Asca Corporation, Eiko Ishioka, Fusako Tamura, 77 Tenjin-cho, Shinjuku, Tokyo 162-0808, Japan; +81 3 6802 4616, FAX +81 3 6802 4615, inquiry@sciencemag.jp; **asia news editor** Richard Stone (Beijing: rstone@aaas.org); **contributing correspondents** Dennis Normile [Japan: +81 (0) 3 3391 0630, FAX +81 (0) 3 5936 3531; dnormile@gol.com]; Hao Xin [China: +86 (0) 10 6307 4439 or 6307 3676, FAX +86 (0) 10 6307 4358; cindyhao@gmail.com]; Pallava Bagla [South Asia: +91 (0) 11 2271 2896; pbagla@vsnl.com]

EXECUTIVE PUBLISHER **Alan I. Leshner**
PUBLISHER **Beth Rosner**

Fulfillment Systems and Operations (membership@aaas.org); **director** Waylon Butler; **senior systems analyst** Nomuna Nyamaa; **customer service supervisor** Pat Butler; **specialists** Latoya Casteel, LaVonda Crawford, Vicki Linton, April Marshall; **data entry supervisor** Cynthia Johnson; **specialists** Shirlene Hall, Tarrika Hill, William Jones

Business Operations and Administration director Deborah Rivera-Wienhold; **assistant director, business operations** Randy Yi; **manager, business analysis** Michael LoBue; **manager, business operations** Jessica Tierney; **financial analysts** Priti Pamnani, Celeste Troxler; **rights and permissions: administrator** Emilie David; **associate** Elizabeth Sandler; **marketing director** Ian King; **marketing managers** Allison Pritchard, Alison Chandler, Julianne Wielga; **marketing associates** Aimee Aponte, Mary Ellen Crowley, Adrian Parham, Wendy Wise; **marketing executive** Jennifer Reeves; **director, site licensing** Tom Ryan; **director, corporate relations** Eileen Bernadette Moran; **publisher relations, eresources specialist** Kiki Forsythe; **senior publisher relations specialist** Catherine Holland; **publisher relations, east coast** Phillip Smith; **publisher relations, west coast** Philip Tsolakidis; **fulfillment supervisor** Iquo Edim; **fulfillment coordinator** Carrie MacDonald; **marketing associate** Mary Lagnaoui; **electronic media: manager** Lizabeth Harman; **project manager** Trista Snyder; **assistant manager** Lisa Stanford; **senior production specialists** Christopher Coleman, Walter Jones; **production specialists** Nichele Johnston, Kimberly Oster

Advertising director, worldwide ad sales Bill Moran

Product (science_advertising@aaas.org); **midwest/west coast/w. canada** Rick Bongiovanni: 330-405-7080, FAX 330-405-7081; **east coast/e. canada** Laurie Faraday: 508-747-9395, FAX 617-507-8189; **uk/europe/asia** Roger Goncalves: TEL/FAX +41 43 243 1358; **japan** Mashy Yoshikawa: +81 (0) 3 3235 5961, FAX +81 (0) 3 3235 5852; **senior traffic associate** Deiandra Simms

Commercial Editor Sean Sanders: 202-326-6430

Project Director, Outreach Brianna Blaser

Classified (advertise@sciencecareers.org); **u.s.: sales manager** Daryl Anderson: 202-326-6543; **midwest** Tina Burks: 202-326-6577; **east coast** Alexis Fleming: 202-326-6578; **west/south central** Nicholas Hintibidze: 202-326-6533; **sales coordinators** Rohan Edmonson, Shirley Young; **international: sales manager** Tracy Holmes: +44 (0) 1223 326525, FAX +44 (0) 1223 326532; **sales** Susanne Kharraz, Dan Pennington, Alex Palmer; **sales assistant** Lisa Patterson; **japan** Mashy Yoshikawa: +81 (0) 3 3235 5961, FAX +81 (0) 3 3235 5852; **advertising support manager** Karen Foote: 202-326-6740; **advertising production operations manager** Deborah Tompkins; **senior production specialist/graphic designer** Amy Hardcastle; **senior production specialist** Robert Buck; **senior traffic associate** Christine Hall;

AAAS Board of Directors retiring president, chair James J. McCarthy; **president** Peter C. Agre; **president-elect** Alice Huang; **treasurer** David E. Shaw; **chief executive officer** Alan I. Leshner; **board** Alice Gast, Linda P. B. Katehi, Nancy Knowlton, Cherry A. Murray, Julia M. Phillips, Thomas D. Pollard, David S. Sabatini, Thomas A. Woolsey

AAAS
ADVANCING SCIENCE, SERVING SOCIETY

"WEE SLEEKIT BEASTIE"

To celebrate the International Year of Astronomy, children in eight Scottish schools vied to create new constellations out of eight stars they are studying. The winning entry, a mouse by 11-year-old Laura Doliczny of Edinburgh, overlaps six official constellations, including Orion, Cepheus, and Taurus. Aldebaran is at the base of the tail; Mu Cephei is the eye.

Robot Rat "Sees" With Whiskers

Most robots view the world with camera eyes. Now researchers at the University of Sheffield and the Bristol Robotics Laboratory in the United Kingdom have built a ratlike robot that feels its way with quivering whiskers.

With its ability to gauge the textures and shapes of objects, the "SCRATCHbot" (Spatial Cognition and Representation Through active touCH) could help explore areas where normal robots can't see clearly, such as dark or dusty environments or even underwater, says robot builder Tony Prescott, a computational neuroscientist.

In real rats, the whiskers sweep back and forth about 20 times a second, bending when they touch something. Receptors in the whisker follicles then send messages to the brain. The robot's whiskers vibrate up to six times per second, feeding sensory information back to a computer-simulated rat brain. Older "rat" robots could move sensors back and forth, but SCRATCHbot can move its whiskers in many different planes and spread or bunch them to explore different areas, says Prescott. This helps provide a more realistic model of the neural networks behind whisker control, observes whisker robotics expert Anil Seth of the University of Sussex in the United Kingdom.

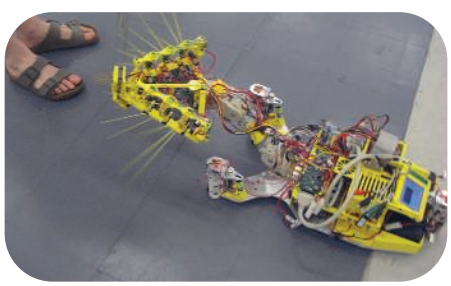

The technology could be used to help locate fire survivors in a smoky building or, less glamorously, to assess the texture of carpets or floors as part of a robot vacuum cleaner, says Prescott. He's now working on smartening up his rat with a simulated hippocampus—a brain area that can memorize maps of an environment.

Obamology

Hey, they never did this with George W. Bush! The American Sociological Association, meeting in San Francisco, California, in August, will be examining the presidency in-depth in sessions held under the heading "The Sociological Significance of President Barack Obama."

- Plenary Session: "Why Obama Won (and What that Says About Democracy and Change in America)"
- Presidential Panel: "A Defining Moment? Youth, Power and the Obama Phenomenon"
- Presidential Panel: "Through the Lens of Gender, Race, Sexuality and Class: The Obama Family and the American Dream"
- Thematic Session: "Understanding Democratic Renewal: The Movement to Elect Barack Obama"
- Thematic Session: "The Future of Community Organizing During an Obama Presidency"
- Thematic Session: "Asian-American Movements, Identities, and Politics: A New Racial Project in the Obama Years?"
- Open Forum: "Does the Obama Administration Need a Social Science Scholars Council?"

Into the Mouth of the Hadrosaur

A dental exam has supplied evidence that *Edmontosaurus*—one of the most common dinosaurs of the late Cretaceous, some 67 million years ago—chewed unlike any animal alive today.

Edmontosaurus belonged to a group of plant-eating dinosaurs called ornithopods. In 1984, researchers studying the sutures between bones in fossil skulls concluded that ornithopods had flexible upper jaws. When the lower jaw clamped shut, they said, the pressure would spread outward from both sides of the upper jaw. The upper rows of teeth would then grind against the lower teeth, rather than slicing as they do in other dinosaurs.

Now three paleontologists have acquired the strongest independent evidence yet for this unique jaw motion. Vincent Williams of the University of Leicester in the United Kingdom and colleagues examined microscopic wear patterns on 13 teeth from a 13-meter-long *Edmontosaurus* found in Wyoming. The dinosaur and its close kin, known as hadrosaurs, had as many as 1000 teeth in multiple rows that moved forward as functional teeth were worn down, says Leicester co-author Mark Purnell.

Patterns of tiny scratches on the teeth revealed that the jaws moved just as had been predicted, the team reported last week in the *Proceedings of the National Academy of Sciences*. "They would have been able to process very tough vegetation," such as horsetails, says co-author Paul Barrett of the Natural History Museum in London.

Paleontologist Lawrence Witmer of Ohio University College of Osteopathic Medicine in Athens calls the study "one of the best microwear papers I've seen." But he still isn't convinced that the upper jaw could flex.

Rows of unerupted teeth in the lower jaw below the chewing surface look like overlapping leaves.

CREDITS (TOP TO BOTTOM): COURTESY OF ROYAL ASTRONOMICAL SOCIETY; MARTIN PEARSON AND BEN MITCHINSON; VINCE WILLIAMS

Published by AAAS

Q&A with HHMI's new leader
134

Science meets art in reconstructing our ancestors
136

ENERGY

DOE's Push to Train a New Generation Falters in House

How will the United States find the talent to fuel its clean-energy economy? Secretary of Energy Steven Chu has a solution—a 10-year, $1.7 billion education program called RE-ENERGYSE (REgaining our ENERGY Science and Engineering Edge)—and the physics Nobelist says there's no time to waste. But Congress may prefer to wait until next year.

President Barack Obama announced the RE-ENERGYSE initiative on 27 April in a speech to the National Academy of Sciences. He called it a way "to inspire tens of thousands of American students to pursue careers in … clean energy." Two weeks later, Obama included a $115 million down payment as part of the Department of Energy's (DOE's) 2010 budget request to Congress.

Chu hopes RE-ENERGYSE will turn DOE into a major player on the federal science-education scene. The 2010 request alone is nearly 10 times what DOE's Office of Workforce Development for Teachers and Scientists, the home for most of the department's efforts in the broader field of science, technology, engineering, and mathematics (STEM) education, now spends. But RE-ENERGYSE is also a different type of education program. Instead of revolving around the department's national labs, RE-ENERGYSE would involve the broader academic community and reach from elementary schools to postdoctoral research.

DOE officials say the country needs to do more to prepare a workforce capable of making the necessary breakthroughs in clean energy. Toward that end, RE-ENERGYSE is expected to complement existing federal programs aimed at attracting students into STEM fields.

"We are investing a lot in green technology deployment," says energy Under Secretary Kristina Johnson, an engineer, entrepreneur, and former university provost who has been tapped to coordinate the initiative. "But I'm concerned that we are going to wake up one day and find that we don't have the people to get the job done. I saw that happen with the photonics industry, and we don't want to repeat that mistake."

Johnson says DOE's senior managers, including science Under Secretary Steven Koonin, are still working out the details of the initiative, which will be managed by the Office of Energy Efficiency and Renewable Energy. DOE budget documents describe plans to divvy up $80 million in 2010 among Ph.D. and postdoctoral fellowships, new master's programs in energy studies, and research opportunities for undergraduates. Most of the remaining $35 million would go to seed technical training programs at community colleges, with an unspecified amount for outreach to elementary and secondary school students and teachers.

In contrast, the workforce development program within the Office of Science, run by Bill Valdez, had a budget of only $8 million in 2008. It grew to $13 million this year, along with $12.5 million in one-time funding to launch a graduate fellowship program that's expected to support 80 students starting in 2010–11. Other Office of Science programs also fund graduate students on grants, but energy technology typically isn't high on their list.

"Universities are structured to produce chemists and physicists and mathematicians. But very few produce wind-turbine designers," says Valdez. Adds Johnson, a former dean of engineering at Duke University, "A lot of universities have begun programs to marry engineering and management. But they haven't focused on the new energy economy."

DOE has struggled to assert its role in science education. The National Science Foundation is the dominant federal player—with an education budget this year of nearly $1 billion—and the Department of Education is the federal agency with explicit responsibility for the subject. The various mission agencies, notably NASA and the National Institutes of Health, have also carved out niches within their own fields.

Under President George H. W. Bush, Energy Secretary James Watkins led an interagency panel on science education and used his position as a bully pulpit. But his efforts to beef up the department's programs met with resistance from Congress, which has traditionally been skeptical of giving

CREDIT: JEFFERSON LAB

Taking a fling. Middle school teachers learn about the laws of motion during a summer program at DOE's Thomas Jefferson National Accelerator Facility in Newport News, Virginia.

Published by AAAS

False clues to genomic riches
142

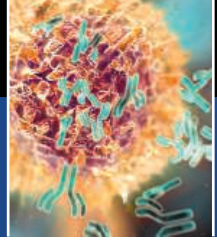

Buzz over B cells
144

DOE a bigger role in STEM education, especially at the precollege level. By the end of the decade, appropriators had sent DOE officials a clear message that they felt the department's strengths lay elsewhere. "It's certainly had its ups and downs," says James Decker, a physicist and longtime senior manager of DOE science programs who retired in 2006. "I'm not sure exactly why. It's not because of any review that said its programs weren't any good."

There's an old adage that "the president proposes and Congress disposes," and late last month, the House energy and water appropriations subcommittee reminded Chu and the new Administration of that rule (*Science*, 3 July, p. 20). Taking up DOE's 2010 budget request, the panel agreed that improving U.S. science education is important but said that DOE needs to do a better job of explaining how RE-ENERGYSE fits into existing programs at other federal agencies. Instead, legislators gave Chu $7 million to get started and told him to come back next year when he's worked out the details, in coordination with the White House Office of Science and Technology Policy.

The recent growth in Valdez's budget builds upon energy legislation passed in 2005 that endorses a bigger role for DOE in education. "Every university has some type of energy program, but there was never any money," says Raymond Orbach, who led the Office of Science under President George W. Bush and who promoted summer internships that give schoolteachers a chance to do research at the labs. "Once we got an authorization, we tried to beef up the program. The interest is already there."

The subcommittee's vote is only the first step in a lengthy budget process. And although Chu is not likely to abandon his signature education program, a former aide to the committee predicts that it will require some heavy lifting to get RE-ENERGYSE back on track this year.

Mike Lubell, head of the Washington, D.C., office of the American Physical Society, hopes that Chu succeeds. "Getting kids fired up about the opportunities and challenges in the field is terribly important," he says. "Improving STEM education in the United States is tough. But this is far more complex and will take a heck of a lot longer."

–JEFFREY MERVIS

CREDITS (TOP TO BOTTOM): NIH; CIRM

BIOMEDICAL RESEARCH

Researchers Generally Happy With Final Stem Cell Rules

Scientists expressed satisfaction this week with the final guidelines on research with human embryonic stem (ES) cells issued on Monday by the National Institutes of Health (NIH).

The new rules—which set out criteria for determining which ES cell lines can be used in federally funded experiments—give NIH discretion to approve old lines that don't meet stringent modern ethical requirements. And they call for NIH to set up a registry of eligible lines. The rules add up to "a major step in the right direction for stem cell research," says stem cell researcher George Daley of Harvard University.

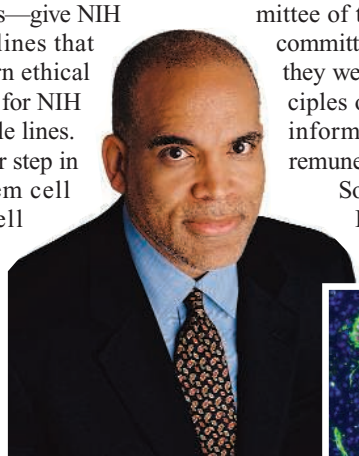

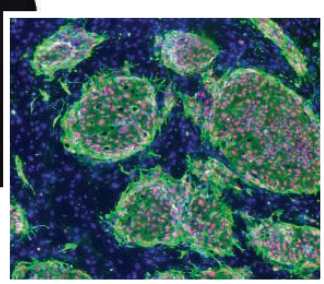

Ready to roll. NIH Director Raynard Kington introduces two-track procedure for vetting cell lines.

Like draft guidelines issued in April (*Science*, 24 April, p. 446), the new rules limit federal funding to research using ES cells derived from surplus embryos donated by couples receiving fertility treatment. (ES cell lines must still be derived using nonfederal funds; Congress has barred NIH from funding such work.) The big question researchers had was whether the 21 lines approved for use under the Bush Administration, which are still used in many research labs, would qualify under detailed provisions for informed consent by embryo donors that are spelled out in the guidelines. The answer is there will be no automatic "grandfathering" in of the Bush lines. However, a working group will deal with them on a case-by-case basis, recommending that they be approved if they conform to the spirit if not the letter of the guidelines.

As acting NIH Director Raynard Kington explained at a press conference, there will be separate channels for determining whether a cell line is eligible depending on whether it was derived before or after 7 July, the effective date of the guidelines. For those derived on or after that date, there will a routine administrative review to see that they conform with informed-consent requirements. If such lines are derived outside the United States, NIH will decide if the rules under which they were obtained are "at least equivalent" to NIH rules, said Kington.

Determining eligibility of cell lines derived before 7 July will require a "more complicated exercise of judgment," said Kington. For this, a task force—a subcommittee of the NIH director's advisory committee—will determine whether they were obtained within the principles of the guidelines, including informed consent and absence of remuneration for embryos.

Some scientists, such as Kevin Eggan of Harvard, were disappointed that NIH didn't open the door to the use of embryos created for research purposes—including through somatic cell nuclear transfer (cloning) and parthenogenesis (from an unfertilized egg). But "on balance, the guidelines are a vast improvement over the draft guidelines," says Eggan. "The establishment of the registry is an important improvement, as is the clearly established route to approval for lines that need 'grandfathering.' " Stem cell researcher Sean Morrison of the University of Michigan, Ann Arbor, lauds NIH for "a really good job." He also says establishment of a new registry is "really important because it was going to take enormous resources for each individual institution to ascertain for themselves" whether a given line qualified for federal support.

Kington predicted that both the new NIH stem-cell registry and the working group, comprising nine or 10 scientists, ethicists, and members of the public, will be in business within the next 2 months.

–CONSTANCE HOLDEN

Published by AAAS

OPINION POLLS

An Inside/Outside View of U.S. Science

The U.S. public respects scientists and thinks what they do is important. But few think U.S. science outperforms the rest of the world. And neither do a majority of scientists. Three surveys conducted this spring by the Pew Research Center offer some fresh insights into what both the public and scientists think about science and its impact on society.

This spring, Pew surveyed two groups of adults and members of AAAS (which publishes *Science*). Its findings about the public's general knowledge of science—a barely passing grade of 65% on 12 factual questions (to see how you stack up, go to pewresearch.org)—mirror the results of similar studies over the years by many organizations. But Pew added a new wrinkle by asking both scientists and the public what they think about current hot topics and other matters, as well as having scientists assess the state of their profession. (The online survey went to a sample of 10,000 AAAS members, excluding schoolteachers, and had a 25% response rate.)

To nobody's surprise, there's a wide gap between the scientific community and the public on some issues. For example, 84% of the former and only 49% of the latter say that humans contribute to global warming. Likewise, 88% of scientists versus 32% of the broader adult population say that natural processes have led living things to evolve over millions of years. But the survey uncovered important nuances to even these hot-button issues. As the report notes, "those who say science sometimes conflicts with their religious beliefs are only slightly less likely than those who see no conflict to say that scientists contribute a great deal to society."

Some of the results may raise eyebrows. Only 49% of scientists—and a scant 17% of the general public—think that the United States is the dominant scientific power in the world. And the public is not sure whether the federal government helps or hinders innovation. Although 60% think federal investments are "essential" for progress in science, 57% believe that government programs are "usually wasteful and inefficient." Scientists are less critical of government, with only 37% seeing it as wasteful. At the same time, a mere 20% of them think that companies do it right compared with 37% of the general public.

–JEFFREY MERVIS

POLITICAL IDEOLOGY

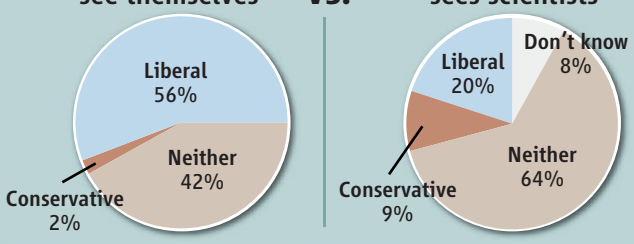

PARTY AFFILIATION

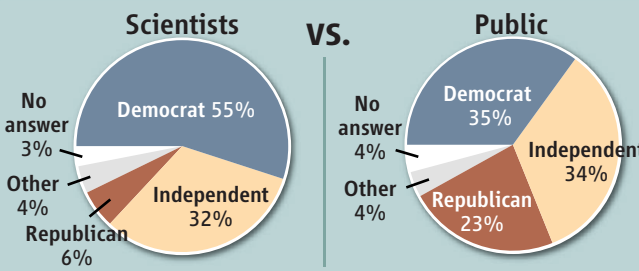

Taking sides. The public imagines scientists to be less politically partisan than they actually are. And scientists are decidedly more liberal/Democratic than the general population.

SCIENTISTS VS. PUBLIC SUPPORT FOR ...

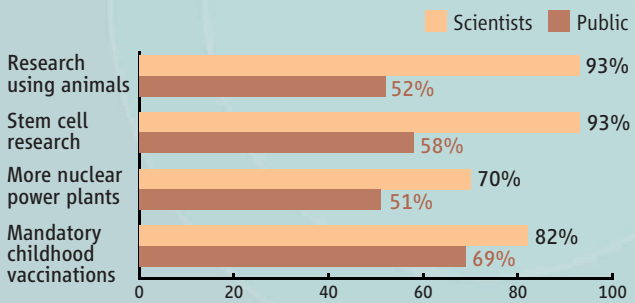

In my opinion. Although both scientists and the public are on the same side of these four policy issues, they attract substantially more support among scientists.

THE OBAMA EFFECT

Greatest U.S. achievements

2009		1999
12%	Space/moon landing	18%
10%	Obama election	NA
5%	Medical breakthroughs	7%
5%	Technology	12%
4%	Civil rights	4%

A decade's difference. The public is much less likely today than it was 10 years ago to tout scientific achievements among the country's greatest achievements, while last fall's victory by Barack Obama looms large in their minds.

THE BUSH EFFECT

Greatest U.S. failures (since 1989)

Renewable energy	12%
Training next generation	9%
Addressing climate change	7%
Restrictions on stem cells	7%
Engaging the public	6%
Politicizing science	6%

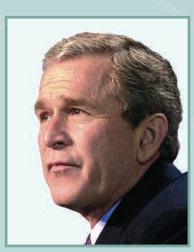

A presidential backlash? The policies of George W. Bush appear prominently when scientists are asked to list the country's greatest scientific failures in the past 20 years.

PHOTOS (LEFT TO RIGHT): UPI/NEWSCOM; ZUMA PRESS/NEWSCOM

BIGGEST OBSTACLES TO RESEARCH

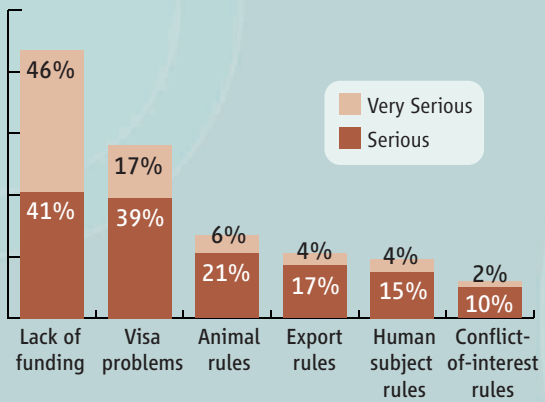

Blocking the way. Scientists say that a shortage of funds and visa delays are their two biggest encumbrances.

SELLING OUT?

Choosing to make lots of money leads to ...

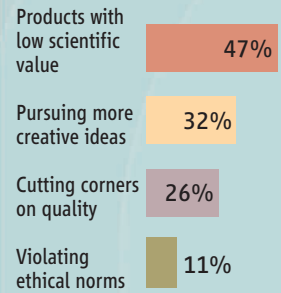

Cash calls. The lure of financial rewards can degrade or improve the quality of their research, scientists report.

BIGGEST CAREER HURDLES (BY FIELDS)

	Biology/ Medical	Chemistry	Geo-sciences	Physics/ Astronomy	TOTAL
Economic issues	64%	61%	47%	41%	56%
Job market	39%	34%	44%	38%	36%
Education	11%	12%	14%	11%	12%
Personal sacrifices	11%	7%	6%	8%	9%
Lack of vision/creativity	7%	6%	11%	9%	7%

Research roadblocks. Life scientists were most likely to identify funding support as their biggest obstacle, while poor job prospects weighed mostly heavily on geoscientists.

SPREADING THE WORD

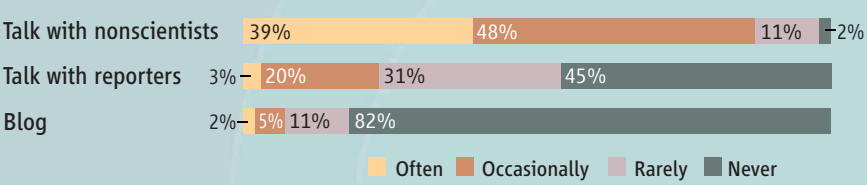

Stay in touch. Almost one in four scientists reports having at least occasional contact with the media, but few blog about their profession.

AAAS MEMBERS WHO TOOK THE SURVEY

GENDER		NATIONALITY		EMPLOYMENT SECTOR		FIELD		TYPE OF WORK	
Men	72%	U.S.-born	81%	Academic	63%	Biological/Medical	51%	Basic	49%
Women	26%	Foreign-born citizen	9%	Industry	15%	Chemistry	14%	Applied	46%
AGE		Noncitizen	9%	Government	9%	Geosciences	6%		
18–34	20%	**EMPLOYMENT STATUS***		Nonprofit	8%	Physics/Astronomy	8%		
35–49	19%	Employed	81%	Other	5%	Other	19%		
50–64	33%	Retired	19%						
65+	26%	Student	16%						

*nonexclusive

A representative sample of AAAS members answered the online survey, according to Pew researchers, who excluded precollege teachers and nonscientists.

DATA SOURCE: PEW RESEARCH CENTER; (IMAGE, RIGHT) HEIDI SAGERUD

ScienceNOW.org

From *Science*'s Online Daily News Site

Social Security Stolen Simply
Keeping your Social Security number secret may not be enough to protect you from identity theft. According to a new study, a crook need only figure out where and when you were born—information often easily found on social networking sites such as Facebook—to guess your number in as few as 1000 tries. Those individuals particularly at risk were born in smaller states after 1989, when receiving a Social Security number at birth became the norm. http://bit.ly/1a4zKa

Ida Dethroned
Remember Ida? It's been barely 2 months since the fossil primate made her debut on the History Channel, where she was called a "missing link" between humans and primitive primates and a "revolutionary scientific find that will change everything." But Ida may be robbed of her claim to that title by a new fossil primate from Asia. http://bit.ly/HZqxE

Finally, an Average Black Hole
Heavyweight and lightweight black holes abound in the universe, but nobody has detected a middleweight—and some scientists argue they don't exist. Now, astronomers say they have found the first conclusive evidence for one of these elusive objects on the fringe of a distant galaxy. Estimated to be at least 500 times more massive than the sun, the discovery could plug a large gap in the cosmic menagerie, though it creates unanswered questions about this type of black hole's origins. http://bit.ly/j9iZm

How the Piranha Got Its Teeth
Piranhas have long been a staple of horror movies, and it's no wonder. Their razor-sharp teeth can tear chunks of flesh from creatures many times their size. Now scientists have rediscovered a fossil piranha jaw that shows how the fish got those choppers. http://bit.ly/16lo8x

Read the full postings, comments, and more on **sciencenow.sciencemag.org**.

Published by AAAS

NEWSMAKER INTERVIEW

Hughes's Tjian Holds to a 'Global' Standard of Merit

Biochemist Robert Tjian, 59, took the helm of the Howard Hughes Medical Institute (HHMI) in April at a challenging time, after its endowment, which had stood at $17.5 billion last August, had been battered by the economic recession. One of his first actions was difficult: He notified HHMI's 350 investigators at universities and scientists at its research center, Janelia Farm in Ashburn, Virginia, that their budgets will likely be trimmed 5.5% in 2010. But Tjian points out that the blow, which won't affect new and early-career scientists, will be softened by federal stimulus money for biomedical research. The trim also pales compared with the 10% cut his predecessor, Thomas Cech, made in the budget in 2002 after the dot-com bubble burst.

Tjian, a longtime Hughes investigator at the University of California, Berkeley (*Science*, 3 October 2008, p. 35), is upbeat about his plans to revamp programs. He says he wants to expand the charity's reach abroad, noting that China and other countries are increasingly the source of new scientific talent. On 25 June, Tjian spoke with *Science* in his office in Chevy Chase, Maryland, pausing between meetings dressed casually in jeans. His comments have been edited for brevity and clarity.

–JOCELYN KAISER

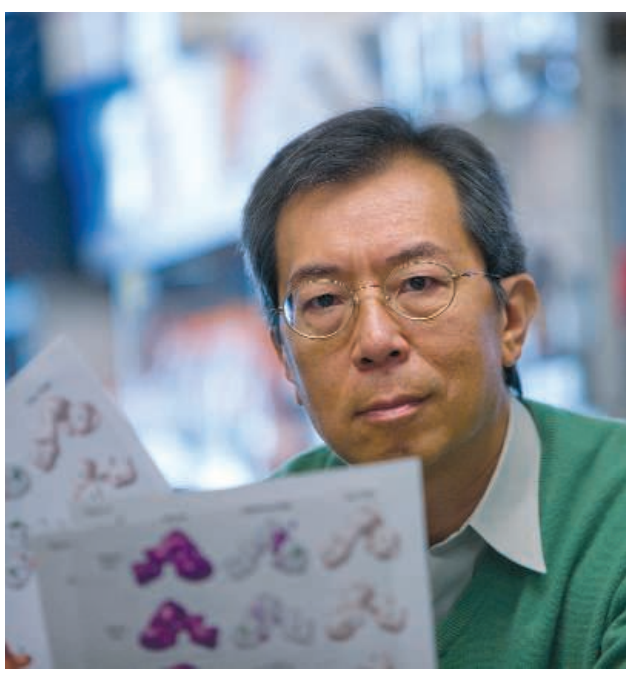

Q: What are your first priorities?

R.T.: I will be putting a lot of emphasis into our international research programs and our international educational programs. Partly because my view is very global. I don't draw the line on where I should be helping scientific endeavor stopping at the border. Partly because our scientists in the U.S., where are they coming from? They're coming from everywhere. Many of them come here and don't leave; some of them go back. I think we can do a lot of good by promoting both of those.

Q: Will the current HHMI research scholars in places such as Latin American and Eastern Europe worry that you're going to kill their program?

R.T.: They already know that we'll be phasing out their program. They'll have an opportunity to reapply. The best people will likely still be in our program. The criteria that we should always have been using is, "Are they comparable to the scientists we're funding here?" They're either at the Hughes standards or they're not.

Q: Is the idea also to expand to more parts of the world?

R.T.: For sure. Asia is one place that I'd certainly be looking at, but you shouldn't limit it to that.

Q: What else are you working on?

R.T.: I'm looking at the education programs in existence here for a decade or more. Do they still make sense now? We know how to do this at the higher levels. And so the first thing I did, I doubled the number of slots for postdocs. Some of the programs that we're running in undergraduate education here I find quite appealing. I'm going to bring back some form of graduate student fellowships. Hughes could make a huge difference by making it easier for exceptionally talented foreign students to come here.

But it's kind of difficult to reach into the high school and junior-high levels to make a big impact. So much of our efforts have been very local, counties in Maryland or Virginia. Should we go nationally? [President Barack] Obama's trying to do this, and it's tough. I'm going to relook at that.

Q: Like Janelia Farm, your recently announced center in South Africa [for studying HIV and tuberculosis] was a departure for HHMI. Do you expect to start more centers?

R.T.: In South Africa, the motivation there was purely humanitarian, medical, extreme need. We happened to have two investigators who knew this stuff. It was serendipitous. But it also tells you that the Hughes can be very flexible.

Q: Tell me about your plans for expanding into plant biology.

R.T.: We're a medical research organization. So how does a plant fit in? Very simply, the same way as yeast fits in, as *Drosophila* fits in: It's a model organism. [Cech] asked a group of plant biologists to tell us where the needs are, and it became quite obvious that this was one of those bizarre situations where the funding in the U.S. was actually lagging behind the funding in other countries. But yet we have some real talent, so we thought, "What a great opportunity."

Q: What is happening with your endowment since last August, when it was $17.5 billion?

R.T.: Broadly speaking, we've probably had the same kind of impact as many, many endowments, so somewhere in the 20% to 25% range, and some of that's already been mitigated—we had a pretty strong March, April, and May. [In April], I announced an up to 5% reduction for our all-science programs. It's not that I looked at the books and said, "Oh my God, we're running out of money." It's more a way of planning ahead.

Q: I've heard that recruiting group leaders to Janelia Farm has been difficult because of its remote location, even though it is just 48 kilometers outside Washington, D.C.

R.T.: I think that its remote site poses a significant challenge but that that is more than probably compensated for by a lot of other advantages of being there. So it's water under the bridge, the site. Given that, though, I'd say it's very successful and it can get more successful. It's like starting a biotech company. The first group to hire is really tough because everybody's wondering, "Is it going to be a total failure?" I think we're kind of past that.

Published by AAAS

SCIENTIFIC COMMUNITY

Resignations Highlight Disagreement On Vaccines in Autism Group

A prominent member of the science advisory board for Autism Speaks, the largest private funder of autism research, resigned last week citing his disagreement with efforts to study vaccines as a possible cause of autism. Eric London, a psychiatrist and chief science advisor for the New York State Autism Consortium, says that funding such research, in addition to being wasteful, unduly heightens parents' concerns about the safety of immunization. London's departure is a sign of growing frustration in the research community, says Alison Singer, a former high-ranking leader of Autism Speaks who resigned from the group in January.

"We believe that the question of whether immunization is associated with an increased risk for [autism spectrum disorders] is of extremely high priority."

—GERALDINE DAWSON, AUTISM SPEAKS

Since its founding 4 years ago by former NBC executive Bob Wright and his wife, Autism Speaks has committed $128 million in research grants through 2014. The group has won widespread praise for raising awareness of autism spectrum disorders (ASD)—the odds of a child being diagnosed are 1:150—and for advocating federal support of autism research (*Science*, 5 January 2007, p. 27).

But an increasing number of researchers and parents are concerned about the organization's position that vaccines may cause some cases of autism. Although numerous scientific studies have searched for a link, they have found none. Autism Speaks holds that vaccines or other environmental agents may cause ASD in a subset of medically or genetically predisposed individuals. "We believe that the question of whether immunization is associated with an increased risk for ASD is of extremely high priority," clinician-researcher Geraldine Dawson, the chief science officer at Autism Speaks, wrote in January to the Centers for Disease Control and Prevention.

That same month, Singer, then executive vice president of communications and awareness at Autism Speaks, resigned. She says Bob Wright wanted her to endorse a boost in federal research on the role of vaccines. "I felt very strongly that it sent the wrong signal," Singer says. "The science is saying it's time to move on."

London says the same concerns prompted his resignation from Autism Speaks' Scientific Affairs Committee. "If Autism Speaks' misguided stance continues, there will be more deaths and potentially the loss of herd immunity which would result in serious outbreaks of otherwise preventable disease," he wrote.

Dawson responds that Autism Speaks spends only about 2% of its $33 million research budget on research related to vaccines. Dawson rejects the argument that this research raises parents' concerns about vaccines. She claims it does the opposite: "We feel that by addressing questions parents are raising with ongoing rigorous research, that that serves to increase confidence" in the safety of vaccines.

"If Autism Speaks' misguided stance continues, there will be more deaths and potentially the loss of herd immunity which would result in serious outbreaks of otherwise preventable disease."

—ERIC LONDON, NEW YORK STATE AUTISM CONSORTIUM

In April, Singer cofounded a new group called the Autism Science Foundation to fund research, in particular small pilot projects—but not on vaccines. Singer declines to say how much money the group has raised so far, but she vows to keep overhead low; the organization is currently working out of her basement.

–ERIK STOKSTAD

CREDITS (TOP TO BOTTOM): COURTESY OF AUTISM SPEAKS; COURTESY OF ERIC LONDON

ScienceInsider

From the *Science* Policy Blog

A third case of oseltamivir-resistant swine flu, announced last week in Hong Kong, **has flu experts worried that resistance to the drug is spreading.** Unlike two cases reported in Denmark and Japan, the Hong Kong patient hadn't taken oseltamivir herself. That suggests she picked up a resistant strain from someone else. Meanwhile, a reporter for *Science* learned firsthand about **China's quarantine process** for swine flu.

The **Czech Academy of Sciences is fighting for its future** after the government proposed a budget that slashes the academy's funding in half by 2012. The plan would divert money from the basic research institutes the academy runs to more applied science efforts.

A Senate spending panel said in a recent report that the way the National Science Foundation (NSF) handled an Internet porn scandal points to **"systemic work-force management problems"** that have created "a hostile work environment" for its 1300 employees. The legislators said that part of the problem is NSF's use of short-term "rotators" from academia to serve as senior program managers.

John Niederhuber, director of the National Cancer Institute, fired back last week in response to a front-page article in *The New York Times* that harshly critiques how cancer research is funded. In a lengthy rebuttal in the 30 June issue of the *NCI Cancer Bulletin*, Niederhuber gave several examples of NCI's creativity—including its cancer genome project and planned physical science–oncology centers.

The Wellcome Trust is **pouring nearly $50 million into bolstering research capacity in Africa.** The U.K. biomedical research charity announced pan-African research partnerships involving more than 50 universities and research institutions as part of a 5-year initiative. Each consortium has a different focus, including infectious disease research and "ecosystem and population health."

For details and other science policy news, go to **blogs.sciencemag.org/scienceinsider**.

Published by AAAS

Bringing Hominins Back to Life

To reconstruct our ancestors, paleoartists weave art and science together in a sometimes uneasy marriage. The result is lifelike models that influence how both researchers and the public view ancient humans

TRUMANSBURG, NEW YORK—On a recent Sunday, John Gurche's studio in this small town north of Ithaca was playing host to much of the human family. Busts of seven hominins—the group made up of humans and their ancestors but not other apes—were arranged on a low table. Three black-haired australopithecines, including "Lucy's" species, stared with glowering eyes under furrowed brow ridges. Then came *Homo erectus*, looking pensive with its prominent jaw and large eyes, followed by big-brained *H. heidelbergensis*. Next in line was the hulking head of a Neandertal, looking ever so human despite its large nose and thick brows. Finally, wild-eyed and somewhat out of place, sat the tiny head of *H. floresiensis*, a.k.a. the Hobbit, a creature that researchers still do not know where to place on the human family tree.

In the morning, Gurche would pack up the heads in crates and drive them to the Smithsonian Institution in Washington, D.C., where they will be displayed next year in the National Museum of Natural History's new Hall of Human Origins. The result, says Richard Potts, head of the Smithsonian's Human Origins Program, will be a chance for museum visitors to "look into the eyes of our ancestors." It will also be another job done for Gurche, one of an elite group of paleoartists (see sidebar, p. 139), who combine cutting-edge research and exquisite artistry to bring hominins back to life in museum displays, magazines, and documentaries.

As the number of hominin fossil discoveries has exploded in recent years, researchers and paleoartists alike have been working overtime to refine their visions of what our ancestors looked like. In the past, because of gaps in the fossil record, paleoartists tended to represent early humans as "halfway between a chimp and a human," says Zeresenay Alemseged, chair of anthropology at the California Academy of Sciences in San Francisco. But recent finds, including candidate hominins dated to 5 million to 7 million years ago, "have affected not only the way that paleoanthropologists look at human evolution but the necessity for paleoartists to distinguish between these early species."

As the science advances, so does demand by museum directors and magazine editors for increasingly lifelike, three-dimensional hominin recreations, says Gurche. That demand has been fueled in part by the film industry's sophistication at creating fantastical creatures, which has spurred paleoartists

Coming to life. Paleoartist Elisabeth Daynès puts the finishing touches on an australopithecine in her Paris studio.

to adopt makeup and modeling techniques for maximum realism.

The interplay between art and science makes reconstruction "a two-way street," says Gary Sawyer, who has been reconstructing hominins at the American Museum of Natural History (AMNH) in New York City for more than 30 years. The artists must track researchers' latest anatomical interpretations, and reconstruction helps scientists think about issues such as "what kind of muscles a hominin had and how it walked on the landscape," says Alemseged. "But the end product should be seen as an artistic creation."

Some researchers argue that reconstructions influence how scientists view ancient hominins and interpret their behavior. "The scientific community requires a lengthy period of time to absorb and adapt to new ideas, and these illustrations are often part of the process by which you see the change," says Stephanie Moser, an archaeologist at Southampton University in the United Kingdom. "These artistic representations are part of the knowledge cycle and not outside it."

Yet the comfort level about reconstructions varies among scientists. AMNH paleoanthropologist Ian Tattersall, who has collaborated with Sawyer and other paleoartists, says he wishes they weren't necessary. "I would rather not do these, but we have an obligation to the public, which ultimately supports this research and wants to see its results. But [reconstructions] require lots of decisions that science can't answer." Did our earliest ancestors smile? How fat were they? "The reconstructions allow us to ask the questions but not to answer them," says Tattersall.

Online
sciencemag.org
Podcast interview with author Michael Balter.

Neandertals: Brutes or brothers?

Researchers and paleoartists have been working together since the 19th century, when the first hominin fossils were discovered. The effects of science on the art and vice versa were obvious almost immediately. One celebrated battle of reconstructions was sparked by the 1908 discovery of a nearly complete Neandertal skeleton at La Chapelle-aux-Saints in southern France. French paleontologist Marcellin Boule concluded that the Neandertal did not walk fully erect and played no part in human ancestry. The artist he enlisted created a brutish, stooped, hairy creature, more ape than human. But Scottish anatomist Arthur Keith, who had concluded that Neandertals were ancestral to modern humans, commissioned a rival drawing of the La Chapelle-aux-Saints Neandertal sitting on a rock and looking very human as it pensively knapped a stone tool. Boule's brutish conception dominated until at least the 1950s, when new fossils and research convinced most anthropologists that Neandertals were either our ancestors or our very close relatives. (The latter view predominates today; see *Science*, 13 February, p. 870.) Thus, today's Neandertal reconstructions tend to emphasize their humanity.

Part of the shift, some researchers say, can be explained by a change in social attitudes, as in the 1960s Neandertals came to be seen as more peaceful. "Reconstructions tend to reflect our deep-seated views" of hominins, says paleoanthropologist Steven Churchill of Duke University in Durham, North Carolina. "Do you assume that they are like us but just a little more primitive or that they were very different? It affects how questions are asked."

Whether the art influences the science,

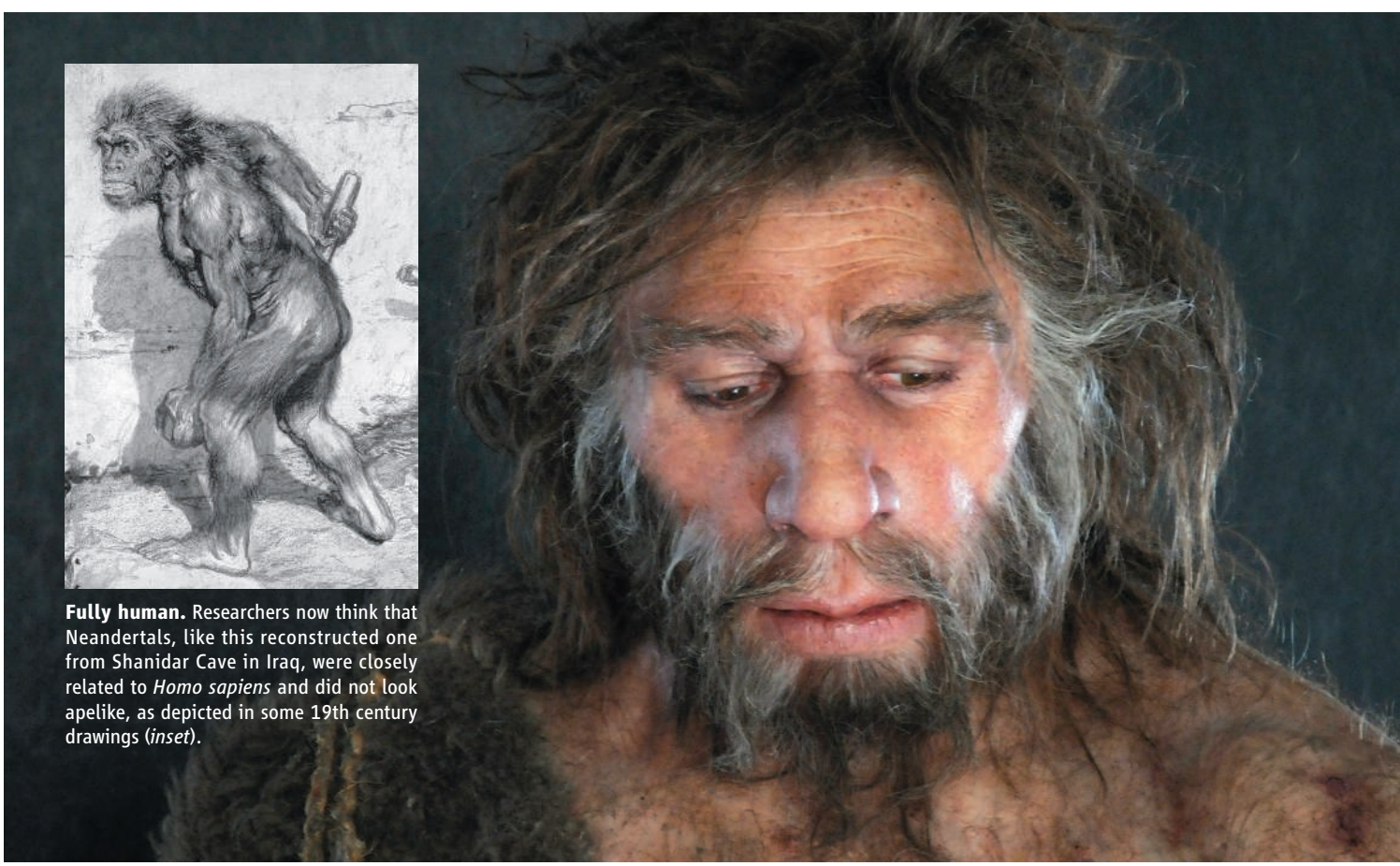

Fully human. Researchers now think that Neandertals, like this reconstructed one from Shanidar Cave in Iraq, were closely related to *Homo sapiens* and did not look apelike, as depicted in some 19th century drawings (*inset*).

CREDITS: (OPPOSITE) ©2007 PHOTO PHILLIPE PLAILLY EURELIOS/RECONSTRUCTION ATELIER DAYNÈS PARIS; (RIGHT) ©2008 PHOTO SEBASTIEN PLAILLY EURELIOS/RECONSTRUCTION ATELIER DAYNÈS PARIS; (INSET) MARY EVANS PICTURE LIBRARY/ILLUSTRATED LONDON NEWS LTD.

Published by AAAS

the artists work hard to insure that science drives their creations. Each job is unique, but paleoartists usually start with plaster or urethane skull casts of a hominin; for fragile or incomplete skulls, they use computed tomography scans to create a "virtual" plastic cast. Then the artists painstakingly model the muscles, glands, and fat tissues of the face with clay, making educated guesses about how thick each tissue should be and guided by dissections of primates and forensic anthropology techniques. After making a new cast in urethane or acrylic plastic, the paleoartist then painstakingly inserts individual hairs, often from humans, and paints and makes up the face. A similar process is followed with the rest of the body, for which the thickness of skeletal bones and the depth of muscle insertions guide the artists as they decide how slim or stocky to craft the body.

Although paleoartists normally consult closely with researchers, reconstructions take months to prepare and are sometimes out of date before they are finished. For example, in 2007, Paris-based paleoartist Elisabeth Daynès reconstructed the hobbit for the Musée de l'Homme in Paris. But she wasn't able to incorporate new evidence that the tiny hominin's shoulders were hunched forward (*Science*, 7 December 2007, p. 1531). Her newly completed second version, for the Swedish Museum of Natural History in Stockholm, gets the shoulders right and also includes new data showing that the hobbit's feet were particularly large.

Likewise, last year, *National Geographic* commissioned Netherlands-based paleoartists and twin brothers Adrie and Alfons Kennis to create a reconstruction of a female Neandertal nicknamed Wilma. The Kennis brothers gave Wilma penetrating blue eyes to go with her red hair, which ancient DNA studies suggest some Neandertals might have had. But then the magazine's editors spotted a study concluding that the mutation for blue eyes arose only about 10,000 years ago, after Neandertals were extinct. The editors first tried to use PhotoShop to change the eye color to brown, but the result "just looked dead," says *National Geographic* science editor James Shreve. "So I called the [scientist], and he said they could have had hazel eyes. So we gave her hazel eyes."

Adrie Kennis, who with Alfons has created many hominin reconstructions for European museums, says such compromises are necessary. "If only the scientists made the reconstructions, they would be dull. … We have to put a character on the face." For example, one key decision paleoartists face is whether to color the sclera of hominin eyes white, as in modern humans, or dark, as in many primates. In modern humans, eye whites make it easier for us to see where our fellow humans are gazing, thus enhancing social communication. But researchers know nothing about the sclera of earlier hominins. "It's a soft tissue we have no data on," says Potts, who adds that he and Gurche discussed at length how to handle the eyes of Gurche's sculptures for the human evolution hall.

Another issue is whether to put smiles on the ancient faces. "The fear muscles in great apes were co-opted for smile muscles in humans. We've gone back and forth, how much should they grimace and how much should they smile." In the end, Potts says, they have often gone for a neutral, "almost Mona Lisa kind of effect."

In contrast, when reconstructing a 3.3-million-year-old australopithecine child for *National Geographic*, the Kennis brothers opted to put a gooey smile on its face. But they did that without input from the fossil's discoverer, Alemseged. He was still excavating the skeleton and says he "was not comfortable" collaborating with the reconstruction. Instead, the twins worked from photos of the skull and a cast of another juvenile australopithecine as well as chimpanzee skulls. "The Kennis brothers are great artists," says Tattersall. "But I am not sure I would want to reconstruct the Dikika baby from photos. There is a huge temptation to anthropomorphize."

Yet another question mark is skin color. Gurche says he varies the hue of his creations depending on the latitude they lived in and so how much sunlight they were exposed to. Thus, he makes those australopithecines and other hominins who lived close to the equator—such as the hobbit and the African version of *H. erectus*—darker-

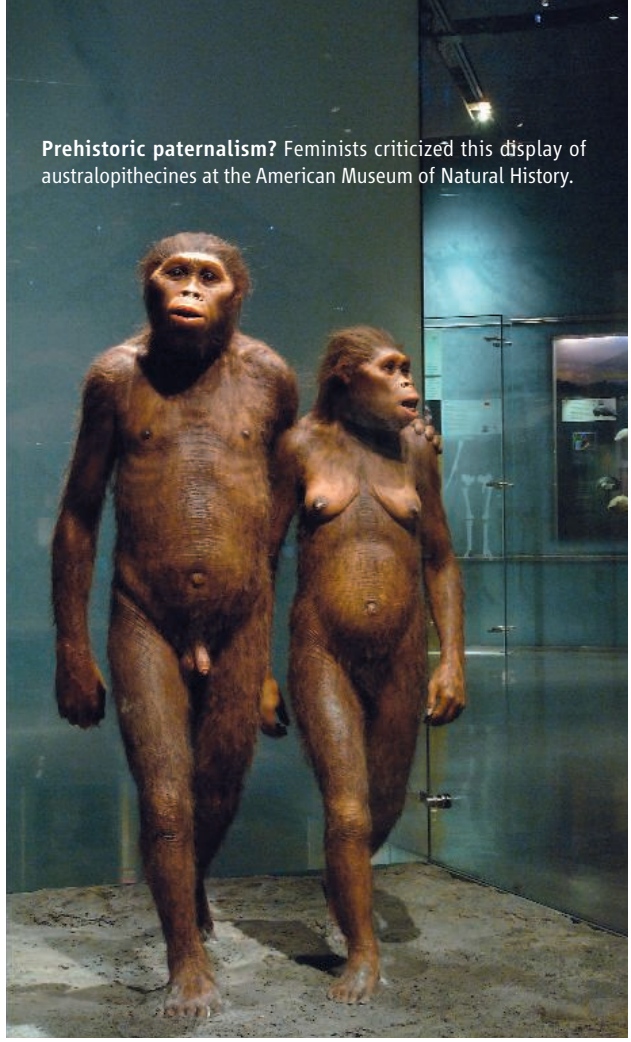

Prehistoric paternalism? Feminists criticized this display of australopithecines at the American Museum of Natural History.

Two artists, two views. The single skull of *Homo floresiensis* yields faces with different skin color and nose sizes, in reconstructions by Elisabeth Daynès (*left*) and John Gurche (*right*).

CREDITS (TOP TO BOTTOM): JULIE PRISLOE, (LEFT) © 2009 PHOTO SEBASTIEN PLAILLY/RECONSTRUCTION ATELIER DAYNÈS PARIS; (RIGHT) JOHN GURCHE

Published by AAAS

EVOLVING ARTISTS

How do you become a paleoartist? Judging from the successful few whose work shapes our ideas of ancient humans (see main text), there's no standard career path, but hefty doses of both artistic talent and scientific knowledge are essential. Although it may seem a rarefied field, the tradition of creating scientific depictions of ancient humans stretches back to the 19th century, when scientists began digging up Neandertals and other hominins and eagerly sought artists to depict their discoveries.

Today, paleoartists increasingly seek scientific training. For example, John Gurche, 57, loved both art and science as a child in Kansas. At age 10, he sculpted a series of heads depicting the stages of human evolution—a precocious version of work he has done for the Smithsonian Institution. He earned a master's degree in anthropology but quickly went into art rather than research, inspired by American artist Jay Matternes, who painted some of the first depictions of the australopithecine "Lucy" and produced numerous illustrations for *National Geographic*. "I saw that Jay Matternes was the main guy in the niche I was trying to bust into," says Gurche, adding that he and his contemporaries have now shifted the field from a focus on two-dimensional paintings to three-dimensional, lifelike models.

In the 1980s, Gurche began working in the lab of University of California, Santa Cruz, anthropologist Adrienne Zihlman, where he helped dissect the bodies of gorillas, chimps, and an orangutan. "John did so many measurements," Zihlman recalls. "Nothing was guesswork. How big was the eyeball and the socket, how thick was the fat around the cheeks." From his dissections and trips to Africa to view hominin fossils, Gurche put together a 60-page book for his own use on how to reconstruct a lifelike hominin from a skull or a smattering of postcranial bones.

A somewhat different career path was taken by Elisabeth Daynès, 49, who trained as an artist while growing up in Béziers, in the south of France. After moving to Paris, she specialized in makeup for cinema and theater and also became expert at making realistic masks. In 1988, a museum near the Lascaux Cave in the French Dordogne spotted her work and asked her to create a display including a mammoth and a group of early humans. Bitten by the prehistory bug, Daynès began working in anthropology labs to perfect her techniques. Her reconstructions have appeared in museums around Europe and on the covers of *National Geographic* and *Science* (2 March 2001). "She has this passion for her work that is hard to believe," says Zeresenay Alemseged, chair of anthropology at the California Academy of Sciences in San Francisco.

Like Daynès, Adrie and Alfons Kennis, 42, also began as artists. The identical-twin brothers attended art school in the Netherlands and intended to become art teachers. Their interest in human evolution began when they were 8 years old and made a clay model of a Neandertal to put on their Christmas tree, says Adrie. That passion turned into a full-time career in the late 1990s for the Arnhem, Netherlands–based pair. Their work is featured in numerous European museums and has also appeared on the cover of *National Geographic*.

Gurche, Daynès, and the Kennis brothers have all managed to convert their passions into successful businesses. But they are not alone. A handful of up-and-coming paleoartists wait in the wings to become members of this elite group.

–M.B.

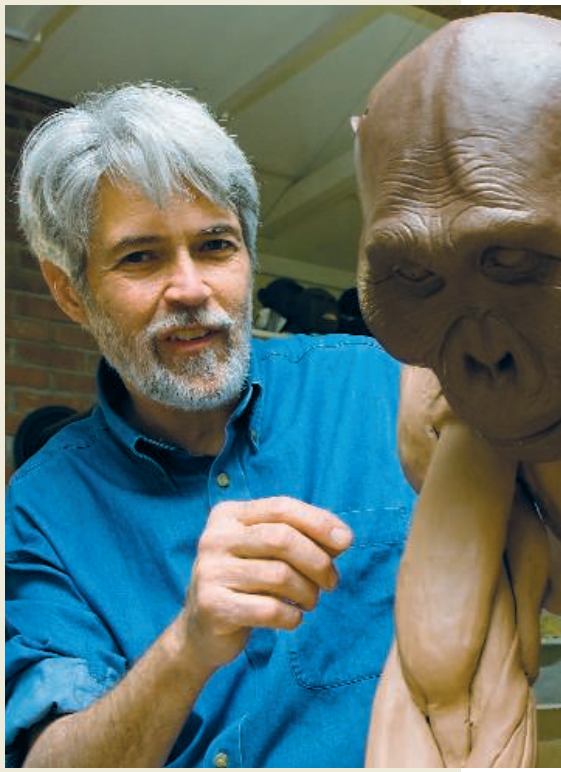

By the book. John Gurche uses 60 pages of rules to guide him in his reconstructions.

"Wilma" and the twins. Alfons (*left*) and Adrie Kennis with a female Neandertal work in progress.

CREDITS (TOP TO BOTTOM): COURTESY OF ALFONS KENNIS; AMNH/RODERICK MICKENS

skinned, whereas australopithecines from southern Africa and central-Asian *H. erectus* are depicted with somewhat lighter skin.

Such decisions sometimes run up against modern cultural debates, as Tattersall found out in the late 1980s when he collaborated with paleoartists to create a diorama at AMNH based on hominin footprints from Laetoli, Tanzania. The exhibit included a replica of the footprints and the figures of two australopithecines, a larger male and a smaller female, walking closely together with the male's arm around the female's shoulder.

"We were excoriated by the feminists for such a paternalistic image," says Tattersall, who insists that the footprints indicate the two individuals were walking so closely together that they had to be touching. One of the critics was University of California, Santa Cruz, anthropologist Adrienne Zihlman, who in a 1997 edited volume criticized the still-controversial assumption that size differences in australopithecines represent males and females rather than different species. She also challenged the notion "that the more powerful male protects and reassures the frightened and presumed weaker female." In her view, much of the work that human evolution researchers do today is based on conjecture as well as hard science. The paleoartists, Zihlman told *Science*, "are doing what the rest of us do. Most of what we do is part art and part science."

But if the union between art and science is at times an uneasy one, it is nevertheless a marriage from which everyone, including the public, seems to benefit. Says Sawyer: "This is the closest we are ever going to get to knowing what these hominins really looked like."

–MICHAEL BALTER

PANDEMIC INFLUENZA

Straight From the Pig's Mouth: Swine Research With Swine Influenzas

If the novel H1N1 virus behaves like its ancestors, humans may have a rough road ahead, especially if takes hold on hog farms

To borrow a line from the movie *Babe* about a precocious piglet, there was a time, not so long ago, when pig flu researchers were afforded little respect except by other pig researchers. Important swine influenza discoveries were relegated to *Veterinary Microbiology* and other specialty journals, while highly lethal avian influenza won all the headlines. But now, pig studies have taken on a new cachet because of the swine origins of the 2009 A(H1N1) strain that's causing the current pandemic—and the community's eerily prescient predictions that something like it was bound to make headway in humans. "If we don't have veterinarians working with good medical scientists here, we're in real doo-doo," says veterinarian and swine influenza expert Jürgen Richt of Kansas State University's College of Veterinary Medicine in Manhattan.

Human influenza researchers, who mainly work with ferrets and mice as models, have turned up provocative findings about the new virus in a remarkably short time. Yet the veterinarians who do most of the flu studies with pigs, primarily to help pig farmers, are well placed to make a unique contribution. They know the closest relatives of the novel H1N1 virus intimately, and their studies are offering critical clues to its genetic origins as well as sobering insights about how it may evolve.

Pigs have long been known to play a special role in the spread of influenza viruses among different species. Pigs' tracheal cells have receptors on the surface that welcome both avian and human strains. Human cells, in contrast, by and large shut out bird influenzas. (The H5N1 that causes deadly avian influenza has mostly infected chicken farmers who are exposed to huge doses of virus.) This makes the pig a potential mixing vessel for viruses from different species to combine genes—a process called reassortment—possibly creating dangerous new human strains. But pig viruses circulating in pigs have been something of a bore until recently: The "classical" swine influenza virus isolated in 1930 in the United States remained stable for decades. "You could bet your house on that guy," says virologist Richard Webby of St. Jude Children's Research Hospital in Memphis, Tennessee.

Then in 1997, an H3N2 that was mostly human in origin emerged in North American pigs, and the next year, researchers found a human/avian/swine H3N2 mishmash—a triple reassortant—that quickly became the dominant virus in pigs. Triple reassortants have continued to evolve in pigs at a breakneck pace, mixing and matching genes with aplomb. "They're quite promiscuous," says veterinarian Amy Vincent, a leading swine flu researcher at the National Animal Disease Center in Ames, Iowa, part of the U.S. Department of Agriculture (USDA).

Although the 2009 A(H1N1), also a triple reassortant, descends from this family of swine viruses, it is the first one that readily transmits the disease from human to human. No one yet knows why it has this property, but Vincent and others say close comparisons among the new variant and its older relatives may uncover the genetic properties that enable it to spread and thrive in humans. They wonder, too, whether the new virus will share its ancestor's penchant for reassortment, which has kept pig researchers scrambling to keep up with new strains. "It's been a very confusing picture for the last 12 years," says virologist Christopher Olsen, whose group at the University of Wisconsin, Madison, School of Veterinary Medicine was one of the first to isolate the pig triple reassortants.

Vincent and her colleagues have discovered what they contend is an important factor driving the success of the triple reassortants in pigs. Influenza has eight genes: six code for internal proteins and two for the surface proteins hemagglutinin and neuraminidase (the "H" and "N" in H1N1). All of the triple reassortants that have established themselves in swine populations contain the same internal genes. Vincent's group calls this the triple reassortant internal gene (TRIG) cassette. "This TRIG cassette may be a very fit combination of influenza A genes that are able to pick and choose neuraminidase and hemagglutinin genes," says Kelly Lager, who works with Vincent. "If the TRIG cassette does in humans what it does in pigs, that's not a good thing."

Lager, Vincent, and Webby signaled TRIG's dangerous potential for humans in a paper they published in the 26 December 2007 issue of the *Proceedings of the National Academy of Sciences*. The study focused on two highly similar H2N3 viruses isolated the year before from pigs on different commercial farms in Missouri that had no known connections. They found that the pigs had picked up both the H2 and the N3 from birds, possibly from pond water contaminated by infected waterfowl. The last H2 seen in humans caused a pandemic in 1957. "That was a wake-up call to us and our human health partners," says Vincent. "Many of us would not have immunity to H2N2 that circulated in the late '50s."

The novel H1N1 now circulating in humans has a key difference from the triple reassortants in North American pigs: Two of its genes trace back to Eurasian swine. One codes for neuraminidase, which the TRIG routinely replaces. But the other codes for matrix, an internal protein. So the new virus, in effect, violates TRIG. "The Eurasian matrix is the wild card," says Vincent, who says it is a "good hunch" that it may shed light on the novel H1N1's spread among humans.

Kansas State's Richt, who formerly worked with the USDA

Intentional infection. USDA's Amy Vincent (*right*) and Kelly Lager have put the novel virus into pigs to see how it behaves.

CREDIT: NATIONAL ANIMAL DISEASE CENTER/USDA/ARS

Published by AAAS

group, thinks the Eurasian neuraminidase is the wild card. Richt agrees that the TRIG cassette is important to the ascendancy of the triple reassortant viruses in pigs but says only three polymerase genes—not matrix or the two other internal genes—must remain the same. Mechanistically, neuraminidase also makes sense, he says, because it codes for a protein that controls how much virus a cell releases, or sheds. And more shedding means more virus is sprayed by a cough or dripped from a nose, increasing the chance of transmission.

Richt is keeping an open mind; he's particularly interested in engineering the Eurasian matrix and neuraminidase genes into an unusual swine flu virus that infected 26 people who visited a pig barn at the Huron County Fair in Norwalk, Ohio, in August 2007. "The Ohio virus shed like crazy," notes Richt. The virus did not transmit among humans, but Vincent and colleagues warned about its potential in a paper published online in January in *Veterinary Microbiology*. "This report underscores the need for vigilance in examining influenza A viruses from swine (and other species) for human potential in addition to the major focus currently placed on avian influenza viruses," they wrote. Ultimately, Richt would like to conduct pig and monkey experiments with newly constructed Ohio–novel H1N1 hybrids to see how different gene combinations affect their replication and spread.

Malik Peiris, a virologist at Hong Kong University who did key work with the H5N1 virus, cautions that several factors may account for the novel H1N1's success in humans. "The Eurasian matrix and neuraminidase are obvious suspects because these are new, but sometimes it's the constellation, the fitting together of things, rather than one thing," he says.

Peiris's own lab has focused on another baffling riddle about the new virus: Where did it come from? To date, the novel H1N1 virus has surfaced in pigs at only two farms, one in Canada and, more recently, one in Argentina. Officials suspect that in each case a human transmitted the virus to the herds. Adding to the mystery, a detailed genetic study by Peiris and colleagues published online in *Nature* on 11 June shows that the closest known isolates to the novel strain circulated in pigs more than a decade ago, suggesting that the new virus lurked undetected in pigs for many years. Or maybe, as the *Nature* paper suggests, the virus hid in birds or some other species. "We've been a strong advocate for not blaming the pig without evidence," says Ian Brown, whose group at the Veterinary Laboratories Agency (VLA) in Surrey, U.K., was the first to report that experimentally infected pigs could transmit the new virus to other pigs.

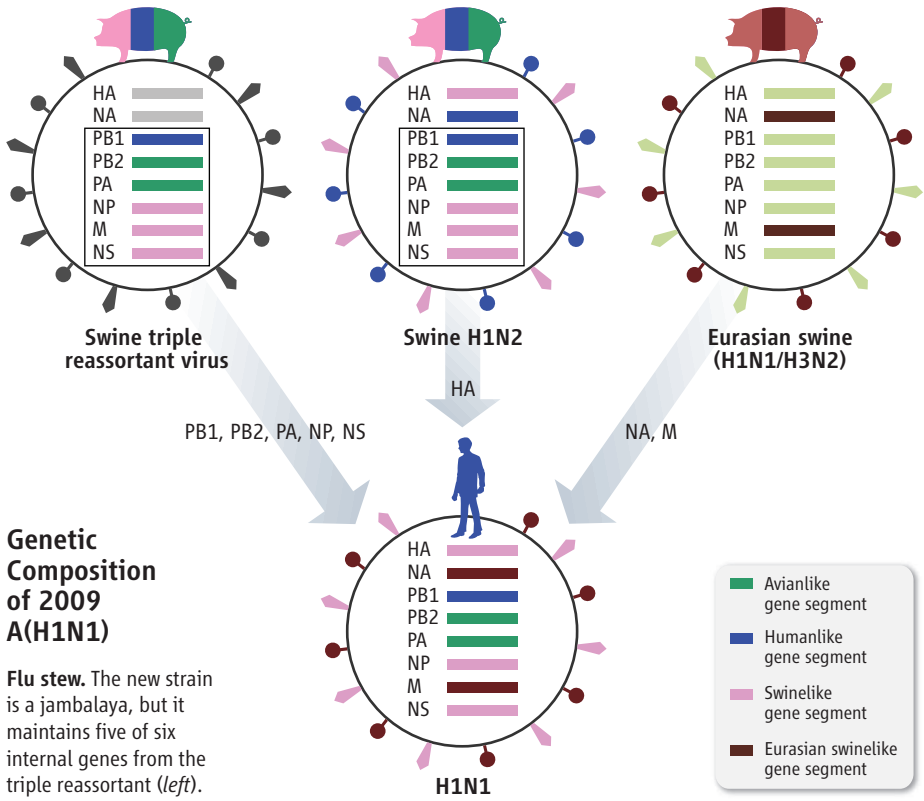

Genetic Composition of 2009 A(H1N1)

Flu stew. The new strain is a jambalaya, but it maintains five of six internal genes from the triple reassortant (*left*).

CREDIT: ADAPTED FROM JÜRGEN A. RICHT/KANSAS STATE UNIVERSITY

David Swayne, director of USDA's Southeast Poultry Research Laboratory in Athens, Georgia, says the evidence is leaning against birds as the missing link. His group recently tested the new virus in turkeys, chickens, ducks, and Japanese quail. Although some became infected, none transmitted the virus.

Peiris and many other researchers suspect that the virus circulated in pigs and went unnoticed because of patchy surveillance. That said, Peiris, who has sampled pigs each month for several years in a Hong Kong slaughterhouse, doubts that the virus circulated near him. "If it happened in Hong Kong, we definitely would have picked it up," he says. Similarly, VLA's Brown and USDA's Vincent say it's unlikely that passive surveillance—which relies on farmers and vets reporting cases of sick pigs—in Europe and the United States would have missed the novel virus if it caused disease in commercial herds. "It's quite conceivable that the parent viruses were kicking around in pigs in Mexico and Central America, because there's no surveillance there," suggests Peiris.

Researchers widely agree that countries everywhere need to step up surveillance for the virus in pigs. There's also growing interest in making a novel H1N1 vaccine for swine, says Richt, who has been contacted by several companies. But right now, no government has allocated money for increased surveillance, and there's no market to prevent a disease that so far has affected just two herds.

Humans, of course, can spread the virus, and, in a bizarre twist, an increasing worry is that we will start routinely infecting pigs. Preliminary data from USDA suggest that pigs have limited immunity against the new strain, indicating that virus should spread easily among animals, as happened in Canada, Argentina, and the U.K. experiment. "The chances are high that this will eventually become pandemic in pigs," says Richt. And that, says Peiris, "opens another Pandora's box." If the novel H1N1 infects many pigs, it increases the likelihood of the virus mixing with an avian strain that humans have no immunity to, like the deadly H5N1. "I wouldn't put that high on the probability scale, but that is quite a scary scenario," says Peiris.

Brown counters that both the 1918 and 1968 human pandemic viruses went into pigs without later returning to wreak havoc in humans. "We only have $n = 2$, and that's not a lot to go on, but they didn't evolve into something that came back in a more dangerous form," says Brown. "The biggest threat to public health now is people and the virus evolving in them."

Then again, the University of Wisconsin's Olsen, who has studied a bevy of swine influenzas, has this advice about what these viruses might do: "Never say never. And never say always." **–JON COHEN**

GENETICS

Genomic Clues to DNA Treasure Sometimes Lead Nowhere

Geneticists used to think that important DNA sequences always reject mutations. Now they are not so sure what sequence conservation really means

For many biologists, evolution does more than organize the history of life. It also guides them to hidden treasures in our DNA. When a gene works, evolution holds on to it, keeping its sequence intact even as bases around it change over time. Genome researchers had come to depend on this conservation to steer them to critical regions in the genome: If a stretch of DNA remains unchanged across different species, that DNA is probably performing a vital function. But as Eddy Rubin found out, that's not always the case.

For several years, Rubin, Len Pennacchio, and their colleagues at the Lawrence Berkeley National Laboratory (LBNL) in California have combed the genome for regions that regulate genetic activity. Because the so-called enhancers that they study can influence genes thousands of bases away, there are few obvious landmarks to help locate them. So the researchers looked at "ultraconserved" 200-base-long sequences previously found to be identical in rats, mice, and humans and at others that were similar even in fish. The strategy worked—or so they thought. When they inserted those sequences into mice, more than half turned on an accompanying reporter gene in particular tissues at a specific developmental stage.

But when the LBNL team looked deeper at four promising candidates, they were surprised that none of them caused any obvious problem when deleted from the mouse genome. "There are a lot of [sequences] that we thought if we knocked [one] out, it would kill the animal," Rubin recalls—but that didn't happen.

Results like these are causing Rubin and others to take a closer look at just how tightly conservation and function are linked. A growing number of examples show that not all conserved sequences are important and, worse, that not all important sequences are conserved. That second observation—which would have been considered heresy until about a decade ago—means that researchers who had typically relied on conservation to guide them could have missed critical genes or unknown regulatory regions. "It does question an awful lot about what's going on," says Laurence Hurst, an evolutionary geneticist at the University of Bath in the United Kingdom. But even as he and others scramble to understand how the "conservation equals function" rule has failed them, they are uncovering profound new subtleties in how genes are controlled and how they adapt during evolution.

Missing function

The most extensive data relating function and conservation come from the 2007 results of the pilot phase of the ENCyclopedia Of DNA Elements (ENCODE) consortium, which examined a selected 1% of the human genome. Along with many other tests, the researchers evaluated conservation of these human DNA sequences by comparing them with related regions in other vertebrates or between people.

For most regions, mutations that have accumulated over time have resulted in many differences between the bases. The longer it's been since two species parted ways, the more differences there are. But some sequences, particularly in genes, differ less than others. If a sequence is more conserved than expected, researchers ascribe the difference to "constraint," inferring that mutations were rejected during evolution because they reduced the organism's fitness. In genes, those mutations could be particularly deleterious and often are quickly weeded out.

The ENCODE team estimated that about 5% of the human genome is constrained to some degree, as hinted by previous studies. Of this, only about 25% to 30% matched with protein-coding regions. (Overall, protein-coding genes represented only about 1.5% of the DNA in the ENCODE regions.) Most of the remaining constrained sequence was transcribed into RNA—despite being "noncoding" DNA. The constraint suggested that this RNA might help regulate genetic activity.

To test this idea, the ENCODE team assessed biochemical activity throughout the chosen regions, including the constrained noncoding sequences. The researchers looked at whether the DNA binds transcription factors and whether either the DNA or the proteins that package it are chemically altered to silence or stimulate its activity.

CREDIT: MATTHEW TWOMBLY

Published by AAAS

"We expected all the other [biochemically] functional sequences that we identified to start overlapping the remaining 75% [of the constrained regions]," says Elliott Margulies of the National Human Genome Research Institute in Rockville, Maryland, but only about 60% showed any clear signal in their assays. That leaves 15% of the sequences showing some constraint for no apparent reason.

Some researchers have suggested that the missing functionality is a laboratory artifact: The sequences' true role would be apparent only in a more challenging real-life environment. But in work published in the January issue of *PLoS Genetics*, Jianzhi Zhang and his colleagues at the University of Michigan, Ann Arbor, found no correlation between the degree of conservation in a sequence and its function, even for yeast genes that proved essential in 400 highly varied conditions. "It was not due to the mismatch between lab and environment," concludes Zhang.

Indeed, some conserved regions may truly have no function. "Simply because a sequence is conserved, one should not jump to conclusions," cautions Eugene Koonin of the National Center for Biotechnology Information in Bethesda, Maryland, especially if the conservation is weak. Conserved noncoding introns within eukaryotic genes, for example, may have survived not because they do anything but because "selective pressure might not have been sufficient over all this span of evolution to get rid of them," he says.

Lack of constraint

Researchers can rationalize the existence of constrained sequences that have no detected function, but they are truly baffled when clearly important sequences seem hardly more conserved than the rest of the genome. In one early example, Hurst and his Bath colleague Nick Smith showed 10 years ago that dozens of essential genes, without which mice die, have accumulated as many mutations since mice diverged from rats as have nonessential genes, whose absence is tolerated.

Hurst recalls that when he began, "molecular biologists said, 'Why would you want to do that?' " The reason, he says, is that he had begun to realize that the widespread confidence in the connection between conservation and function had virtually no experimental backing. The study is now regarded as seminal, but for many years, the result "just seemed to be completely overlooked," Hurst says.

Since then, other worrisome data have appeared. In a 2003 paper, for example, Koonin and his colleagues found only a modest correlation between sequence conservation and function, a connection detectable only after they sampled enough genes to make it statistically significant. And the ENCODE pilot results have confirmed Hurst's suspicions. "Of all of these functional sequences, a large portion showed no evidence of evolutionary constraint," says Margulies. "That was the big surprise." Ongoing ENCODE analyses have not shed any new light on this mystery.

Researchers are keen to understand how important sequences evade evolutionary pressure, and they have proposed many explanations. One is that a sequence may play a vital role in only one of the compared species but not in others. Sequences that fish use for fins, for example, may mutate without penalty in other vertebrates. Comparing many different species, some close and some distant, reveals such lineage-specific genes, says Ross Hardison of Pennsylvania State University, University Park. Comparing many species should also reveal when important genes are free to mutate because another gene picks up the slack. Rubin, for one, thinks this is a common occurrence. "I think there's a lot of redundancy," he says.

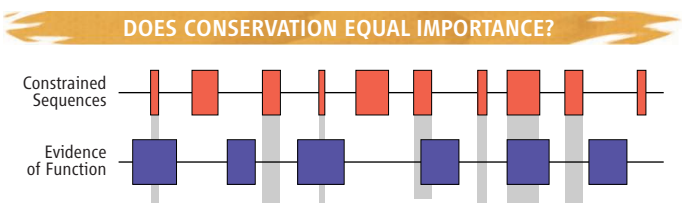

Imperfect correlation. Not all DNA conserved between species (red) coincides with functional sequence (blue) and vice versa.

Sometimes, biochemical assays may detect activity that has no cellular impact, making nonconserved sequences—such as those in the ENCODE data set—seem important when they really are not. "You might get reproducible transcription, or reproducible protein binding to DNA at specific locations, but they have no biological consequence to the organism," says Margulies.

Beyond sequence

Other, more subtle types of constraints exist that researchers are only now coming to appreciate. "Our view of functional sequences and evolutionary constraint in some ways has been tainted by the first functional sequence that we've known about—namely, protein-coding genes," says Margulies. For example, mutations that create a new three-base codon for the same amino acid and thus leave the protein intact were long thought to be unconstrained because they supposedly have no consequence. (TTT and TTC both code for phenylalanine, for example.) But researchers have found that even these "synonymous" mutations make an evolutionary difference. In one recent example, Joshua Plotkin of the University of Pennsylvania and his colleagues made more than 150 versions of a gene for green fluorescent protein, varying the sequence at synonymous sites. In *Escherichia coli*, the amount of protein varied 250-fold, in large part because codons differentially affected the stability of the messenger RNA produced, they reported in the 10 April issue of *Science* (p. 255).

For noncoding regions, constraint may depend on other properties that are still only partially understood. For example, if the DNA (and thus the RNA transcribed from it) includes nearly complementary segments oriented in opposite directions, the two resulting RNA segments can fold together to form a "stem-loop" structure. Such structures form a key piece of many regulatory RNA molecules and thus tend to be conserved, but their sequence signature is completely different from that of proteins.

The DNA sequence also modifies the interactions with regulatory, DNA-binding proteins. In the 17 April issue of *Science* (p. 389), Margulies, Boston University chemist Thomas Tullius, and their colleagues explored how the local sequence of DNA alters its shape and thus its accessibility to solvent molecules. This approach, Margulies says, "can identify roughly twice as much sequence that's under evolutionary constraint as some of these other methods that look at primary sequence alone."

Clearly, assessing the importance of a DNA sequence is harder than just comparing its bases between species. What researchers need is more data, both genetic and functional, in a variety of species, individuals, and tissues, says Ewan Birney of the European Bioinformatics Institute in Hinxton, U.K., to understand the ways that the conservation-function link breaks and, from there, to discern both the mechanisms of genetic regulation and the complex ways that evolution creates and preserves functions. "Constraint is still an enormously useful tool to identify important sequences in the human genome," notes Greg Cooper of the University of Washington, Seattle. But it doesn't find everything. "Truth be told," he adds, "we really don't know what we're missing." **–DON MONROE**

Don Monroe is a freelance writer based in New Jersey.

CREDIT: ADAPTED FROM MARGULIES *ET AL.*, *GENOME RESEARCH* 2007

IMMUNOLOGY

Take-Charge B Cells Create a Buzz

Long regarded as the source of antibodies, B cells are gaining new respect because some appear to fine-tune the overall immune response

Immunologists who study B cells have been feeling left out. For years, their colleagues who specialize in T cells—another kind of lymphocyte in the immune system—have rhapsodized about regulatory T cells. The top immunology journals, and even broader interest titles such as *Science* and *The New England Journal of Medicine*, have published paper after paper exploring how regulatory T cells—fondly known as Tregs—dial down immune attacks and stave off autoimmune diseases (*Science*, 6 August 2004, p. 772). And B cell researchers have had to sit silently while seminar speakers talked up Tregs' potential for treating everything from allergies to organ rejection to cancer. B cells, in contrast, haven't sparked this attention, often being dismissed as mere antibody factories.

But that may be changing. In the past few years, researchers have discovered that certain B cells appear to share with Tregs the responsibility for keeping the immune system under control. Like Tregs, these B cells, which some experts have named regulatory B cells, or Bregs, release anti-inflammatory molecules and can forestall autoimmunity when infused into mice.

Scientists studying regulatory B cells had a hard time convincing some of their colleagues that such cells even exist. Now they have a persuasive case—at least in rodents. Yet much about these cells remains murky. Researchers are still wrestling with fundamental questions, such as which B cells are regulators, what triggers them to assume the role, and how they exert their influence on the immune system. Even the terminology is up in the air, as some immunologists bridle at the term "regulatory B cells," contending that it suggests a misleading equivalence with Tregs. The field also features its own version of the nature-vs.-nurture debate over the origin of regulatory B cells. "Whether they are different from the start or whether they need different environmental conditions to develop isn't clear," says pathologist Atul Bhan of Harvard Medical School in Boston.

Nevertheless, some scientists are predicting big things for these cells, which may play roles in autoimmune disorders and cancer. For example, it might be possible to harness the cells to quell the self-directed immune attacks of diseases such as lupus and multiple sclerosis (MS)—much as researchers are trying to do with Tregs. "They will be as interesting and as important as all the subsets of regulatory T cells," says immunologist Thomas Tedder of Duke University Medical Center in Durham, North Carolina.

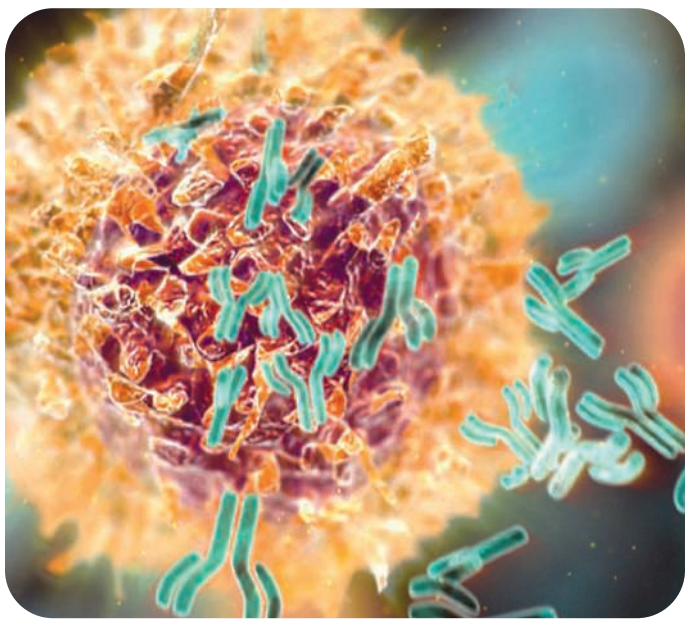

In control. Most B cells make antibodies (*above*), but others may regulate immune responses and protect us from autoimmunity.

CREDIT: F. HOFFMANN-LA ROCHE LTD.

More than an antibody machine

When most people think of B cells, they think of antibodies. After a pathogen infiltrates the body, mature B cells that recognize it specialize into plasma cells that do little else during their 1- or 2-week life span than churn out the microbe-fighting proteins. Over the years, however, researchers have expanded B cells' job description. B cells can also serve as antigen-presenting cells, showing off molecular bits of microbes to other immune cells and helping initiate a counterattack.

The first papers to suggest that B cells more broadly orchestrate immune responses date from the 1970s. According to immunologist Frances Lund of the University of Rochester in New York, the field was slow to embrace the idea because scientists were convinced that the cytokines, chemical messengers for the immune system, released by B cells had little impact on other cells. A 2000 *Nature Immunology* paper by Lund and her colleagues helped change researchers' minds. The team found that the cytokine cocktail emitted by B cells determines whether helper T cells specialize for fighting certain bacteria and viruses or for fighting parasitic worms.

That finding indicated that B cell cytokines could rouse the immune system, not that they could tame it. By showing that B cells also do the latter, two key papers made 2002 a watershed year for the field. In one study, Bhan and colleagues investigated B cell–deficient mice that they had induced to develop an autoimmune intestinal inflammation similar to human colitis. Immunologists knew that Tregs making the cytokine interleukin-10 can soothe an overactive immune system, so the researchers identified a subset of B cells that produce IL-10 and showed that transferring those cells into the mice could stem the gut inflammation. B cells unable to manufacture IL-10 had no effect. In the second study, immunologists Stephen Anderton, Simon Fillatreau, David Gray, and colleagues, all then at the University of Edinburgh in the United Kingdom, revealed similar results for EAE, the rodent equivalent of MS. Adding IL-10–making B cells to mice that were missing their entire B cell repertoire could alleviate the autoimmune condition. "Those papers were the first to demonstrate in a systematic way that IL-10 production by B cells could regulate immune responses," says Lund.

The identity of these managerial cells sparked the closest thing the field has to a controversy. B cells come in multiple varieties, or subsets, each of which sports a unique combination of protein markers on its surface. Which subtypes serve as regulators remains a matter of dispute. What researchers have yet to discover, says Claudia Mauri, an immunologist and Breg evangelist at University College London, is the B cell equivalent of Foxp3, a transcription factor that distinguishes some kinds of regulatory T cells because it is not made in other T cell types.

In lieu of a distinctive marker, Tedder's group has been sifting through mouse B cells

Published by AAAS

for those that make IL-10. The cytokine isn't an ideal identifier, however, because other immune cells that may contaminate samples can fashion it. Nonetheless, Tedder's team says it has isolated a lymphocyte subset called B10 cells that constitutes 1% to 3% of the B cells in the spleen and accounts for almost all of the IL-10 released by B cells. Tedder is convinced that these are regulatory B cells.

Mauri and her colleagues also went looking for IL-10–producing B cells in the spleen and found a different variety, known as T2-marginal zone precursor cells. The two groups' cells differ in one significant way: Unlike Tedder's B10 cells, Mauri's still appear immature, meaning they don't have the pattern of surface markers indicating that they have completed their development. Despite that, these precursor cells had the power to curb autoimmunity, the team revealed in 2007. Infusions of them reduced joint damage in mice that had arthritis and prevented rodents with healthy cartilage from developing the autoimmune condition. Mature marginal zone B cells weren't protective, however.

Whether the cells have finished development relates to the question of which antigens—if any—are necessary to spur Bregs into action. Mature B cells mobilize in response to particular antigens. When you have the flu, for example, only those mature B cells whose surface-bound antibody receptors match the flu virus's proteins transform into plasma cells that then secrete those antibodies in large quantities. But callow B cells can't yet recognize antigens, Mauri says, suggesting that Bregs don't require such specific stimulation.

The rival teams could both be right. Just as there are multiple subsets of Tregs—more than 30, by one researcher's count—there are probably several varieties of Bregs, Tedder says.

Stimulating questions

What drives a B cell to take control versus fulfilling its more typical destiny of becoming a plasma cell? According to one scenario, a select few B cells are born immune-system managers, specializing for the job during their development in the bone marrow. That same type of early commitment characterizes one subset of Tregs, so it could hold true for Bregs, too. Some researchers hold a more democratic view. "It's possible that any B cell could become a regulatory B cell," says Fillatreau, who's now at the Deutsches Rheuma-ForschungsZentrum Berlin, a rheumatology institute in Berlin. All it might take, he says, is the right stimulation.

In a study published last year, Fillatreau, Anderton, and Gray argue that the decisive signal comes through Toll-like receptors (TLRs), proteins on the surface of some body cells that detect pathogen molecules. TLR activation is necessary, whether the B cell is going to make antibodies or regulate, the team notes. However, the researchers hypothesize that stimulation of certain TLRs ramps up IL-10 output, turning a B cell into a regulator. Prodding other TLRs would yield a defensive B cell.

Why B cells might respond differently to different TLRs—and thus to different pathogens—isn't clear. But as a way to prevent autoimmunity, reliance on these receptors to induce Bregs makes sense, says neuroimmunologist Amit Bar-Or of McGill University in Montreal, Canada. Even as the immune system reacts to TLR activation and rapidly deploys cells to fight a pathogen, it's also creating a force of regulatory cells to rein in the counterattack before collateral damage to body tissues results, he explains.

The most recent word on Breg origins came in a paper published last month in *The Journal of Immunology* in which Tedder and colleagues further refined the picture of B10 cells. After tracking their maturation in culture, the scientists discovered that some spleen cells started down the road toward becoming B10 cells but became functional IL-10 releasers only after prodding by molecules from other immune cells or pathogens. The work suggests that nature and nurture conspire to generate regulatory B cells.

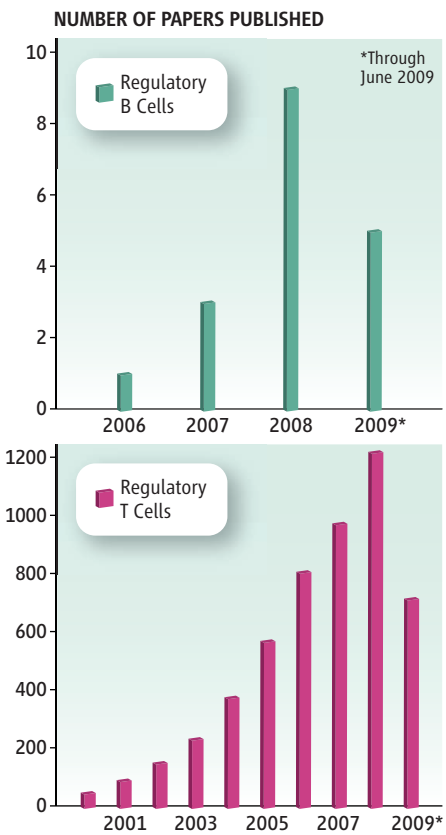

Slow growth. Regulatory B cell papers aren't as common as Treg papers, but the numbers are growing.

SOURCE: PUBMED

The human touch

Breg researchers have a clear hurdle to overcome before more immunologists—and biotech companies—pay further attention. "The next stage is to prove that they exist in humans," says Mauri. So far, immunologists have seen only hints of the cells' presence in people. Two years ago, for instance, Bar-Or and colleagues reported that B cells in MS patients pump out less IL-10.

Even without confirmation, researchers are already thinking of ways to put the cells to work. One option is to fine-tune an increasingly common treatment for autoimmune diseases such as rheumatoid arthritis and lupus. The therapy involves doses of the antibody rituximab, which knocks out all B cells in the body (*Science*, 23 November 2007, p. 1232), including ones that trigger autoimmunity by releasing self-directed antibodies or stimulatory cytokines. But the treatment fails in some patients, perhaps because the drug also culls Bregs. "We might remove all the bad B cells, but we might also remove the good B cells," says Mauri. If researchers can nail down cell surface markers found on Bregs but not on other B cells, they might be able to target only the "bad" B cells.

In other situations, the goal might be to get rid of the Bregs. Evidence suggests that the cells can abet cancer. For example, tumors abound in the peritoneal cavity, which teems with IL-10–making B cells, notes Lund. She adds that B cells often infiltrate tumors, perhaps drawn there by chemicals secreted by cancer cells trying to fend off immune attacks.

Although they are hopeful about Bregs' potential, researchers are also aware that, at least so far, Tregs have fallen short of their great medical expectations. Only a handful of clinical trials that involve Treg transfers have started, and a previous attempt to rouse the cells with an antibody nearly killed six people (*Science*, 24 March 2006, p. 1688).

And many questions about Bregs remain. The cells' involvement with Tregs is uncertain. How Bregs' other cytokines, including TGF-β, help IL-10 squelch autoimmunity is unclear. Whether the most famous B cell product—antibodies—have a role in the immune-soothing effect of Bregs is unknown. "That's why the field is so exciting. We don't know the answers to these big, important questons," says Tedder.

–MITCH LESLIE

4000 years of science 149

Fatigue and materials failure 156

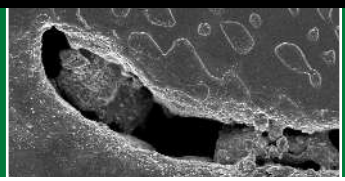

LETTERS | BOOKS | POLICY FORUM | EDUCATION FORUM | PERSPECTIVES

LETTERS

edited by Jennifer Sills

Saving African Lions

THE TRUTH ON AFRICAN SOIL IS DIFFERENT FROM THE OPINIONS formed by J. Guo and experts interviewed for the News Focus story "Will captive breeding save Africa's king of beasts?" (17 April, p. 331). The planned reintroduction programs do not involve lions cowed with sticks to ensure compliant behavior during a wilderness stroll with picture-posing tourists. The African Lion and Environmental Research Trust (ALERT) is certainly not following a "standard reintroduction protocol"—rather, it uses a highly innovative and experimental procedure constantly and objectively evaluated for effectiveness.

The inescapable facts are that lions are a bit thin on the ground at the present time, the great majority of protected areas in Africa are depopulated in terms of lions, and ALERT has received a great number of expressions of interest from various African government bodies to restore lion populations, and thereby system biodiversity and function, in such areas.

ALERT has a unique approach to restoring such populations. Others might opine that this constitutes no more than a drop in the bucket, but we believe that is better than the present empty container.

ANDREW CONOLLY

African Lion and Environmental Research Trust, Gweru, Zimbabwe. E-mail: awc@africanencounter.org

A Standardized Response to Biological Invasions

THE POLICY FORUM "WILL THREAT OF BIOlogical invasions unite the European Union?" (P. E. Hulme *et al.*, 3 April, p. 40) emphasized the major regulatory and political challenges faced by European institutions. However, they are not alone in facing the tremendous threat of biological invasions; this is a global challenge with infrastructure needs described nearly a decade ago (*1*). Hulme *et al.* emphasized that the perspective of Europe as the source, rather than recipient, of invasive alien species (IAS) needs revision. Other continents and countries face similar challenges. For example, as major forces in the world economy, China and the United States import and export substantial quantities of goods, which makes these two nations leading sources and recipients of IAS (*2*). However, inadequate funding, inappropriate methodology, and inconsistent data assembly have precluded generation of IAS inventories and have rendered conclusions about the percentage of IAS in the total flora and fauna of a region ambiguous. The number of information networks devoted to IAS is increasing globally, which may help to integrate IAS research at all scales, particularly if data sharing and compatibility can be improved. However, standardized information and technological platforms to share such information are lacking (*3*).

The concept of the European Centre for Invasive Species Management (ECISM), proposed by Hulme *et al*., could be extrapolated to all of the continents and adopted by every country with standardized methodology and scientific initiatives, much as the BioNET Locally Owned and Operated Partnerships are facilitating global collaboration in taxonomy (*4*). National and regional networks to share invasive species information should also freely share standardized tools, as is the goal of the Invasives Information Network of the Inter-American Biodiversity Information Network and the Global Invasive Species Information Network (*5*).

Combating the menace of invasions in a particular continent is not sufficient to manage this important global issue.

IRFAN RASHID,[1]* GYAN PRAKASH SHARMA,[2] KAREN J. ESLER,[2] ZAFAR A. RESHI,[1] ANZAR A. KHUROO,[1] ANNIE SIMPSON[3]

[1]Department of Botany, University of Kashmir, Srinagar, Jammu and Kashmir 190 006, India. [2]Centre for Invasion Biology, Department of Conservation Ecology and Entomology, Stellenbosch University, Stellenbosch 7602, South Africa. [3]National Biological Information Infrastructure, U.S. Geological Survey, Reston, VA 20192, USA.

*To whom correspondence should be addressed. E-mail: ecoirfan@yahoo.co.in

References

1. A. Ricciardi *et al.*, *Bioscience* **50**, 239 (2000).
2. P. T. Jenkins, H. A. Mooney, *Biol. Invasions* **8**, 1589 (2006).
3. J. Graham *et al.*, *Bioscience* **58**, 263 (2008).
4. A. Taylor, *Syst. Biodivers.* **2**, 111 (2004).
5. A. Simpson *et al.*, *Biol. Invasions* **8**, 1579 (2006).

Response

THE RECENT AVAILABILITY OF CONTINENTwide data on alien species, their pathways of entry, and probable impacts on the environment and economy (*1*) provide a strong platform on which to build a European strategy on invasive species (*2*). However, appropriate databases alone are not enough. Neither New Zealand nor Australia have access to the breadth of data now available to Europe, but through dedicated government agencies, these two countries invest heavily in border biosecurity and the management of alien invasions. For this reason, we recommend that the European Parliament consider establishing a single agency, the European Centre for

Letters to the Editor

Letters (~300 words) discuss material published in *Science* in the previous 3 months or issues of general interest. They can be submitted through the Web (www.submit2science.org) or by regular mail (1200 New York Ave., NW, Washington, DC 20005, USA). Letters are not acknowledged upon receipt, nor are authors generally consulted before publication. Whether published in full or in part, letters are subject to editing for clarity and space.

CREDIT: ALERT

Cell sizers and timers

158

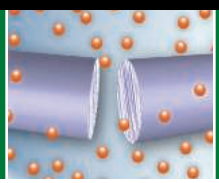

Advanced colloidal assembly

159

Invasive Species Management (ECISM), which will not only continue to update and manage the European alien species inventory but also provide advice, target new research, coordinate surveillance and response, identify emerging threats, support training, and increase public awareness (*3*).

The aims of a global information network are certainly laudable (*4*), but the focus has been on appropriate cyber-infrastructures rather than on applying the information to mitigate the effects of biological invasions (*5*). In the United States, more than 300 invasive species databases exist, more than half of which are online (*6*), yet under the National Invasive Species Management Plans, integration of this information through a single portal is not a goal (*7*). Invasive species databases, such as the Delivering Alien Invasive Species Inventories for Europe (DAISIE) Web portal (*8*), work best when they are designed to target the specific needs of regulatory and legislative institutions responsible for addressing threats to the environment, human health, or the economy (*9*). Once databases have been optimized to address management responsibilities and policy concerns, they can be further utilized to influence global international organizations such as the World Trade Organization (WTO). This pivotal link between alien species data and policy response is not explicit in current efforts to develop a global invasive species database (*4*, *5*). The outcome of the current discussions about a European invasive species strategy will not only send signals to other nations regarding the way forward on these issues, but will also clarify the future prospects of a globally supported strategy on invasive species.

PHILIP E. HULME,[1]* WOLFGANG NENTWIG,[2] PETR PYŠEK,[3] MONTSERRAT VILÀ[4]

[1]The Bio-Protection Research Centre, Lincoln University, Post Office Box 84, Canterbury, New Zealand. [2]Institute of Ecology and Evolution, University of Bern, Baltzerstrasse 6, CH-3012 Bern, Switzerland. [3]Institute of Botany, Academy of Sciences of the Czech Republic, CZ-252 43 Průhonice, and Department of Ecology, Charles University, CZ-128 01 Viničná 7, Prague, Czech Republic. [4]Estación Biológica de Doñana (EBD-CSIC), Avinguda Américo Vespucio, E-41092 Sevilla, Spain.

*To whom correspondence should be addressed. E-mail: philip.hulme@lincoln.ac.nz

References

1. DAISIE, *Handbook of Alien Species in Europe* (Springer, Dordrecht, Netherlands, 2009).
2. European Commission (EC), *Towards an EU Strategy on Invasive Species* [COM(2008) 789, EC, Brussels, 2008].
3. P. E. Hulme *et al. Neobiota* **8**, 3 (2009).
4. A. Ricciardi *et al.*, *Bioscience* **50**, 239 (2000).
5. J. Graham *et al.*, *Bioscience* **58**, 263 (2008).
6. A. W. Crall *et al.*, *Front. Ecol. Environ.*, **4**, 414 (2006).
7. National Invasive Species Management Plan, www.invasivespeciesinfo.gov/council/nmp.shtml (National Invasive Species Council, Washington, DC, 2008).
8. www.europe-aliens.org (DAISIE, Wallingford, UK, 2009).
9. P. E. Hulme *et al.*, in *Handbook of Alien Species in Europe*, DAISIE, Eds. (Springer, Dordrecht, Netherlands, 2009), pp. 1–14.

Neuroscientists Need Neuroethics Teaching

WITH THE ADVANCEMENT OF NEUROSCIENCES in recent years, there is a growing need to ensure that its students are educated in applied neuroethics as part of their formal studies. However, neuroethics education is not commonly an integrated part of neuroscience training. Discussions we have had with members of the Russell group, an association of the 20 major research-intensive universities in the United Kingdom, indicate that the majority of their neuroscience students do not receive formal neuroethics teaching.

Neuroscience research findings have begun to have far-reaching ethical implications on education, treatment, and even the law. For example, ascertaining that cognitive enhancing drugs not only improve performance in neuropsychiatric groups, but may also enhance cognition in young healthy adults has raised concerns and debate about the safety, access, and equity in education, work, and academic settings where taking drugs for enhancement purposes is becoming increasingly widespread (*1*, *2*). Functional magnetic resonance imaging has been used to identify residual cognitive function and conscious awareness in patients assumed to be in a vegetative state, yet who retain cognitive abilities that have evaded detection using standard clinical methods (*3*). Several companies offer neuromarketing and brain-based lie-detection services, which has raised concerns from the academic community at large about the use and misuse of neuroscientific results (*4*).

Neuroethical issues are surely going to become ever more pertinent with new developments in imaging analysis techniques, the simultaneous integration of multiple neuroimaging systems, and the linking of genetics with imaging. Although we realize that both students and lecturers are often plagued with already challenging schedules, we propose that as standard good practice, academic departments should ensure that mechanisms are in place for teaching neuroethics. A solid education in the neurosciences should encompass the ability to consider the ethical implications of one's research. Such an education will ultimately also promote future neuroscientists integrating socially relevant questions into their research and ensuring from an early stage that the public at large is supportive of advances in neuroscience.

BARBARA J. SAHAKIAN[1,2] AND SHARON MOREIN-ZAMIR[1]

[1]Department of Psychiatry, University of Cambridge School of Clinical Medicine, Addenbrooke's Hospital and the MRC/Wellcome Trust Behavioural and Clinical Neuroscience Institute (BCNI), University of Cambridge, Cambridge, UK. [2]Oxford Uehiro Centre for Practical Ethics, University of Oxford, Oxford, UK.

References

1. B. Sahakian, S. Morein-Zamir, *Nature* **450**, 1157 (2007).
2. H. Greely *et al.*, *Nature* **456**, 702 (2008).
3. A. M. Owen *et al.*, *Science* **313**, 1402 (2006).
4. E. Racine *et al.*, *Nat. Rev. Neurosci.* **6**, 159 (2005).

CORRECTIONS AND CLARIFICATIONS

Books *et al.*: "Pages to turn on a lazy day" (5 June, p. 1267). Contributor Barbara Fischer's affiliation was incorrect. She is at the University of Bern.

Perspectives: "What determines coral health?" by V. M. Weis and D. Allemand (29 May, p. 1153). The affiliation of Denis Allemand was incomplete. It should have read: "Centre Scientifique de Monaco, Avenue Saint-Martin, MC 98000 Monaco, Principality of Monaco, and Faculty of Science, University of Nice-Sophia Antipolis, F 06108 Nice Cedex 2, France. E-mail: allemand@centrescientifique.mc." The figure credit for panels D and E was incorrect. It should have read: "Panels D and E taken at Centre Commun de Microscopie Electronique, University of Nice-Sophia Antipolis."

Books *et al.*: "Three takes on people and water" (1 May, p. 593). The film *Blue Gold* was produced in the United States, and Ireen van Ditshuyzen's film is *Onze Kust* (Our Coast).

Reports: "Green evolution and dynamic adaptations revealed by genomes of the marine picoeukaryotes *Micromonas*" by A. Z. Worden *et al*. (10 April, p. 268). The affiliation listed for authors Panaud and Piegu was incorrect. They are at the Laboratoire Genome et Développement des Plantes, UMR CNRS/Institut pour la Recherche et le Développement/University of Perpignan Via Domitia, Université de Perpignan, 66860 Perpignan, France.

Reports: "A recessive mutation in the APP gene with dominant-negative effect on amyloidogenesis" by G. Di Fede *et al*. (13 March, p. 1473). The fourth sentence of the penultimate paragraph (p. 1476) of the main text describes a mutation at codon 673. The amino acid change should be Ala^{673} to Thr^{673} (A673T) rather than Ala to Tyr.

Reports: "Conductance of a single conjugated polymer as a continuous function of its length" by L. Lafferentz *et al*. (27 February, p. 1193). In addition to Leonhard Grill, Stefan Hecht (sh@chemie.hu-berlin.de) may be contacted as a corresponding author.

Reports: "DNA from pre-Clovis human coprolites in Oregon, North America" by M. T. P. Gilbert *et al*. (9 May 2008, p. 786). There were typographic errors in rows 5 and 6 of the second column (labeled Hg) in Table 1. In row 5, B§,§§ should have been B2§. In row 6, B2† should have been B†§§. The authors acknowledge H. Poinar, S. Fiedel, C. King, A. Devault, K. Bos, M. Kuch, and R. Debruyne for pointing out the error.

TECHNICAL COMMENT ABSTRACTS

Comment on "DNA from Pre-Clovis Human Coprolites in Oregon, North America"

Hendrik Poinar, Stuart Fiedel, Christine E. King, Alison M. Devault, Kirsti Bos, Melanie Kuch, Regis Debruyne

Gilbert *et al*. (Reports, 9 May 2008, p. 786) analyzed DNA from radiocarbon-dated paleofecal remains from Paisley Cave, Oregon, which ostensibly demonstrate a human presence in North America predating the well-established Clovis complex. We question the authenticity of their DNA results and argue that in the absence of intact stratigraphy and diagnostic artifacts, and in view of carbon isotope anomalies, the radiocarbon dates of the oldest specimens are unreliable.

Full text at www.sciencemag.org/cgi/content/full/325/5937/148-a

Response to Comment by Poinar *et al*. on "DNA from Pre-Clovis Human Coprolites in Oregon, North America"

M. Thomas P. Gilbert, Dennis L. Jenkins, Thomas F. G. Higham, Morten Rasmussen, Helena Malmström, Emma M. Svensson, Juan J. Sanchez, Linda Scott Cummings, Robert M. Yohe II, Michael Hofreiter, Anders Götherström, Eske Willerslev

The arguments of Poinar *et al*. neither challenge our conclusions nor would contribute to the verification of our data. We counter their questions about the authenticity of our ancient DNA results and the reliability of the radiocarbon data and stand by the conclusion that our data provide strong evidence of pre-Clovis Native Americans.

Full text at www.sciencemag.org/cgi/content/full/325/5937/148-b

Comment on "DNA from Pre-Clovis Human Coprolites in Oregon, North America"

Paul Goldberg, Francesco Berna, Richard I. Macphail

Gilbert *et al*. (Reports, 9 May 2008, p. 786) presented DNA analysis of coprolites recovered from an Oregon cave as evidence for a human presence in North America before the Clovis culture. Results of our micromorphological and Fourier transform infrared spectroscopy analyses of one of the reported coprolites are difficult to reconcile with the DNA results identifying the coprolite as human.

Full text at www.sciencemag.org/cgi/content/full/325/5937/148-c

Response to Comment by Goldberg *et al*. on "DNA from Pre-Clovis Human Coprolites in Oregon, North America"

Morten Rasmussen, Linda Scott Cummings, M. Thomas P. Gilbert, Vaughn Bryant, Colin Smith, Dennis L. Jenkins, Eske Willerslev

Goldberg *et al*. use data from micromorphological and Fourier transform infrared analyses to argue that Paisley Cave pre-Clovis coprolite 1374-5/5D-31-2 is of herbivore, rather than human, origin. We argue that the diagnostic capability of the techniques used by Goldberg *et al*. are limited, and we present new genetic data that support our original claims.

Full text at www.sciencemag.org/cgi/content/full/325/5937/148-d

Published by AAAS

HISTORY OF SCIENCE

Babylon, Newton, and All That

Michael D. Gordin

Everyone agrees that science has a history. Reflect a little, and you'll realize that science must have many histories: For while we often talk about a generalized ideal of "science," we usually hold in our minds one of several specific sciences, each with its own set of questions and stories. And then there is the inescapable fact that nothing humanly produced takes place in the same way everywhere. Warfare is global, too, but no one expects it to have a single history. You can write a history of science, but never the history of science.

Science
A Four Thousand Year History
by Patricia Fara
Oxford University Press, Oxford, 2009.
424 pp. $34.95, £20.
ISBN 9780199226894.

Which brings us to Patricia Fara's ambitious and intriguing *Science: A Four Thousand Year History*. In a series of short chapters—49, self-consciously grouped in seven groups of seven—Fara aims to chronicle the sheer multiplicity of endeavors that have been labeled as "science," "natural history," "natural philosophy," "mathematics," or any other such designation. It is a huge task, and one would be well within one's rights to expect such a venture to be necessarily incoherent, even impossible. This book will not fully resolve those doubts: there are the inevitable incoherences and impossibilities. But Fara (a historian of science at Cambridge University) has made an impressive and commendable effort to square the circle, to tell science's history, from the beginning.

When was that, exactly? Fara starts with Babylon, which is as good a place as any. The arithmetical records of Babylonian astronomy comprise perhaps the oldest documented investigations of the natural world: they are quantitative and collaborative and seek to predict the future positions of celestial bodies. But they also possess two features that confound any simple identification with "science": they lack geometric or physical models for the heavens, remaining content with numerologic regularities; and they are saturated with astrology. Fara selects Babylon as her origin not despite these features but because of them. It is the very dissonance, the jumbling together of incongruities, that fascinates her. (This is also why sevens percolate throughout her account—a tip of the hat to the many number mystics of past science. To appease the Babylonians, it would have been better to choose six, but no matter.)

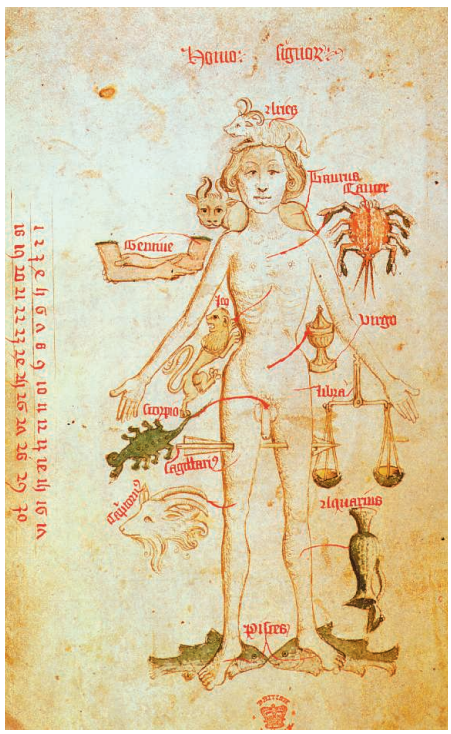

Astrological medicine. Zodiac man (1486) displays the association between parts of the body and star signs.

CREDIT: FROM *GUILDBOOK OF THE BARBER SURGEONS OF YORK*/THE BRITISH LIBRARY/THE ART ARCHIVE

Fara has not one birthplace for science, but three. The book is almost unique among popular surveys of the history of science in devoting substantial attention to the Chinese natural philosophical heritage. Almost as ancient as the Babylonian tradition, this is certainly the oldest continuous one, and Fara draws from recent scholarship to flesh out an interesting picture. But this attention peters out fairly early, as the book shifts to the more canonical origin for science.

That would be Europe. For all the attention that Fara devotes to debunking heroic narratives supposedly perpetrated by most historians of science—Isaac Newton draws her particular ire—from Babylon and China she goes on to replicate much of the standard narrative: first Greece, next a light touch on Rome (mostly Galen), the Christian West through to the early modern era, and then a slower pace from the 18th century to the present (with a heavy, some might say excessive, attention to developments in Britain). We only glimpse China once or twice more and never really see Latin America or Africa except from shipboard. (On the other hand, her account of science and medieval Islam is spot on.)

The author claims that she is offering a corrective to typical treatments in "[o]ld-fashioned histories of science," although the offenders are never specified and haven't been much in evidence for over a generation. The revisions are well chosen and include the importance of medieval universities, the role of public display, and the crucial science-religion interaction (not hostility). The details of her story are drawn substantially from the historical literature of recent years. But there are some unfortunate omissions, such as the exciting recent research in the history of alchemy—a far cry from the mystical, secret preoccupation Fara depicts, and instead something we might recognize as early chemistry.

Fara tries to situate certain heroes in context, so they don't stand as lone geniuses: "During their own lifetimes, scientific heroes often appeared less important than they do in retrospect, when they are admired for leading presciently towards a future that their contemporaries could not possibly have known about." Very true. So Newton is exposed, warts and all, and Galileo is shoehorned into a brief chapter with the rest of early modern astronomy. But these figures are replaced by new, only slightly less canonical heroes: René Descartes gets a chapter all to himself, and Francis Bacon appears often as a beacon. Perhaps the history of science does need to take its heroes down a peg, but replacing them with the very next tier is surely a stopgap solution.

Fara's *Science* attempts to span four thousand years, and it would be churlish to quibble and pettifog about this anecdote or that interpretation. The book can be read with profit as a general introduction to some of what has been happening in the history of science since the 1980s. It offers pretty exciting material. But fundamentally the scale of Fara's project overwhelms it. More science, however defined, has been done since 1945 than in all of history until then. Because Fara boldly takes the long view, she is regrettably forced to foreshorten the recent past. Instead of providing a rousing crescendo, the book's discussion of the present almost whimpers: "The problem is not that scientific technology is in itself bad, but that it can too easily become a tool for domination and coercion." Of science's many histories there is surely more to be said.

10.1126/science.1175513

The reviewer is at the Department of History, Princeton University, 129 Dickinson Hall, Princeton, NJ 08544–1017, USA. E-mail: mgordin@princeton.edu

AGRICULTURE

Tofu Was Just a Start

Michael A. Grusak

The World of Soy

Christine M. Du Bois, Chee-Beng Tan, and Sidney W. Mintz, Eds.

University of Illinois Press, Urbana, 2008.
350 pp. $40, £30.99.
ISBN 9780252033414.

How much soy have you eaten today? If you believe not much, then you'd better think again. Did you know that after 3000 years as an important food crop in China, soybean production in the United States rose from only negligible harvests just a century ago to almost 90 million metric tons in 2006–2007 (*1*)? Or that a comparable rise in production has been witnessed jointly in Brazil and Argentina, but occurring over just the past 50 years?

The diffusion of this versatile bean into diverse foodways and different agricultural economies around the globe and the range of factors that have influenced this diffusion are chronicled in a series of invited chapters in *The World of Soy*. The volume, edited by anthropologists Christine Du Bois, Chee-Beng Tan, and Sidney Mintz, presents an informative history of the expansion of soy into one of today's major agricultural commodities. However, its true appeal is as an ethnographic case study on how a new food is accepted and incorporated into societies' food and agricultural cultures.

Humans have made extensive use of the soybean plant. It has been grown as forage for livestock, but its current importance is as a seed crop. Oil and lecithin (an emulsifier) extracted from soybean seeds are pervasive in processed foods. They may have been part of that soy you ate today, being found in, for example, grain products, canned goods, peanut butter, chocolate products, ice cream, margarine, salad dressing, and various frozen foods. Soy oil also serves a multitude of industrial applications, such as in paints, plastics, or (more recently) soy diesel. The seed meal that remains after oil extraction is a good source of protein for humans and other animals, and the use and development of this meal as a food product is an underlying theme of this book.

The early use and continued acceptance of soy required technological advances to convert the poorly digestible seed, with its undesirable flavor (a result of lipid oxidation), into tasty and nutritionally beneficial products. Home-based and community-based procedures were developed to grind and cook the seeds, and various chemical agents or plant extracts were identified to coagulate the curds. These were then processed into tofu (bean curd) and other soy products. Fermentation, another simple and easily transferable food technology, was also used to modify the taste of the products and to further enhance their nutritional value.

The contributors present the expansion of soy use throughout China and from China to other countries in South Asia in relation to cultural factors specific to China, Japan, South Korea, Vietnam, and Indonesia. The early movement of soy is believed to have been linked to the diffusion of Buddhism: visitors to Buddhist temples and traveling Buddhist monks are thought to have spread knowledge of soybean agronomics and soy-processing technologies. However, as the volume reveals, the acceptance of soy in different countries and regions was also linked to the ways in which soy's taste could either mimic other foods or be integrated with existing flavors of the local cuisine. Today, as testament to the cultural endurance of diverse soy foods, one can experience a range of unique and fanciful soy-based feasts in Sichuan cuisine, identify with the central roles of soy sauce and miso paste in the standard Japanese taste, appreciate the importance of chang (fermented soybean products) in Korean cuisine, or sample the fermented traditional soyfoods oncom or tempe in Indonesian dishes.

Traditional production. Hani women in Yunnan Province, China, preparing tofu.

CREDIT: YANN LAYMA/THE IMAGE BANK/GETTY IMAGES

The early, slow diffusion of soy was based primarily on taste and food-technology factors. In contrast, as the chapters on its growth to a major agricultural commodity in the United States, Brazil, and Argentina show, the more recent spread was grounded in soy's role as a source of raw ingredients. The authors discuss a broad range of factors that have driven soy's expansion, such as its use as an oil source, government policies, continued advances in processing, cost competitiveness with other crop-based products, improved agronomics (including transgenics), war, famine, the marketing of farm machinery, and the use of soy meal in animal feed. Interestingly, with the shift to soy as a source of ingredients, the target of its "acceptance" has moved toward the realm of the producer (farmers and agribusiness) and away from the consumer. However, consumers still play a critical role in determining soy's use. The growing demand for animal products throughout the world and the use of soy meal in animal feed mean that most of the protein derived from soybeans now goes to chickens, swine, cattle, and fish. Chickens, it turns out, eat more soy than humans, and if one factors in the soy oil used in deep-fat fryers, they are the world's primary consumer of soy products.

Du Bois, Tan, and Mintz have done an excellent job combining a series of chapters from diverse authors into a seamless read. *The World of Soy* provides an informative account of a legume equally ancient and modern. As the globe's population continues to grow and food security and nutrition become increasing concerns, the competing uses of soy as human food or animal feed will surely be debated. The issues and ideas raised in the volume should help readers understand the factors that will enable soy (and possibly other crops) to meet the growing needs of humans.

The reviewer is at the USDA–Agricultural Research Service Children's Nutrition Research Center, Department of Pediatrics, Baylor College of Medicine, Houston, TX 77030, USA. E-mail: mgrusak@bcm.tmc.edu

References

1. U.S. Department of Agriculture (USDA) Foreign Agricultural Service, "Oilseeds: World market and trade" (Circular Series FOP 1-08, USDA, Washington, DC, 2008).

10.1126/science.1175152

ENERGY

Nuclear Waste Management in the United States—Starting Over

The debate has begun again over the disposition of nuclear fuel and waste.

Rodney C. Ewing[1] and Frank N. von Hippel[2]

The recent action to shelve Yucca Mountain as the potential geologic repository for U.S. "spent" (i.e., no longer usable) nuclear fuel (SNF) and high-level nuclear waste (HLW) (*1*) brings to a close a 30-year effort to develop and implement a policy for nuclear wastes in the United States. Selection by Congress in 1987 of Yucca Mountain in Nevada as the only site to be investigated condemned the United States to pursue a policy that had no backup if Yucca Mountain failed politically or technically.

Abandoning Yucca Mountain will mean that another destination must be found for SNF and the solidified HLW from three U.S. Department of Energy (DOE) sites that had military reprocessing plants and from a pre-1973 commercial reprocessing plant. The country will be left with some combination of three basic options: (i) indefinitely store in 35 states and 75 reactor sites, 10 of which have been decommissioned (*2*–*4*); (ii) consolidate from at least the decommissioned sites at one or more central storage sites; and (iii) restart the process of locating and developing one or more geologic repositories.

Advocates of SNF reprocessing have been energized by the Yucca Mountain decision, but reprocessing would not obviate the need for a geological repository. It only has the political advantage of providing an interim destination for the SNF. A thorough assessment of various proposals to simplify the U.S. radioactive waste problem by separating out long-lived transuranic elements and fission products and fissioning and transmuting them, respectively, found that the efforts would be extremely costly and benefits would be marginal (*5*). Also, the U.S. example would provide civilian cover for other nations interested in acquiring separated plutonium for weapons—which is exactly why the United States reconsidered its pro-reprocessing policy after India's 1974 nuclear test, which used plutonium that had been separated for civilian purposes with U.S. assistance (*6*). France and Japan maintain their commitment to reprocessing, but the United Kingdom is quitting, and a dozen countries that were sending their SNF to France, Russia, and the United Kingdom for reprocessing have not renewed their contracts (*7*).

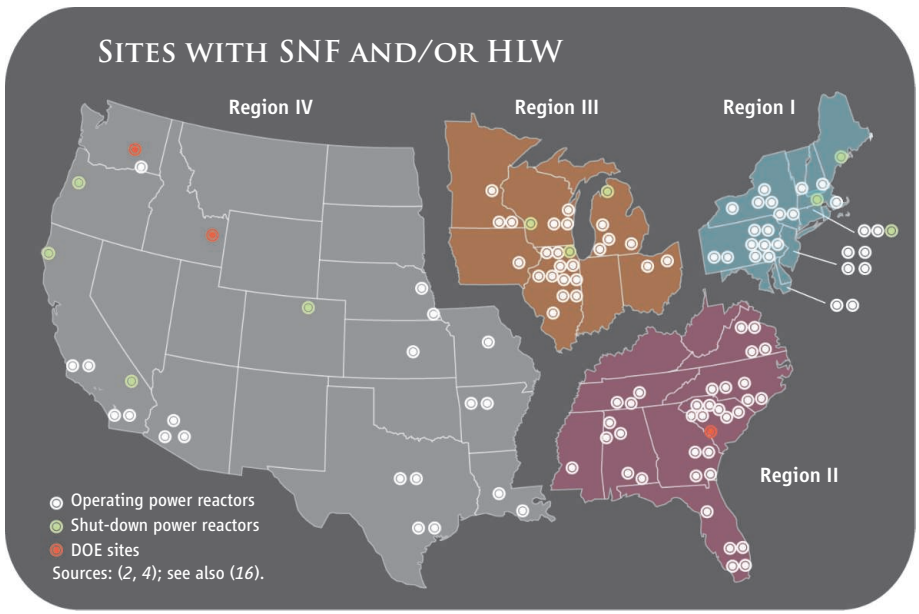

The U.S. Nuclear Regulatory Commission (NRC) is considering extending on-site storage, as a stopgap measure, on the basis of a decision that SNF can be safely stored in dry casks at reactor sites for up to 60 years after reactor operating licenses expire (*8*). This reflects the reality that storing old SNF in dry casks is a safe short-term option. Few are comfortable, however, with the idea of indefinite storage of SNF and HLW on the surface at about 80 locations.

What Went Wrong?

A geologically complex site. Although there is great attraction to isolating nuclear waste in the arid and remote region of Yucca Mountain, there are unresolved scientific and technical issues. The UO_2 in SNF is not stable under the oxidizing conditions in Yucca Mountain and would convert rather rapidly to more soluble higher oxides. Substantial amounts of water exist in the pores and fractures of the volcanic tuff. The geologic complexity of the Yucca Mountain site, including seismicity and relatively recent volcanism, and the proposed reliance on engineered barriers, notably titanium drip shields to protect the casks from water, make the safety analysis complicated and less than convincing (*9*).

In contrast, two countries that are currently developing underground SNF repositories, Sweden (*10*) and Finland (*11*), have chosen stable granitic host rock permeated with oxygen-depleted water. Their strategy uses copper canisters surrounded by protective bentonite clay, and the estimated failure rate of the canisters is extremely low. France, Belgium, and Switzerland are actively investigating potential repositories in clay. The great age and stability of the granite and clay host rocks increase confidence in long-term predictions of repository performance.

Changing performance standard. There was no U.S. Environmental Protection Agency (EPA) performance standard throughout most of the design process for the Yucca Mountain repository. In September 2008, the belatedly issued new standard extended the proposed regulatory period to 1,000,000 years, a significant change from the earlier proposal of only 10,000 years.

Looking forward, there are two important issues related to the standard. First, the present standard is site-specific, rather than a general requirement of performance and safety. Second, the compliance period is based on

SOURCE CREDIT: U.S. NUCLEAR REGULATORY COMMISSION

[1]Department of Geological Sciences, University of Michigan, Ann Arbor, MI 48109–1005, USA. E-mail: rodewing@umich.edu [2]Program on Science and Global Security, Princeton University, Princeton, NJ 08542–4601, USA. E-mail: fvhippel@princeton.edu

a recommendation from a committee of the U.S. National Academy of Sciences' National Research Council that it should extend to the time when peak potential risks may occur, generally hundreds of thousands of years hence (*12*). The uncertainties in projecting performance over hundreds of thousands of years are real and cannot be avoided. The use of "quantitative" performance assessment for licensing placed an enormous burden on the demonstration of compliance over such long periods. Yet, Congress's selection of Yucca Mountain prevented the DOE from pursuing strategies that might have reduced the importance of "unknowables," such as locating the repository where volcanism and seismicity are not major factors.

Unreliable funding source. The original Nuclear Waste Policy Act of 1982 provided funding for development of a repository by creating the Nuclear Waste Fund from a tax on electricity generated by nuclear power. However, expenditures for repository development were subject to annual congressional appropriations. Indeed, it is that appropriation process that is being used to put the Yucca Mountain repository on hold.

Management failures. Development of the licensing basis for a site as complex as Yucca Mountain is inherently difficult, but the DOE, with its limited expertise, continual turnover of personnel, changing design requirements, and poor oversight of contractors, allowed the project to grow to a size that was both unnecessary and unmanageable. The department already has spent $13.5 billion in 2007 dollars on researching the site and projects a final cost of $76 billion (not including $20 billion for transportation) for 122,100 tons of SNF (*13*).

Attempt to override local opposition. The decision to proceed with the Yucca Mountain project in the face of strong public and political opposition in Nevada was a mistake. For projects that will take decades to complete, sustained local opposition has every chance of prevailing. The successful siting efforts in Scandinavia have involved local communities in the decision-making process and given them a veto at each stage (*14*). Also, the communities that have finally volunteered to host repositories already have nuclear power plants, are comfortable with nuclear technology, and have an interest in helping to find a path forward from surface storage to underground disposal.

What Should a New Policy Include?

Regional solutions. The DOE should be relieved of the responsibility for management and disposition of used nuclear fuel from commercial nuclear power plants. The states that have the SNF should be provided with the means and motivation for developing acceptable interim storage sites or geologic repositories. The NRC has organized the distribution of nuclear power plants into four regions: northeast, southeast, midwest, and west (see figure, page 151) (*16*). This could also be an appropriate way to divide up the country for locating interim storage facilities or regional repositories. These regions would provide a variety of possible geological media for a repository, including granite, shale, salt, and volcanic tuff.

States within a given region should have primary responsibility for developing solutions unique to their own situations. In some cases, extended on-site or centralized interim storage may be acceptable. Other states or regions may move forward without delay to site and develop a geologic repository. Transportation problems would be greatly reduced because the distances to regional repositories are much shorter than the distance between reactors east of the Mississippi and Nevada. Funding would be provided from the Nuclear Waste Fund (with a current balance of over $20 billion) (*16*) to organizations established by the states or regions or their nuclear utilities for the development of an interim storage facility and/or a geologic repository. Continued funding would come from the 10th-of-a-cent tax on each kilowatt-hour of electricity generated by nuclear power plants in each region. This regional approach for the 104 U.S. reactors would not be too different from the current approach in Europe, where SNF and HLW from ~150 reactors and reprocessing plants is to be moved to a number of national geologic repositories in a variety of rock types. The DOE would remain responsible for management and disposal of low-level, transuranic, and HLW waste generated by nuclear weapons and naval reactor programs.

Local acceptance. In addition to requiring compliance with federal standards and regulations, the local community and state should make the final siting decision. Local communities at potential storage and repository sites should have early and continued involvement in the process, including funding that would allow them to retain technical experts.

EPA regulation. It may be appropriate to leave to the EPA regulation of the environmental impact of the "back end" of the fuel cycle for commercial nuclear power plants. The Waste Isolation Pilot Plan in New Mexico is a successfully operating geologic repository for transuranic waste regulated by the EPA. The EPA should establish a generic, i.e., not site-specific, performance standard for the containment of long-lived radioisotopes in geological repositories.

Each of these proposals will experience stiff opposition. The main goal, however, should be to provide the United States with multiple alternatives and substantial public involvement in an open siting and design process that requires acceptance by host communities and states. International experience suggests that investigation of multiple sites is affordable. In the meantime, dry-cask on-site SNF storage is a relatively safe interim strategy that will give the United States the time required to develop a permanent, long-term solution.

References and Notes

1. The energy section of the Obama Administration's outline of the priorities of its fiscal year 2010 budget concludes, "The Yucca Mountain program will be scaled back to those costs necessary to answer inquiries from the Nuclear Regulatory Commission, while the Administration devises a new strategy toward nuclear waste disposal" (*17*).
2. Operating reactors from NRC, www.nrc.gov/info-finder/reactor/#USMap.
3. Decommissioned reactors with SNF on site from (*4*).
4. National Research Council, *Going the Distance? The Safe Transport of Spent Nuclear Fuel and High-Level Radioactive Waste in the United States* (National Academies Press, Washington, DC, 2006), table 5.2.
5. National Research Council, *Nuclear Wastes, Technologies for Separations and Transmutation* (National Academy Press, Washington, DC, 1996).
6. G. Perkovich, *India's Nuclear Bomb* (Univ. of California Press, Berkeley, CA, 1999), pp. 28 and 30.
7. F. N. von Hippel, *The Costs and Benefits of Reprocessing: Why Reprocessing Persists in Some Countries and Not in Others (Nonproliferation Education Center, Washington, DC, 2009).*
8. NRC, Waste confidence decision update. *Fed. Regist.* **73**, 59551 (2008).
9. A. M. Macfarlane, R. C. Ewing, Eds., *Uncertainty Underground—Yucca Mountain and the Nation's High-Level Nuclear Waste* (MIT Press, Cambridge, MA, 2006), 431 pp.
10. Forsmark, Sweden, SNF disposal site, www.world-nuclear-news.org/WR_Forsmark_for_Swedish_nuclear_waste_0306091.html.
11. Olkiluoto, Finland, repository (4 June 2009); www.world-nuclear-news.org/WR-Approval_for_expanded_Olkiluoto_repository-0406098.html.
12. National Research Council, *Technical Bases for Yucca Mountain Standards* (National Academy Press, Washington, DC, 1995), 205 pp.
13. DOE, *Analysis of the Total System Life Cycle Cost of the Civilian Radioactive Waste Management Program, Fiscal Year 2007* (DOE/RW-0591, DOE, Washington, DC, 2008).
14. Organization for Economic Cooperation and Development, *Public Information, Consultation, and Involvement in Radioactive Waste Management* (OECD Nuclear Energy Agency, Paris, 2003).
15. In addition to sites shown in the figure, SNF is stored at the never-operated GE Morris, IL, reprocessing plant; an additional DOE site with HLW is the decommissioned commercial reprocessing plant, West Valley, NY. There is no SNF or HLW in Alaska, Hawaii, Puerto Rico, or the Virgin Islands.
16. The U.S. Department of the Treasury does not report the balance. The National Association of Regulatory Utility Commissioners (NARUC), in a resolution adopted on 18 February 2009, claims a balance of $22 billion (*18*).
17. Office of Management and Budget, in *A New Era of Responsibilities: Renewing America's Promise* (Government Printing Office, Washington, DC, 2009), pp. 63–65; www.whitehouse.gov/omb/assets/fy2010_new_era/Department_of_Energy.pdf.
18. NARUC, *Resolution in Support of Ensuring the Federal Government Fulfills Its Obligation to Remove Spent Nuclear Fuel from Present Reactor Storage Sites*; www.naruc.org/Resolutions.cfm.

10.1126/science.1174594

ATMOSPHERE

Smoke and Climate Change

Since preindustrial times, increasing soot concentrations have strongly reduced cooling by anthropogenic aerosols.

Johannes Quaas

Anthropogenic pollution forms small liquid or solid particles in the atmosphere. These aerosols—emitted directly, for example, as soot particles from smoke (see the figure), or formed from pollution gases, such as sulfate particles—are of nanometer to micrometer size. Some particles absorb sunlight, contributing to climate warming; others reflect sunlight, leading to a relative cooling. The global mean effect of anthropogenic aerosols is a cooling, but the relative contributions of the different types of aerosols determine the magnitude of this cooling. On page 187 of this issue, Myhre (*1*) offers new insights into these aerosol effects on climate by showing that the relative increase in light absorption by anthropogenic smoke since preindustrial times was larger than the increase in light scattering by other anthropogenic aerosols. His results substantially advance the level of scientific understanding of how aerosols affect climate.

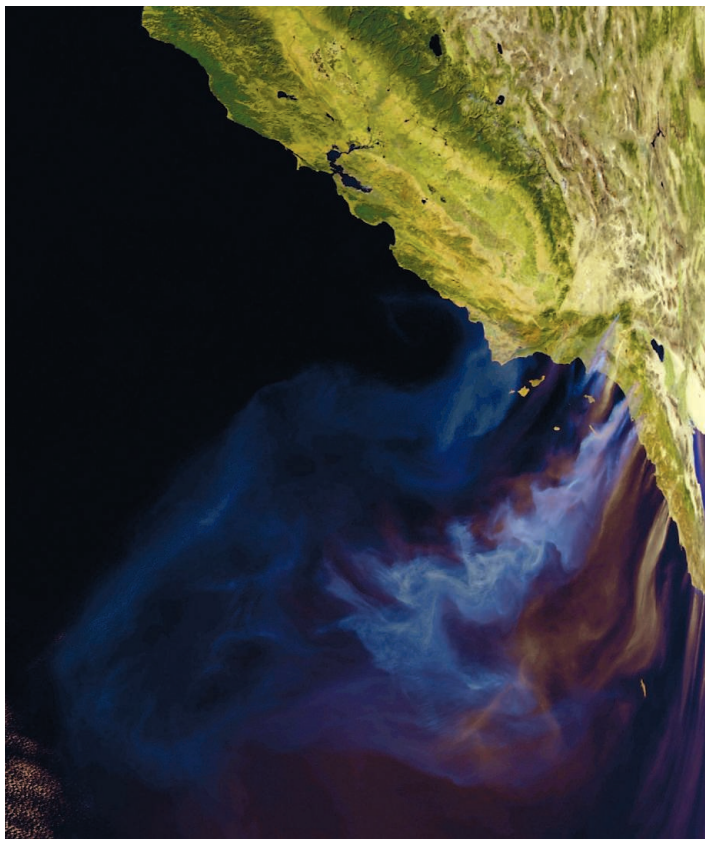

Going up in smoke. Light absorption by smoke—such as from forest fires in California, observed here by EUMETSAT's MetOp satellite (*13*)—is key to understanding how anthropogenic aerosols affect climate change.

CREDIT: EUMETSAT

For more than a decade, climate models have been used to assess the climate effects of aerosols (*2*). Over the 20th century, aerosol cooling has offset a part of the warming induced by anthropogenic greenhouse gases. Indeed, whereas early climate change simulations neglecting the aerosol cooling effect overestimated the anthropogenic warming relative to the observed temperature record, current climate models can reproduce the observed warming over the 20th century.

In such models, the global-mean warming is determined by the balance of the "radiative forcings" (warming by greenhouse gases and cooling by aerosols) and climate sensitivity (the surface temperature change for a given radiative forcing). Given that the greenhouse-gas forcing is well understood and can be predicted skillfully (*2*), uncertainties in the 20th-century aerosol cooling and climate sensitivity in the models balance each other. A large aerosol cooling implies a large climate sensitivity (*3*). The greenhouse-gas forcing must have been larger than aerosol cooling because overall, climate warmed over the 20th century (*4*).

A large fraction of anthropogenic aerosols consists of sulfate, which forms through chemical processing from sulfur dioxide, emitted jointly with carbon dioxide in fossil fuel combustion. In many regions of Earth, the sulfate aerosol concentration has declined in recent decades after pollution-reduction legislation was introduced (*5*). Because sulfate aerosols remain in the atmosphere for days, whereas carbon dioxide remains there for a century or more, the greenhouse-gas effect accumulates, whereas aerosol cooling is tightly linked to current emissions. Aerosol cooling thus offsets part of the greenhouse-gas warming—a masking effect that may be removed suddenly when fossil fuel combustion emissions are cleaned up or fuel combustion is stopped (*6*).

A reliable quantification of the aerosol radiative forcing thus is essential to understand climate change. Recent improvements in satellite observations have enabled measurement-based estimates of the global aerosol forcing (*7*–*9*). These estimates yielded systematically larger aerosol cooling than do climate model calculations. Part of this discrepancy can be explained by different assumptions made in the two approaches (*10*); for example, models and satellite data interpretations may use different estimates of the anthropogenic fraction of aerosol, or make different assumptions about aerosol forcing in cloudy skies and above bright surfaces. However, a large part of the discrepancy has remained unexplained.

Myhre now convincingly explains most of the remainder of the discrepancy. With a systematic set of sensitivity studies, he determines the relative importance of the various assumptions. He shows that with a consistent data set of anthropogenic aerosol distributions and properties, the data-based and model-based approaches converge.

The author argues that since preindustrial times, the soot particle concentration increased much more than did the rest of the aerosols. Most aerosols mainly scatter sunlight, but soot also strongly absorbs solar radiation. In both cases, the effect at Earth's surface is less incoming radiation; but at the top of the atmosphere, where the Earth system's energy balance is determined, scattering has a cooling effect, whereas absorption has a warming effect. If soot—and thus absorption—increases more than does scattering, the aerosol cooling of the Earth system is smaller than it would otherwise be. Myhre shows that when this absorption effect is properly represented in the satellite-based approach, the global-mean forcing is reduced, in better agreement with the model-based computation.

Max Planck Institute for Meteorology, Bundesstr. 53, D-20146 Hamburg, Germany. E-mail: johannes.quaas@zmaw.de

Published by AAAS

The study by Myhre is an important advance toward quantifying the aerosol radiative forcing (and hence climate sensitivity), but many questions remain. Models continue to give diverging results, particularly with respect to regional aerosol effects (*11*). Furthermore, aerosols affect the energy balance not only directly (the effect studied by Myrhe) but also indirectly, particularly by altering cloud brightness, abundance, and geometry, as well as the distribution of precipitation (*2*, *12*). These indirect effects may be substantial but are not well understood. Better understanding of the physical processes of aerosol-cloud interactions is essential for improving their representation in climate models. This has to involve observations and modeling at the process scale, as well as constraints at the large scale through better use of improving satellite data.

References and Notes

1. G. Myhre, *Science* **325**, 187; published online 18 June 2009 (10.1126/science.1174461).
2. Intergovernmental Panel on Climate Change (IPCC), *Climate Change 2007: The Physical Science Basis, Summary for Policymakers* (Cambridge Univ. Press, Cambridge, 2007).
3. M. O. Andreae, C. D. Jones, P. M. Cox, *Nature* **435**, 1187 (2005).
4. T. L. Anderson *et al.*, *Science* **300**, 1103 (2003).
5. M. Wild *et al.*, *Science* **308**, 847 (2004).
6. G. P. Brasseur, E. Roeckner, *Geophys. Res. Lett.* **32**, L23704 (2005).
7. N. Bellouin *et al.*, *Nature* **438**, 1138 (2005).
8. Y. J. Kaufman *et al.*, *Geophys. Res. Lett.* **32**, L17804 (2005).
9. J. Quaas, O. Boucher, N. Bellouin, S. Kinne, *J. Geophys. Res.* **113**, D05204 (2008).
10. N. Bellouin *et al.*, *J. Geophys. Res.* **113**, D10205 (2008).
11. M. Schulz *et al.*, *Atmos. Chem. Phys.* **6**, 5225 (2006).
12. J. Quaas *et al.*, *Atmos. Chem. Phys. Discuss.* **9**, 12731 (2009).
13. EUMETSAT is the European Organisation for the Exploitation of Meteorological Satellites. Its MetOp satellite is the first European polar-orbiting satellite dedicated to operational meteorology (www.esa.int/esaME/index.html).

10.1126/science.1176991

EVOLUTION

How Did the Turtle Get Its Shell?

Details of embryonic skeletal and muscular organization provide evidence for the evolution of the turtle shell.

Olivier Rieppel

In *On the Origin of Species*, Darwin asserted: "Monstrosities cannot be separated by any clear line of distinction from mere variations" (*1*). But encased in its shell, the turtle appears to be just such a monstrosity. No other animal, living or extinct, has its body enclosed within a bony shell that is similarly constructed in its entirety. Over the last few years, developmental biologists have started to tackle the question of how the turtle shell evolved. On page 193 of this issue, Nagashima *et al*. (*2*) provide a detailed account of muscular and skeletal changes during the embryogenesis of the modern turtle, and in drawing parallels between these early developmental changes and what is seen in ancestral turtles, provide insights into how turtle shell evolution might have occurred.

Nagashima *et al*. show that formation of the dorsal part of the turtle shell (carapace) results from complex changes in developmental pathways. Yet, commenting on the turtle shell in his classic textbook on *Vertebrate Paleontology and Evolution*, paleontologist Robert Carroll maintained that "developmental specialization does not provide any hint as to the way in which this pattern evolved phylogenetically" (*3*). The clash here is between a transformationist as opposed to an emergentist view of morphological evolution.

The classic transformationist approach sees morphological evolution as a result of natural selection working on variation manifest in reproducing organisms. Under this paradigm, the turtle carapace would have evolved from osteoderms. These are small bony plates that develop (ossify) within the deep layer of the skin (dermis) of reptiles such as crocodiles or some lizards. The lineage ancestral to turtles would have developed a dense osteoderm covering, the individual elements eventually coalescing to form larger bony plates. Fusion of osteoderms with the underlying ribs would explain how the ribs became incorporated in the carapace (*4*, *5*). Two problems remain unexplained in this scenario: How do bones that form in the skin fuse with underlying ribs that normally grow into the lateral body wall? And why is it that uniquely in turtles the shoulder blade lies inside the ribcage, instead of being located outside the ribcage as in all other tetrapods?

Origin of the shell. Skeletal and muscular development during early turtle embryogenesis provides insights into how the modern turtle shell evolved. Shown is the Chinese soft-shelled turtle, *Pelodiscus sinensis*.

CREDIT: DORLING KINDERSLEY/GETTY IMAGES

The assumption of the transformationist view is that the shoulder girdle moved backward during the evolution of turtles, so that it would be located inside the shell, which itself incorporates the ribs. But modern turtle embryos do not show any posterior dislocation of the shoulder girdle during development (*6*), drawing this hypothesis into question.

The emergentist approach seeks to understand the origin of genuinely novel structures such as the turtle shell as a result of developmental modifications. It is under this paradigm that the study by Nagashima *et al*. gains merit. A distinctive feature of the turtle embryo is a disk-shaped thickening of the dermis on the back that forms a carapacial disk (precursor to the carapace). Differentiation of epithelial cells in the margin of the carapacial disk (the carapacial ridge) is thought to organize carapace development. This is based on similarity to the regulation of tetrapod limb development by cells at the apical ridge of limb buds (*7*). The ribs then grow into the carapacial disk to initiate ossification (*8*–*10*) of the costal plates that will constitute parts of the mature shell. A similar function is assigned to embryonic trunk vertebrae, whose spines grow into the carapacial disk to induce the formation of the neural plates of the carapace.

Nagashima *et al*. observed that during early development of the Chinese soft-shelled turtle *Pelodiscus sinensis* (see the figure), translocation of the ribs to a position outside the shoulder blade involves folding of the lateral body wall along a line that defines the later formation of the carapacial ridge.

Rowe Family Curator of Evolutionary Biology, Department of Geology, The Field Museum, 1400 South Lake Shore Drive, Chicago, IL 60605–2496, USA. E-mail: orieppel@fieldmuseum.org

This folding restricts rib growth to the horizontal plane of the carapacial disk and also maintains the shoulder blade in its superficial position relative to the folded body wall. This organization is thought to characterize ancestral turtles. Some muscles that develop from the muscle plate that is associated with the folding body wall even retain their "ancestral connectivities" in the adult.

The work by Nagashima *et al*. adds to the interpretation of a recently described ancestral turtle, *Odontochelys semitestacea*, from southwestern China, collected in 220-million-year-old marine sediments (*11*). This species had a complete ventral armor (plastron), but the carapace remained incomplete. A series of neural carapace plates developed from underlying vertebrae, and whereas the ribs were broadened as in a modern turtle embryo, they did not form connecting plates, nor did any other elements of the carapace ossify. Osteoderms were absent, and the shoulder girdle was located in front of the anteriormost trunk rib. Nagashima *et al*. hypothesize that in this ancestral turtle, the carapacial ridge was differentiated only along the side of the trunk, remaining incomplete anteriorly and posteriorly. Only later during the evolution of turtles would the carapacial ridge be completed, causing the anteriormost trunk rib to grow across the shoulder blade and localizing the latter inside the ribcage. This corroborates the interpretation of *O. semitestacea* as an ancestral turtle, rather than representing a specialized early side branch of turtles that reduced the carapace in adaptation to aquatic habits, as fossil and living sea turtles do (*12*). And it further supports the hypothesis that the position of the shoulder blade inside the rib cage results from a redirection of rib growth, rather than from a posterior dislocation of the shoulder girdle.

References

1. C. Darwin, *On the Origin of Species* (John Murray, London, ed. 1, 1859), p. 8.
2. H. Nagashima *et al*., *Science* **325**, 193 (2009).
3. R. L. Carroll, *Vertebrate Paleontology and Evolution* (Freeman, San Francisco, 1988), p. 210.
4. M. S. Y. Lee, *Science* **261**, 1716 (1993).
5. W. G. Joyce *et al*., *Proc. R. Soc. Lond. B Biol. Sci.* **276**, 507 (2009).
6. A. C. Burke, *Am. Zool.* **31**, 616 (1991).
7. A. C. Burke, *J. Morphol.* **199**, 363 (1989).
8. S. Kuraku *et al*., *Evol. Dev.* **7**, 3 (2005).
9. S. F. Gilbert *et al*., *Evol. Dev.* **3**, 47 (2001).
10. J. A. Cebra-Thomas *et al*., *Mol. Dev. Evol.* **304B**, 558 (2005).
11. C. Li *et al*., *Nature* **456**, 497 (2008).
12. R. R. Reisz, J. J. Head, *Nature* **456**, 450 (2008).

10.1126/science.1177446

ASTRONOMY

Sunspot Flows and Filaments

Numerical simulations capture the detailed structure and dynamics of sunspots.

Göran Scharmer

Sunspots consist of a dark central umbra and a brighter, filamentary surrounding penumbra (see the figure). What causes these features? Some clues come from the fact that the brightness is associated with energy loss by radiation; this provides a connection to the mechanisms responsible for the energy flow from the solar interior to its visible surface. On page 171 of this issue, Rempel *et al*. (*1*) report comprehensive numerical simulations that reproduce the structure and dynamics of sunspots. The results help to address fundamental questions about the fine structure of sunspots and their surroundings.

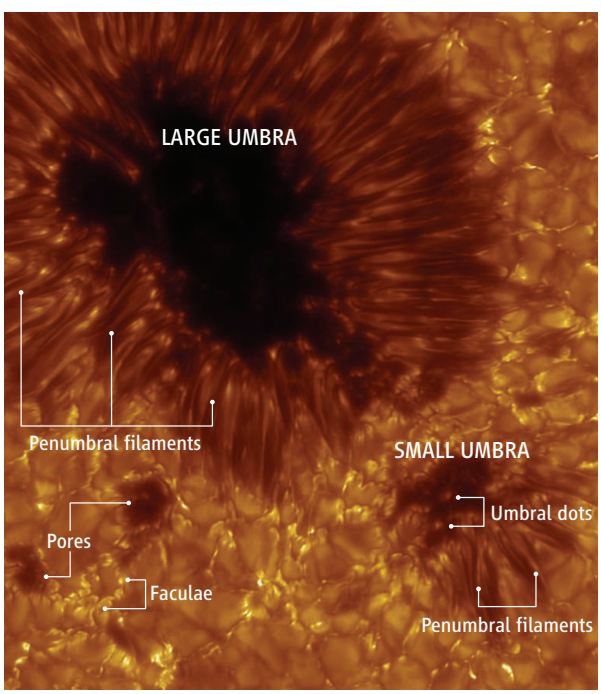

CREDIT: ROYAL SWEDISH ACADEMY OF SCIENCES

Spot on. Sunspots are large concentrations of strong magnetic field in the solar atmosphere. The simulations by Rempel *et al*. explain the connection between strong horizontal Evershed flows and convection in their outer filamentary part (the penumbra). The picture shows a sunspot observed with the Swedish 1-m Solar Telescope on La Palma, using a filter that emphasizes the upper photosphere and small-scale magnetic fields (bright patches or faculae) surrounding the sunspot.

The solar photosphere is the layer that we can most easily observe, constituting the boundary between the optically opaque interior and the transparent exterior. In the field-free photosphere, convective hot upflows lose their buoyancy by radiative cooling, turning first into horizontal flows and then into cool, dense downflows. Details of this radiative cooling near the surface strongly influence not only the morphology of the observed solar fine structure, but also the fate of convective downflows as they descend back into the deeper layers. This convection is thus to a large extent driven by surface cooling rather than by heating from below (*2*).

Understanding the details of this convection requires time-dependent three-dimensional (3D) simulations that include radiative energy transfer processes. Such simulations of field-free solar convection closely match the observed structure and evolution of granulation as well as spectral line shapes and spatial intensity variations (*2*). Similar simulations (*3*, *4*), but including small amounts of magnetic flux, reproduce observed faculae (the bright patches between the granules commonly found in the vicinity of sunspots) (see the figure). Simulations of much larger flux concentrations, sunspots, present a much more difficult problem.

In 1941, Ludwig Biermann recognized that the reduced brightness of sunspot umbrae could be due to suppression of the convective energy flux by their strong magnetic field. But this led to the problem of explaining why sunspots are not completely dark. Simulations of sunspot umbrae (*5*) demonstrate the formation of narrow plumes within which the magnetic field is expelled by overturning convection, leading to the formation of bright umbral dots.

The brightness of penumbrae can similarly only be explained by a convective energy flux. However, the predominantly horizontal magnetic field and the filamentary structure of pen-

Institute for Solar Physics, Royal Swedish Academy of Sciences and Department of Astronomy, Stockholm University, AlbaNova University Center, SE-10691, Sweden. E-mail: scharmer@astro.su.se

umbrae suggest that this convection must be different from that in umbrae. In 1909, Evershed discovered strong radial outflows in penumbrae that seemed to be unrelated to penumbral convection. Until recently, these flows—called the Evershed effect—and the filamentary structures have been attributed to flows in nearly horizontal flux tubes embedded in a more vertical magnetic field (*6*, *7*). Such models cannot, however, explain the penumbral heat flux (*8*, *9*). While leaving the Evershed effect unexplained, Spruit and I have therefore proposed that the filamentary structure of the penumbra, as well as the large azimuthal variations in field strength and inclination, may be caused by overturning convection opening up radially aligned nearly field-free gaps just below the visible surface (*9*).

The first 3D simulations of sunspots (*10*, *11*), although limited to azimuthally narrow slices of a sunspot, did provide consistency with several observed aspects of penumbrae. They demonstrated convection in radially aligned sheet-like structures with strongly reduced field strength and systematic (but weak) radial outflows. This led us to the conclusion that the Evershed flow is identical to the horizontal component of penumbral convection (*12*). Rempel *et al*. now present simulations of two sunspots of opposite polarities and not just thin slices of a sunspot as in the earlier simulations (*10*, *11*). They describe properties of the sunspots that are consistent not only with the inner but also the outer penumbra, where the magnetic fields are nearly horizontal and the Evershed flows are very strong. They confirm the convective origin of the Evershed flow and convincingly show that penumbral convection, apart from the strong asymmetry introduced by the inclined magnetic field, is similar to field-free convection with respect to flow velocities and length scales.

Outside the simulated sunspots (*1*, *10*, *11*) are seen granules and small-scale magnetic features consistent with earlier simulations of field-free convection (*2*) and faculae (*3*, *4*). The interiors of the spots show bright umbral dots, in agreement with simulations of umbral convection (*5*). In contrast to simplified models and simulations, these new 3D ab initio simulations are not restricted to individual structures or specific mechanisms, and they reproduce a variety of nonmagnetic and magnetic solar structures and dynamics within a single simulation—these are good reasons to be confident in this simulation and the conclusions it leads to. In particular, the subsurface convective energy flux, the inclined magnetic field, and the radiative cooling near the visible surface are the main drivers of the observed penumbral filamentary structure. The radial Evershed flow is the most prominent visible manifestation of penumbral convection in these filaments. Reproducing these complex features in a single simulation is a major breakthrough in solar physics.

Direct observational evidence for the azimuthal component of overturning penumbral convection has only recently been reported (*13*, *14*). More observations of sunspot magnetic fields and flows at very high spatial resolution are needed. As the spatial resolution of simulations and our understanding of the subsurface structure of the magnetic field improves, we expect an even more detailed agreement between simulations and observations, such as those of long penumbral filaments with contiguous dark cores (*15*).

References

1. M. Rempel, M. Schüssler, R. H. Cameron, M. Knölker, *Science* **325**, 171 (2009); published online 18 June 2009 (10.1126/science.1173798).
2. Å. Nordlund, R. F. Stein, M. Asplund, *Living Rev. Sol. Phys.* **6**, 2 (2009).
3. C. U. Keller, M. Schüssler, A. Vögler, V. Zakharov, *Astrophys. J.* **607**, L59 (2004).
4. M. Carlsson, R. F. Stein, Å. Nordlund, G. B. Scharmer, *Astrophys. J.* **610**, L137 (2004).
5. M. Schüssler, A. Vögler, *Astrophys. J.* **641**, L73 (2006).
6. B. Montesinos, J. H. Thomas, *Nature* **390**, 485 (1997).
7. R. Schlichenmaier, K. Jahn, H. U. Schmidt, *Astrophys. J.* **493**, L121 (1998).
8. R. Schlichenmaier, S. K. Solanki, *Astron. Astrophys.* **411**, 257 (2003).
9. H. C. Spruit, G. B. Scharmer, *Astron. Astrophys.* **447**, 343 (2006).
10. T. Heinemann, Å. Nordlund, G. B. Scharmer, H. C. Spruit, *Astrophys. J.* **669**, 1390 (2007).
11. M. Rempel, M. Schüssler, M. Knölker, *Astrophys. J.* **691**, 640 (2009).
12. G. B. Scharmer *et al.*, *Astrophys. J.* **677**, L149 (2008).
13. K. Ichimoto *et al.*, *Science* **318**, 1597 (2007).
14. V. Zakharov *et al.*, *Astron. Astrophys.* **488**, L17 (2008).
15. G. B. Scharmer *et al.*, *Nature* **420**, 151 (2002).

10.1126/science.1175752

MATERIALS SCIENCE

Predicting Fatigue Failures

Jamie J. Kruzic

New methods for predicting fatigue may extend the usefulness of materials that actively resist cracking.

Engineers who design structures often start at the end: They consider how the materials used will fail. Structures must be overdesigned—a bridge may be able to withstand twice the expected load when it is first built—but over time, repeated cycles of loading and unloading introduce defects in the materials that can ultimately lead to fatigue failure; for example, a paper clip that is bent back and forth until eventually it snaps. Predicting failure is easier for ductile than for brittle materials, and designers can accurately model their response to fatigue loading (*1*). However, many relatively brittle materials, such as advanced ceramics, intermetallics, and composites of brittle and ductile materials, are seeing increased use due to their favorable low-density or high-temperature properties. New methods are needed to predict when and how these materials will fail due to cyclic fatigue loading.

Failure models in different materials must take into account how they fail at a microscopic level. Ductile materials can deform before they fail, because atoms can easily rearrange within the crystal grains facilitated by defects known as dislocations. Our paper clip failed after work hardening—too many dislocation defects were produced, making further atomic rearrangement difficult. The metal then becomes brittle and cracks. If we used a testing rig to determine the fatigue response of the paper clip metal alloy, we could deterministically predict the future behavior of paper clips of any size and geometry with reasonable accuracy.

School of Mechanical, Industrial, and Manufacturing Engineering, Oregon State University, Corvallis, OR 97331, USA. E-mail: jamie.kruzic@oregonstate.edu

Materials that are intrinsically brittle tend to fail all at once, as happens when we drop a dish and it shatters. In brittle materials, atoms within crystal grains are less mobile, and although they withstand compression forces better than ductile materials, they tend to crack rather than deform. Cracks can nucleate from a single heterogeneous site, and the distribution of such sites is difficult to assess. Thus, if we drop several dishes from the same height, only some may break. Designs with brittle materials demand testing of hundreds of samples and determining the statistical probabilities of failure.

Composite materials, advanced ceramics, and intermetallic materials tend to fail in a way that is intermediate between these extremes. They can resist immediate failure by cracking better than traditional brittle materials,

but like ductile metals, they are susceptible to fatigue failures over time. Because fatigue failures in these materials occur very differently than in ductile metals, traditional methods for fatigue predictions are not appropriate (*1*).

The need for accurate fatigue prevention is driven by the replacement of traditional metal alloys in many structural applications, such as lightweight composites for aerospace structures and aircraft and new high-temperature materials for engine applications. For example, the Boeing 787 Dreamliner will use composite materials for ~50% of the primary structure (*2*), and the GE engine that will power it will use lightweight intermetallic titanium aluminide turbine blades in the lower-pressure sections (*3*). Although such materials can be used safely based on empirical experience and overdesign strategies, optimizing the performance improvements requires more sophisticated approaches to accurately predict fatigue life.

Replacement materials for human bones and teeth, which are natural composites, present another example of this transformation. Metal orthopedic and dental implants now have competition from less ductile but lighter zirconia-based implants. These materials can resist crack propagation because they undergo a phase transformation when stressed that expands their crystal lattice and compresses the tip of the emerging crack (see the figure, panel C). Similar in effect, many other materials and composites rely on crack bridging mechanisms to hold cracks together and resist crack growth.

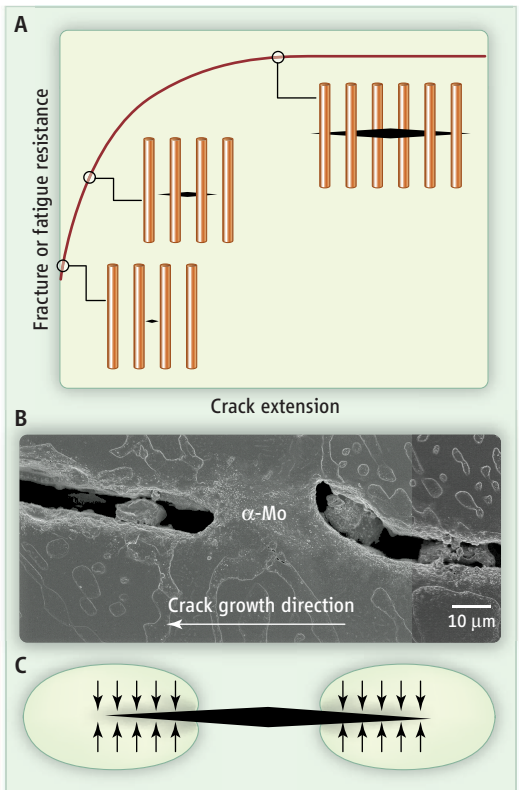

Bridging the road to fracture. (**A**) Crack bridging stops the lengthening (extension) of cracks that lead to material failure. In this *R*-curve, cracking resistance is lowest when a crack initiates in the matrix, increases as the reinforcing phases hold the crack together, and then saturates as the reinforcement begins to fail. (**B**) Crack bridging by a ductile α-Mo metal phase helps to arrest cracks in an experimental high-temperature Mo-Si-B alloy targeted for future turbine engine applications (*13*). (**C**) A schematic showing how the growth of crack tips can be suppressed by phase transformations that prevent further growth. Externally applied stresses are intensified near crack tips and cause the region around the crack (blue) to change phase. The greater volume of the new phase creates compressive stresses on the crack (shown as arrows) and pushes the tips closed.

For either mechanism of cracking resistance, the cracks that form during actual use are initially very small (micrometer scale). They can behave in a way that is vastly different from that of the millimeter-scale cracks studied in laboratory tests using standardized techniques developed for traditional metal alloys (*4*, *5*). This difference is a notable problem in predicting fatigue failures in modern advanced materials.

In crack bridging (see the figure, panel A), a small crack situated between reinforcing fibers or layers needs only to overcome the cracking resistance of the matrix in order to propagate. However, once the crack has propagated around the reinforcing phase, that phase can hold the crack together and increase crack propagation resistance. This rising fracture or fatigue resistance with crack extension, called a rising *R*-curve, is seen across a broad range of materials, including some advanced metal alloys (see the figure, panel B), ceramics, intermetallic compounds, and human bone and dentin.

To utilize the enhanced cracking resistance of materials with rising *R*-curves, a designer must be able to predict whether fatigue cracks will arrest during cyclic loading or grow and lead to fracture. Several proposed approaches directly measure fatigue crack propagation resistance; others rely on indirect measurements.

Among direct methods, the fatigue threshold *R*-curve appears promising with regard to its predictive capabilities (*6*). The fatigue threshold is defined as the stress intensity, which is a function of applied stress and crack size, below which cracks do not propagate under cyclic loading. Here, the *R*-curve tracks how this threshold increases as cracks grow longer. Cracks that will benignly arrest can be discriminated from those that will grow to failure for a given loading level and crack size. Although this prediction method has not been tested under fatigue conditions, it has been effective for predicting the strength of bridging toughened ceramics under monotonically increasing loading conditions (*7*).

One type of indirect method is an extension of the above concept in which the stresses resulting from crack bridging or phase transformations are quantified, allowing prediction of the *R*-curve behavior. Many methods for quantifying bridging stresses have been developed (*8*–*11*), and recently some of those have been applied to predict fatigue threshold *R*-curves (*6*). This approach speeds the evaluation of a material; direct methods are usually more costly and time consuming because of the difficulty and length of fatigue experiments, and for certain materials, such as advanced silicon nitride ceramics, such experiments are so far impossible.

In a second type of indirect method, many specimens that appear crack-free based on external observations are exposed to fatigue conditions until they fail. Based on these data and on assumptions of how the fatigue crack grew to cause fracture, an effective crack growth law for naturally occurring internal flaws can be calculated. This method ignores the details of how resistance to the fatigue crack propagation changes with crack size and is limited by the assumptions used. However, for certain cases it works well; for example, materials such as high-strength and high-toughness bridging ceramics, where the *R*-curves initially rise steeply and the natural flaw sizes fall into a tight range (*12*).

The continuous development of advanced materials ensures that a "one size fits all" approach will no longer serve the engineering community in terms of predicting and preventing fatigue failures and reducing their associated costs. New prediction methods must be continuously developed that keep pace with the challenges posed by new specialized and complex structural materials. Meeting such challenges will allow optimization of recent designs and the implementation of even higher-performance materials in future designs.

References and Notes

1. R. O. Ritchie, *Int. J. Fract.* **100**, 55 (1999).
2. J. R. Wilson, *Aerosp. Am.* **46**, 32 (2008).
3. *The Engine Yearbook 2006* (Aviation Industry Press, London, 2005), vol. 2.
4. J. H. Andreasen, C. V. Moller, B. L. Karihaloo, *J. Am. Ceram. Soc.* **78**, 406 (1995).
5. J. J. Kruzic, J. P. Campbell, R. O. Ritchie, *Acta Mater.* **47**, 801 (1999).

6. J. J. Kruzic, R. M. Cannon, J. W. Ager, III, R. O. Ritchie, *Acta Mater.* **53**, 2595 (2005).
7. J. J. Kruzic, R. Satet, M. J. Hoffmann, R. M. Cannon, R. O. Ritchie, *J. Am. Ceram. Soc.* **91**, 1986 (2008).
8. G. Pezzotti, *J. Raman Spectrosc.* **30**, 867 (1999).
9. T. Fett, *J. Am. Ceram. Soc.* **78**, 945 (1995).
10. T. Fett, D. Munz, X. Dai, K. W. White, *Int. J. Fract.* **104**, 375 (2000).
11. T. Fett, D. Munz, G. Thun, H.-A. Bahr, *J. Am. Ceram. Soc.* **78**, 949 (1995).
12. T. Fett, M. Riva, M. J. Hoffmann, R. Oberacker, *J. Test. Eval.* **37** (2009).
13. J. J. Kruzic, J. H. Schneibel, R. O. Ritchie, *Scr. Mater.* **50**, 459 (2004).
14. I gratefully acknowledge support from the NSF (award 0547394).

10.1126/science.1173432

CELL BIOLOGY

Sizing Up the Cell

Bruce A. Edgar[1] and Kerry J. Kim[2]

Control over cell division depends on coordinately functioning sensors of cell size and age.

The coordination of cell growth and division is responsible for fundamental characteristics of cells such as their size: Fast growth with slow division makes big cells, whereas slow growth with fast division makes small cells. Yet despite decades of effort, the kinetics of cell growth and its influence on cell division have remained elusive topics, at least for animal cells. Is cell growth linear (constant) or exponential (proportional to cell size)? Does cell division occur after cells have grown beyond a minimum size, or is there rather some "age of consent" for division, or both? A report by Tzur *et al*. on page 167 of this issue (*1*) combines a new experimental method with careful mathematical analysis to answer these questions for cultured mammalian lymphoblasts.

In principle, one could measure size-dependent growth rates by following individual cells through time, but current technology does not allow this on a large scale. Instead, Tzur *et al*. used a method originally proposed by Collins and Richmond (*2*) to infer growth rates from the distribution of cell sizes in a population of asynchronously dividing cells. At steady state, the size distribution of cells in a population is constant because growth (which increases cell size) is balanced by division (which produces small cells). Collins and Richmond derived a relation that equates the size-dependent growth rate to the distribution of all cell sizes and the size distributions of dividing and newborn cells. Intuitively, if one observes very few cells with a volume of, say, 1 picoliter, this might be because (i) cells of this size grow very quickly (and spend very little time at this volume), (ii) most newborn cells are larger than this, or (iii) most cells divide before reaching this size. By having the three size distributions in the Collins-Richmond relation, the effects of (ii) and (iii) can be estimated, and one can infer the cell growth rate for cells of any size.

The most difficult aspect of applying the Collins-Richmond relation is measuring the sizes of newborn and dividing cells. To do this, Tzur *et al*. grew the lymphoblasts loosely attached to a membrane, such that after division, one of the daughter cells was released from the membrane for sizing. The size distribution of dividing cells was inferred under the assumption that the volume of the cell just before division was the same as the total volume of the two resulting newborns. Plugging their cell volume distributions into the Collins-Richmond equation revealed that lymphoblast growth is exponential after early G_1 phase of the cell division cycle (the phase just prior to DNA replication), followed by a growth deceleration for the very largest cells (see the figure).

The finding that growth is exponential during most of the cell cycle suggests that lymphoblasts must have a robust mechanism to maintain their size during each cycle. Otherwise, small differences in the size of cells at division would be amplified each generation. The conclusions of Tzur *et al*. differ sharply from an earlier study of rat Schwann cells (*3*), which concluded that those cells grew rather linearly and probably had no special mechanism for maintaining a constant size. For Schwann cells, size at division depended on the relative concentrations of a circulating growth factor (insulin-like growth factor) that affected size but not division, and a mitogen (glial growth factor) that promoted both. Yet the two studies are difficult to compare because the cells and methods are very different, leaving the meaning of the discrepancy unclear (*4*). Regardless, the implication of a cell-sizing mechanism in at least one animal cell type offers the opportunity to pinpoint the underlying mechanism.

Tzur *et al*. were also able to track the sizes of a synchronized population of newborn cells (just released from the membrane) over several cycles, something rarely done with animal cells. They found that for cells of equal age, the larger is more likely to divide. Similarly, for two cells of equal size, the older cell is more likely to divide. This implies that

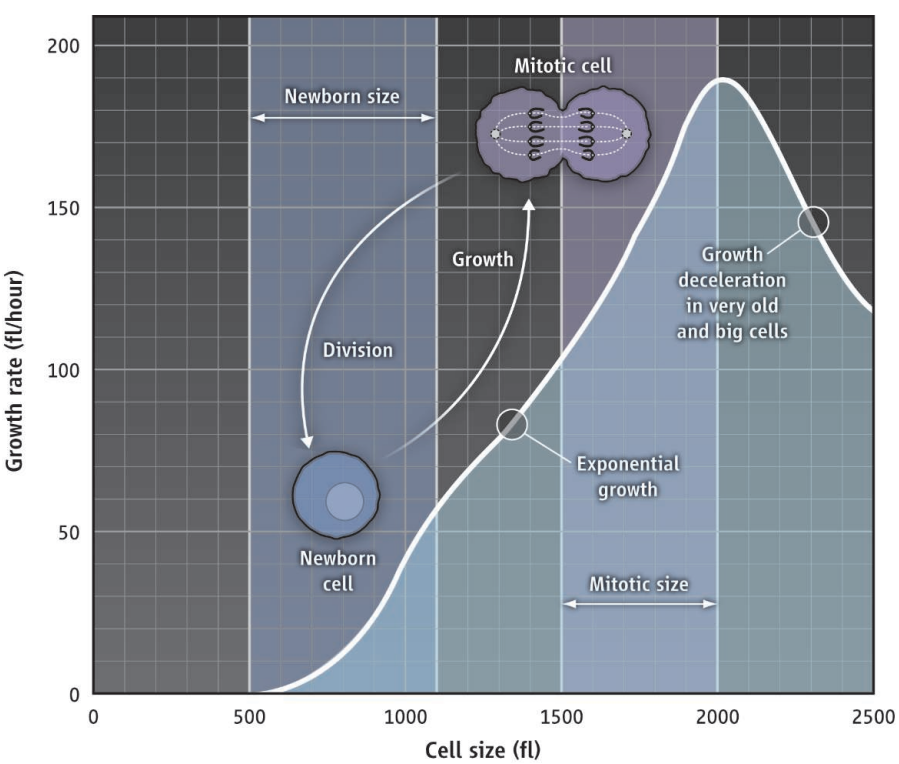

Grow and divide. Animal cell growth is exponential during most of the cell division cycle; fl, femtoliters.

CREDIT: C. BICKEL/*SCIENCE*

[1]Fred Hutchinson Cancer Research Center, Seattle, WA 98109, USA. [2]Center for Cell Dynamics, Friday Harbor Labs, University of Washington, Friday Harbor, WA 98250, USA. E-mail: bedgar@fhcrc.org; kjkim@u.washington.edu

lymphoblast division is regulated by both cell size and age—that both a "sizer" and a "timer" are involved.

Numerous molecular mechanisms that might constitute cell sizers or timers have been proposed. Perhaps the best-informed ideas come from studies of yeasts, where the kinetics of cell growth and division and the molecules controlling them are relatively well understood. A bona fide sizer was recently proposed for *Schizosaccharomyces pombe*, a fission yeast that grows as a rod and divides at a constant length (*5*). In this case, a factor (Pom1) tethered at the cell ends was proposed to inhibit activators of division in the cell's center. As the cell elongates, it eventually passes a critical length at which Pom1's influence no longer reaches to the cell's center, triggering division. This is an attractive mechanism for a rod-shaped cell but seems unlikely to apply generally, especially for cells with different shapes. In the budding yeast *Saccharomyces cerevisiae*, and probably also in many mammalian cells, a growth or size threshold must be surpassed to initiate S phase of the cell cycle (when DNA replication occurs), and division into two daughter cells (mitosis, or M phase) follows automatically in a stereotyped sequence of events suggestive of a timer. In these cases, the various sizer and timer mechanisms proposed are potentially quite general.

One popular model invokes the rate of production of a limiting cell cycle activator as a critical parameter. This activator is envisioned to be produced at a constant rate per unit of cytoplasm and progressively concentrated in an organelle of fixed volume (e.g., the nucleus) or on target binding sites of fixed number (e.g., chromosomes). As the cell grows and the activator accumulates at its targets, it eventually reaches a threshold necessary to trigger cell cycle progression (normally, $G_1 \rightarrow S$ phase progression). With this arrangement, the sizer senses a metabolic index rather than size, and so a cell's size at division will be affected by its nutrient status and growth factor milieu, as well as the status of genes involved in cell growth and metabolism. Indeed, this is the rule from yeast to human cells (*6*).

There are many cell cycle activators that could fill the role of a limiting regulator in such a system. Likely candidates include the G_1 cyclins and cyclin-dependent kinases that promote S phase, origin-licensing factors (such as Cdc6 and Cdt1), and transcription factors that activate cell cycle genes (such as E2F). If the size-sensing cell cycle activator were stable and accumulated in one cell cycle phase (e.g., G_1) but was periodically degraded in another (e.g., S or at the $M \rightarrow G_1$ phase transition), as many of these factors are, then the sizing mechanism could also function effectively as a timer. Cell cycle suppressors might also act as size sensors if they were sequestered or degraded in a growing compartment, or as timers if their activity were periodically gated. Indeed, many of the core cell cycle regulators are able to affect cell size in dose dependency experiments, and so it has been expected for many years that some of these must function naturally as size sensors and timers. Precisely which factor fills this role in any particular biological context still needs to be determined, but given the marvelous diversity of cell types, stereotypical sizes, and proliferation styles found in nature, we are likely to find many different flavors of cell sizers and timers.

References

1. A. Tzur, R. Kafri, V. S. LeBleu, G. Lahav, M. W. Kirschner, *Science* **325**, 167 (2009).
2. J. F. Collins, M. H. Richmond, *J. Gen. Microbiol.* **28**, 15 (1962).
3. I. J. Conlon, G. A. Dunn, A. W. Mudge, M. C. Raff, *Nat. Cell Biol.* **3**, 918 (2001).
4. S. Cooper, *BMC Cell Biol.* **5**, 35 (2004).
5. J. B. Moseley, A. Mayeux, A. Paoletti, P. Nurse, *Nature* **459**, 857 (2009).
6. M. N. Hall, M. C. Raff, G. Thomas, *Cell Growth: Control of Cell Size* (Cold Spring Harbor Laboratory Press, Cold Spring Harbor, NY, 2004).

10.1126/science.1177203

MATERIALS SCIENCE

Oriented Assembly of Metamaterials

The creation of complex materials may be aided by advanced colloidal assembly methods involving anisotropically shaped particles.

Kathleen J. Stebe,[1*] Eric Lewandowski,[1] Moniraj Ghosh[2]

Regular assemblies of colloidal particles have many potential uses from self-assembled electronics to biosensors. Recent advances in particle self-assembly suggest that such assemblies may also provide a simple route to metamaterials at infrared and visible length scales. Such metamaterials may, for example, be used to create cloaking devices or light-based circuits based on manipulations of local optical electric fields rather than on the flow of electrons (*1*).

Metamaterials are periodically structured composites with unit cells smaller than the wavelength used to interrogate them (*2*). By tailoring the unit cells to create a wide range of responses, technologies that were once the realm of fantasy—from computing with light to invisibility cloaks and superlenses—become reality. Such materials are relatively easy to create for use at radio frequencies, where the subunits need only be a few millimeters in size. However, use at optical and infrared wavelengths requires the assembly of three-dimensional micrometer- and nanometer-scale structures. This task is extremely challenging, but recent studies of particle self-assembly point the way to metamaterials at relevant length scales.

Metamaterials contain inclusions deliberately embedded in host media. The size, shape, and electromagnetic properties of the inclusions, along with inclusion density, arrangement, and alignment, determine their effective properties in a given host. Negative index of refraction metamaterials have been demonstrated in the optical range, made by serial approaches based on lithography (*3*, *4*). If, instead, metamaterials were designed to incorporate anisotropic nanoparticles through self-assembly, cumbersome lithographic approaches could be avoided.

An extensive library of anisotropic microparticles and nanoparticles now exists (*5*), allowing inclusion size and shape to be readily selected. Particles can be synthesized from many different materials, which can be selected for their electromagnetic properties. However, incorporating the particles as inclusions in self-assembled metamaterials requires techniques for assembly with control over particle orientation and spatial arrangement in periodic structures.

Convective assembly is a promising technique for creating close-packed assemblies of particles. The method is easy, inexpensive, and amenable to creating relatively large, defect-free periodically ordered structures of spherical particles. New assembly methods are also being developed to promote oriented assembly of anisotropically shaped particles in close-packed structures and to control deposition of particles in prescribed spatial locations on substrates, with potential for creating non–close-packed structures. We review

[1]Department of Chemical and Biomolecular Engineering, University of Pennsylvania, Philadelphia, PA 19104, USA. [2]Department of Chemical and Biomolecular Engineering, Johns Hopkins University, Baltimore, MD 21218, USA. *E-mail: kstebe@seas.upenn.edu

a few advances that are compatible with convective assembly, which enables mass production by continuous printing methods. The further development of these approaches is key to establishing robust methods for oriented assembly of metamaterials (*6*) (see the figure).

In convective assembly, a substrate is immersed in a colloidal suspension. The solvent forms a three-phase contact line where solvent, substrate, and vapor meet. As solvent evaporates, colloidal particles collect at the contact line. When particles protrude through the liquid-vapor interface, they create excess surface area and therefore excess surface energy. This energy diminishes as particles approach, creating capillary attraction that draws particles together to form an ordered structure (the nucleus). Continued evaporation collects particles near the nucleus, where they assemble into the growing colloidal crystal (*7*). Colloidal crystals are also grown from evaporating drops of suspensions in what is termed "drop-casting."

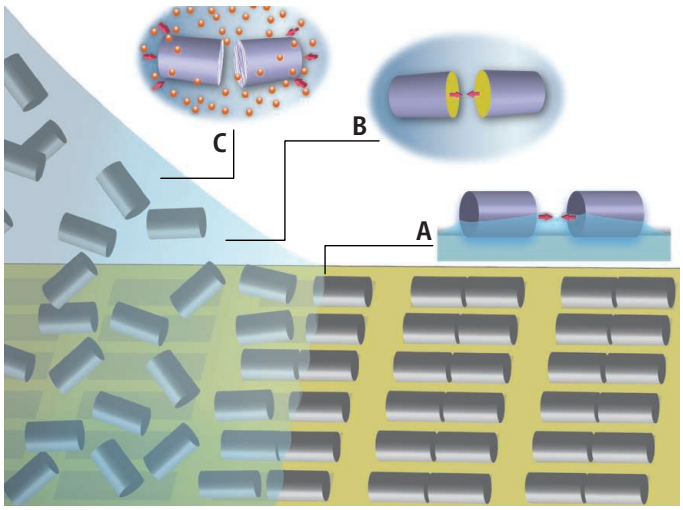

Metamaterial formed by convective assembly of anisotropic particles. Preferred locations can be lithographically defined or imposed by patterned evaporation. Oriented colloidal crystal nuclei could form by shape-dependent capillary interactions near the contact line (**A**). Oriented aggregation can be dictated by hydrophobic interactions created by selective surface functionalization (**B**) or by selective surface roughening to orient depletion attraction in bulk (**C**).

Ming *et al*. have recently used these techniques to make close-packed assemblies of anisotropic particles (nanorods, polyhedra, nanocubes, and bipyramids) into highly ordered structures in three dimensions (*8*). However, more systematic studies will be required to identify the conditions that promote such oriented assembly. To do so, two fundamental issues need to be addressed.

First, the particle orientation in colloidal crystal nuclei must be controlled. Solutions to this problem will likely use shape-dependent capillary interactions. Nuclei form near the contact line when particles protrude through the interface; particle shape and surface energy strongly influence the interfacial deformation fields and can be used to create orientation-dependent capillary interactions (see the figure). At free liquid-vapor interfaces, capillary interactions have been used to promote end-to-end or side-to-side assembly of elliptical microparticles (*9*). To promote formation of oriented nuclei in convective assembly, oriented capillary assembly of anisotropically shaped particles protruding through interfaces near contact lines should be studied (see the figure, panel A).

Second, means to dictate oriented assembly of particles in solution need to be developed. A recent numerical study predicts that elongated nanoparticles should readily form oriented liquid crystalline phases driven by the trade-off between translational and orientational entropy (*10*). In two recent experimental studies, particle orientation has been tuned by tailoring surface properties.

Rycenga *et al*. (*11*) tailored the surface energies of silver nanocubes by using self-assembled monolayers to render certain faces hydrophobic. When dispersed in an aqueous phase, the silver nanocubes form different structures depending on how many nanocube faces were functionalized. This approach could be used to orient any anisotropic particle (see the figure, panel B). Zhao and Mason (*12*) exploited depletion attraction and tailored surface roughness. In mixed suspensions of nanoscale and larger colloidal particles, the smaller particles are excluded from regions between the larger particles (see the figure, panel C). The resulting osmotic-pressure gradients push the larger particles together. Surface roughness increases this attraction by enhancing nanoparticle exclusion. Using these ideas, the authors assembled anisotropic particles with selected rough faces into highly ordered close-packed phases.

Methods have also been developed to deposit microscale and nanoscale particles in desired locations from evaporating suspensions to form non–close-packed structures. These will be useful for metamaterials with unit cells larger than the inclusion. For example, Aizenberg *et al*. have used lithographically defined attractive and repulsive regions on the substrate (*13*). When a drop of colloidal suspension evaporates on these surfaces, particles deposit on the attractive regions, and are drawn into ordered structures by capillary attraction. In another technique (*14*, *15*), particles near the contact line are swept into grooves cut into solid substrates as the contact line recedes. Within the grooves, the particles assemble into aggregates as solvent evaporates.

In these methods, spacing between the aggregates is defined by the spacing between the lithographically defined attractive regions or between the grooves on the substrate (see the figure). A particularly novel method reported by Harris *et al*. exploits the dependence of surface tension on temperature and evaporative cooling of the interface. By using a mask to pattern evaporation, patterned surface tension gradients were created. These gradients drove patterned flows within the drop. Particles were convected and deposited in patterns dictated by the flow (*16*).

These advances in colloidal science suggest that oriented assembly of anisotropic materials with three-dimensional control over particle position and orientation will soon be feasible. Such approaches present important opportunities in metamaterials design in the infrared and optical regimes. The challenge now is to move from hit-or-miss assemblies of academic interest to the creation of technologically relevant devices that combine particle and patterned assembly via large-scale processes.

References

1. N. Engheta, *Science* **317**, 1698 (2007).
2. N. Engheta, R. Ziolkowski, *Metamaterials: Physics and Engineering Explorations* (Wiley-IEEE, Piscataway, NJ, 2006).
3. V. M. Shalaev *et al.*, *Opt. Lett.* **30**, 3356 (2005).
4. J. Valentine *et al.*, *Nature* **455**, 376 (2008).
5. S. C. Glotzer, M. J. Solomon, *Nat. Mater.* **6**, 557 (2007).
6. J. H. Lee, Q. Wu, W. Park, *Opt. Lett.* **34**, 443 (2009).
7. N. Denkov *et al.*, *Langmuir* **8**, 3183 (1992).
8. T. Ming *et al.*, *Angew. Chem. Int. Ed.* **47**, 9685 (2008).
9. J. C. Loudet, A. M. Alsayed, J. Zhang, A. G. Yodh, *Phys. Rev. Lett.* **94**, 018301 (2005).
10. B. S. John, C. Juhlin, F. A. Escobedo, *J. Chem. Phys.* **128**, 044909 (2008).
11. M. Rycenga, J. M. McLellan, Y. Xia, *Adv. Mater.* **20**, 2416 (2008).
12. K. Zhao, T. G. Mason, *Phys. Rev. Lett.* **99**, 268301 (2007).
13. J. Aizenberg, P. V. Braun, P. Wiltzius, *Phys. Rev. Lett.* **84**, 2997 (2000).
14. Y. D. Yin, Y. Lu, B. Gates, Y. N. Xia, *J. Am. Chem. Soc.* **123**, 8718 (2001).
15. Y. Huang, X. F. Duan, Q. Q. Wei, C. M. Lieber, *Science* **291**, 630 (2001).
16. D. J. Harris, H. Hu, J. C. Conrad, J. A. Lewis, *Phys. Rev. Lett.* **98**, 148301 (2007).

10.1126/science.1174401

Drug Discovery and Natural Products: End of an Era or an Endless Frontier?

Jesse W.-H. Li and John C. Vederas*

Historically, the majority of new drugs have been generated from natural products (secondary metabolites) and from compounds derived from natural products. During the past 15 years, pharmaceutical industry research into natural products has declined, in part because of an emphasis on high-throughput screening of synthetic libraries. Currently there is substantial decline in new drug approvals and impending loss of patent protection for important medicines. However, untapped biological resources, "smart screening" methods, robotic separation with structural analysis, metabolic engineering, and synthetic biology offer exciting technologies for new natural product drug discovery. Advances in rapid genetic sequencing, coupled with manipulation of biosynthetic pathways, may provide a vast resource for the future discovery of pharmaceutical agents.

Just over 200 years ago, a 21-year-old pharmacist's apprentice named Friedrich Sertürner isolated the first pharmacologically active pure compound from a plant: morphine from opium produced by cut seed pods of the poppy, *Papaver somniferum* (*1*). This initiated an era wherein drugs from plants could be purified, studied, and administered in precise dosages that did not vary with the source or age of the material. Pharmaceutical research expanded after the Second World War to include massive screening of microorganisms for new antibiotics because of the discovery of penicillin. By 1990, about 80% of drugs were either natural products or analogs inspired by them. Antibiotics (e.g., penicillin, tetracycline, erythromycin), antiparasitics (e.g., avermectin), antimalarials (e.g., quinine, artemisinin), lipid control agents (e.g., lovastatin and analogs), immunosuppressants for organ transplants (e.g., cyclosporine, rapamycins) and anticancer drugs (e.g., taxol, doxorubicin) revolutionized medicine. Life expectancy in much of the world lengthened from about 40 years early in the 20th century to more than 77 years today. Although the expansion of synthetic medicinal chemistry in the 1990s caused the proportion of new drugs based on natural products to drop to ~50% (Fig. 1), 13 natural product–derived drugs were approved in the United States between 2005 and 2007, with five of them being the first members of new classes (*2*).

With such a successful record, it might be expected that the identification of new metabolites from living organisms would be the core of pharmaceutical discovery efforts. However, many pharmaceutical firms have eliminated their natural product research in the past decade. Although more than 100 natural product–based drugs are in clinical studies, this represents about a 30% drop between 2001 and 2008. Is the era of discovery of new drugs from natural sources ending?

Department of Chemistry, University of Alberta, Edmonton, Alberta T6G 2G2, Canada.

*To whom correspondence should be addressed. E-mail: john.vederas@ualberta.ca

What Challenges Face Drug Discovery from Natural Sources?

Most of the current difficulties can be divided into two categories: the prevailing paradigm for drug discovery in large pharmaceutical industries, and technical limitations in identifying new compounds with desirable activity.

The pharmaceutical environment. The double-digit yearly sales growth that drug companies typically enjoyed until about 10 years ago has led to unrealistically high expectations by their shareholders and great pressure to produce "blockbuster drugs" with more than $1 billion in annual sales (*3*). In the blockbuster model, a few drugs make the bulk of the profit. For example, eight products accounted for 58% of Pfizer's annual worldwide sales of $44 billion in 2007. When such drugs lose patent protection, their sales revenue can drop by 80%. About 25% of the current U.S. drug market will lose patent protection within 4 years (*4*). This will remove more than $63 billion in annual income for pharmaceutical industries by 2014. Competition from generic drug manufacturers, which are generally not involved in drug discovery, accounts for 67% of all prescriptions in the United States and is encouraged by health agencies to reduce costs.

The financial outlook for firms doing drug discovery is further encumbered by extensive litigation, costs of competitive marketing, and increasing expectations for safety both by the public and by regulatory agencies such as the U.S. Food and Drug Administration (FDA). FDA approvals of new drugs reached a 24-year low as of 2007, and drugs approved in Europe have been rejected by that agency. As an example of legal costs, after the withdrawal of the anti-inflammatory drug Vioxx because of a potential increase in risk of heart attack and stroke, Merck had to set aside $970 million to pay for associated legal expenses in 2007, and another $4.85 billion for upcoming U.S. legal claims (*5*). One approach to dealing with rising costs and a dwindling pipeline of new drugs is purchase of other companies that have such resources. Recent examples include the purchase of Wyeth by Pfizer for $68 billion and the acquisition of Schering-Plough by Merck for $41 billion (*6*). Such large sums affect the way drug discovery is done: Firms involved in drug discovery must hit the target not only accurately, but very quickly and very profitably. However, for reasons outlined below, natural product sources are currently not very amenable to rapid high-throughput screening (HTS) for desirable activity as drugs

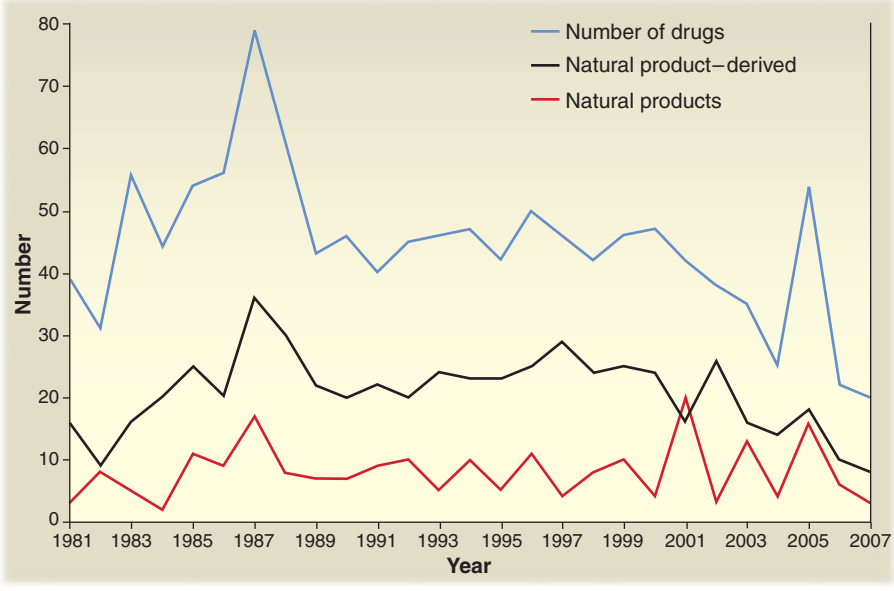

Fig. 1. Number of drugs approved in the United States from 1981 to 2007.

(*7*). Furthermore, in contrast to synthetic libraries, hits from natural sources are likely to have complex structures with numerous oxygen-containing substituents and an abundance of centers of stereochemistry (*8*). This slows the identification process and contributes to problems of supply and manufacture.

Difficulties in discovering natural product drug candidates. Historically, screening of natural materials for biological activity has worked well. Considering only polyketide metabolites, just over 7000 known structures have led to more than 20 commercial drugs with a "hit rate" of 0.3%, which is much better than the <0.001% hit rate for HTS of synthetic compound libraries (*9*). Although the hopes for useful leads from unfocused combinatorial chemistry libraries of mixtures have long since evaporated, pharmaceutical discovery efforts currently favor HTS of massive libraries of pure synthetic compounds. The output has been quite low, but any hits are usually easy to make and modify with simple chemistry. Libraries of pure compounds present in known amounts are also "screen friendly" and accommodate the desire for short timelines in examination of a large number of molecules. The recognition that such libraries are inherently limited prompts increasing interest in "diversity-oriented synthesis" and libraries of "privileged structures" (often based on known drugs or natural frameworks) to produce more complex molecules with a better chance of desirable bioactivity (*10*).

HTS of natural sources also presents a variety of difficulties. Problems of reliable access and supply, especially with respect to higher plants and marine organisms, are compounded by intellectual property concerns of local governments and the Rio Convention on Biodiversity (*11*). Seasonal or environmental variations in the composition of living organisms can cause problems with initial detection of active compounds as well as subsequent repetition of assays or purification. Loss of source is also possible: Current extinction rates for natural species of higher plants are estimated to be a factor of 100 to 1000 over natural background (*12*). It has been suggested that 15,000 out of 50,000 to 70,000 medicinal plant species are threatened with extinction (*12*). Even if supply is easy and guaranteed, the initial extract of the natural material usually consists of a complex mixture after fractionation. It may contain only very small quantities of a bioactive substance, often as a mixture with structurally related molecules. The initial concentration of an interesting compound may be too low to be effectively detected by HTS, or the assay may be obscured by poor solubility or by fluorescent or colored contaminants. The key compound may be unstable in the mixture. A further complication can be synergistic (or antagonistic) activity of two constituents that may then diminish or disappear upon separation. For example, a number of bacteriocins (antimicrobial peptides from bacteria) must function as two-component systems to display full activity (*13*). Finally, considerable time is often required to complete structural characterization to determine whether the molecule is already known.

A prevailing sentiment in many pharmaceutical organizations is that screening of natural product sources is a difficult effort with a high probability of duplication; that is, the result may be a known compound that cannot be patented. However, fewer than 1% of microorganism species are easily cultured, and perhaps fewer than 15% of higher plant species have been examined for bioactivity (*14*). Certain insects and other animals have been targeted for specific bioactivities, such as toxins (*15*), but are not generally subjected to HTS efforts. Clearly the biological resource is there, but access and examination are problematic, especially if there is pressure for a short time frame for discovery of new leads.

What Tools Are Emerging to Enhance and Accelerate Drug Discovery from Natural Sources?

Several interlocking phases of exploration of natural sources can be considered: access to the biological resource, appropriate screening of that resource to locate a useful activity, analysis of the structure of the key compound, generation of analogs for optimal activity, and production of the target drug.

Biological resources. Traditionally, soil bacteria (especially actinomycetes), fungi, and higher plants were main sources for drug discovery. Pharmaceutical firms increasingly abandoned screening of microorganisms after 1990 because of decreasing success rates. Common antibiotics such as streptomycin occur in ~1% of soil actinomycetes and display activity in screens; this activity masks interesting new antimicrobials, which may be produced at a frequency of less than 1 in 10 million fermentations. A solution pursued by Cubist Pharmaceuticals is to massively increase the number of fermentations (to many millions per year) while miniaturizing their size, using calcium alginate beads as the containers (*16*). This approach is coupled to an assay with engineered *Escherichia coli* strains that are resistant to common well-known antibiotics. However, despite the urgent need to find new antibiotics effective against life-threatening organisms resistant to current therapy, many pharmaceutical firms do not develop such drugs. Sales and "blockbuster potential" are limited by the short duration of treatment with antibiotics relative to other drugs, such as cholesterol-lowering or hypertensive agents, which are consumed daily for prolonged periods and relieve

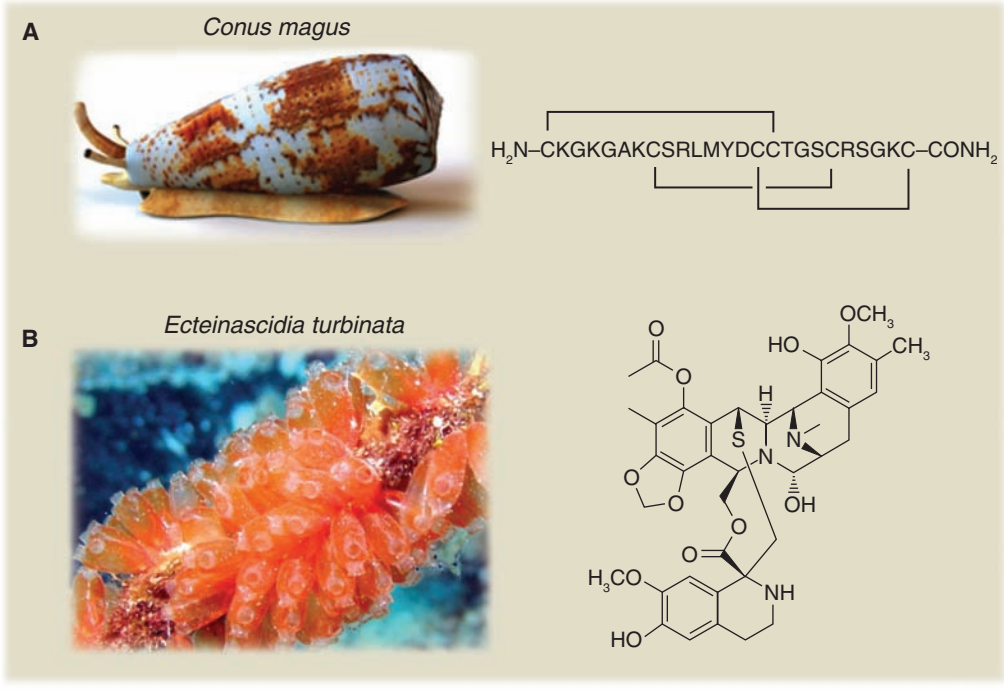

Fig. 2. Marine sources of drugs. (**A**) Ziconotide (Prialt) from *Conus magus*. Abbreviations for amino acids: A, Ala; C, Cys; D, Asp; G, Gly; K, Lys; L, Leu; M, Met; R, Arg; S, Ser; T, Thr; Y, Tyr. (**B**) Trabectedin (Yondelis) from *Ecteinascidia turbinata*. [Image of *C. magus* from (*45*), reprinted by permission of Macmillan Publishers Ltd.; image of *E. turbinata* by Florent Charpin, reprinted by permission of *Florent's Guide to the Tropical Reefs* (http://reefguide.org)]

symptoms rather than provide a cure. Nonetheless, development costs, standards for safety, and requirements for limited side effects are similar for both antibiotics and "long-term" drugs.

Although plants remain a major source of new drugs, with 91 compounds in clinical trials as of late 2007, cyanobacteria (*17*) and marine organisms (*18*) have been actively investigated in recent decades, especially for neurotoxic and cytotoxic compounds. Ziconotide (Prialt), a peptide toxin from cone snails (Fig. 2A), was approved in 2004 for treatment of chronic pain resulting from spinal cord injury. A tropical sea squirt has yielded the cytotoxic trabectedin (Yondelis) (Fig. 2B), which is approved in Europe since 2007 for treatment of advanced soft-tissue sarcoma (*19*). Useful organisms may exist in extreme environments, such as at great sea depths (*20*), in thermal vents, or in salt lakes. An appealing example is the identification of haloduracin, a two-component lantibiotic (lanthionine-containing peptide antibiotic) from *Bacillus halodurans*, which grows at an extreme pH of >9.0 (*21*). A well-known lantibiotic is nisin A, which is used to preserve food and is very active against Gram-positive bacteria resistant to conventional antibiotics. However, nisin's therapeutic potential is blocked by its instability at neutral pH or above. Van der Donk and co-workers reasoned that base-stable lantibiotics may be produced by bacteria growing in alkaline environments (*21*). Using bioinformatics, they found haloduracin, which can survive pH ranges well above that of human serum. Although haloduracin's solubility is limited, it provides a basis for development of new lantibiotics with drug potential.

It may initially appear that there are few unexplored locations to look for natural sources of drug candidates, but enormous numbers of species have remained unexamined. There are claims that more than 99% of all bacteria cannot be cultured, and that in marine environments there may be 3.7×10^{30} microorganisms, many of which may produce fascinating natural products as drug candidates (*22*). To address this, in 1998 the concept of metagenomics was proposed to look at genes and their function in samples obtained directly from the environment (*23*). This field has exploded as faster and cheaper gene sequencing is becoming available (*24*) in combination with the ability to rapidly sort cells from the environment and efficiently clone genes in improved vectors (*25*). Together with automated screening techniques, the metagenomic approach could afford access to the pool of 99% of unexamined microorganisms. However, at present most pharmaceutical firms do not appear to be undertaking efforts in this direction for drug discovery.

Appropriate screening. It is likely that natural products represent privileged structures for drug discovery. This suggestion is supported by the fact that there are a limited number of protein folds known, and that natural products must bind to some of these in order to be biosynthesized and to fulfill their inherent function in the producing organisms. Hence, many of them may be structurally favored to bind to enzymes or protein receptors. However, as described above, the complexity of the initial natural extract can make it unfavorable for HTS. The ideal approach to overcome this obstacle would be automated separation of all constituents in the organism into individual components, coupled with full spectroscopic identification prior to HTS. Although this is not yet achievable, Ireland and co-workers (*26*) recently automated fractionation of crude extracts of natural materials from marine sources using desalting followed by high-performance liquid chromatography (HPLC) on highly efficient monolithic columns. This was in turn coupled to mass spectrometric analysis and collection on HTS plates. The process produces highly purified samples in 96-well plates, which are generated as replicates for initial screening as well as for a material archive. It is claimed that typically only three compounds per well are observed (*26*). Testing of a 15,360-member library of this type against hamster cell lines allowed identification of novel compounds with antitumor potential selective for breast cancer despite the co-occurrence of general cytotoxins in the same extract.

The efficiency of HTS can be greatly enhanced by using the best target to achieve "smart screening." One approach mentioned above is the use of organisms resistant to common known antibiotics, as used by Cubist. An innovative alternative was developed at Merck to identify broad-spectrum antibiotics (Fig. 3) (*27*). It uses a two-plate assay, in which one plate has *Staphylococcus aureus* bearing a plasmid that produces antisense RNA to a key fatty acid synthase enzyme (e.g., FabF) and the other is a *S. aureus* control plate without capability to produce the antisense RNA. The antisense RNA causes degradation of the mRNA at the 5′ end for the key enzyme, thereby enhancing the organism's sensitivity for inhibitors of that particular protein catalyst. This approach enables more sensitive detection of activity, and also permits identification of individual targets in complex systems through parallel screening with different antisense RNAs. The hit rate for such screening of more than 250,000 natural product extracts was high (0.3%). More important, it identified a new target, bacterial fatty acid synthesis, and novel antibiotics, platensimycin A and platencin.

Increasingly, multiple targets are being investigated with the use of cells. An interesting example is single-cell screening of inhibitors of phosphorylation (kinase) signaling pathways using flow cytometry (*28*). This phosphospecific flow cytometry (phosphoflow) makes multiple quantitative measurements of phosphorylation levels of different signaling proteins by measuring specific fluorescently labeled antibodies that recognize them after phosphate at-

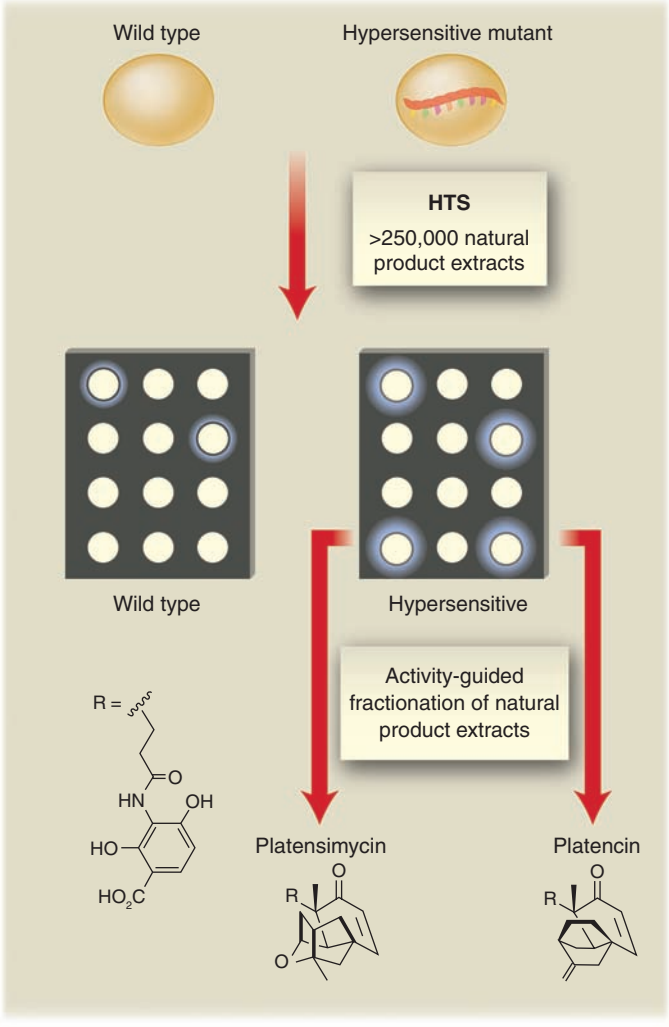

Fig. 3. HTS using differential-sensitivity whole-cell two-plate agar diffusion (the Merck platensimycin assay). The strain expressing antisense RNA to FabH or FabF enzymes of fatty acid biosynthesis is hypersensitive to inhibitors of those proteins. The approach identified two new antibiotics, platensimycin and platencin.

tachment. The effect of natural product libraries can be rapidly and quantitatively measured on single cells. Cell-based assays have also recently been used to find rapamycin analogs that lack the drug's usual immunosuppressive activity but protect nerve cells in models of stroke (*29*).

Analysis of the structure of active compounds. Structure elucidation on small quantities of material has been greatly assisted by advances in mass spectrometry and multidimensional nuclear magnetic resonance (NMR) spectroscopy. It is beyond the scope of this review to discuss the details of these techniques. However, automated coupling of mass spectrometry to separation by HPLC and HTS library creation clearly accelerates the identification of known compounds and possible hits. Cryoprobes for NMR spectroscopy have greatly enhanced sensitivity and have markedly reduced the amount of material required for analysis; for smaller compounds (molecular weight 200), useful proton spectra require 2 μg of material and carbon correlation spectra can be obtained on 0.2 mg (*30*). Comparison of NMR signal positions to corresponding databases of known compounds can hasten dereplication (i.e., recognition of known compounds). Efforts are also under way to automatically capture substances from HPLC separations by solid-phase extraction and then elute directly into an NMR cryoprobe for analysis.

Generation of analogs. Traditionally, structure-activity relationships in bioactive natural products were examined by simple chemical transformations. For example, methylation of the side chain of the cholesterol-lowering agent lovastatin produces simvastatin (Zocor) (Fig. 4), an improved drug that had sales in excess of $4.3 billion in 2006 (before loss of patent protection). The developing understanding of secondary metabolite biogenesis allows use of biosynthetic enzymes or genetically altered organisms to generate derivatives of drugs. Tang and co-workers used an esterase (LovD), which normally attaches the side chain of lovastatin, to make a series of analogs, including simvastatin (*31*). The esterase normally uses a 2-methylbutyrate attached as a thioester to a large protein as its acylating agent for the corresponding alcohol. However, a variety of simple thioesters could be substituted to give efficient conversion to many analogs.

Combinatorial biosynthesis, especially using modular polyketide synthases (PKSs) and nonribosomal peptide synthetases (NRPSs), holds great promise (*32*). PKSs and NRPSs are large multidomain enzymes that sequentially condense short fatty acids and α–amino acids, respectively. They resemble assembly lines for making a metabolite by chain elongation and functional group transformation, and can be altered to make new compounds. However, the results of mutation are frequently unpredictable, and the levels of product formation can be very low. The growing understanding of linkers between individual domains in these proteins as well as protein-protein interactions between domains may solve this problem. One approach to overcoming difficulties resulting from introduction of a modified domain is directed evolution to increase production by the chimera. Only three rounds of mutagenesis and screening of modest libraries (10^3 to 10^4 clones) of an NRPS domain were sufficient to give substantial improvement of production of an isoleucine-containing analog of andrimid (Fig. 4) having better antibiotic properties (*33*). In a different example, direct mutation of a PKS domain combined with inactivation of a gene responsible for post-assembly oxidation gave nystatin analogs (Fig. 4) with improved antifungal activity and lower toxicity (*34*). Inactivation of a post-PKS P450 that oxidizes a methyl to the C16 carboxyl in nystatin, coupled with mutation of the enoyl reductase activity in the NysC PKS module, affords methyl derivatives with a conjugated heptaene moiety (as opposed to an interrupted hexaene). The best compounds are effective against disseminated candidosis in mouse models and are considerably less toxic than amphotericin B. However, such generation of new analogs using combinatorial biosynthesis can require extensive time and effort, and is currently not matched to the requirements of HTS.

Production of target compounds. The traditional approach to optimal production of drugs by microorganisms is to "mutate and screen" for strain improvement, as was done in the 1940s for penicillin. This methodology can readily yield enhancement of drug production by two to three orders of magnitude, and in some cases by four to five orders of magnitude (*35*). At present, this tactic is difficult to beat, and molecular biological manipulations have been more successful only in isolated cases. An interesting example is the improvement of production of doramectin (Dectomax) (Fig. 4), an antiparasitic agent in the avermectin family (*36*). The initial production strain was a mutant of *Streptomyces avermitilis* lacking a dehydrogenase and an O-methyl transferase. This strain can be fed cyclohexane carboxylic acid as the initiator to give doramectin

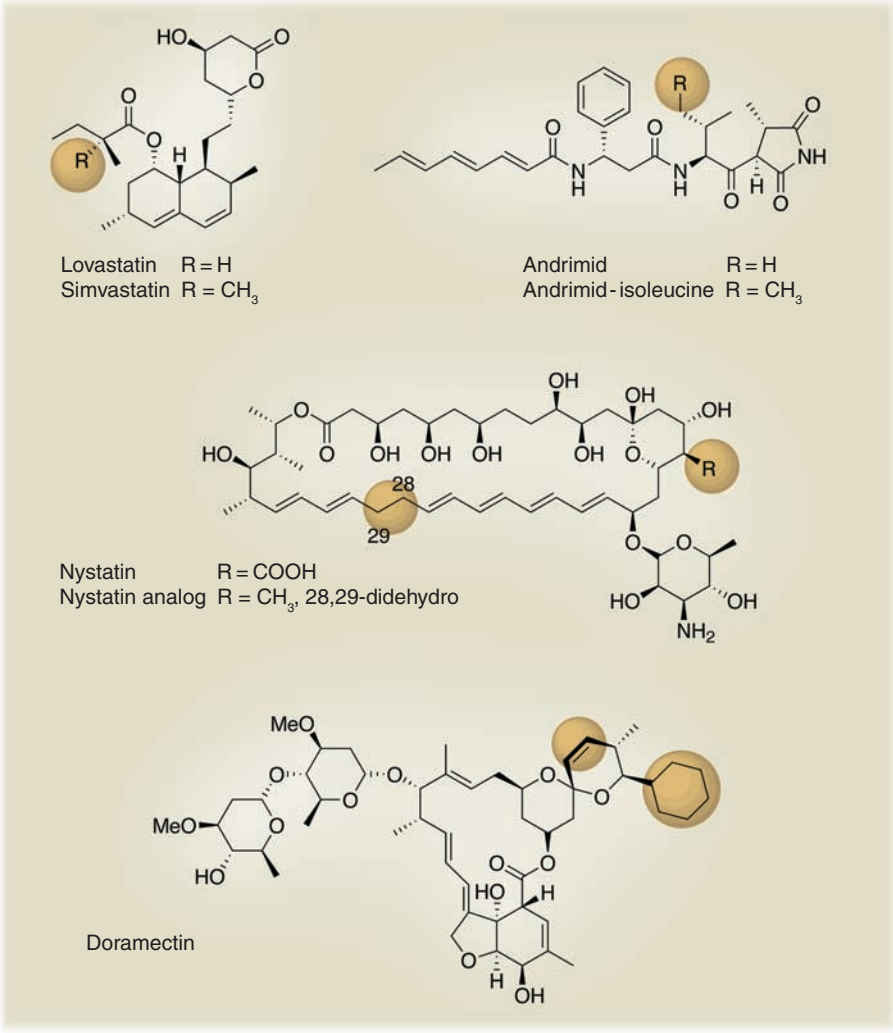

Fig. 4. Drug analogs produced by modification of biosynthetic genes. Shaded areas indicate sites of altered structure; Me, methyl.

together with a side product having a hydroxyl at C-23 instead of a double bond. DNA shuffling of the *aveC* gene and screening gave a new gene that encoded 10 amino acid mutations and reduced the unwanted contaminant for an overall improvement of production by a factor of 23. Natural products, including those from bacteria, can of course also be made or improved synthetically. For example, a large amount of effort has gone into synthetic analogs of epothilone B, a promising anticancer drug (*37*).

Drugs with complex structures from higher plants present a challenge if they are found in small concentrations. An example is the antitumor agent taxol (paclitaxel), which occurs in the bark of the pacific yew tree *Taxus brevifolia* (*38*). Initially it was predicted that treatment of ovarian cancer and melanoma cases in the United States would require the destruction of more than 360,000 yew trees annually. However, a semisynthetic route to taxol from 10-deacetylbaccatin, which was isolated from the needles of the European yew *T. baccata*, was developed that averted the devastation of trees.

In the past decade, taxol has been commercially produced by Bristol-Myers Squibb by plant cell fermentation (PCF) technology. However, for a number of other drugs there are substantial difficulties in getting sufficient production by PCF (*39*). An alternative approach is heterologous expression of the biosynthetic pathway in yeast or bacteria, frequently with modification of the genes to optimize production (synthetic biology). A well-known example is the effort to produce the antimalarial drug artemisinin in *E. coli* and yeast (*40*). Artemisinin from *Artemesia annua* is a sesquiterpenoid that is effective against multi–drug-resistant *Plasmodium* species but is expensive for Third World patients. The Keasling group (*40*) has engineered *E. coli* to produce its precursor, artemisinic acid, in concentrations of up to 300 mg per liter. This required extensive work, including engineering a mevalonate pathway to produce ample amounts of precursor for isoprenoid synthesis, optimization of expression of amorphadiene synthase (the key terpene cyclase), and incorporation of a modified version of amorphadiene oxidase (the P450 that converts amorphadiene to artemisinic acid). The work demonstrates that many complex natural products from plants can be engineered into heterologous hosts for fermentative production.

What Are the Future Prospects for Natural Product Drugs?

With the current framework of HTS in major pharmaceutical industries and increasing government restrictions on drug approvals, it is possible that the number of new natural product–derived drugs could go to zero. However, this is likely to be temporary, as the potential for new discoveries in the longer term is enormous. Access to rapid and inexpensive genome sequencing via 454 sequencing (*41*) or single-molecule real-time (SMRT) (*42*) methods will fully enable metagenomics for unculturable organisms. It will also uncover "silent pathways" in plants (*43*) to afford access to a large collection of new products and biocatalysts. It will allow preservation of any threatened species, through cataloging of its genetic blueprint, and may permit recovery of extinct organisms. Estimates for the total number of living species range from 2 million to 100 million, with one claim of 30 million species just for insects. Hence, the number of biosynthetic products and enzymes remaining to be examined is huge. Systems biology could eventually map the likely metabolism for most species. Such a library of biochemical transformations could be a magnificent tool for the design and generation of new products. Just as synthetic chemists currently plan total syntheses of a target compound using established reagents and well-precedented transformations, synthetic biologists will be able to call on vast arrays of enzymes to rationally make complex molecules. Directed evolution and site-specific mutation can optimize the desired activity of such proteins. Rapid gene sequencing of individual humans will enhance the development of personalized medicine—the use of an individual's DNA sequence as a basis for drug selection (*44*). This could satisfy the current expectations for high levels of safety by predicting side effects and assisting the correct choice of therapeutic drugs. New gene-mapping techniques will facilitate speedy diagnostic tests to determine causes of illness, including infections. This could lessen the indiscriminate use of antibiotics and thereby reduce the development of bacterial resistance to such drugs.

To achieve the potential of facile genome sequencing, the development of robust platforms is essential for heterologous expression of genes of novel biosynthetic pathways. Expression of biosynthetic enzymes often requires considerable effort. Problems of codon usage and optimization (requiring gene synthesis), of protein localization and modification, and of metabolite toxicity to the producing organism are only a few of the difficulties. The solutions will involve modifications of organisms that are already widely used (e.g., *E. coli*, *Saccharomyces cerevisiae*). For example, enhancement of primary precursor production can be coupled with programmed control of promoters and modifications to enhance the stability of foreign proteins. Active export of toxic target metabolites could potentially be engineered using drug resistance transporters. It is likely that such expression platforms will initially be demonstrated in academic laboratories prior to use in pharmaceutical industry. Although the current industry model for drug discovery does not favor natural products, the resource is so vast as to seem unlimited, and these emerging tools will provide exhilarating discoveries leading to new medicines.

References and Notes

1. G. R. Hamilton, T. F. Baskett, *Can. J. Anaesth.* **47**, 367 (2000).
2. A. L. Harvey, *Drug Discov. Today* **13**, 894 (2008).
3. N. N. Malik, *Drug Discov. Today* **13**, 909 (2008).
4. S. Houlton, *Chem. World* (January 2009), p. 12.
5. J. M. Wolsing, *Defense Counsel J.* (July 2008), p. 209.
6. L. M. Jarvis, *Chem. Eng. News* **87**, 5 (16 March 2009).
7. F. E. Koehn, G. T. Carter, *Nat. Rev. Drug Discov.* **4**, 206 (2005).
8. M. S. Butler, *J. Nat. Prod.* **67**, 2141 (2004).
9. K. J. Weissman, P. F. Leadlay, *Nat. Rev. Microbiol.* **3**, 925 (2005).
10. D. J. Newman, *J. Med. Chem.* **51**, 2589 (2008).
11. B. E. Kirsop, *J. Ind. Microbiol. Biotechnol.* **17**, 505 (1996).
12. V. Brower, *J. Natl. Cancer Inst.* **100**, 838 (2008).
13. S. Garneau, N. I. Martin, J. C. Vederas, *Biochimie* **84**, 577 (2002).
14. A. Saklani, S. K. Kutty, *Drug Discov. Today* **13**, 161 (2008).
15. S. Mouhat, N. Andreotti, B. Jouirou, J. M. Sabatier, *Curr. Pharm. Des.* **14**, 2503 (2008).
16. R. H. Baltz, *Curr. Opin. Pharmacol.* **8**, 557 (2008).
17. N. V. Wase, P. C. Wright, *Expert Opin. Drug Discov.* **3**, 903 (2008).
18. J. W. Blunt *et al.*, *Nat. Prod. Rep.* **26**, 170 (2009).
19. D. S. Dalisay, S. L. Lievens, J. P. Saludes, T. F. Molinski, *Nat. Rev. Drug Discov.* **8**, 69 (2008).
20. D. Skropeta, *Nat. Prod. Rep.* **25**, 1131 (2008).
21. L. E. Cooper, A. L. McClerren, A. Chary, W. A. van der Donk, *Chem. Biol.* **15**, 1035 (2008).
22. J. Kennedy, J. Marchesi, A. D. W. Dobson, *Microb. Cell Fact.* **7**, 27 (2008).
23. J. Handelsman, M. R. Rondon, S. F. Brady, J. Clardy, R. M. Goodman, *Chem. Biol.* **5**, R245 (1998).
24. N. Blow, *Nature* **453**, 687 (2008).
25. P. Hugenholtz, G. W. Tyson, *Nature* **455**, 481 (2008).
26. T. S. Bugni *et al.*, *J. Nat. Prod.* **71**, 1095 (2008).
27. H. Jayasuriya *et al.*, *Angew. Chem. Int. Ed.* **46**, 4684 (2007).
28. P. O. Krutzik, J. M. Crane, M. R. Clutter, G. P. Nolan, *Nat. Chem. Biol.* **4**, 132 (2008).
29. B. Ruan *et al.*, *Proc. Natl. Acad. Sci. U.S.A.* **105**, 33 (2008).
30. G. Lang *et al.*, *J. Nat. Prod.* **71**, 1595 (2008).
31. H. Zhou, X. Xie, Y. Tang, *Curr. Opin. Biotechnol.* **19**, 590 (2008).
32. K. J. Weissman, R. Müller, *ChemBioChem* **9**, 826 (2008).
33. M. A. Fischbach, J. R. Lai, E. D. Roche, C. T. Walsh, D. R. Liu, *Proc. Natl. Acad. Sci. U.S.A.* **104**, 11951 (2007).
34. T. Brautaset *et al.*, *Chem. Biol.* **15**, 1198 (2008).
35. C. Olano, F. Lombo, C. Mendez, J. A. Salas, *Metab. Eng.* **10**, 281 (2008).
36. K. Stutzman-Engwall *et al.*, *Metab. Eng.* **7**, 27 (2005).
37. J. Mulzer, K. H. Altmann, G. Höfle, R. Müller, K. Prantz, *C. R. Chim.* **11**, 1336 (2008).
38. 2004 Greener Synthetic Pathways Award: Bristol-Myers Squibb Company, Development of a Green Synthesis for Taxol Manufacture via Plant Cell Fermentation and Extraction (www.epa.gov/greenchemistry/pubs/pgcc/winners/gspa04.html), accessed 6 April 2009.
39. S. C. Roberts, *Nat. Chem. Biol.* **3**, 387 (2007).
40. J. D. Keasling, *ACS Chem. Biol.* **3**, 64 (2008).
41. J. M. Rothberg, J. H. Leamon, *Nat. Biotechnol.* **26**, 1117 (2008).
42. J. Eid *et al.*, *Science* **323**, 133 (2009); published online 20 November 2008 (10.1126/science.1162986).
43. E. Lewinsohn, M. Gijzen, *Plant Sci.* **176**, 161 (2009).
44. S. S.-J. Lee, A. Mudaliar, *Science* **323**, 342 (2009).
45. K. Garber, *Nat. Biotechnol.* **23**, 399 (2005).

46. Supported by the Natural Sciences and Engineering Research Council of Canada, the Canada Research Chairs program, and the University of Alberta.

10.1126/science.1168243

Traction on Immobilized Netrin-1 Is Sufficient to Reorient Axons

Simon W. Moore, Nicolas Biais, Michael P. Sheetz*

During embryonic development, axons are guided to their target by patterning proteins encountered along their trajectory (*1*). These cues can be linked to the cells that produce them or secreted into the extracellular matrix. Whether secreted cues provide traction for the growth cone when attached to the extracellular matrix is unclear. For instance, the secreted cue netrin can diffuse through collagen to induce axon outgrowth at a distance, and its release from a micropipette can influence the extension of axons in culture (*2*, *3*). However, netrins are also known to bind to extracellular matrix components and can function when attached directly to or in close proximity to the cells that produce them (*2*, *4*, *5*). The substrate associations of netrin may simply buffer their concentration distribution by slowing their dispersion. We tested whether growth cones exert a traction force directly on netrin-1 that is sufficient to reorient their axons.

As they extend ventrally in the spinal cord, spinal commissural neuron (SCN) axons are attracted to netrin-1 released by the floor plate. When dissociated SCNs were presented with an unrestrained silica bead with covalently attached netrin-1 (*6*), their growth cones captured and transported it down the axon (Fig. 1A and movie S1). However, when presented with a netrin-1–coated bead immobilized to the substrate, a distinct reorientation of the axon was observed (Fig. 1, A and B, and movies S2 and S3). Thus, immobilized netrin-1 was sufficient to reorient the axon. Moreover, the retrograde transport of an unrestrained bead as well as the reorientation toward immobilized beads indicated that the growth cone generated force on netrin-1. To test this possibility, we measured the pulling forces on netrin-1 by presenting SCN growth cones with optically trapped beads. Growth cones rapidly (~4.5 min) generated pulling forces in excess of 63 pN (Fig. 1C and movie S4). Such pulling forces were not observed on uncoated beads (Fig. 1C). Similarly, when growth cones encountered beads coated with the repellent cue bone morphogenetic protein (BMP) 7 (*7*), they rapidly collapsed and rarely exerted forces above 25 pN (Fig. 1C and movie S5). Chemoattraction to netrin-1 required the transmembrane receptor deleted in colorectal cancer (DCC) (*8*). When the interaction between netrin-1 and DCC was decreased by competition with a recombinant soluble form of the extracellular domain of DCC (Dfc) or when DCC function was disrupted with an antibody (AF5), pulling of netrin-1–coated beads was disrupted (Fig. 1C). Thus, SCN growth cones exerted a specific pulling force that appeared to be directly on netrin-1 and to require the receptor DCC.

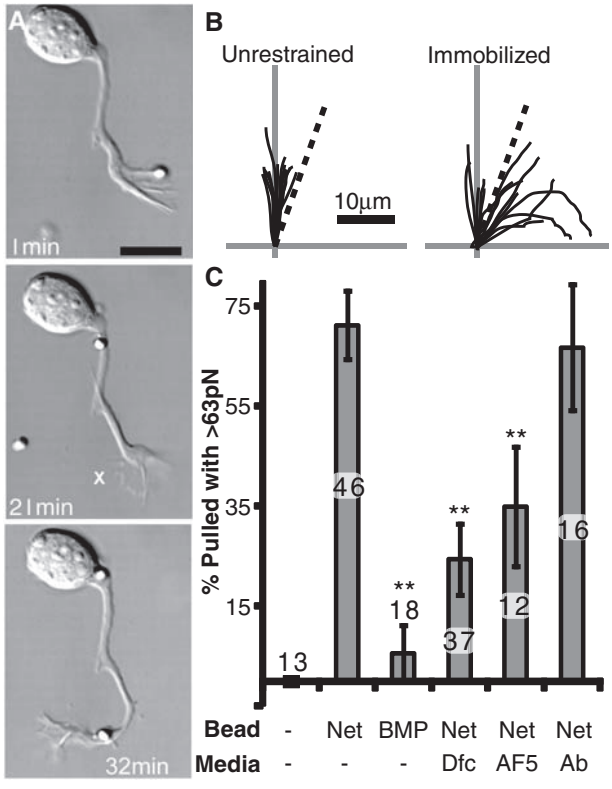

Fig. 1. (**A**) A netrin-1 bead is presented and released upon contact on one side of the growth cone (top). After 22 min, another bead is presented, but this time it is attached to the substrate (marked X, middle). Scale bar indicates 10 μm. (**B**) Traces of axons confronted with unrestrained or immobilized netrin-1 beads. Vertical axis is the initial trajectory of the axon, whereas the dotted line marks a 20° angle. None of the 13 axons assayed turned at an angle >20° when unrestrained, whereas 10 of the 15 axons reoriented to immobilized beads. (**C**) Percent of beads pulled with >63 pN within 8 min (Ab, unspecific antibodies). The number of growth cones assayed is indicated above or within each bar. Error bars are SEM, and $^{**}P < 0.01$ relative to netrin-1 (Tukey).

To understand what the magnitude of these pulling forces represented, we needed to compare them to the normal pulling events of an advancing growth cone. Growth cones generated a forward locomotive force (*9*); however, the distribution and magnitude of these forces within a growth cone were unclear. By using the calibrated deflections of microfabricated polyacrylamide pillars, we measured the simultaneous, local pulling events of extending SCN axons (fig. S1 and movie S6). Pulling forces ranged from 2 to 37 pN, although the majority (>90%) occurred between 4 and 15 pN and the average was 9 pN (n = 2789, fig. S1E). Thus, the pulling forces observed on netrin-1 beads were more than sevenfold higher than the average local pulling forces of SCN growth cones.

The mechanical interaction between the growth cone and netrin-1 may play a role in other aspects of the response to netrin-1. For instance, mechanical extension of adhesion site proteins can expose buried sequences that transduce mechanical force into intracellular signaling cascades (*10*, *11*). Future studies are needed to define how netrin-1 triggers the intracellular signaling required to coordinate the reorientation of the axon.

References and Notes

1. A. B. Huber, A. L. Kolodkin, D. D. Ginty, J. F. Cloutier, *Annu. Rev. Neurosci.* **26**, 509 (2003).
2. T. E. Kennedy, T. Serafini, J. R. de la Torre, M. Tessier-Lavigne, *Cell* **78**, 425 (1994).
3. J. R. de la Torre *et al.*, *Neuron* **19**, 1211 (1997).
4. M. S. Deiner *et al.*, *Neuron* **19**, 575 (1997).
5. M. Brankatschk, B. J. Dickson, *Nat. Neurosci.* **9**, 188 (2006).
6. Materials and methods are available as supporting material on *Science* Online.
7. A. Augsburger, A. Schuchardt, S. Hoskins, J. Dodd, S. Butler, *Neuron* **24**, 127 (1999).
8. K. Keino-Masu *et al.*, *Cell* **87**, 175 (1996).
9. P. Lamoureux, R. E. Buxbaum, S. R. Heidemann, *Nature* **340**, 159 (1989).
10. Y. Sawada *et al.*, *Cell* **127**, 1015 (2006).
11. A. del Rio *et al.*, *Science* **323**, 638 (2009).
12. We thank T. E. Kennedy for critical reading, N. Gauthier for discussion, and support from NIH grants PN2 EY016586-02 (S.W.M. and M.P.S.) and AI079030 (N.B.).

Supporting Online Material

www.sciencemag.org/cgi/content/full/325/5937/166/DC1
Materials and Methods
Fig. S1
Movies S1 to S6

20 March 2009; accepted 5 May 2009
10.1126/science.1173851

Department of Biological Sciences, Columbia University, 1212 Amsterdam Avenue, New York, NY 10027, USA.

*To whom correspondence should be addressed. E-mail: ms2001@columbia.edu

Cell Growth and Size Homeostasis in Proliferating Animal Cells

Amit Tzur,[1]* Ran Kafri,[1]* Valerie S. LeBleu,[2] Galit Lahav,[1] Marc W. Kirschner[1]†

A long-standing question in biology is whether there is an intrinsic mechanism for coordinating growth and the cell cycle in metazoan cells. We examined cell size distributions in populations of lymphoblasts and applied a mathematical analysis to calculate how growth rates vary with both cell size and the cell cycle. Our results show that growth rate is size-dependent throughout the cell cycle. After initial growth suppression, there is a rapid increase in growth rate during the G_1 phase, followed by a period of constant exponential growth. The probability of cell division varies independently with cell size and cell age. We conclude that proliferating mammalian cells have an intrinsic mechanism that maintains cell size.

A cell's growth may have a complex relationship to milestones in its life, specifically to its position in the cell cycle. In one model, growth rate is proportional to cell size at any time during the cell cycle (in whatever terms size is measured, e.g., volume, mass, or protein content); this constitutes exponential growth for an individual cell. Alternatively, the growth rate might be constant, producing a linear increase in size (*1*, *2*). These alternative models have important implications for how cell size is regulated. Specifically, the size of the daughter cells upon division is variable. If the larger daughter grows more rapidly than the smaller, as in the exponential model, cell size variation in the population would increase in each generation. Because this does not occur, we know that if growth is exponential—or, more generally, if it increases with cell size—some mechanism must limit size variation in cells (*3*–*5*).

In budding yeast, there is evidence both for a size-dependent growth rate (*6*) and for a process that coordinates growth with division in a way that potentially limits size variation (*1*, *7*–*9*). Whether there are similar growth controls in bacteria remains controversial (*10*–*12*). In metazoan cells, it is unclear whether such regulation exists at all. Because somatic cells do not grow as isolated cells, their size regulation might simply be the result of separate growth and mitogenic signals from the environment. Studies on primary Schwann cells suggested such a model; they provided evidence for a constant rate of growth independent of cell size (*13*–*15*). Yet these conclusions are also controversial (*16*, *17*), and other measurements of growth in mammalian cells have suggested that growth rate is proportional to size (*18*), implying a cell-sizing mechanism (*19*).

Attempts to measure growth during the cell cycle from time-series measurements confront major challenges. To obtain this information requires accuracy that is currently unattainable (*2*). Distinguishing between exponential and linear growth would need a resolution of <6% in volume (*20*). Even careful interferometric measurements in the classic experiments by Zetterberg and Killander

[1]Department of Systems Biology, Harvard Medical School, Boston, MA 02115, USA. [2]Division of Matrix Biology, Beth Israel Deaconess Medical Center and Harvard Medical School, Boston, MA 02215, USA.

*These authors contributed equally to this work.
†To whom correspondence should be addressed. E-mail: marc@hms.harvard.edu

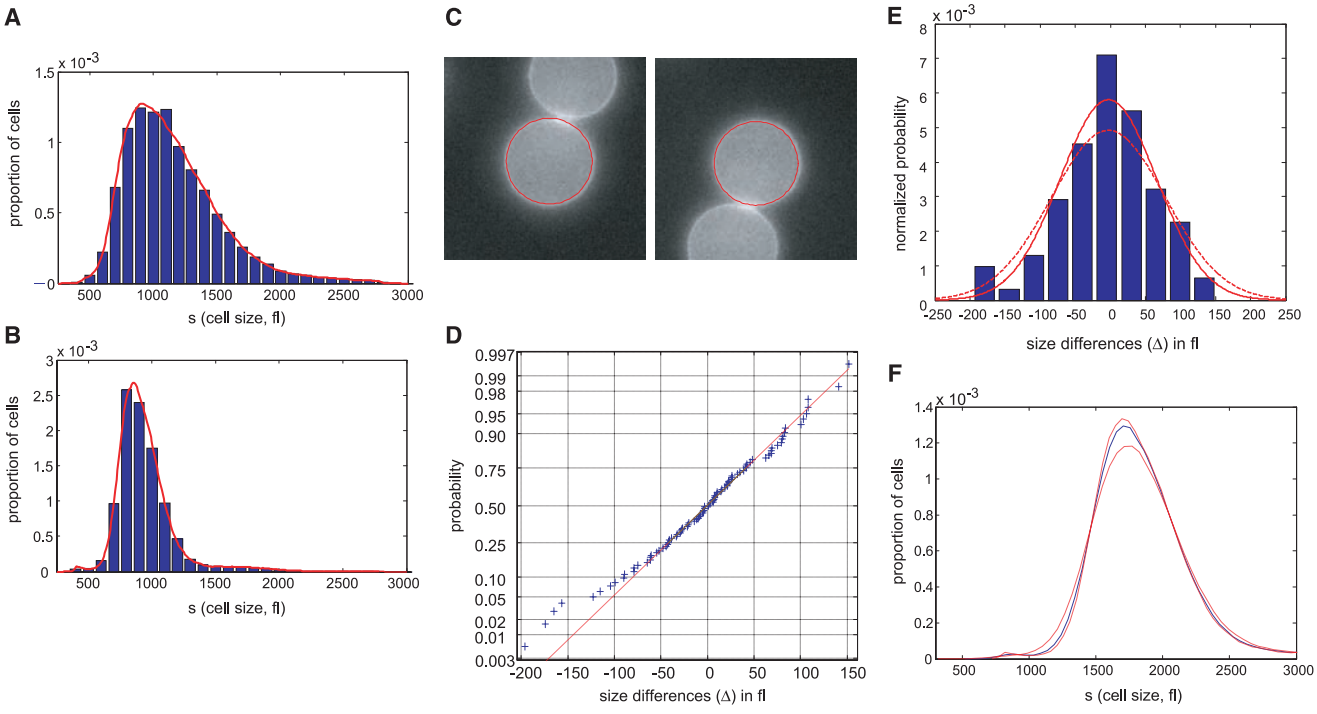

Fig. 1. Extracting parameters for calculating the size dependency of cell growth rate. (**A** and **B**) Size distribution of asynchronous steady-state populations (A) and newborn populations (B), shown by histograms (blue) and kernel density estimates (red). (**C**) L1210 cells, membrane-labeled with green fluorescent protein, were imaged while exiting mitosis. Each cell was fitted in a circle at maximum diameter. See (*20*) for details and error. (**D**) A quantile normal probability plot showing the normality of the daughter cell volume differences, Δ. (**E**) Distribution of size differences between daughter cells. A single parameter for the variance, σ^2, of the Gaussian estimate (solid red line) for the distribution, $\delta(\Delta)$. Also shown is the distribution corresponding to the upper confidence interval of the Gaussian estimate (dashed red line). (**F**) Mitotic size distribution calculated by convolving newborn size distribution with $\delta(\Delta)$. Confidence intervals of the $\delta(\Delta)$ distribution were used to generate the confidence of the mitotic size distribution (shown in red). See (*20*) for details.

failed to reach clear conclusions regarding the kinetics of cell growth (*21*, *22*).

Attempts to improve statistical accuracy by measuring large populations of cells foundered on the need to synchronize cells without affecting growth. Cell cycle inhibitors induce synchrony by blocking the nuclear cycle, but their effects on growth are unclear. Other procedures such as trypsinization, elutriation, and mitotic shake-off can also perturb the population in ways that are difficult to evaluate (*23*). In the 1960s, elegant mathematical approaches for extracting the rate of cell growth versus cell size were developed (*12*, *24*). These depend on isolating pure populations of both newborn and dividing cells, which has been difficult to achieve. Moreover, even with high-quality data, the analysis is ambiguous and incorrect (see below). We have now overcome these difficulties by combining a gentle cell synchronization technique (*25*) with mathematical analysis to determine accurately the growth function for lymphoblastoid leukemia cells.

Measuring the size dependency of growth in asynchronous populations. To calculate the dependence of growth rate on size, we applied a method that analyzes an asynchronous population at steady state, proposed by Collins and Richmond in 1962 (*12*). Specifically, at steady state, the number of cells smaller than size s increases only when cells larger than s divide and decreases only when cells smaller than s grow in size. Because the proportion of cells of any given size does not change with time, these two numbers must be equal (fig. S1).

Despite its mathematical simplicity, the Collins-Richmond method has been difficult to implement. In addition to the readily obtainable asynchronous size distribution, the method requires the size distribution of both the newborn subpopulation and the distribution of cells just before they divide, both of which are difficult to obtain. Under assumptions of unknown validity, the method has been used to suggest an exponential cell growth rate for bacteria (*12*) and for mammalian cells (*18*).

We can now obtain these distributions without unproven assumptions. To obtain the subpopulation of newborns, we grew mouse lymphoblasts (L1210) on a coated nitrocellulose membrane constantly bathed in a closed system (*25*). As these cells divide, one of the two daughters detaches from the membrane and the newborn cells are gently eluted. The remaining daughters can grow and divide, continually providing newborn cells. Two of the three needed size distributions are thus readily measured by Coulter Counter (Beckman Coulter Inc.): those for the unsynchronized populations (Fig. 1A) and newborn populations (Fig. 1B).

It is very difficult to isolate a uniform population of cells just before they divide. Instead, we calculate the mitotic (predivision) size distribution by combining the size distribution of newborns (Fig. 1B) with an experimentally determined size correlation between two daughter cells (Fig. 1, C to E). Specifically, the mitotic size distribution $f_m(s)$ (Fig. 1F) is calculated from the convolution $f_m(s) = (f_0 * \delta)(s)$, where $\delta(\Delta)$ is the distribution of the difference, Δ, in size between daughter cells emerging from mitosis (subtraction directionality is random), and f_0 is the size distribution of newborns. This calculation is valid only to the extent that Δ is independent of cell size, which we confirmed experimentally (*20*) (fig. S9). Volume differences between daughter cells closely follow a Gaussian distribution (σ = 66.8 ± 10 fl) and correspond to 7% of mean newborn volume. Comparing this value with the size variation of unrelated newborns (20.4%) demonstrates the remarkable accuracy of cytokinesis.

We thus have the data needed for the Collins-Richmond method without unproven assumptions. Equation 1 expresses the cell growth rate υ as a function of cell size s from three measurements: (i) the asynchronous size probability distribution, $f_a(s)$ [or $F_a(s)$ in its cumulative form]; (ii) the newborn cumulative size probability distribution, $F_0(s)$; and (iii) the distribution of differences between newborns, $\delta(\Delta)$:

$$\upsilon(s) = 2\alpha\frac{F_0(s)}{f_a(s)} - \alpha\frac{(F_0 * \delta)(s)}{f_a(s)} - \alpha\frac{F_a(s)}{f_a(s)} \quad (1)$$

where α is the fraction of dividing cells per unit time. The three terms on the right side of Eq. 1 represent the fact that the actual increase of cell number in a steady-state population (the rightmost or "population increase" term) must be balanced by cell growth rate (υ) on one hand and by division rate (i.e., the "newborns" and "mitotics" terms) on the other hand (fig. S1).

Applying Eq. 1 to our data sets shows how growth rate varies with cell size in the asynchronous population. Plots for L1210 mouse lymphoblasts (Fig. 2A) and MOLT4 human lymphoblasts (fig. S2) show similar relationships of growth rate and size. In both cell lines, larger cells are observed to have higher growth rates throughout

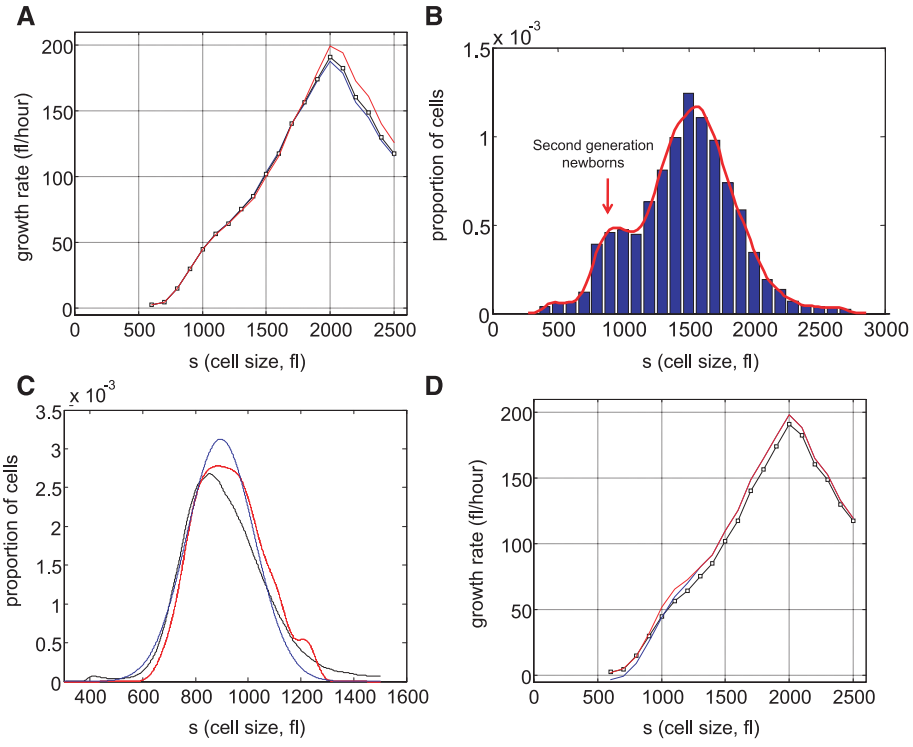

Fig. 2. Growth rate as a function of cell size. (**A**) Mean growth rate as a function of cell size for L1210 cells. Curve (black) was calculated from the Coulter Counter measurements of asynchronous size distribution (10^6 cells) and the size distribution of newborns (10^5 cells) together with the daughter cell correlation (see Fig. 1) using the Collins-Richmond method. Also shown are the curves based on the assumption of symmetric division (blue) and on a variance for daughter cell differences that is 2 times the measured value (red). Because of the large numbers of cells in the data sets, errors in growth rate obtained from this calculation are <1 fl/hour (*20*). (**B**) Bimodal size distribution of synchronous L1210 population at time t = 9 hours. The left mode represents second-generation newborns generated completely in suspension. (**C**) The similarity in the size distribution of the newborns freshly eluted from membrane versus the size distribution of newborns generated in suspension. The black curve corresponds to the size distribution of eluted newborns. We calculate the size distribution of the second-generation newborns (blue curve). The two size modes at t = 9 hours were separated using a Gaussian extrapolation. The red curve is an alternative extrapolation of the same distribution obtained by a method used later in the study to calculate the probabilities of cell division (see text). (**D**) The Collins-Richmond growth plot (black curve) was recalculated using second-generation newborns. Red and blue curves represent the different methods of extrapolating newborns.

most of the cell size range. However, beyond a critical size (cell volume = 2000 fl for L1210, 2500 fl for MOLT4), the trend is reversed and growth rates decline with increased size (Fig. 2A and fig. S2). Note that 65% of the L1210 population would have divided before reaching this size.

Although release of the unattached daughter cell would appear to be gentle and unperturbing, there is still concern that the daughter cell size distribution could be affected by the membrane. To test for this, we examined the size distribution of newborns produced completely in suspension, at the start of the second cell cycle (Fig. 2B). As shown in Fig. 2C, this estimated newborn distribution is very similar to that of the newborns obtained directly by elution, and, when integrated into the Collins-Richmond equation, the plot is nearly identical to that calculated from the eluted newborns (Fig. 2D).

Although growth rate appears to depend on size, growth rate heterogeneity in the population for each cell size can weaken this conclusion (*20*). Thus, even with a complete data set such as the one we have obtained, the Collins-Richmond method is inadequate to portray the growth of an individual cell over time. Resolution requires additional information that we obtain from an analysis of growth as a function of time.

Time dependency of growth. The synchrony of newborns eluted from the membrane allowed us to follow the change in the distribution of cell size with time (Fig. 3A). Specifically, we compared pairs of size distributions, f_n and f_{n+1}, sampled from the synchronized population at 1-hour intervals, $\Delta t = t_{n+1} - t_n = 1$ hour. Within such short time intervals, the growth of any single cell i can be accurately estimated by a simple linear function, $s^i(t) = s_0^i + \beta_n^i(t - t_n)$, regardless of the underlying complexity of the "real" growth function (*20*). Here, β_n^i and s_n^i are the growth constant and size of cell i in time interval n, respectively [i.e., time interval (t_n, t_{n+1})]. Cell-to-cell variation in growth rates is captured by the distribution of β_n^i values in each of the time intervals. Our aim is to calculate the average rate β_n at which cells grow in each time interval, as well as to provide an estimate for the cell-to-cell variation. We use β_n to denote the average of all β_n^i values in time interval n:

$$\beta_n = \frac{1}{N_t}\sum_{i=1}^{N_t}\beta_n^i \qquad (2)$$

Implementation of our method requires an assumption about the initial conditions of the time course. Specifically, we must specify how growth rates, $\{\beta_0^1, \beta_0^2, \ldots, \beta_0^i\}$, are to be paired with the measured sizes, $\{s_0^1, s_0^2, \ldots, s_0^i\}$, in the newborn population. The simplest possibility is that for newborn subpopulations, growth rate and size are independent. To test this assumption, we repeated the calculation with a different assumption: that growth rates are proportional to, rather than independent of, the cells' birth size. This latter simplification uses exponential, $s^i(t) = s_0^i \exp[k_n^i(t - t_n)]$, rather than linear functions to estimate growth in the separate time intervals; here, k_n^i is the exponential growth constant of cell i at time interval n.

Using the linear estimates, $s^i(t) = s_0^i + \beta_n^i(t - t_n)$, the growth rate υ of any single newborn cell is equal to its growth constant, β_0^i. By contrast, using the exponential functions, the growth rate of a newborn cell is given by $\upsilon = k_0^i s_0^i$. With the exponential estimates, it is k_n^i, rather than the actual growth rate, that is independent of cell size in the newborn population. As shown in Fig. 3, B and E, our method yields the same result regardless of whether linear or exponential estimates were used. This shows the power of our data to produce a single conclusion regardless of the specifics of the simplifying assumptions. Note that the assumption of growth constants (β or k) that are independent of cell size is invoked only for newborns; at the later time points, cells

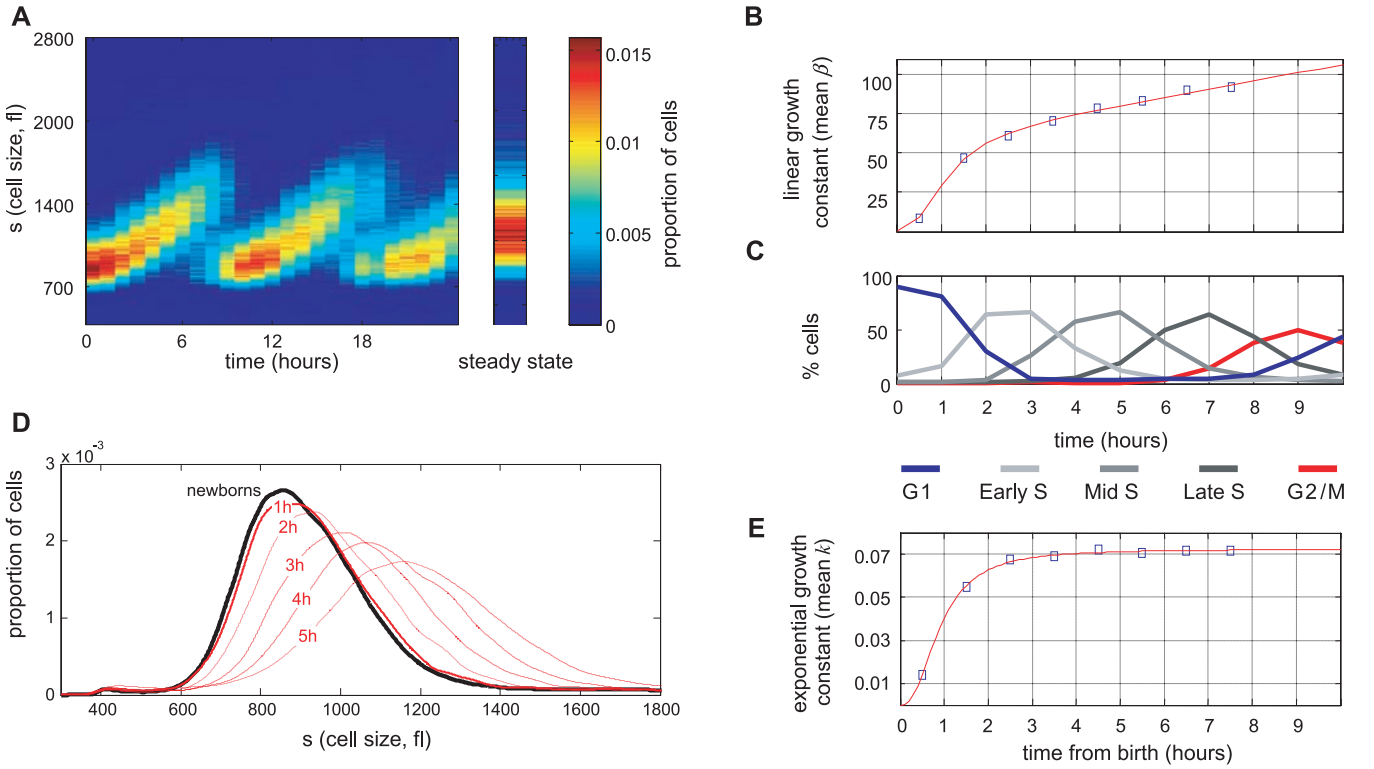

Fig. 3. Growth rate as a function of cell cycle. (**A**) Newborn L1210 cells were incubated at 37°C. Aliquots of cells were taken every hour from 0 to 24 hours to measure the size distribution of the synchronous population as it progressed through 2.5 cycles. Proportions of cells at any given size are visualized by color (see color bar at far right). Also shown is the time-invariant steady-state distribution of the asynchronous population. (**B**) Mean linear growth constants β_n (fl/hour) for each of the time intervals as calculated from Eqs. 3 to 6. (**C**) Distribution of cell cycle stages. (**D**) Growth repression visualized from raw size distribution measurements. Size distributions of the synchronized L1210 population are shown for early times in the cell cycle just after release from the membrane. The size distribution of newborns (black curve) is compared with distributions from t = 1 hour (heavy red curve) and t = 2 to 5 hours (lighter red curves). There is very little change from t = 0 to t = 1 hour, indicative of the growth repression during the first hour. The larger shifts in the size distribution for later times indicate faster growth later in the cell cycle. (**E**) Mean exponential growth constants k_n (hour^{-1}) for each of the time intervals as calculated in (*20*).

with larger growth constants will have accumulated more mass and volume than cells with smaller growth constants and will inevitably be larger.

With the linear estimates, we calculate growth rates by representing the size of a cell at time n, s_n^i, as a sum of its newborn size, s_0^i, together with a size difference c_n^i; that is, $s_n^i = s_0^i + c_n^i$ (every size is compared to the initial newborn size). With this notation, relying on the simplifying assumption described above, we search for the set of values $\{c_n^1, c_n^2, c_n^3, \ldots, c_n^N\}$ that, when randomly paired with and added to the measured sizes from the newborn population, would produce a set of values $\{x^1, x^2, \ldots, x^N\}$ (i.e., $x^i = c_n^j + s_n^i$) that have the same probability distribution as the measured cell sizes $\{s_n^1, s_n^2, \ldots, s_n^N\}$ from time interval n.

In more conventional statistical language, we describe the probability distribution of c_n^i with $\varphi_n(c)$ and use c_n to denote the mean c value at time $t = n$. We express the measured distribution f_n, from time n, as a convolution of the measured distribution of newborn sizes f_0 with $\varphi_n(c)$, $f_{n(\text{measured})} = f_{0(\text{measured})} * \varphi_n$ (Eq. 3), and solve for $\varphi_n(c)$ by numerical deconvolution. From $\varphi_n(c)$ we use Eq. 4 to calculate the mean value c_n for each time point; we then use Eqs. 5 and 6 to relate the calculated c_n values to the mean growth rates β_n:

$$f_n(s) = \int_{c=0}^{\infty} f_0(s-c)\varphi_n(c)dc \qquad (3)$$

$$c_n = \int c\varphi_n(c)dc = \langle c_j^i \rangle \qquad (4)$$

$$\beta_n = c_n - \sum_{j=0}^{n-1} \beta_j \Delta t \qquad (5)$$

Because $\Delta t = 1$,

$$\beta_n = c_n - \sum_{j=0}^{n-1} \beta_j \qquad (6)$$

In Eq. 3, f_0 and f_n are experimentally measured distributions; thus, by numerical deconvolution, we solve Eq. 3 for the probability distribution $\varphi_n(c)$. We can then recursively calculate mean growth values for each time interval by plugging the calculated c_n into Eq. 6, where c_n is simply the average of the probability distribution $\varphi_n(c)$. After independently calculating the growth estimates for each of the 1-hour segments throughout the cell cycle, the true functional form of the growth function was reconstituted by linking the successive 1-hour segments (*20*). Thus, Eqs. 3 to 6, and their more general formulation in (*20*), provide a means of calculating the average growth rate between any two time points if the size distributions at these time points and the size distribution of newborns are known.

Figure 3B shows the results of applying Eqs. 3 to 6 to the synchronized population of L1210 mouse lymphoblasts. It reveals that the average rate of cell growth β_n, calculated by the linear segmental estimates, increases rapidly at the early stages of cell cycle and is then followed by a slower linear increase until cell division starts (see Fig. 3C, which relates Fig. 3B to cell cycle stages). The suppression of growth in G_1 (Fig. 3B) can be directly observed from the experimental size distribution curves for the synchronous L1210 populations (Fig. 3D).

Using the exponential growth model (*20*), the post-G_1 period is seen to be described precisely with an exponential growth rate constant of $k = 0.07$ hour^{-1} or a growth rate of $0.07s$ (Fig. 3E). Combined, Fig. 3B and Fig. 3E provide a description of cell growth. In Fig. 3B, growth is expressed with a linear growth constant, β (fl/hour), which increases with time in the post-G_1 period, whereas in Fig. 3E, growth is expressed with an exponential constant, k (hour^{-1}), which does not change during that same period.

From the resulting distributions $\varphi_n(c)$, we calculate that the total variation in growth rates in the population is CV = 49%. This variation is composed from the size variation and a variation in exponential constants, which were independently calculated as 32% and 18%.

This analysis allows us to interpret the Collins-Richmond plot (Fig. 2A) in terms of growth rate changes during the cell cycle. In Fig. 3B, the growth rate β increases from 10 fl/hour during G_1 to 90 fl/hour as cells progress toward division. From Fig. 3 we now realize that this factor of 9 increase is largely localized to the early G_1 phase—an age dependency that is lost in the Collins-Richmond representation because of a poor correlation between cell size and age (*20*) (figs. S3 and S4).

Dependence of cell division on time and size. These results require some size control mechanism to limit the dispersion in cell sizes. To test for the possibility that there is a size gate that shortens the cell cycle for large cells, we examined the interval in which most cells divide (9 to 12 hours after birth; Fig. 3A). By using the growth constants that we determined in Fig. 3E and comparing the measured size distributions from two consecutive times, we can calculate the frequency of cell divisions in this population as a function of cell cycle time (Fig. 4). To take one example, consider the number of cells that, at 8 hours after birth, are contained in the size interval (s_1, s_2) (cells larger than s_1 and smaller than s_2). Given a value of $k = 0.07$ hour^{-1} (Fig. 3E), at 9 hours after birth, these same cells will be contained by the interval $\{s_1 \exp(0.07), s_2 \exp(0.07)\}$. Any deviation from this equivalence can only occur by division. To avoid confusion with newborn cells, we calculate the division frequencies using cells of size 1500 fl or larger, where the proportion of newborns is negligible (Fig. 1B).

We found that for cells of the same age, the likelihood of division increases with cell size (Fig. 4A). Also, for cells of the same size, older cells have a greater chance to divide than do younger cells (Fig. 4B). Thus, the likelihood of cell division, ψ, is governed by both cell age τ and cell size s. More explicitly, the probability for cell division follows a differential form,

$$d\psi = \left(\frac{\partial \psi}{\partial \tau}\right)_s d\tau + \left(\frac{\partial \psi}{\partial s}\right)_\tau ds \qquad (7)$$

where the dependency of cell division on cell size and age is captured by the partial derivatives $[\partial\psi(\tau,s)/\partial\tau]_s$, where size is held constant, and $[\partial\psi(\tau,s)/\partial s]_\tau$, where age is held constant.

Our current measurements lack the accuracy to obtain these partial derivatives to high precision. Nonetheless, by relying on linear fit estimates, we can obtain approximations for their magnitudes: roughly $(\partial\psi/\partial s)_\tau = 0.0002 \pm 0.0001$ fl^{-1} at 9 hours after birth and 0.0004 ± 0.0001 fl^{-1} at 12 hours after birth, and $(\partial\psi/\partial\tau)_s = 0.008 \pm 0.03$ hour^{-1} for cells of volume 1500 fl and 0.1 ± 0.02 hour^{-1} for cells of volume 2400 fl.

Discussion. The size of a cell reflects the relationship between its growth rate and division

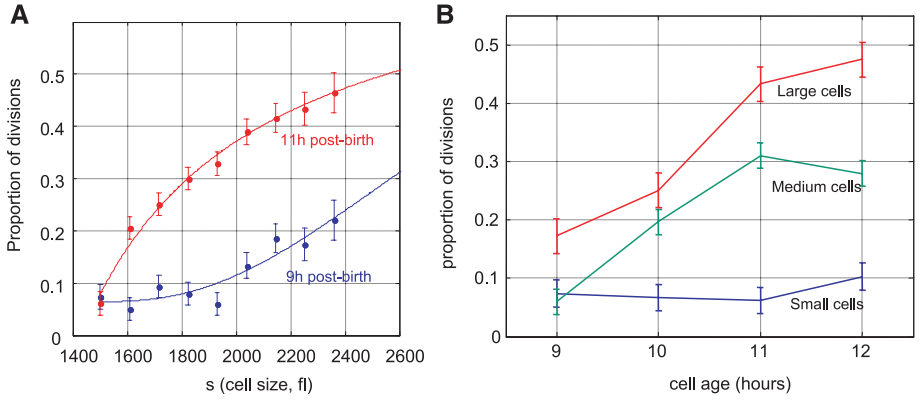

Fig. 4. Frequency of cell division as a function of cell size and age. (**A**) For cells of the same age, the probability of division increases with cell size. Proportions of cells that have divided at any specified size are shown for cells at 9 hours after birth (blue curve) and 11 hours after birth (red curve). At 11 hours after birth, about 20% of all cells of size 1600 fl divide. Size distributions were calculated on the basis of a Gaussian kernel. (**B**) For cells of the same size, the probability of division increases with cell age. Division frequencies as a function of age (each time point represents a 1-hour interval starting at the indicated times) are shown for cells with size ranging from 1500 to 1850 fl (blue curve), from 1850 to 2200 fl (green curve), and from 2250 to 2500 fl (red curve).

frequency. It has been difficult to study in metazoan cells, due primarily to the lack of sufficiently accurate, sensitive, and reliable means of measurement. We have addressed these deficiencies with mathematical and experimental methods that allow us to describe the growth of individual cells during the cell cycle from measurements made on very large samples. Although we are measuring the cell volume, other studies have shown that the buoyant density of cells remains constant through the cell cycle, implying that volume can be used as a surrogate for mass (*26*, *27*).

For mouse lymphoblastoid cells, we find an accelerative growth phase in G_1 (where an exponential rate constant is itself time-dependent), followed by a period of stable exponential growth during the rest of the cell cycle. Thus, at least for this cell type, our results settle a long-standing controversy of whether mammalian cell growth can be described by linear or exponential kinetics. The true growth function across the cell cycle is neither a simple exponential nor a linear function, and it is size-dependent. Therefore, mammalian cells must possess a cell-autonomous intrinsic size regulator that couples cell growth to the cell cycle.

In fission yeast, entry into mitosis has been shown to be size-dependent, whereas in budding yeast, division is set by a "timer" activated at the start point (*1*). For lymphoblasts, we find that growth and division are independently determined by cell size and age. The correlation between size and division in mammalian cells thus cannot be a simple consequence of either size-independent processes that govern cell cycle duration or a size gate that feeds back on the timing of the cell cycle.

Our data contrast with the data from Raff and colleagues (*13*) on adherent Schwann cell cultures, where a linear dependence of growth on size was suggested. This might reflect differences between adherent and suspension cell populations, their use of drugs to induce synchrony, or the difference in the type of cell studied. In addition, their Schwann cells were allowed to grow without division, reaching an extreme size (*13*). We found that very large cells above a critical cell size (2000 fl for L1210 cells—a size never attained by most of the growing cells in the culture) displayed growth behavior different from the cells that divided at smaller size. In this regime, growth is no longer proportional to size and could appear linear.

Although much has been learned about growth and cell division in mammalian cells, the circuits that coordinate these processes have not yet been investigated. The analytical tools presented here should facilitate the study of the biochemical circuitry responsible for setting the size and maintaining the limits of cell size variation, despite the potentially disruptive consequences of size dependence of growth. Given the very large size differences of different somatic cell types, the processes governing cell size would be expected to be deeply enmeshed in developmental mechanisms and subject to physiological constraints.

References and Notes

1. P. Jorgensen, M. Tyers, *Curr. Biol.* **14**, R1014 (2004).
2. J. M. Mitchison, *Int. Rev. Cytol.* **226**, 165 (2003).
3. E. Trucco, *Bull. Math. Biophys.* **32**, 459 (1970).
4. E. Trucco, G. I. Bell, *Bull. Math. Biophys.* **32**, 475 (1970).
5. J. J. Tyson, K. B. Hannsgen, *J. Math. Biol.* **22**, 61 (1985).
6. S. G. Elliott, C. S. McLaughlin, *Proc. Natl. Acad. Sci. U.S.A.* **75**, 4384 (1978).
7. P. Jorgensen, J. L. Nishikawa, B.-J. Breitkreutz, M. Tyers, *Science* **297**, 395 (2002); published online 27 June 2002 (10.1126/science.1070850).
8. D. R. Kellogg, *J. Cell Sci.* **116**, 4883 (2003).
9. S. Di Talia, J. M. Skotheim, J. M. Bean, E. D. Siggia, F. R. Cross, *Nature* **448**, 947 (2007).
10. H. E. Kubitschek, *Biophys. J.* **8**, 1401 (1968).
11. H. E. Kubitschek, *J. Bacteriol.* **168**, 613 (1986).
12. J. F. Collins, M. H. Richmond, *J. Gen. Microbiol.* **28**, 15 (1962).
13. I. Conlon, M. Raff, *J. Biol.* **2**, 7 (2003).
14. I. J. Conlon, G. A. Dunn, A. W. Mudge, M. C. Raff, *Nat. Cell Biol.* **3**, 918 (2001).
15. P. Echave, I. J. Conlon, A. C. Lloyd, *Cell Cycle* **6**, 218 (2007).
16. S. Cooper, *BMC Cell Biol.* **5**, 35 (2004).
17. A. Sveiczer, B. Novak, J. M. Mitchison, *Theor. Biol. Med. Model.* **1**, 12 (2004).
18. E. C. Anderson, G. I. Bell, D. F. Petersen, R. A. Tobey, *Biophys. J.* **9**, 246 (1969).
19. H. Dolznig, F. Grebien, T. Sauer, H. Beug, E. W. Mullner, *Nat. Cell Biol.* **6**, 899 (2004).
20. See supporting material on *Science* Online.
21. D. Killander, A. Zetterberg, *Exp. Cell Res.* **38**, 272 (1965).
22. A. Zetterberg, D. Killander, *Exp. Cell Res.* **39**, 22 (1965).
23. S. Cooper, *Cell. Mol. Life Sci.* **60**, 1099 (2003).
24. G. I. Bell, E. C. Anderson, *Biophys. J.* **7**, 329 (1967).
25. V. S. LeBleu, M. Thornton, R. G. Gonda, C. E. Helmstetter, *Cytotechnology* **51**, 149 (2006).
26. E. C. Anderson, D. F. Petersen, R. A. Tobey, *Biophys. J.* **10**, 630 (1970).
27. M. R. Loken, H. E. Kubitschek, *J. Cell. Physiol.* **118**, 22 (1984).

28. We thank C. Helmstetter and J. Horn for sharing plans and construction of the newborn cell device; S. Cooper for suggesting we consider that device for cell cycle studies; J. Levy for discussions and for advice with the mathematical analyses; J. Waters and the Nikon Imaging Centre for help with the microscopy; C. Mock for cell sorting; G. Charras and T. Balla for reagents; and S. Tal, J. Toettcher, P. Bordalo, R. Milo, T. Mitchison, P. Jorgensen, G. Charras, E. Zlotorynski, S. Dumont, N. Shoresh, and M. Springer for advice and critical reading. Supported by NIH grant GM083303 (G.L.), a Human Frontier Science Program fellowship (R.K.), and NIH grant GM026875.

Supporting Online Material

www.sciencemag.org/cgi/content/full/325/5937/167/DC1
Materials and Methods
Figs. S1 to S11
Tables S1 and S2
References

31 March 2009; accepted 15 May 2009
10.1126/science.1174294

REPORTS

Penumbral Structure and Outflows in Simulated Sunspots

M. Rempel,[1]* M. Schüssler,[2] R. H. Cameron,[2] M. Knölker[1]

Sunspots are concentrations of magnetic field on the visible solar surface that strongly affect the convective energy transport in their interior and surroundings. The filamentary outer regions (penumbrae) of sunspots show systematic radial outward flows along channels of nearly horizontal magnetic field. These flows were discovered 100 years ago and are present in all fully developed sunspots. By using a comprehensive numerical simulation of a sunspot pair, we show that penumbral structures with such outflows form when the average magnetic field inclination to the vertical exceeds about 45 degrees. The systematic outflows are a component of the convective flows that provide the upward energy transport and result from anisotropy introduced by the presence of the inclined magnetic field.

Sunspots are dark patches on the visible solar surface that harbor strong magnetic fields up to 4000 G (*1*, *2*). Their central region, the umbra, is the darkest part, with a brightness of about 20% of the ambient value and a largely vertically oriented magnetic field; the brighter, filamentary penumbra shows a more inclined field and a nearly horizontal plasma outflow of several $km \cdot s^{-1}$, the Evershed flow, which was named after its discoverer (*3*). Although a number of simplified (and partly conflicting) models have been suggested to explain the structure and outflows of penumbrae (*4*), a comprehensive theoretical understanding of the basic mechanisms does not exist.

Here, we present ab initio numerical simulations of complete sunspots embedded in a realistic solar convection zone and atmosphere, including all relevant physical processes: compressible magnetohydrodynamics, partial ionization, and radiative energy transport. Previous attempts to simulate penumbral structure in small slablike sections of sunspots (*5*, *6*) resulted in rather narrow penumbral regions. The generally used periodic boundary conditions at the sides of

[1]High Altitude Observatory, National Center for Atmospheric Research (NCAR), Post Office Box 3000, Boulder, CO 80307, USA. [2]Max-Planck-Institut für Sonnensystemforschung, Max-Planck-Straße 2, 37191 Katlenburg-Lindau, Germany.

*To whom correspondence should be addressed. E-mail: rempel@hao.ucar.edu

the computational box tend to suppress the extended horizontal field structures associated with sunspot penumbrae. Hence, we have carried out a simulation of a pair of big sunspots (diameter 35 Mm) of opposite magnetic polarity, thereby facilitating the development of strongly inclined field between the spots. Our numerical box had a horizontal extension of 98 Mm by 49 Mm and a depth of 6.1 Mm. The spatial grid resolution was 32 km in the horizontal directions and 16 km in the vertical. The sunspots evolved for 3.6 hours during the simulation, which was sufficient to study the penumbral structure and dynamics; processes that evolve on longer time scales, such as moat flows, were not fully developed in this simulation. However, the surface evolution of magnetic field shows clear indications of bipolar magnetic features transported away from the spots beyond the penumbra boundary. This is reminiscent of observations of so-called "moving magnetic features" (*7*) (movie S1 displays the temporal evolution of B_z on the visible solar surface; the gray scale ranges from −3.5 kG to +3.5 kG) (*8*).

The simulated penumbrae show the largest extension between the sunspots of opposite polarity (Fig. 1A). The periodic horizontal boundary conditions provide three different distances: 46 Mm (middle of box) and 52 Mm in the x direction between opposite polarity spots and 49 Mm in the y direction between the same polarity spots. The spots show a dark umbra with some brighter umbral dots, preferentially in the weaker spot on the left. A deep magnetic structure underlies the visible penumbra, particularly so between the sunspots (Fig. 1B). A movie covering 1 hour of temporal evolution of the properties displayed in Fig. 1 (movie S2) shows the inward progression of filaments in the inner penumbra.

The umbral regions have a brightness of 0.15 to $0.2I_0$, where I_0 is the average quiet-Sun value, a Wilson depression of the visible surface by 550 to 600 km, and vertical field strengths (B_z) up to 4 kG (Fig. 2). The quantities described here are averaged in space and time as described in the Fig. 2 legend. The penumbrae have much weaker B_z, horizontal fields (B_x) with peak values around 2 kG at the inner penumbral boundaries, and an average brightness of about $0.7I_0$. The penumbral regions exhibit systematic outflows with average horizontal velocities (v_x) of up to 6 km·s^{-1}. The onset of these flows is closely related to the magnetic field inclination: Where the average inclination with respect to the vertical exceeds 45°, there are systematic average outflows. With growing distance from the umbra, the outflow velocity increases, and the field becomes more inclined and is nearly horizontal in the outer penumbra. These properties are consistent with observational results (*1*, *9*).

The simulated penumbra shows strong structuring in terms of elongated narrow filaments (Fig. 3). In the inner part, the magnetic field shows strong variations of the inclination between 40° and nearly 90° on scales of less than 200 km. Further out, regions with strongly inclined fields dominate. The velocity structure is analogous: Radial outflows are concentrated in highly inclined filaments and become stronger and azimuthally more extended in the outer penumbra, where the field is almost uniformly horizontal. Vertical (up- and downward) flows occur in narrow filaments throughout the whole penumbral region.

Analyzing the penumbral structure in vertical cuts, we find that the outflows reach their peak velocities (exceeding 10 km·s^{-1}) near the visible surface (Fig. 4). This reflects the strong height gradient of pressure and density in these layers: Rising hot plasma turns over, and the resulting horizontal flow is guided outward from the spot by the strong and inclined magnetic field. Although the vertical field in the sunspot umbra only permits convection in the form of narrow columnar

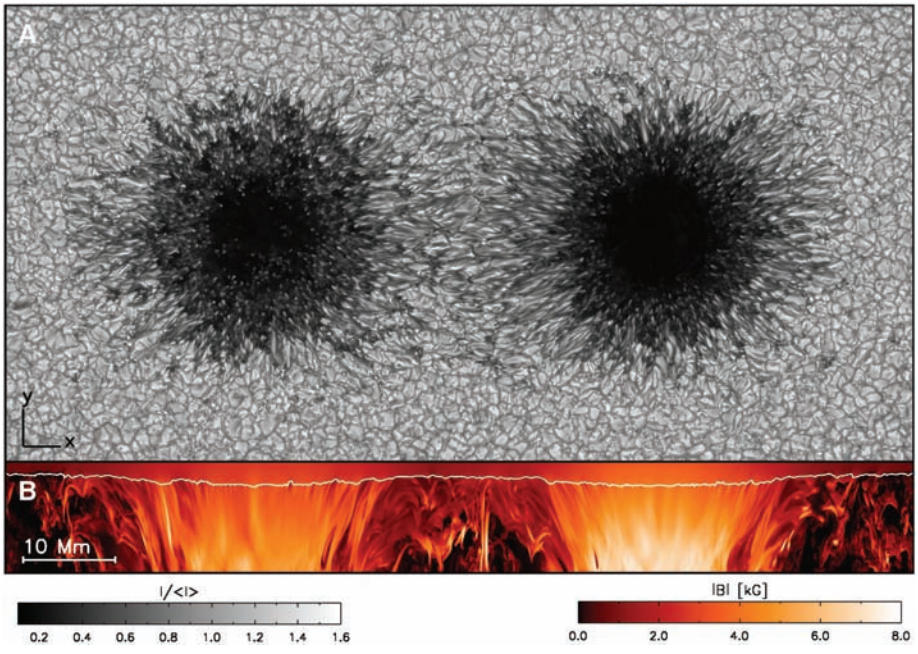

Fig. 1. Snapshot from the simulation. (**A**) Surface brightness map of the sunspot pair and the surrounding convective pattern (granulation). (**B**) Color representation of the field strength (saturated at 8 kG) in a vertical cut through the midplane of the simulation box at $y = 25$ Mm. The vertical direction is stretched by a factor of 2. The white line indicates the height level of the visible surface (optical depth unity).

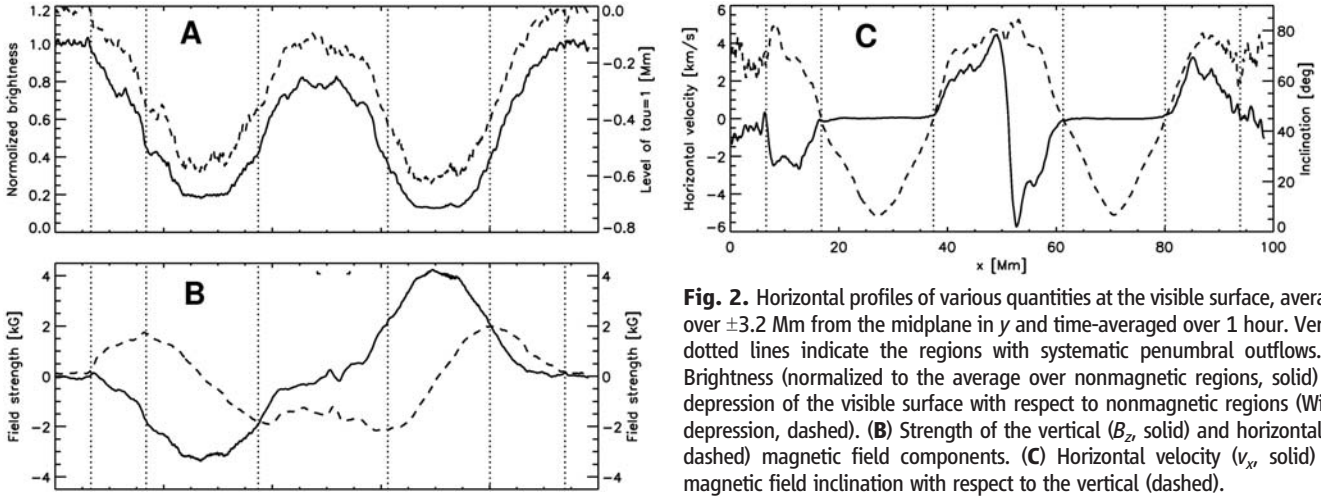

Fig. 2. Horizontal profiles of various quantities at the visible surface, averaged over ±3.2 Mm from the midplane in y and time-averaged over 1 hour. Vertical dotted lines indicate the regions with systematic penumbral outflows. (**A**) Brightness (normalized to the average over nonmagnetic regions, solid) and depression of the visible surface with respect to nonmagnetic regions (Wilson depression, dashed). (**B**) Strength of the vertical (B_z, solid) and horizontal (B_x, dashed) magnetic field components. (**C**) Horizontal velocity (v_x, solid) and magnetic field inclination with respect to the vertical (dashed).

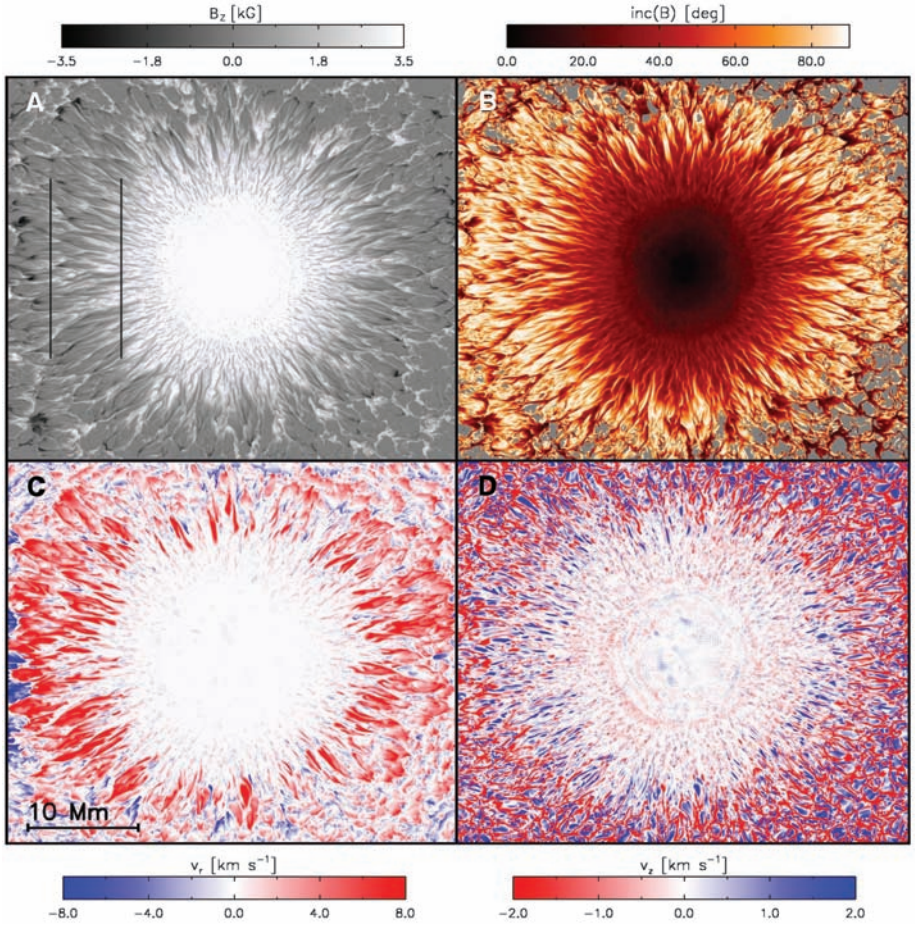

Fig. 3. Magnetic field and velocity structure at the visible surface for the sunspot on the right side of Fig. 1. (**A**) Vertical field component (saturated at ±3.5 kG). The vertical lines indicate the positions of the cuts shown in Fig. 4. (**B**) Inclination angle of the magnetic field with respect to the vertical direction (gray indicates $|B| < 200$ G). (**C**) Radial outflow velocity (saturated at ±8 km·s^{-1}, red indicates outflows). (**D**) Vertical velocity (saturated at ±2 km·s^{-1}, red indicates downflows).

structures (*10*), the inclined field in the penumbra favors sheetlike upflows, which are radially extended and narrow in the azimuthal direction (*6*). Together with the preferred weakening of the vertical field component resulting from flux expulsion by the expanding rising plasma, this explains the azimuthal structuring and the large azimuthal variations of the field inclination in the inner penumbra. The influence of horizontal flows on the field structure depends on the location in the penumbra. In the inner penumbra, they remain rather weak and have therefore only a limited back reaction on the field structure. In the outer penumbra, they become sufficiently strong to bend over field lines, leading to more extended patches of horizontal field and flows. In addition to the strong localized outflows near the visible surface, there is a large-scale flow cell with plasma rising and diverging around the spot, as is evident by the general reddish color in the representation of the horizontal velocity in Fig. 4. Systematic inflows (comprising very little mass flux) are apparent in the uppermost layers of the simulation box. Because these regions are strongly affected by the upper (closed) boundary, it is not clear whether the inflows could possibly be related to the observed inverse Evershed effect in the chromosphere (*11*).

The central penumbral region between the spots has a mean bolometric brightness of $I_p = 0.68I_0$ (averaged over $y = \pm 3.2$ Mm from the midplane of the computational box and between the central vertical dotted lines indicated in Fig. 2). The mean brightness of the upflow areas is $1.1I_p$, whereas that of downflow areas is $0.92I_p$. The corresponding values for undisturbed granulation are $1.11I_0$ and $0.88I_0$, respectively, implying they have similar properties. However, the penumbral region shows a root means square (rms) bolometric brightness contrast of 25.2%, which is substantially larger than the corresponding granulation value of 17.3%. Observations also imply a positive corre-

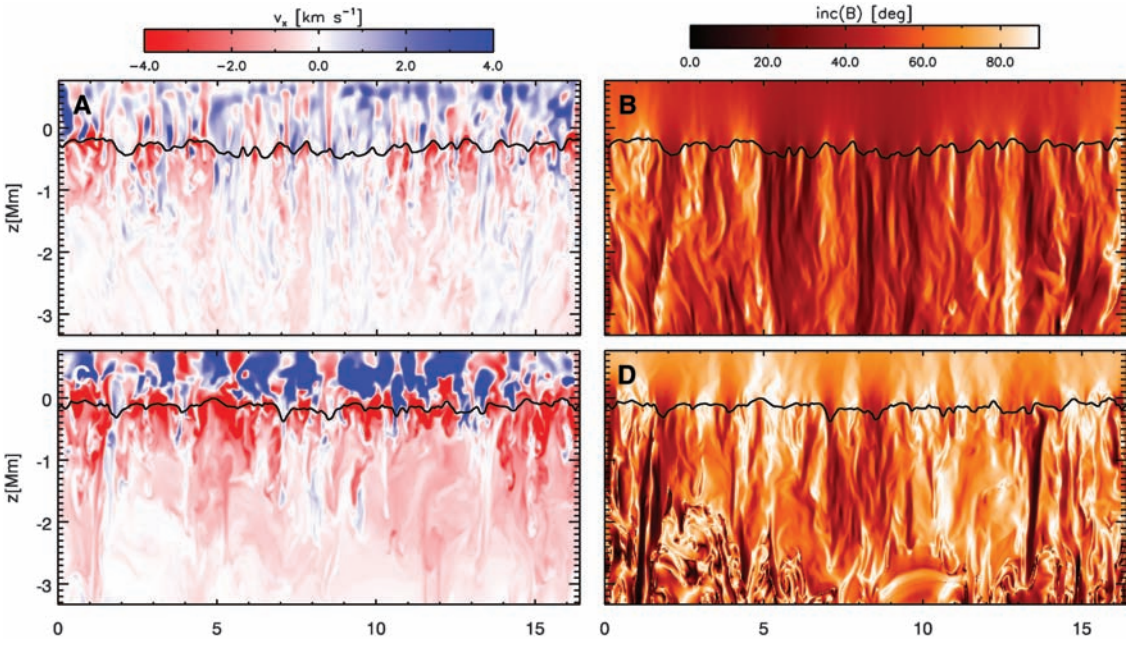

Fig. 4. Vertical cuts through the penumbra (indicated by the black lines in Fig. 3A). The vertical direction is stretched by a factor of 2. Shown are the horizontal velocity component v_x (left) and the field inclination (right). (**A** and **B**) Inner penumbra (right line in Fig. 3A). (**C** and **D**) Outer penumbra (left line in Fig. 3A). The color representation of v_x is saturated at ±4 km · s^{-1}. Black lines indicate the visible surface (optical depth unity).

lation between brightness and vertical flow direction (*12*). This constitutes evidence for a convective flow pattern that transports the energy flux emitted in the penumbra. Other studies show a correlation between intensity and line-of-sight velocities (*13*), which for sunspots observed outside the center of the solar disk is dominated by the horizontal Evershed flow. This is consistent with our findings, because in the penumbra the horizontal flow velocity is correlated with the vertical flow direction.

Our detailed analysis (*8*) shows that the spatial scales of the flows providing the major part of the convective energy transport are similar for both undisturbed granulation and penumbra. The primary difference is that there is no preferred horizontal direction for granulation, whereas the energy-transporting flows in the penumbra are distinctly asymmetric: Convective structures are elongated in the radial direction of the sunspot. These properties were already indicated in earlier simulations (*5*, *6*) and suggested as an explanation for the Evershed outflow in (*14*). The simulation shown here confirms this suggestion and demonstrates the convective nature of a fully developed penumbra.

The horizontal asymmetry of the convective flows is also manifest in the correlation of 0.42 between the corresponding flow component (v_x) and the brightness. We find that the rms of the outflowing velocity component (v_x) in the penumbra is much larger than the transverse component (v_y) (perpendicular to the filament direction), showing an asymmetry similar to that found by the scale analysis. The total rms velocity profile as a function of depth is very similar to its counterpart for undisturbed granulation, apart from a slightly higher peak value, confirming the physical similarity of convection in granulation and penumbra.

The mass flux and energy flux show similar properties with respect to the length scales and asymmetry (*8*), indicating that most of the outflowing material emerges, turns over, and descends within the penumbra. In the deeper layers, there is some contribution (of the order of 10 to 20%) to both energy and mass fluxes by the large-scale flow cell surrounding the sunspots.

The analysis of our simulations indicates that granulation and penumbral flows are similar with regard to energy transport; the asymmetry between the horizontal directions and the reduced overall energy flux reflect the constraints imposed on the convective motions by the presence of a strong and inclined magnetic field. The development of systematic outflows is a direct consequence of the anisotropy, and the similarities between granulation and penumbral flows strongly suggest that driving the Evershed flow does not require physical processes that go beyond the combination of convection and anisotropy introduced by the magnetic field. Weaker laterally overturning flows perpendicular to the main filament direction explain the apparent twisting motions observed in some filaments (*15*, *16*) and lead to a weakening of the magnetic field in the flow channels through flux expulsion (*6*).

Although our simulation of large sunspots is realistic in terms of relevant physics, it does not faithfully reproduce all aspects of the morphology of observed penumbral filaments. The penumbral regions are considerably more extended than in previous local simulations, but they are still somewhat subdued, probably owing to the proximity of the periodic boundaries. The filaments in the inner penumbrae appear to be too fragmented, and short, dark lanes along bright filaments (*17*) form only occasionally, likely a consequence of the still-limited spatial resolution of the simulation. Lastly, the initial condition of the magnetic field underlying the sunspot is quite arbitrary, owing to our ignorance of the subsurface structure of sunspots. Notwithstanding these limitations, the present simulations are consistent with observations of global sunspot properties, penumbral structure, and systematic radial outflows. These and earlier simulations (*5*, *6*, *10*) suggest a unified physical explanation for umbral dots as well as inner and outer penumbrae in terms of magnetoconvection in a magnetic field with varying inclination. Furthermore, a consistent physical picture of all observational characteristics of sunspots and their surroundings is now emerging.

References and Notes

1. S. K. Solanki, *Astron. Astrophys. Rev.* **11**, 153 (2003).
2. J. H. Thomas, N. O. Weiss, *Annu. Rev. Astron. Astrophys.* **42**, 517 (2004).
3. J. Evershed, *Mon. Not. R. Astron. Soc.* **69**, 454 (1909).
4. J. H. Thomas, N. O. Weiss, *Sunspots and Starspots* (Cambridge Univ. Press, Cambridge, 2008).
5. T. Heinemann, Å. Nordlund, G. B. Scharmer, H. C. Spruit, *Astrophys. J.* **669**, 1390 (2007).
6. M. Rempel, M. Schüssler, M. Knölker, *Astrophys. J.* **691**, 640 (2009).
7. M. Kubo, T. Shimizu, S. Tsuneta, *Astrophys. J.* **659**, 812 (2007).
8. More detailed information about the physical model, the numerical code, and the simulation setup is available as supporting material on *Science* Online.
9. R. Keppens, V. Martinez Pillet, *Astron. Astrophys.* **316**, 229 (1996).
10. M. Schüssler, A. Vögler, *Astrophys. J. Lett.* **641**, L73 (2006).
11. D. Dialetis, P. Mein, C. E. Alissandrakis, *Astron. Astrophys.* **147**, 93 (1985).
12. J. Sánchez Almeida, I. Márquez, J. A. Bonet, I. Domínguez Cerdeña, *Astrophys. J.* **658**, 1357 (2007).
13. L. R. Bellot Rubio, R. Schlichenmaier, A. Tritschler, *Astron. Astrophys.* **453**, 1117 (2006).
14. G. B. Scharmer, Å. Nordlund, T. Heinemann, *Astrophys. J. Lett.* **677**, L149 (2008).
15. K. Ichimoto *et al.*, *Science* **318**, 1597 (2007).
16. V. Zakharov, J. Hirzberger, T. Riethmüller, S. Solanki, P. Kobel, *Astron. Astrophys.* **488**, L17 (2008).
17. G. B. Scharmer, B. V. Gudiksen, D. Kiselman, M. G. Löfdahl, L. H. M. Rouppe van der Voort, *Nature* **420**, 151 (2002).

18. High-performance computing resources were provided by NCAR's Computational and Information Systems Laboratory. NCAR is sponsored by NSF.

Supporting Online Material

www.sciencemag.org/cgi/content/full/1173798/DC1
Materials and Methods
SOM Text
Figs. S1 to S4
References
Movies S1 and S2

19 March 2009; accepted 8 June 2009
Published online 18 June 2009;
10.1126/science.1173798
Include this information when citing this paper.

Quantum Walk in Position Space with Single Optically Trapped Atoms

Michal Karski,* Leonid Förster, Jai-Min Choi, Andreas Steffen, Wolfgang Alt, Dieter Meschede, Artur Widera*

The quantum walk is the quantum analog of the well-known random walk, which forms the basis for models and applications in many realms of science. Its properties are markedly different from the classical counterpart and might lead to extensive applications in quantum information science. In our experiment, we implemented a quantum walk on the line with single neutral atoms by deterministically delocalizing them over the sites of a one-dimensional spin-dependent optical lattice. With the use of site-resolved fluorescence imaging, the final wave function is characterized by local quantum state tomography, and its spatial coherence is demonstrated. Our system allows the observation of the quantum-to-classical transition and paves the way for applications, such as quantum cellular automata.

Interference phenomena with microscopic particles are a direct consequence of their quantum-mechanical wave nature (*1*–*5*). The prospect to fully control quantum properties of atomic systems has stimulated ideas to engineer quantum states that would be useful for applications in quantum information processing, for example, and also would elucidate fundamental questions, such as the quantum-to-classical transition (*6*). A prominent example of state engineering by controlled multipath interference is the quantum walk of a particle (*7*). Its classical counterpart, the random walk, is relevant in many aspects of our lives, providing insight into diverse fields: It forms the basis for algorithms (*8*), describes diffusion processes in physics or biology (*8*, *9*), such as Brownian motion, or has been used as a model for stock market prices (*10*). Similarly, the quantum walk is expected to have

Institut für Angewandte Physik der Universität Bonn Wegelerstraße 8, 53115 Bonn, Germany.

*To whom correspondence should be addressed. E-mail: karski@uni-bonn.de (M.K.); widera@uni-bonn.de (A.W.)

implications for various fields, for instance, as a primitive for universal quantum computing (*11*), systematic quantum algorithm engineering (*12*), or for deepening our understanding of the efficient energy transfer in biomolecules for photosynthesis (*13*).

Quantum walks have been proposed to be observable in several physical systems (*12*, *14*, *15*). Special realizations have been reported in either the populations of nuclear magnetic resonance samples (*16*, *17*) or in optical systems, in either frequency space of a linear optical resonator (*18*), with beam splitters (*19*), or in the continuous tunneling of light fields through waveguide lattices (*20*). Recently, a three-step quantum walk in the phase space of trapped ions has been observed (*21*). However, the coherent walk of an individual quantum particle with controllable internal states, as originally proposed by Feynman (*22*), has so far not been observed. We present the experimental realization of such a single quantum particle walking in a one-dimensional (1D) lattice in position space. This basic example of a walk provides all of the relevant features necessary to understand the fundamental properties and differences of the quantum and classical regimes. For example, the atomic wave function resulting from a quantum walk exhibits delocalized coherence, which reflects the underlying quantum interference. Simultaneous detection of internal state and the atomic position in the lattice by an optical microscope allows for local quantum state tomography of the wave function. This is an important requirement to realize applications in quantum information science, such as the quantum cellular automaton (*23*–*25*).

In the classical random walk on a line, a coin is tossed in each time step. Depending on the outcome (heads or tails), a walker takes one step to the left or to the right. After N time steps, the probability of finding the walker at a certain site on the line follows a binomial distribution with a width increasing proportional to $\sqrt{N}$.

In the quantum case, the walker can be brought in a coherent superposition of going to the right or left. This can be realized by adding internal states to the walker, providing an additional degree of freedom, which can be used to control the system. We consider a two-level particle with internal states $|0\rangle$ and $|1\rangle$. In every step of the walk, the coin operator brings each internal state into a coherent superposition of the two states. The essence of the general quantum walk is to entangle this internal state with the position of the corresponding wave packet by a state-dependent transport. This can be realized by shifting both internal states into opposite directions, which coherently delocalizes the particle over two lattice sites. Repetition of the unitary coin-shift operation sequence results in the so-called

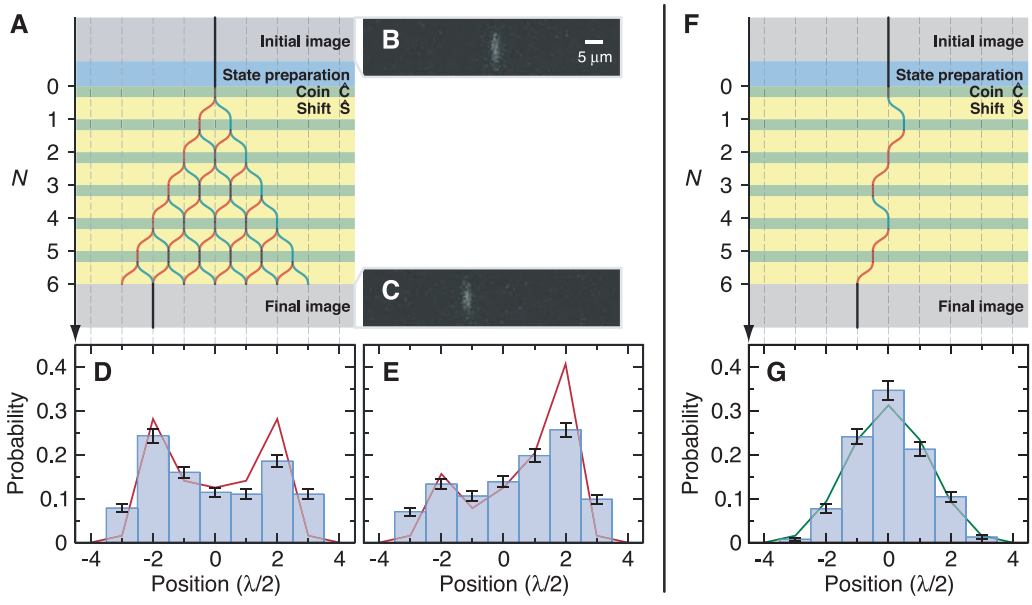

Fig. 1. (**A**) Schematic experimental sequence for the quantum walk showing the paths for the internal states $|0\rangle$ (green) and $|1\rangle$ (red). The walking distance is extracted from the initial (**B**) and final (**C**) fluorescence image. The results of several hundreds of identical realizations form the probability distribution, which is symmetric for the initial state $(|0\rangle + i|1\rangle)/\sqrt{2}$ (**D**) and antisymmetric for the initial state $|1\rangle$ (**E**). The analogous random walk sequence (**F**) yields a binomial probability distribution (**G**). The displayed path is one of many random paths that the atom can take. Measured data are shown as a histogram, and the theoretical expectation for the ideal case is denoted with a solid line. Error bars indicate the statistical $\pm 1\sigma$ uncertainty.

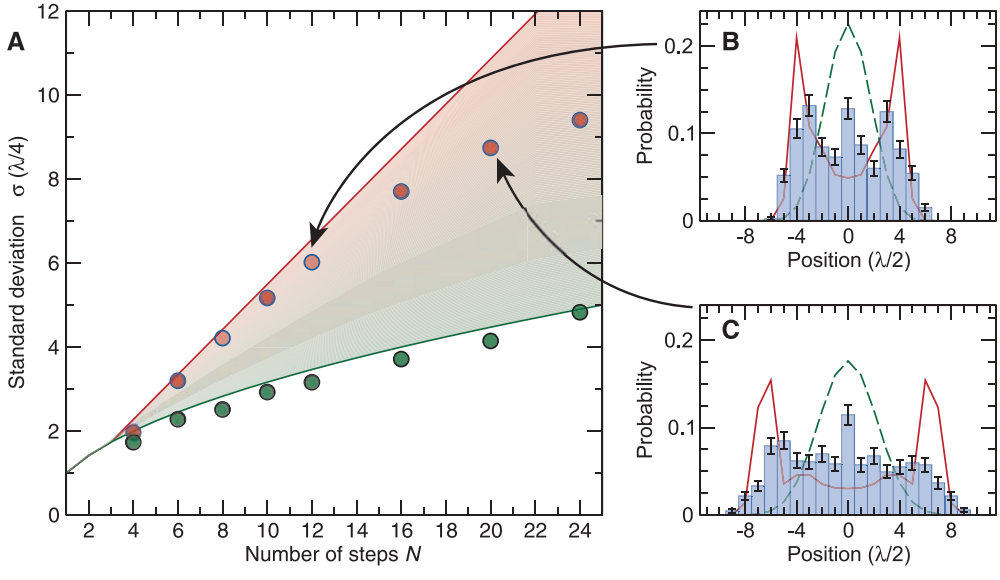

Fig. 2. (**A**) Scaling of the SD of the measured spatial probability distributions for quantum walk (red) and random walk (green). The solid lines indicate the expectations for the ideal cases. Error bars are smaller than the size of symbols. The measured quantum walks follow the ideal linear behavior until, because of decoherence, they gradually turn into a random walk. The probability distributions for N = 12 (**B**) and N = 20 (**C**) show a gradual change from the quantum to a classical shape. The theoretical prediction is shown as a solid line for the pure quantum walk and as a dashed line for the random walk.

quantum walk. After two steps of the quantum walk, two parts of the wave function are recombined at a common lattice site. Being in different internal states, they cannot interfere. The next coin operator, however, mixes the internal states in a deterministic way, which gives rise to quantum interference of the two overlapping wave packets. Further steps result in a multipath interference (Fig. 1A), which then alters the properties of the quantum walk as compared with the classical random walk. In particular, the width of the probability distribution to find the walker at a certain position scales proportional to N for the quantum walk, as in a ballistic transport, in contrast to the diffusive $\sqrt{N}$ scaling of the random walk. The influence of internal states on the quantum walk provides another distinguishing feature: Whereas the probability distribution of the random walk is fully determined by the balance of the coin, the quantum walk distribution strongly depends on the initial internal state of the walker and can be either symmetric or strongly asymmetric for one and the same coin operator (Fig. 1). Furthermore, as the quantum

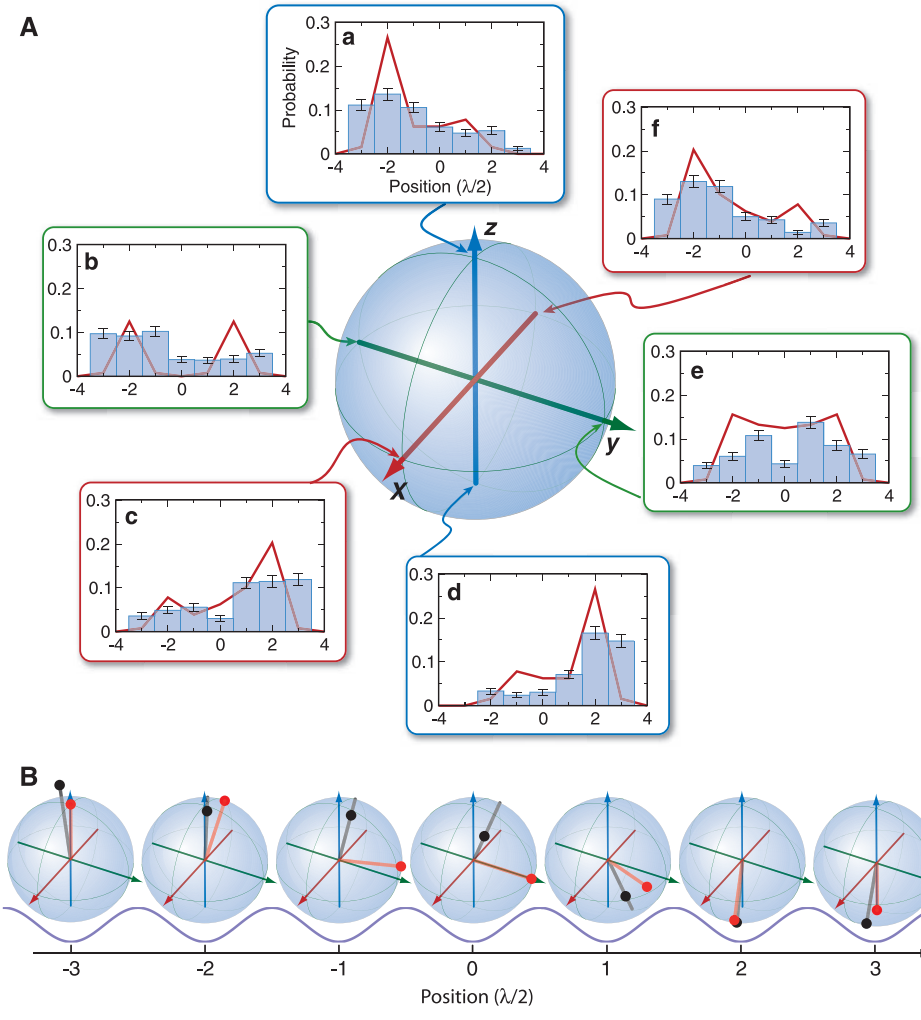

Fig. 3. (**A**) Local quantum state tomography of the atomic wave function after a six-step quantum walk. The distributions belong to the eigenstates of the Pauli spin operators $\hat{\sigma}_i (i = x, y, z)$: (a) $|0\rangle$ (+z axis), (b) $(|0\rangle - i|1\rangle)/\sqrt{2}$ (–y axis), (c) $(|0\rangle + |1\rangle)/\sqrt{2}$ (+x axis), (d) $|1\rangle$ (–z axis), (e) $(|0\rangle + i|1\rangle)/\sqrt{2}$ (+y axis), and (f) $(|0\rangle - |1\rangle)/\sqrt{2}$ (–x axis). (**B**) Reconstructed Bloch vectors at each position in the lattice. The tips of the reconstructed and ideally expected Bloch vectors are shown as black and red dots, respectively. The lines for Bloch vectors extend to the surface of the Bloch sphere to guide the eye; deviations from the surface illustrate the effect of decoherence and measurement errors.

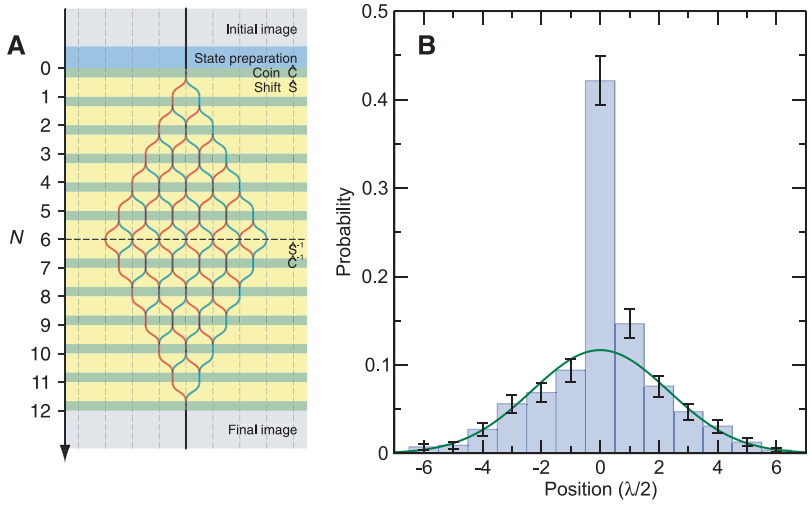

Fig. 4. (**A**) Time-reversal sequence for refocusing the delocalized state of a six-step quantum walk. After six steps, the total application of the coin and shift operator is reversed, where $(\hat{S}\hat{C})^{-1} = \hat{C}^{-1}\hat{S}^{-1}$. (**B**) The resulting probability distribution shows a pronounced peak at the center, to where, ideally, the amplitude should be fully refocused. We observe a refocused amplitude of 30%, surrounded by a Gaussian background (fitted curve).

walk is fully deterministic and unitary, the multipath interference can be reversed by inverting coin and shift operations.

We realize a quantum walk with single laser-cooled cesium (Cs) atoms, trapped in the potential wells of a 1D optical lattice (*12*) with site separation of $\lambda/2 = 433$ nm (here, λ is the wavelength of the lattice laser light). The atoms are thermal with a mean energy of $k_B \times 10\ \mu K$, whereas the optical potential depth is $k_B \times 80\ \mu K$ (here, k_B is the Boltzmann constant). They are distributed among the axial vibrational states with a mean occupation number of $\bar{n}_{ax} = 1.2$. Initially, the atoms are prepared in the $|0\rangle \equiv |F = 4, m_F = 4\rangle$ hyperfine state by optical pumping, where F is the total angular momentum, and m_F its projection onto the quantization axis along the dipole trap axis. Resonant microwave radiation around 9.2 GHz coherently couples this state to the $|1\rangle \equiv |F = 3, m_F = 3\rangle$ state. A $\pi/2$ pulse of 4 μs initializes the system in the superposition $(|0\rangle + i|1\rangle)/\sqrt{2}$. Coin operators are realized in the form of Hadamard-type gates $\hat{C}:\{|0\rangle \rightarrow (|0\rangle - |1\rangle)/\sqrt{2}, |1\rangle \rightarrow (|0\rangle + |1\rangle)/\sqrt{2}\}$. The state-dependent shift operation is performed by continuous control of the trap polarization, moving the spin state $|0\rangle$ adiabatically to the right (whereas state $|1\rangle$ moves to the left) along the lattice axis within 19 μs (*26*). After N steps of coin operation and state-dependent shift, the final atom distribution is probed by fluorescence imaging. From these images, the exact lattice site of the atom after the walk is extracted (*27*) and compared to the initial position of the atom. Spin echo operations are combined with each coin operation (*26*), leading to a coherence time of 0.8 ms.

The final probability distribution $P_N(\xi)$ to find an atom at position ξ after N steps (Fig. 1) is obtained from the distance each atom has walked by taking the ensemble average over several hundreds of identical realizations of the sequence. Ideally, one expects a double-peak distribution with large amplitude close to the edges of the distribution (*7*). The relative heights of the left and right peaks—and therefore the symmetry—depend on the choice of the initial state. Decoherence gradually suppresses the pronounced peaks (*12*, *28*). We compare the measured distributions for the symmetric and asymmetric quantum walks of $N = 6$ steps (Fig. 1, D and E) with the theoretical expectations for the ideal case and find good agreement.

In contrast, a random walk distribution can be recovered by introducing decoherence after each step of the walk. Omitting the spin-echo from the coin operation and additionally waiting 400 μs between coin and subsequent shift operation destroys the phase relation between subsequent steps of the walk. The resulting probability distribution is described by a binomial distribution (Fig. 1G), as expected for a purely classical random walk.

The scaling of the width of the quantum and the random walk distribution with the number of steps is one of the most prominent distinguishing features. We have investigated this scaling behavior for both walks for up to $N = 24$ steps (Fig. 2). For the quantum walk, the width follows closely the expected linear behavior for up to 10 steps. The subsequent deviation is due to decoherence (*26*), which asymptotically turns the quantum walk into a classical random walk. In contrast, for the random walk, the typical square-root scaling is recovered.

To get a more detailed characterization of the wave function prepared by a six-step quantum walk sequence, we extract information on the internal state populations and relative phase by local quantum state tomography. This is based on site-resolved, state-selective detection combined with single-particle operations (*26*, *29*), providing a population distribution for each eigenstate of the Pauli spin operators $\hat{\sigma}_i (i = x,y,z)$ (Fig. 3). Essentially, at each lattice site, the internal quantum state is represented by a vector on the Bloch sphere, which we reconstruct from the result of the tomography. These Bloch vectors fit well to the theoretical prediction at the edges of the distribution, but they show increasing deviations in a region close to the initial site of the walk. At these lattice sites, matter wave interference occurs at almost every step during the sequence, which makes these lattice sites more sensitive to decoherence compared with sites further apart.

The local tomography, however, does not yield information about the off-diagonal elements of the position space density matrix, which essentially contain information about the phase relation between the wave function at different lattice sites rather than at each site. To demonstrate the spatial coherence of the state over all populated lattice sites, we invert the coin operation C^{-1}: $\{|0\rangle \rightarrow (|0\rangle + |1\rangle)/\sqrt{2}, |1\rangle \rightarrow (|0\rangle - |1\rangle)/\sqrt{2}\}$, as well as the shift operation, and continue the walk for six additional steps (Fig. 4). Ideally, the inversion acts as an effective time-reversal and refocuses the multipath interference pattern of the wave function back to the initial lattice site. We find partial refocusing of 30% of the atomic population to the expected lattice site reflecting the fraction of atoms which have maintained coherence throughout the sequence.

We have studied the quantum walk of single neutral atoms in an optical lattice and characterized the quantum state of the delocalized atom. We have found good agreement with the ideal case of a quantum walk for up to 10 steps. Inversion of the walk causes the delocalized wave function to refocus to the initial lattice site. Although the atoms in our experiments are thermally distributed among several vibrational states, we obtain large coherence over a macroscopic distance. In the ideal case, motional state and internal states factorize so that the coherence created in one degree of freedom is not affected by the other. We have found that, as soon as internal and external degrees of freedom are coupled by diabatic transport leading to vibrational excitations, for instance, the matter wave interference is quickly suppressed.

It will be interesting to investigate the behavior of quantum walks for different conditions when coin operations depend on position or time. In particular, monitoring the decay of coherence under the influence of different noise sources will further elucidate the transition from the quantum to the classical regime. Performing the quantum walk with more than one atom and enabling coherent interactions between the atoms (*30*) will realize first operational quantum cellular automata that can be probed by full quantum state tomography, opening another experimental route toward quantum information science.

References and Notes

1. G. Möllenstedt, H. Düker, *Z. Phys. A Hadrons Nucl.* **145**, 377 (1956).
2. O. Carnal, J. Mlynek, *Phys. Rev. Lett.* **66**, 2689 (1991).
3. M. S. Chapman *et al.*, *Phys. Rev. Lett.* **75**, 3783 (1995).
4. M. Weitz, T. Heupel, T. W. Hänsch, *Phys. Rev. Lett.* **77**, 2356 (1996).
5. L. Hackermüller, K. Hornberger, B. Brezger, A. Zeilinger, M. Arndt, *Nature* **427**, 711 (2004).
6. M. A. Schlosshauer, *Decoherence and the Quantum-to-Classical Transition* (Springer, Berlin, ed. 1, 2007).
7. J. Kempe, *Contemp. Phys.* **44**, 307 (2003).
8. M. Barber, *Random and Restricted Walks: Theory and Applications* (Gordon and Breach, New York, ed. 1, 1970).
9. H. C. Berg, *Random Walks in Biology* (Princeton Univ. Press, Princeton, NJ, revised ed., 1993).
10. E. F. Fama, *Financ. Anal. J.* **21**, 55 (1965); reprinted in *Financ. Anal. J.* **51**, 75 (1995).
11. A. M. Childs, *Phys. Rev. Lett.* **102**, 180501 (2009).
12. W. Dür, R. Raussendorf, V. M. Kendon, H. Briegel, *Phys. Rev. A* **66**, 052319 (2002).
13. R. J. Sension, *Nature* **446**, 740 (2007).
14. B. C. Travaglione, G. J. Milburn, *Phys. Rev. A* **65**, 032310 (2002).
15. P. L. Knight, E. Roldán, J. E. Sipe, *Phys. Rev. A* **68**, 020301 (2003).
16. J. Du *et al.*, *Phys. Rev. A* **67**, 042316 (2003).
17. C. A. Ryan, M. Laforest, J. C. Boileau, R. Laflamme, *Phys. Rev. A* **72**, 062317 (2005).
18. D. Bouwmeester, I. Marzoli, G. P. Karman, W. Schleich, J. P. Woerdman, *Phys. Rev. A* **61**, 013410 (1999).
19. B. Do *et al.*, *J. Opt. Soc. Am. B* **22**, 499 (2005).
20. H. B. Perets *et al.*, *Phys. Rev. Lett.* **100**, 170506 (2008).
21. H. Schmitz *et al.*, preprint available at http://arxiv.org/abs/0904.4214 (2009).
22. R. P. Feynman, A. R. Hibbs, *Quantum Mechanics and Path Integrals* (McGraw-Hill, New York, 1965).
23. R. Raussendorf, *Phys. Rev. A* **72**, 022301 (2005).
24. D. J. Shepherd, T. Franz, R. F. Werner, *Phys. Rev. Lett.* **97**, 020502 (2006).
25. K. G. H. Vollbrecht, J. I. Cirac, *Phys. Rev. A* **73**, 012324 (2006).
26. See the supporting material on *Science* Online.
27. M. Karski *et al.*, *Phys. Rev. Lett.* **102**, 053001 (2009).
28. V. Kendon, B. Tregenna, *Phys. Rev. A* **67**, 042315 (2003).
29. W. Rosenfeld, S. Berner, J. Volz, M. Weber, H. Weinfurter, *Phys. Rev. Lett.* **98**, 050504 (2007).
30. O. Mandel *et al.*, *Nature* **425**, 937 (2003).

31. We thank D. Döring, F. Grenz, and A. Härter for help in the construction of the apparatus and A. Rauschenbeutel for valuable discussions. We acknowledge financial support from the Deutsche Forschungsgemeinschaft (research unit 635) and European Commission (Integrated Project on Scalable Quantum Computing with Light and Atoms). M.K. acknowledges support from the Studienstiftung des deutschen Volkes, and J.-M.C. received partial support from the Korea Research Foundation grant funded by the Korean Government (Ministry of Education and Human Resources Development).

Supporting Online Material

www.sciencemag.org/cgi/content/full/325/5937/174/DC1
SOM Text
References

2 April 2009; accepted 3 June 2009
10.1126/science.1174436

Experimental Realization of a Three-Dimensional Topological Insulator, Bi_2Te_3

Y. L. Chen,[1,2,3] J. G. Analytis,[1,2] J.-H. Chu,[1,2] Z. K. Liu,[1,2] S.-K. Mo,[2,3] X. L. Qi,[1,2] H. J. Zhang,[4] D. H. Lu,[1] X. Dai,[4] Z. Fang,[4] S. C. Zhang,[1,2] I. R. Fisher,[1,2] Z. Hussain,[3] Z.-X. Shen[1,2]*

Three-dimensional topological insulators are a new state of quantum matter with a bulk gap and odd number of relativistic Dirac fermions on the surface. By investigating the surface state of Bi_2Te_3 with angle-resolved photoemission spectroscopy, we demonstrate that the surface state consists of a single nondegenerate Dirac cone. Furthermore, with appropriate hole doping, the Fermi level can be tuned to intersect only the surface states, indicating a full energy gap for the bulk states. Our results establish that Bi_2Te_3 is a simple model system for the three-dimensional topological insulator with a single Dirac cone on the surface. The large bulk gap of Bi_2Te_3 also points to promising potential for high-temperature spintronics applications.

Soon after the theoretical prediction (*1*), a new state of quantum matter—the two-dimensional (2D) topological insulator displaying the quantum spin Hall (QSH) effect—was experimentally observed in HgTe quantum wells (*2*). The QSH state (*3*, *4*) has an insulating gap in the bulk and gapless states at the edge where opposite spin states counterpropagate. The two opposite spin states form a single massless Dirac fermion at the edge, and the crossing of their dispersion branches at a time-reversal invariant (TRI) point is protected by the time-reversal symmetry (*5*). The dissipationless edge state transport of the QSH state may enable low-power spintronics devices.

Two-dimensional massless Dirac fermions were experimentally discovered in graphene with two inequivalent massless Dirac points for each spin orientation, giving rise to four copies of massless Dirac fermions in total. This is consistent with the experimentally observed quantized Hall conductance $2e^2/h$ (*6*), as each Dirac fermion leads to a quantized Hall conductance $e^2/2h$ in an external magnetic field (h is Planck's constant). Graphene has an even number of massless Dirac fermions, because no TRI purely 2D free fermion system can have a single or odd number of massless Dirac fermions. However, a single Dirac fermion can occur in a 2D TRI system when it is the boundary of a 3D topological insulator (*7*–*10*), which has a bulk insulating gap and odd number of gapless Dirac cones on the surface. The electrodynamics of the topological insulator is described by an additional topological term in Maxwell's equation (*10*), and the surface state leads to striking quantum phenomena such as an image magnetic monopole induced by an electric charge (*11*) and Majorana fermions induced by the proximity effect from a superconductor (*12*–*14*).

[1]Stanford Institute for Materials and Energy Sciences, SLAC National Accelerator Laboratory, 2575 Sand Hill Road, Menlo Park, CA 94025, USA. [2]Geballe Laboratory for Advanced Materials, Departments of Physics and Applied Physics, Stanford University, Stanford, CA 94305, USA. [3]Advanced Light Source, Lawrence Berkeley National Laboratory, Berkeley, CA 94720, USA. [4]Beijing National Laboratory for Condensed Matter Physics and Institute of Physics, Chinese Academy of Sciences, Beijing 100190, China.

*To whom correspondence should be addressed. E-mail: zxshen@stanford.edu

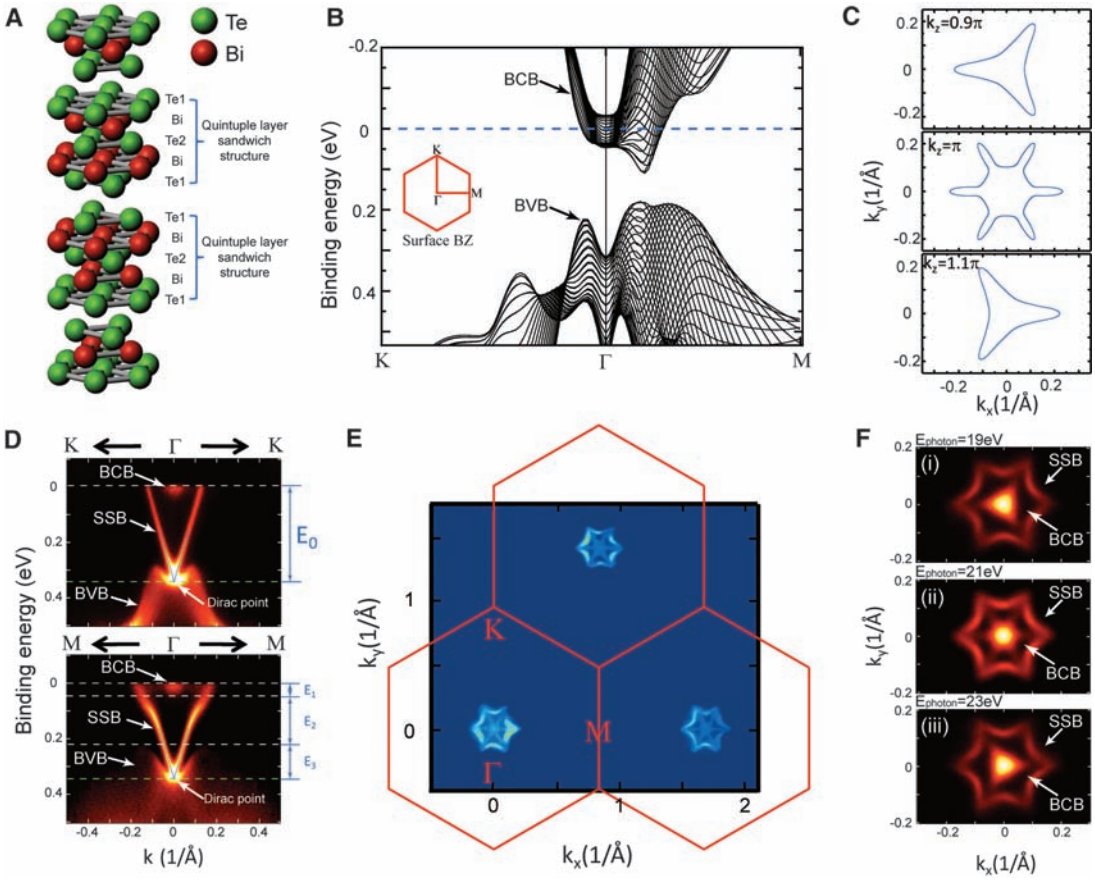

Fig. 1. Crystal and electronic structures of Bi_2Te_3. **(A)** Tetradymite-type crystal structure of Bi_2Te_3. **(B)** Calculated bulk conduction band (BCB) and bulk valance band (BVB) dispersions along high-symmetry directions of the surface BZ (see inset), with the chemical potential rigidly shifted to 45 meV above the BCB bottom at Γ to match the experimental result. **(C)** The k_z dependence of the calculated bulk FS projection on the surface BZ. **(D)** ARPES measurements of band dispersions along K-Γ-K (top) and M-Γ-M (bottom) directions. The broad bulk band (BCB and BVB) dispersions are similar to those in (B), whereas the sharp V-shape dispersion is from the surface state band (SSB). The apex of the V-shape dispersion is the Dirac point. Energy scales of the band structure are labeled as follows: E_0: binding energy of Dirac point (0.34 eV); E_1: BCB bottom binding energy (0.045 eV); E_2: bulk energy gap (0.165 eV); and E_3: energy separation between BVB top and Dirac point (0.13 eV). **(E)** Measured wide-range FS map covering three BZs, where the red hexagons represent the surface BZ. The uneven intensity of the FSs at different BZs results from the matrix element effect. **(F)** Photon energy–dependent FS maps. The shape of the inner FS changes markedly with photon energies, indicating a strong k_z dependence due to its bulk nature as predicted in (C), whereas the nonvarying shape of the outer hexagram FS confirms its surface state origin.

The 3D material HgTe under strain is predicted to have a single Dirac cone on the surface (*15*). However, experiments are difficult to perform under the strain condition. The $Bi_{1-\delta}Sb_{\delta}$ alloy is also predicted to be a 3D topological insulator in the narrow alloying content regime of $\delta = 0.07 \sim 0.22$ (*16*, *17*), and a recent angle-resolved photoemission spectroscopy (ARPES) study reveals the topological nature of the surface state despite its complexity, with as many as five branches crossing the Fermi level (E_F) (*18*).

Recently, a class of stoichiometric materials, Bi_2Te_3, Bi_2Se_3, and Sb_2Te_3, were theoretically predicted to be the simplest 3D topological insulators whose surface states consist of a single Dirac cone at the Γ point (*19*). This simplicity makes them the ideal candidates to realize the magneto-electric effect (*20*). Furthermore, the predicted large bulk gap makes them possible candidates for high-temperature spintronics applications. Independent of the theoretical proposal, an ARPES study (*21*) of Bi_2Se_3 reveals a single surface electron pocket with a Dirac point below E_F. However, a deep bulk electron pocket coexisting with the topologically nontrivial surface states was also observed in the same ARPES experiment. Therefore, the topological insulating behavior in this class of materials has yet to be established experimentally, which is the main goal of the present work.

We performed ARPES and transport experiments to investigate both the bulk and surface state electronic properties of $(Bi_{1-\delta}Sn_{\delta})_2Te_3$ crystals (where δ represents nominal Sn concentration, incorporated to compensate for the n-type doping from vacancy and anti-site defects). Further details of the sample preparation, ARPES, and transport experiments are in the supporting online material (*22*). By scanning over the entire Brillouin zone (BZ), we confirmed that the surface states consist of a single, nondegenerate Dirac cone at the Γ point. At appropriate doping (δ = 0.67%), we found that the bulk states disappear completely at E_F, thus realizing the topological insulating behavior in this class of materials. With a much larger bulk band gap (165 meV) compared to the energy scale of room temperature (26 meV), the topological protection of the surface states in this material could lead to promising applications in low-power spintronics devices at room temperature.

Figure 1 summarizes the bulk and surface electronic structures and Fermi-surface (FS) topology of undoped Bi_2Te_3. The crystal structure of Bi_2Te_3 (Fig. 1A) is of the tetradymite type, which is formed by stacking quintuple-layer groups sandwiched by three sheets of Te and two sheets of Bi within each group (*23*). Ab initio calculations predict that the undoped Bi_2Te_3 is an insulator (Fig. 1B) and that the doped FS (Fig. 1C) from the bulk conduction band projected onto the surface BZ exhibits a triangular or snowflake-like electron pocket centered at the Γ point (Fig. 1C) depending on its k_z position in reciprocal space.

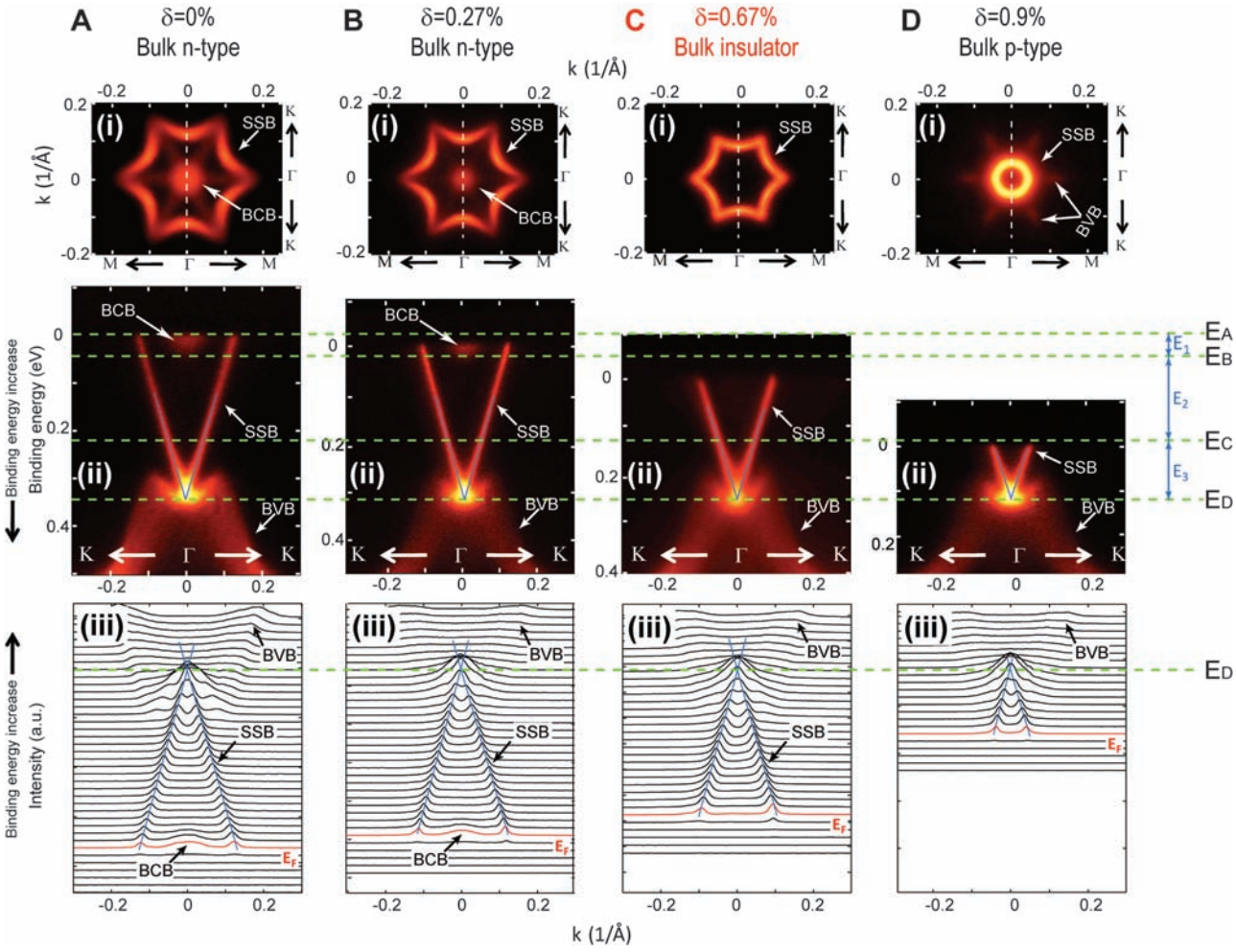

Fig. 2. Doping dependence of FSs and E_F positions. (**A** to **D**) Measured FSs and band dispersions for 0, 0.27, 0.67, and 0.9% nominally doped samples. Top row: FS topology (symmetrized according to the crystal symmetry). The FS pocket formed by SSB is observed for all dopings; its volume shrinks with increasing doping, and the shape varies from a hexagram to a hexagon from (A) to (D). The pocket from BCB also shrinks upon doping and completely vanishes in (C) and (D). In (D), six leaf-like hole pockets formed by BVB emerge outside the SSB pocket. Middle row: image plots of band dispersions along K-Γ-K direction as indicated by white dashed lines superimposed on the FSs in the top row. The E_F positions of the four doping samples are at 0.34, 0.325, 0.25, and 0.12 eV above the Dirac point, respectively. Bottom row: momentum distribution curve plots of the raw data. Definition of energy positions: E_A: E_F position of undoped Bi_2Te_3; E_B: BCB bottom; E_C: BVB top; and E_D: Dirac point position. Energy scales $E_1 \sim E_3$ are defined in Fig. 1D.

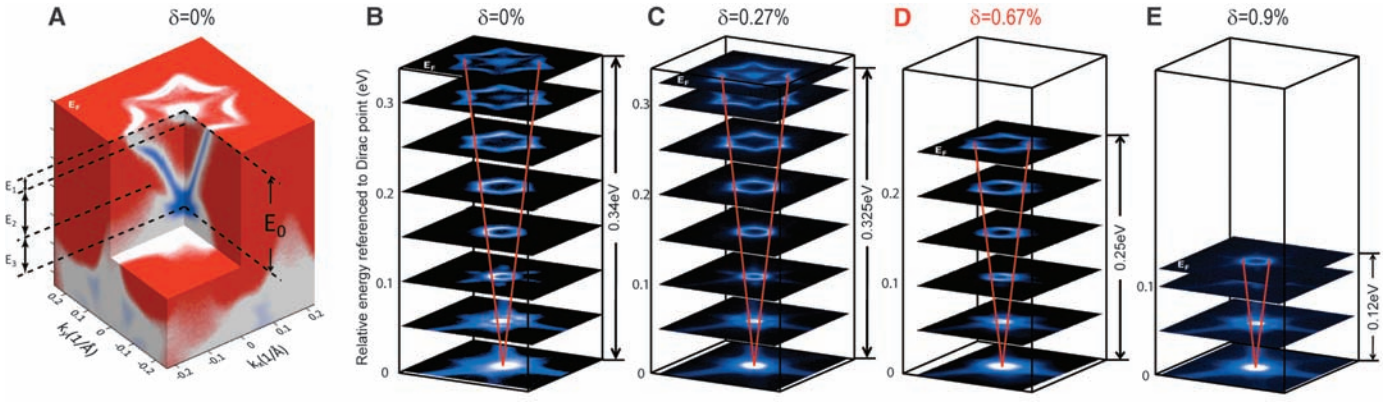

Fig. 3. (**A**) Three-dimensional illustration of the band structures of undoped Bi_2Te_3, with the characteristic energy scales $E_0 \sim E_3$ defined in Fig. 1D. (**B** to **E**) Constant-energy contours of the band structure and the evolution of the height of E_F referenced to the Dirac point for the four dopings. Red lines are guides to the eye that indicate the shape of the constant-energy band contours and intersect at the Dirac point.

Actual band dispersions measured by ARPES experiments along two high-symmetry directions are shown in Fig. 1D. In addition to the broad spectra of the bulk electron pocket on top and the "M" shape valance band at bottom, as predicted in the ab initio calculation, there is an extra sharp V-shape dispersion resulting from the surface state. The linear dispersion in both plots clearly indicates a massless Dirac fermion with a velocity of 4.05×10^5 m/s (2.67 eV·Å) and 3.87×10^5 m/s (2.55 eV·Å) along the Γ-K and Γ-M directions, respectively (*22*), which are about 40% of the value in graphene (*6*) and agree well with our first-principle calculation [by the method described in (*19*)] that yields 2.13 and 2.02 eV·Å along the Γ-K and Γ-M directions, respectively.

This sharp surface state also forms a FS pocket in addition to the calculated FSs from bulk bands. As shown in Fig. 1, E and F(ii), in each BZ there is a hexagram-shaped FS enclosing the snowflake-like bulk FS. A broad FS map covering three adjacent BZs (Fig. 1E) confirms that there is only one such hexagram FS resulting from the V-shape Dirac-type surface state in each BZ. The spin-orbit coupling (SOC) in this material is strong. The level splitting (λ) due to SOC of Bi-6p orbital is λ = 1.25 eV (*19*), about twice that in Au (λ = 0.68 eV) (*24*). Given that our energy and momentum resolution [$\delta E < 0.016$ eV and $\delta k < 0.012$(1/Å) (*22*)] is better than needed to resolve even the much smaller Au surface state splitting [$\Delta E = 0.11$ eV, $\Delta k = 0.023$(1/Å)] (*25*), the fact that we do not observe more than one set of surface state for all dopings and under all experimental conditions—including different photon energies, polarizations, and experimental setups in different synchrotrons—rules out the possibility that the Dirac cone is spin degenerate, and we encourage future spin-resolved ARPES experiments to confirm this. This observation demonstrates that Bi_2Te_3 is an ideal candidate as the parent compound for the simplest kind of 3D topological insulator (*19*)—a simplicity resembling that of the hydrogen atom in atomic physics. In contrast, graphene has two valleys with spin degeneracy, giving a total of four Dirac cones in each BZ, leading to a topological trivial state. Furthermore, because there is only one surface FS pocket in each surface BZ, the surface state will only cross E_F once between Γ and M, rather than the complex crossing of five times as observed in $Bi_{0.9}Sb_{0.1}$ (*3*, *18*).

The surface nature of the hexagram FS resulting from the sharp V-shape dispersion is further established by a photon energy dependence study (Fig. 1F). By varying the excitation photon energy, the shape of the snowflake-like bulk FS changes from a left-pointing triangle [Fig. 1F(i)] to a right-pointing triangle [Fig. 1F(iii)] as a result of the k_z dispersion of the 3D bulk electronic structure (Fig. 1C). In contrast, the shape of the hexagram-like FS does not change with the incident photon energy, confirming its 2D nature (i.e., no k_z dispersion). We note that the perfect Bi_2Te_3 single crystal is predicted to be a bulk insulator, and the electron carriers observed in our experiment arise from crystal imperfections, specifically vacancies and defects (*26*). Given the substantial bulk gap (Fig. 1D), one can tune E_F into the gap by doping holes to compensate for the electron carriers, thus realizing the topological insulator phase in this material. Because the surface state accommodates only a small number of carriers (orders of magnitude less than the bulk), the actual realization of the bulk insulating state by bulk doping is a challenging task. After experimenting with numerous doping levels by different dopants, we found Sn to be a suitable dopant and successfully doped Bi_2Te_3 into its bulk insulating phase. The effect of Sn doping is demonstrated in Fig. 2, where the FSs and band dispersions from samples of four different nominal dopings are shown from panels (A) to (D), respectively.

Taking the Dirac point position as reference, one sees the doping evolution of the FSs (Fig. 2, top row) associated with the downshift of E_F (Fig. 2, middle and bottom rows). With proper doping (Fig. 2C), the topological insulator phase of Bi_2Te_3 can be realized with the E_F residing inside the bulk gap. Unlike a simple circular Dirac cone, the observed surface state in Bi_2Te_3 exhibits richer structure. The 3D spectra intensity plot in (k_x, k_y, E) space (Fig. 3A) and the cross sections of the Dirac-like dispersion at various binding energies (Fig. 3, B to E) are demonstrated. When approaching the Dirac point from E_F, the shape of the surface state FS evolves gradually from a hexagram to a hexagon, then to a circle of shrinking volume, and finally converges into a point, the Dirac point. Comparing the shape of the bulk electron FS and the surface state FS, the hexagram shape of the surface state FS is induced by the band repulsion with the snowflake-shape bulk electron pocket. Because FSs cannot have discontinuities, the "vertices" of the hexagram and hexagon are actually smoothened. From the doping evolution of the FS topology and the band dispersions shown above, we have found convincing evidence that the 0.67% Sn-doped Bi_2Te_3 is a 3D topological insulator with a single Dirac cone and a large bulk band gap. The observations of ARPES are also supported by Hall and resistivity measurements (*22*).

The single Dirac cone of the Bi_2Te_3 family makes it the simplest model system for studying the physics of topological insulators, and the large bulk gap points to promising potential for high-temperature spintronics applications on a bulk material that is easy to produce and manipulate with current standard semiconductor technology.

References and Notes

1. B. A. Bernevig, T. L. Hughes, S.-C. Zhang, *Science* **314**, 1757 (2006).
2. M. König *et al.*, *Science* **318**, 766 (2007).
3. C. L. Kane, E. J. Mele, *Phys. Rev. Lett.* **95**, 226801 (2005).
4. B. A. Bernevig, S.-C. Zhang, *Phys. Rev. Lett.* **96**, 106802 (2006).
5. C. L. Kane, E. J. Mele, *Phys. Rev. Lett.* **95**, 146802 (2005).
6. Y. Zhang, Y.-W. Tan, H. L. Stormer, P. Kim, *Nature* **438**, 201 (2005).
7. L. Fu, C. L. Kane, E. J. Mele, *Phys. Rev. Lett.* **98**, 106803 (2007).
8. J. E. Moore, L. Balents, *Phys. Rev. B* **75**, 121306 (2007).
9. R. Roy, preprint available at http://arxiv.org/abs/cond-mat/0604211v2
10. X.-L. Qi, T. L. Hughes, S.-C. Zhang, *Phys. Rev. B* **78**, 195424 (2008).
11. X.-L. Qi, R. Li, J. Zhang, S.-C. Zhang, *Science* **323**, 1184 (2009).
12. L. Fu, C. L. Kane, *Phys. Rev. Lett.* **100**, 096407 (2008).

13. A. R. Akhmerov, J. Nilsson, C. W. J. Beenakker, *Phys. Rev. Lett.* **102**, 216404 (2009).
14. L. Fu, C. L. Kane, *Phys. Rev. Lett.* **102**, 216403 (2009).
15. X. Dai, T. L. Hughes, X.-L. Qi, Z. Fang, S.-C. Zhang, *Phys. Rev. B* **77**, 125319 (2008).
16. L. Fu, C. L. Kane, *Phys. Rev. B* **76**, 045302 (2007).
17. J. C. Y. Teo, L. Fu, C. L. Kane, *Phys. Rev. B* **78**, 045426 (2008).
18. D. Hsieh *et al.*, *Nature* **452**, 970 (2008).
19. H. Zhang *et al.*, *Nat. Phys.* **5**, 438 (2009).
20. Q. Liu, C.-X. Liu, C. Xu, X.-L. Qi, S.-C. Zhang, *Phys. Rev. Lett.* **102**, 156603 (2009).
21. Y. Xia, *et al.*, *Nat. Phys.* **5**, 398 (2009).
22. Materials and methods are available as supporting material on *Science* Online.
23. R. W. G. Wyckoff, *Crystal Structures* (Wiley, New York, 1964), vol. 2.
24. M. Vijayakumar, M. S. Gopinathan, *J. Mol. Struct.* **361**, 15 (1996).
25. S. LaShell, B. A. McDougall, E. Jensen, *Phys. Rev. Lett.* **77**, 3419 (1996).
26. C. B. Satterthwaite, R. W. Ure Jr., *Phys. Rev.* **108**, 1164 (1957).
27. We thank W. S. Lee, K. J. Lai, B. Moritz, and C. X. Liu for insightful discussions and C. Kucharczyk and L. Liu for assistance on crystal growth. This work was supported by the Department of Energy, Office of Basic Energy Sciences, under contract DE-AC02-76SF00515; H.J.Z., Z.F., and X.D. acknowledge the support by the NSF of China, the National Basic Research Program of China, and the International Science and Technology Cooperation Program of China.

Supporting Online Material
www.sciencemag.org/cgi/content/full/1173034/DC1
Materials and Methods
Figs. S1 to S4
References

4 March 2009; accepted 3 June 2009
Published online 11 June 2009;
10.1126/science.1173034
Include this information when citing this paper.

Dynamics of Chemical Bonding Mapped by Energy-Resolved 4D Electron Microscopy

Fabrizio Carbone,* Oh-Hoon Kwon, Ahmed H. Zewail†

Chemical bonding dynamics are fundamental to the understanding of properties and behavior of materials and molecules. Here, we demonstrate the potential of time-resolved, femtosecond electron energy loss spectroscopy (EELS) for mapping electronic structural changes in the course of nuclear motions. For graphite, it is found that changes of milli–electron volts in the energy range of up to 50 electron volts reveal the compression and expansion of layers on the subpicometer scale (for surface and bulk atoms). These nonequilibrium structural features are correlated with the direction of change from sp^2 [two-dimensional (2D) graphene] to sp^3 (3D-diamond) electronic hybridization, and the results are compared with theoretical charge-density calculations. The reported femtosecond time resolution of four-dimensional (4D) electron microscopy represents an advance of 10 orders of magnitude over that of conventional EELS methods.

Bonding in molecules and materials is determined by the nature of electron density distribution between the atoms. The dynamics involve the evolution of electron density in space and the motion of nuclei that occur on the attosecond and femtosecond time scale, respectively (*1*–*3*). Such changes of the charge distribution with time are responsible for the outcome of chemical reactivity and for phenomena in the condensed phase, including those of phase transitions and nanoscale quantum effects. With convergent-beam electron diffraction (*4*), the static pattern of charge-density difference maps can be visualized, and using x-ray absorption (*5*) and photoemission spectroscopy (*6*–*8*) substantial progress has been made in the study of electronic-state dynamics in bulks and on surfaces. Electron energy loss spectroscopy (EELS) is a powerful method in the study of electronic structure on the atomic scale, using aberration-corrected microscopy (*9*), and in chemical analysis of selective sites (*10*); the comparison with synchrotron-based near-edge x-ray absorption spectroscopy is impressive (*11*). The time and energy resolutions of ultrafast electron microscopy (UEM) (*12*–*16*) provide the means for the study of (combined) structural and bonding dynamics.

Here, time-resolved EELS is demonstrated in the mapping of chemical bonding dynamics, which require nearly 10 orders of magnitude increase in resolution from the detector-limited millisecond response (*17*). By following the evolution of the energy spectra (up to 50 eV) with femtosecond (fs) resolution, it was possible to resolve in graphite the dynamical changes on a millielectronvolt (subpicometer motion) scale. In this way, we examined the influence of surface and bulk atoms motion and observed correlations with electronic structural changes: contraction, expansion, and recurrences. Because the EEL spectra of a specimen in this energy range contain information about plasmonic properties of bonding carriers, their observed changes reveal the collective dynamics of valence electrons.

Graphite is an ideal test case for investigating the correlation between structural and electronic dynamics. Single-layered graphene, the first two-dimensional (2D) solid to be isolated and the strongest material known (*18*), has the orbitals on carbon as sp^2 hybrids, and in graphite the π-electron is perpendicular to the molecular plane. Strongly compressed graphite transforms into diamond, whose charge density pattern is a 3D network of covalent bonds with sp^3 hybrid orbitals. Thus, any structural perturbation on the ultrashort time scale of the motion will lead to changes in the chemical bonding and should be observable in UEM. Moreover, surface atoms have unique binding, and they too should be distinguishable in their influence from bulk atom dynamics.

The experiments were performed on a nm-thick single crystal of natural hexagonal graphite. The sample was cleaved repeatedly until a transparent film was obtained, and then deposited on a transmission electron microscopy (TEM) grid; the thickness was determined from EELS to be 108 nm. The fs-resolved EELS (or FEELS) data were recorded in our UEM, operating in the single-electron per pulse mode (*12*) to eliminate Boersch's space charge effect. A train of 220 fs infrared laser pulses (λ = 1038 nm) was split into two paths; one was frequency-doubled and used to excite the specimen with a fluence of 1.5 mJ/cm^2, and the other was frequency-tripled into the UV and directed to the photoemissive cathode to generate the electron packets. These pulses were accelerated in the TEM column and dispersed after transmission through the sample in order to provide the energy loss spectrum of the material. Details of the clocking and characterization methodology can be found in (*12*, *13*, *16*).

The experimental, static EEL spectra of graphite in our UEM, with graphene (*19*) for comparison, are displayed in Fig. 1A; Fig. 1B shows the results of theoretical calculations (*19*, *20*). The spectral feature around 7 eV is the π plasmon, the strong peak centered around 26.9 eV is the π + σ bulk plasmon, and the weaker peak on its low energy tail is due to the surface plasmon. All these features have been assigned in the literature (*19*–*21*). The agreement between the calculated EEL spectra and the experimental ones is satisfactory both for graphite and graphene. Of relevance to our studies of dynamics is the simulation of the spectra for different *c*-axis separations, ranging from twice as large as naturally occurring (2c/a; a and c are lattice constraints) to 5 times as large (*20*). This thickness dependence is displayed in Fig. 1B.

As displayed in Fig. 1, the surface and bulk plasmon bands (between 13 and 35 eV) can be

Physical Biology Center for Ultrafast Science and Technology, Arthur Amos Noyes Laboratory of Chemical Physics, California Institute of Technology, Pasadena, CA 91125, USA.

*Present address: Ecole Polytechnique Fédérale de Lausanne, CH-1015 Lausanne-Dorigny, Switzerland.
†To whom correspondence should be addressed. E-mail: zewail@caltech.edu

analyzed using two Voigt functions, thus defining the central position, intensity, and width. At different delay times, we monitored the changes and found that they occur in the intensity and position; the width and shape of the two spectral components are relatively unchanged. Fig. 1, C and D, shows the temporal changes of the intensity for both the surface and bulk plasmons. As noted, the behavior of bulk dynamics is "out of phase" with that of the surface dynamics, corresponding to an increase in intensity for the former and a decrease for the latter. Each time point represents a 500-fs change. Within the first 1 ps, the bulk plasmon gains spectral weight with the increase in intensity. With time, the intensity is found to return to its original (equilibrium) value. At longer times, a reverse in sign occurs, corresponding to a decrease and then an increase in intensity—an apparent recurrence or echo occurring with dispersion. The intensity change of the surface plasmon in Fig. 1, C and D, shows a π phase-shifted temporal evolution with respect to that of the bulk plasmon.

The time dependence of the energy position of the different spectral bands is displayed in Fig. 2. The least-squares fit converges for a value of the surface plasmon energy at 14.3 eV and of the bulk plasmon at 26.9 eV, in good agreement with literature reports (*19*–*21*). The temporal evolution of the surface plasmon gives no sign of energy dispersion, whereas the bulk plasmon is found to undergo first a blueshift and then a redshift at longer times (Fig. 2, A and B). The overall energy-time changes in the FEEL spectra are displayed in Fig. 3. To make the changes more apparent, the difference between the spectra after the arrival of the initiating laser pulse (time zero) and a reference spectrum taken at −20 ps before time zero is shown. The most pronounced changes are observed in the region near the energy of the laser itself (2.39 eV), representing the energy-loss enhancement due to the creation of carriers by the laser excitation, and in the region dominated by the surface and bulk plasmons (between 13 and 35 eV). Clearly evident in the 3D plot are the energy dependence as a function of time, the echoes, and the shift in phase.

A wealth of information has been obtained on the spectroscopy and structural dynamics of graphite. Of particular relevance here are the results concerning contraction and expansion of layers probed by diffraction on the ultrashort time scale (*22*). Knowing the amplitude of contraction/expansion, which is 0.6 pm at the fluence of 1.5 mJ/cm^2 (*22*), and from the change of plasmon energy with interlayer distance (Fig. 1), we obtained the results shown in Fig. 2C. The diffraction data, when now translated into energy change, reproduce the pattern in Fig. 2A, with the amplitude being within a factor of two. When the layers are fully separated, that is, reaching graphene, the bulk plasmon, as expected, is completely suppressed (*19*).

The dynamics of chemical bonding can now be pictured. The fs optical excitation of graphite generates carriers in the nonequilibrium state. They thermalize by electron-electron and electron-phonon interactions on a time scale found to be less than 1 ps (*23*), less than 500 fs (*8*), and ~200 fs (*24*). From our FEELS, we obtained a rise of bulk plasmons in ~180 fs (Fig. 3) (*25*), consistent with the limits in (*8*, *23*, *24*). The carriers generated induce a strong electrostatic force between graphene layers, and ultrafast interlayer contraction occurs as a consequence (*22*, *26*). In Fig. 1D, the increase of the bulk plasmon spectral weight on the fs time scale reflects this

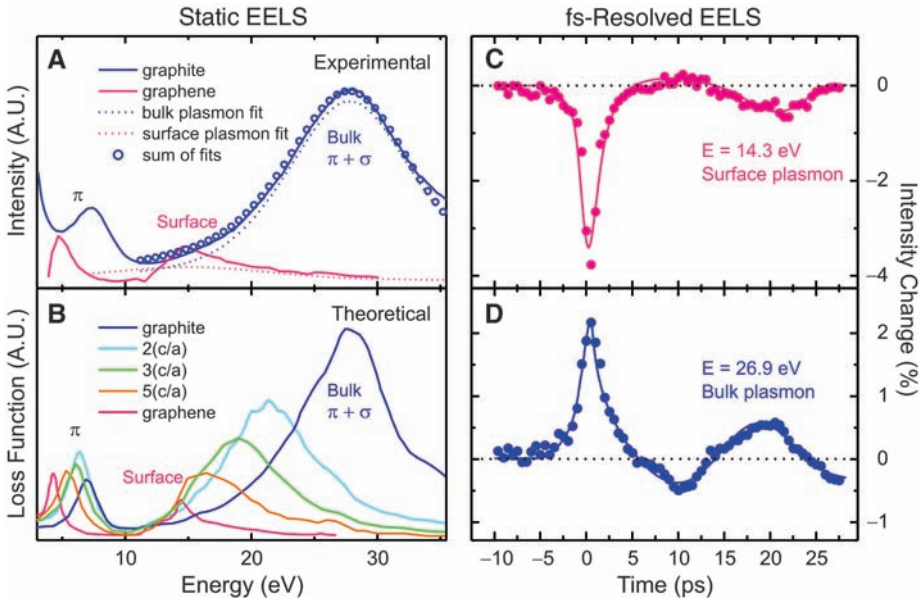

Fig. 1. Static and femtosecond-resolved EELS of graphite. (**A**) The UEM-obtained experimental spectrum of graphite; for comparison with the spectrum of graphene, see (*19*). (**B**) Simulated spectrum for natural graphite, together with the calculated spectra obtained for expanded *c*-axis structures, with the separation being twice, three times, and five times as large as the native one (*20*). The theoretical spectrum of graphene is also displayed (*19*). (**C** and **D**) Peak intensity changes of surface (C) and bulk (D) plasmons as a function of time. Solid lines are guide to the eyes. The increase in intensity for the bulk corresponds to a decrease in intensity for the surface plasmon (i.e., nearly out of phase). The zero of time was determined as shown in Fig. 3.

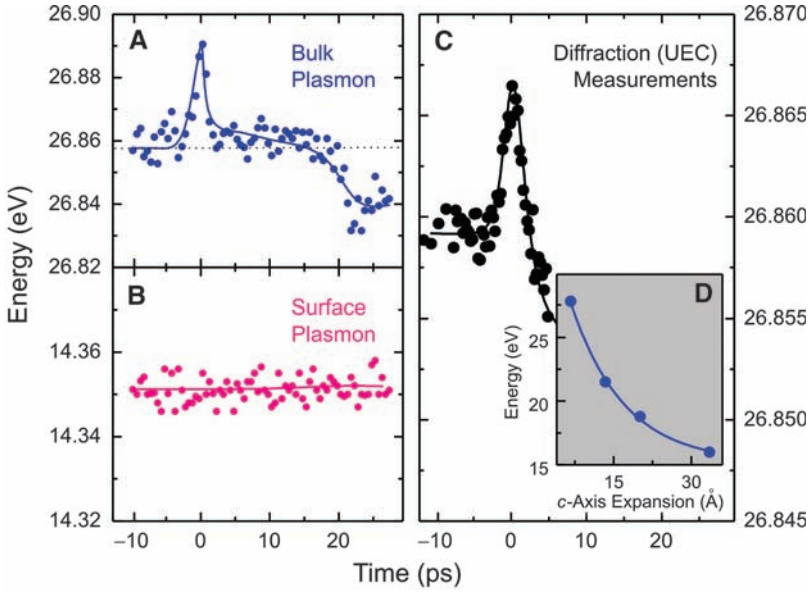

Fig. 2. EELS peak position and diffraction as a function of time. (**A**) Energy dispersion of bulk plasmon. (**B**) Energy dispersion of surface plasmon. (**C**) Energy dispersion predicted from diffraction experiments at 1.5 mJ/cm^2. The energy dispersion associated with structural changes is obtained from (**D**), where the position of the bulk plasmon is plotted against the *c*-axis separation (*20*). The zero of time was determined as shown in Fig. 3.

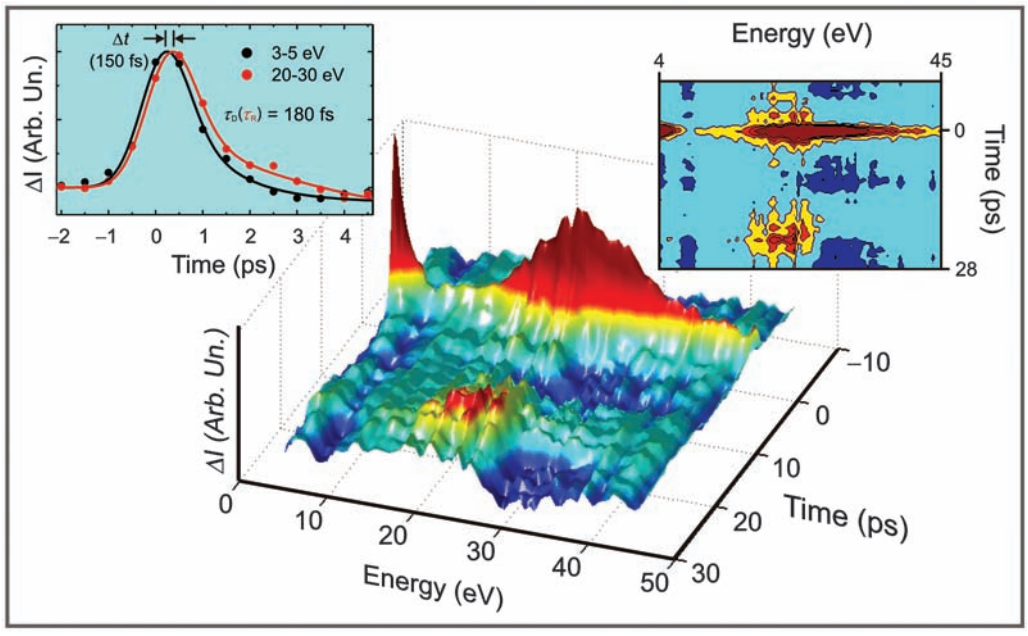

Fig. 3. 3D intensity-energy-time FEELS plot. The plot shows time-energy-amplitude evolution of spectral changes at different time delays. The inset on the right depicts a contour-map version to enhance the visibility of time- and energy-dependent evolution. The zero of change is set to be sky blue in both plots. The inset on the left depicts two transients for the band at the laser energy (3 to 5 eV) and that of the bulk plasmon (26.9 eV). Note the shift from $t = 0$ (*25*). The reported time constant and shift were obtained from two independent measurements made on different specimens.

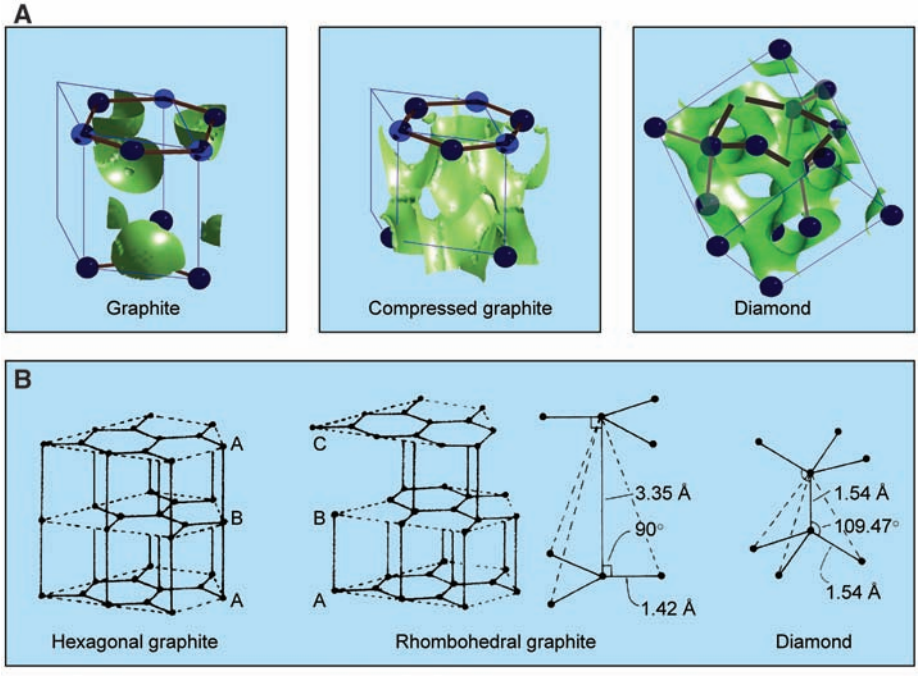

Fig. 4. Charge density distributions and crystal structures. (**A**) Charge density calculated for graphite (c/a = 2.7), compressed graphite (c/a = 1.5), and diamond. All charge densities (ρ) are visualized as constant value surfaces, corresponding to approximately $\rho_{max}/3$. (**B**) Crystal structures and geometrical representations of the transition from graphite to diamond (*34*).

structural dynamics of bond-length shortening because it originates from a denser and more 3D charge distribution. After the compression, a sequence of dilatations and successive expansions along the *c* axis follows, but, at longer times lattice thermalization dephases the coherent atomic motions; at a higher fluence, strong interlayer distance variations occur, and graphene sheets can be detached as a result of these interlayer collisions (*27*–*29*). Thus, the observations reported here reflect the change in electronic structure: contraction toward diamond and expansion toward graphene. The energy change with time correlates well with the EELS change calculated for different interlayer distances (Fig. 1).

We have calculated the charge density distribution for the three relevant structures. The self-consistent density functional theory calculations were made using the linear muffin-tin orbital approximation (*30*), and the results are displayed in Fig. 4. To emphasize the nature of the changes observed in FEELS, and their connection to the dynamics of chemical bonding, we pictorially display the evolution of the charge distribution in a natural graphite crystal, a highly compressed one, and the extreme case of diamond. One can see the transition from a 2D to the 3D electronic structure. The compressed and expanded graphite can pictorially be visualized to deduce the change in electron density as interlayer separations change.

With image, energy, and time resolution in 4D UEM, it is possible to visualize dynamical changes of structure and electronic distribution. Such stroboscopic observations require time and energy resolutions of fs and meV, respectively, as evidenced in the case study (graphite) reported here, and for which the dynamics manifest compression/expansion of atomic planes and electronic sp^2/sp^3-type hybridization change. The application demonstrates the potential for examining the nature of charge density and chemical bonding in the course of physical/chemical or materials phase change. It would be of interest to extend the scale of energy from ~1 eV, with 100 meV resolution (*31*), to the hundreds of eV (*32*) for exploring other dynamical processes (*33*) of bonding.

References and Notes

1. F. Krausz, M. Ivanov, *Rev. Mod. Phys.* **81**, 163 (2009).
2. A. H. Zewail, *Angew. Chem. Int. Ed.* **39**, 2586 (2000).
3. A. H. Zewail, in *Les Prix Nobel: The Nobel Prize 1999*, T. Frängsmyr, Ed. (Almqvist and Wiksell, Stockholm, 2000).
4. J. M. Zuo, M. Kim, M. O'Keeffe, J. C. H. Spence, *Nature* **401**, 49 (1999).
5. Ch. Bressler *et al.*, *Science* **323**, 489 (2009).
6. H. Petek, M. J. Weida, H. Nagano, S. Ogawa, *Science* **288**, 1402 (2000).
7. M. Wolf, G. Ertl, *Science* **288**, 1352 (2000).
8. T. Kampfrath, L. Perfetti, F. Schapper, C. Frischkorn, M. Wolf, *Phys. Rev. Lett.* **95**, 187403 (2005).
9. D. A. Muller *et al.*, *Science* **319**, 1073 (2008).
10. J. M. Thomas, B. G. Williams, T. G. Sparrow, *Acc. Chem. Res.* **18**, 324 (1985).

11. A. P. Hitchcock, J. J. Dynes, G. Johansson, J. Wang, G. Botton, *Micron* **39**, 311 (2008).
12. B. Barwick, H. S. Park, O.-H. Kwon, J. S. Baskin, A. H. Zewail, *Science* **322**, 1227 (2008).
13. H. S. Park, J. S. Baskin, O.-H. Kwon, A. H. Zewail, *Nano Lett.* **7**, 2545 (2007).
14. O.-H. Kwon, B. Barwick, H. S. Park, J. S. Baskin, A. H. Zewail, *Nano Lett.* **8**, 3557 (2008).
15. D. J. Flannigan, P. C. Samartzis, A. Yurtsever, A. H. Zewail, *Nano Lett.* **9**, 875 (2009).
16. F. Carbone *et al*., *Chem. Phys. Lett.* **468**, 107 (2009).
17. T. H. Ellis, L. H. Dubois, S. D. Kevan, M. J. Cardillo, *Science* **230**, 256 (1985).
18. K. S. Novoselov *et al*., *Nature* **438**, 197 (2005).
19. T. Eberlein *et al*., *Phys. Rev. B* **77**, 233406 (2008).
20. G. Marinopoulos, L. Reining, A. Rubio, V. Olevano, *Phys. Rev. B* **69**, 245419 (2004).
21. L. Calliari, S. Fanchenko, M. Filippia, *Surf. Interface Anal.* **40**, 814 (2008).
22. F. Carbone, P. Baum, P. Rudolf, A. H. Zewail, *Phys. Rev. Lett.* **100**, 035501 (2008).
23. K. Ishioka, M. Hase, M. Kitajima, L. Wirtz, A. Rubio, H. Petek, *Phys. Rev. B* **77**, 121402 (2008).
24. K. Seibert *et al*., *Phys. Rev. B* **42**, 2842 (1990).
25. Because FEELS records the energy spectra of all bands in the range studied, we were able to monitor the temporal evolution of the peak at the laser energy (3 to 5 eV), $t = 0$, and compare with that of the bulk plasmon peak (at 26.9 eV). A definite shift (~150 fs) for the latter was observed in two different specimens. With least-squares analysis (rise and decay) we determined the decay of the low-energy band and the rise of the higher-energy band to be ~180 fs. In previous reports (*16*, *22*) the time zero was relative, reflecting the point when the intensity increases (decreases), whereas in this study the time zero was determined from the behavior of the 3 to 5 eV region (at the initial excitation). Thus, all data are analyzed here with this determined value.
26. R. K. Raman *et al*., *Phys. Rev. Lett.* **101**, 077401 (2008).
27. H. O. Jeschke, M. E. Garcia, K. H. Bennemann, *Phys. Rev. Lett.* **87**, 015003 (2001).
28. M. Lenner, A. Kaplan, R. E. Palmer, *Appl. Phys. Lett.* **90**, 153119 (2007).
29. A. Kaplan, M. Lenner, R. E. Palmer, *Phys. Rev. B* **76**, 073401 (2007).
30. S. Y. Savrasov, *A. Kristallogr.* **220**, 555 (2005).
31. A. Yurtsever, M. Couillard, D. A. Muller, *Phys. Rev. Lett.* **100**, 217402 (2008).
32. R. F. Egerton, *Electron Energy-Loss Spectroscopy in the Electron Microscope* (Plenum Press, New York, 1996).
33. C. Bressler, R. Abela, M. Chergui, *Z. Kristallogr.* **223**, 307 (2008).
34. S. Fahy, S. G. Louie, M. L. Cohen, *Phys. Rev. B* **34**, 1191 (1986).

35. This work was supported by the National Science Foundation and the Air Force Office of Scientific Research in the Gordon and Betty Moore Center for Physical Biology at the California Institute of Technology. We thank B. Barwick for helpful and stimulating discussion.

15 April 2009; accepted 1 June 2009
10.1126/science.1175005

Manganese- and Iron-Dependent Marine Methane Oxidation

Emily J. Beal,[1]* Christopher H. House,[1]* Victoria J. Orphan[2]

Anaerobic methanotrophs help regulate Earth's climate and may have been an important part of the microbial ecosystem on the early Earth. The anaerobic oxidation of methane (AOM) is often thought of as a sulfate-dependent process, despite the fact that other electron acceptors are more energetically favorable. Here, we show that microorganisms from marine methane-seep sediment in the Eel River Basin in California are capable of using manganese (birnessite) and iron (ferrihydrite) to oxidize methane, revealing that marine AOM is coupled, either directly or indirectly, to a larger variety of oxidants than previously thought. Large amounts of manganese and iron are provided to oceans from rivers, indicating that manganese- and iron-dependent AOM have the potential to be globally important.

Anaerobic oxidation of methane (AOM) occurs in freshwater samples in the absence of sulfate, provided nitrite or nitrate is present (*1*, *2*). Incubation studies show that the addition of manganese (MnO_2) or iron ($FeCl_2$ and $FeCl_3$) to anoxic sediments and digested sewage increases the ratio of methane oxidized to methane produced (*3*). However, there has been no direct evidence for AOM in the absence of sulfate in marine samples (*4*). Studies of pore-water geochemistry show manganese and iron reduction in areas where AOM occurs (*5*), and the highest AOM rates in marine sediment do not always correlate with the highest sulfate reduction rates (*6*). Furthermore, sediments of the uplifted Franciscan Complex, a paleo-analog of the Eel River Basin (ERB), show methane-derived ^{13}C-depleted carbonate associated with rhodocrosite ($MnCO_3$) (*7*). In addition, there is enrichment of manganese and other metals in methane seep–associated carbonates from the Black Sea (*8*).

Here, we show that birnessite (Fig. 1) and ferrihydrite (Fig. 2) can be used as electron acceptors in marine AOM. Large amounts of manganese [~19 Tg/year (*9*)] and iron [~730 Tg/year (*10*)] are provided to continental margins from rivers (*11*). Iron and manganese are provided to the ERB in this manner by high sediment discharge from the Eel River, which drains the northern California Coast Range (*12*). If the entire global flux of manganese and iron is used to oxidize methane, it could account for about one-fourth of present-day AOM consumption. Even if only a small percentage of the influx of manganese and iron is used for AOM, it still has the potential to be a large methane sink because both manganese and iron can be oxidized and reduced 100 to 300 times before burial (*13*).

Methane-seep sediment from the ERB was incubated with methane, ^{13}C-labeled methane, CO_2, and artificial sulfate-free seawater. Triplicate incubations were given either sulfate, birnessite, ferric oxyhydroxide, ferrihydrite, nitrate, nitrate and sulfate, or no electron acceptor (live control). The birnessite and ferrihydrite experiments were pre-incubated (*14*) to ensure that they were sulfate free. As methane is oxidized, the ^{13}C-label is transferred from methane to CO_2, and thus we can monitor AOM by measuring the ^{13}C enrichment in the CO_2 throughout the experiment. $\delta^{13}CO_2$ values are then converted into the amount of methane oxidized (*15*, *16*).

We measured ^{13}C-enrichment of CO_2 in cultures supplied with sulfate, birnessite, and ferrihydrite, indicating that AOM can proceed in the absence of sulfate if birnessite (Fig. 1) or ferrihydrite (Fig. 2) is present (*17*). Sulfate was measured (SulfaVer4 method; Hach, Loveland, CO) periodically in all live control, birnessite, and ferrihydrite incubations to show that they remained sulfate free (<30 μM sulfate) for the duration of the experiment. An autoclaved bottle (Figs. 1 and 2), containing either birnessite or ferrihydrite, shows that no abiotic isotopic exchange between methane and CO_2 and no abiotic production of sulfate occurs. Incubations with just nitrate, as well as with nitrate and sulfate, appear to inhibit AOM (fig. S1). We also see no evidence for AOM in the presence of ferric oxyhydroxide (fig. S1).

The net reaction for the AOM is often framed as

$$CH_4 + SO_4^{2-} \rightarrow HCO_3^- + HS^- + H_2O \quad (1)$$

AOM with sulfate (Eq. 1) provides organisms with a potential Gibbs free energy of $\Delta G = -14$ kJ/mole for our in situ conditions. All of the sulfate incubations reported here oxidize methane at an approximate rate of 52 μmole/year/cm^3_{sed} (Fig. 1), corresponding to a potential energy gain of 0.7 J/year/cm^3_{sed} (Table 1). However, the oxidation of methane with birnessite (simplified to MnO_2) yields $\Delta G = -556$ kJ/mole at our in situ conditions (Eq. 2).

$$CH_4 + 4MnO_2 + 7H^+ \rightarrow HCO_3^- + 4Mn^{2+} + 5H_2O \quad (2)$$

The observed rate of birnessite-dependent AOM is 14 μmole/year/cm^3_{sed} (Fig. 1), which equals a potential energy gain of 7.8 J/year/cm^3_{sed} (Table 1). Therefore, although the rate of sulfate-dependent AOM is about four times as fast as birnessite-dependent AOM, the birnessite incubations have the potential to gain 10 times as much energy as the sulfate incubations.

[1]Department of Geosciences and Penn State Astrobiology Research Center, The Pennsylvania State University, University Park, PA 16802, USA. [2]Division of Geological and Planetary Sciences, Caltech, Pasadena, CA 91125, USA.

*To whom correspondence should be addressed. E-mail: ejbeal@gmail.com (E.J.B.); chrishouse@psu.edu (C.H.H.)

AOM coupled to ferrihydrite [simplified as $Fe(OH)_3$] reduction (Eq. 3) yields a potential free energy of $\Delta G = -270.3$ kJ/mol at our in situ conditions.

$$CH_4 + 8\,Fe(OH)_3 + 15H^+ \rightarrow HCO_3^- + 8Fe^{2+} + 21H_20 \quad (3)$$

The incubations with ferrihydrite oxidize methane at an average rate of 6 μmole/year/cm^3_{sed} (Fig. 2), corresponding to a potential energy gain of 1.6 J/year/cm^3_{sed} (Table 1). This shows that the microorganisms responsible for ferrihydrite-dependent AOM have the potential to receive energy at about twice the rate of sulfate-dependent AOM, despite the fact that they are oxidizing methane at about one-tenth the rate.

Previous culture studies have found that microorganisms from the Black Sea can reduce manganese oxides more efficiently than ferrihydrite (*18*). This result is consistent with our experiment, where we see that manganese-dependent AOM occurs at a faster rate than iron-dependent AOM. Both manganese- and iron-dependent AOM occur at much slower rates than sulfate-dependent AOM, although they are substantially more energetically favorable. This can be explained by considering that manganese and iron oxides are both solids, and thus less accessible than sulfate. Despite the slower methane oxidation rates of manganese and iron-dependent AOM, it is likely that they are an important part of biogeochemical methane cycling.

There are three known archaeal groups responsible for AOM: ANME-1 and ANME-2 (*19*) and ANME-3 (*20*). ANME commonly have sulfate-reducing bacterial partners, often related to *Desulfosarcinales* and *Desulfobulbus* (*21*–*24*). However, ANME-1 and some ANME-2 have been found to live independently, suggesting that they may not need a physically associated sulfate-reducing bacteria to perform AOM (*19*, *22*). The fact that ANME are often found with sulfate reducers does not necessitate that sulfate is needed for AOM to proceed. Some sulfate-reducing bacteria can facultatively use electron acceptors other than sulfate (*25*–*27*). In fact, one species of *Desulfobulbus* is capable of iron reduction (*28*). The presence of greigite magnetosomes in sulfate-reducing bacteria associated with ANME-2 from the Black Sea further suggests a role in iron cycling (*8*, *29*).

To study the microbial communities responsible for manganese-dependent AOM, we sampled one incubation from each set of conditions at the end of the experiment and determined changes in the microbial assemblage based on 16S rRNA and methyl coenzyme M reductase (*mcr*A) gene diversity. Over the course of the 10-month incubation (*14*), a shift was observed in the archaeal diversity relative to the starting sediment. The proportion of phylotypes associated with the crenarchaeota increased in both the manganese incubation and the live control (sulfate-free, no added electron acceptor), whereas the sulfate incubation supported an increase in euryarchaeota, in particular phylotypes belonging to ANME 2b and 2c (fig. S2). Uncultured phylotypes belonging to Marine Benthic Group D (MBGD) were the most abundant in the starting sediment and remained a substantial component of the archaeal diversity in all treatments, representing 35% or more of the total clones (fig. S2). The metabolic potential of MBGD is not currently known; however, it is interesting to note that the closest cultured relatives of many of the recovered phylotypes are methanogens (80% identity), and their potential role in methane cycling warrants further investigation. An increase in phylotypes associated with the Crenarchaeota Marine Benthic Group C (MBGC), which is absent in the sulfate incubations, was observed in both the manganese and live control incubations (fig. S2).

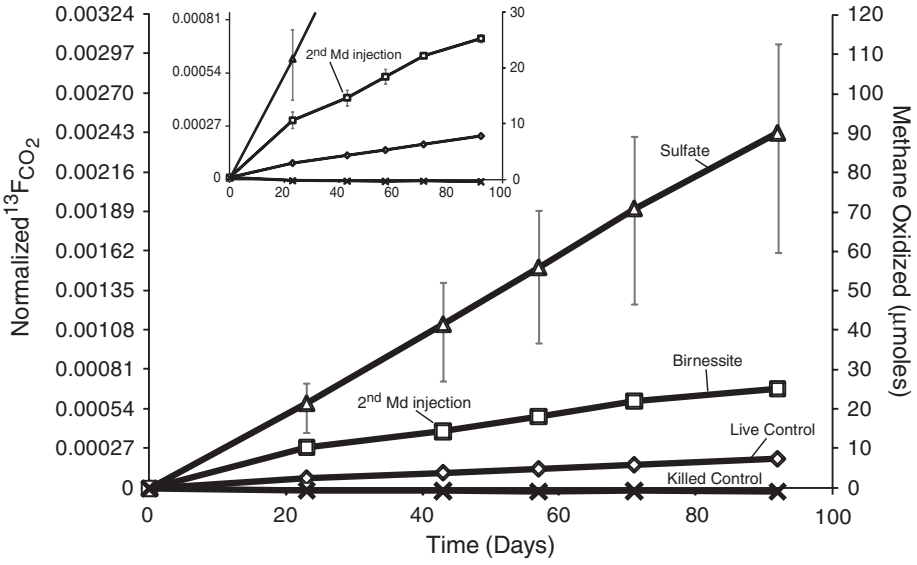

Fig. 1. ^{13}C enrichment of CO_2 reported in $^{13}F_{CO2}$ ($^{13}C/^{13}C+^{12}C$) values and converted to moles methane oxidized. The incubations with manganese (birnessite) oxidize about 3.5 times as much methane as the live control (sulfate free, no provided electron acceptor), indicating that manganese can be used as an electron acceptor in AOM. Error bars represent the range of the triplicate incubations. The standard deviations of the triplicate incubations for the birnessite and live controls are within the symbol for each data point. In addition, when more birnessite is injected into the cultures, the rate of AOM increases ~30%, from ~11 μmole/year/cm^3_{sed} (days 23 to 43) to ~14 μmole/year/cm^3_{sed} (days 43 to 57).

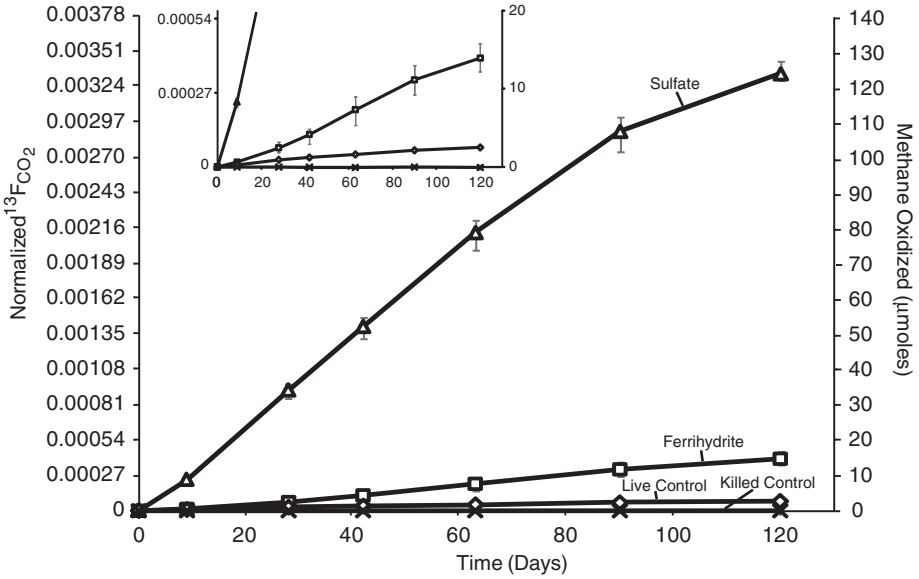

Fig. 2. ^{13}C enrichment of CO_2 reported in $^{13}F_{CO2}$ ($^{13}C/^{13}C+^{12}C$) values and converted moles methane oxidized. The incubations with iron (ferrihydrite) oxidize about 5 times as much methane as the live control (sulfate free, no provided electron acceptor), indicating that iron can be used as an electron acceptor in AOM. Error bars represent the range of data from the triplicate incubations. The standard deviations of the triplicate incubations for the ferrihydrite and live controls are within the symbol for each data point.

16S rRNA phylotypes belonging to the known methanotrophic ANME groups made up a relatively small proportion of all sediment incubations, with ANME-1 representing no more than 5% of the total archaeal diversity. However, analysis of the *mcr*A gene (specific for methanogens and methanotrophic archaea) indicated a greater diversity of the methanotrophic ANME than was recovered by the initial 16S rRNA screen. Specifically, with the exception of the sulfate incubations, the most common *mcr*A gene came from the ANME-1 (~85%) (fig. S2). In the sulfate incubations, ANME-1 represented 42% of the recovered *mcr*A genes, with ANME-2 representing 46%. The manganese and sulfate incubations revealed an increase in diversity supporting a small percentage of ANME-3, not observed in the original sediment or live control (fig. S2).

About 40% of the bacteria found in the birnessite incubation are possible manganese reducers (Fig. 3 and fig. S3). These include clones related to microorganisms found in heavy-metal contaminated sites or from hydrothermal systems. Specifically, the groups Bacteriodes, Proteobacteria (including *Geobacter*), Acidobacteria, and Verrucomicrobia contain representatives likely capable of metal reduction (Fig. 3) (*30*–*33*). Bacteriodes are only present in the manganese and control incubations, whereas Acidobacteria are only present in the manganese incubations (Fig. 3). The clones related to sulfur cycling in the birnessite incubations are almost all sulfur oxidizers, such as the ε-Proteobacteria *Sulfurovumales*. The bacteria in the sulfate incubations are dominated by sulfate reducers, mainly *Desulfobulbus*.

The large change toward manganese reducers observed in the bacterial community from the birnessite incubation suggests that bacteria are playing a vital role in manganese-dependent AOM and that archaea are not solely responsible (Fig. 3). In the birnessite incubation, the relative proportion of ANME-2 decreases, whereas Methanococcoides/ANME-3 increases and ANME-1 stays relatively constant (fig. S2). Overall, our data imply either that manganese-dependent AOM is carried out by ANME-1 and/or Methanococcoides/ANME-3 with a bacterial partner, or that manganese-dependent AOM in this case is not performed by archaea but rather solely by bacteria. If bacteria are indeed solely responsible for manganese-dependent AOM, it is likely that they do not contain the *mcr*A gene, as recently observed for nitrite-dependent AOM (*1*).

Abiotic and biotic processes can oxidize sulfide to sulfur in the presence of metal oxides (*34*, *35*). In principle, sulfur disproportionation producing transient sulfate, mediated perhaps by

Table 1. Rates and potential energy gain from AOM with different electron acceptors.

Reaction	Rate (μmole/year/cm$^3_{sed}$)	Potential energy gain (J/year/cm$^3_{sed}$)
$SO_4^{2-} + CH_4 \rightarrow HCO_3^- + HS^- + H_2O$	52	0.7
$CH_4 + 4MnO_2 + 7H^+ \rightarrow HCO_3^- + 4Mn^{2+} + 5H_2O$	14	7.8
$CH_4 + 8\ Fe(OH)_3 + 15H^+ \rightarrow HCO_3^- + 8Fe^{2+} + 21H_2O$	6	1.6

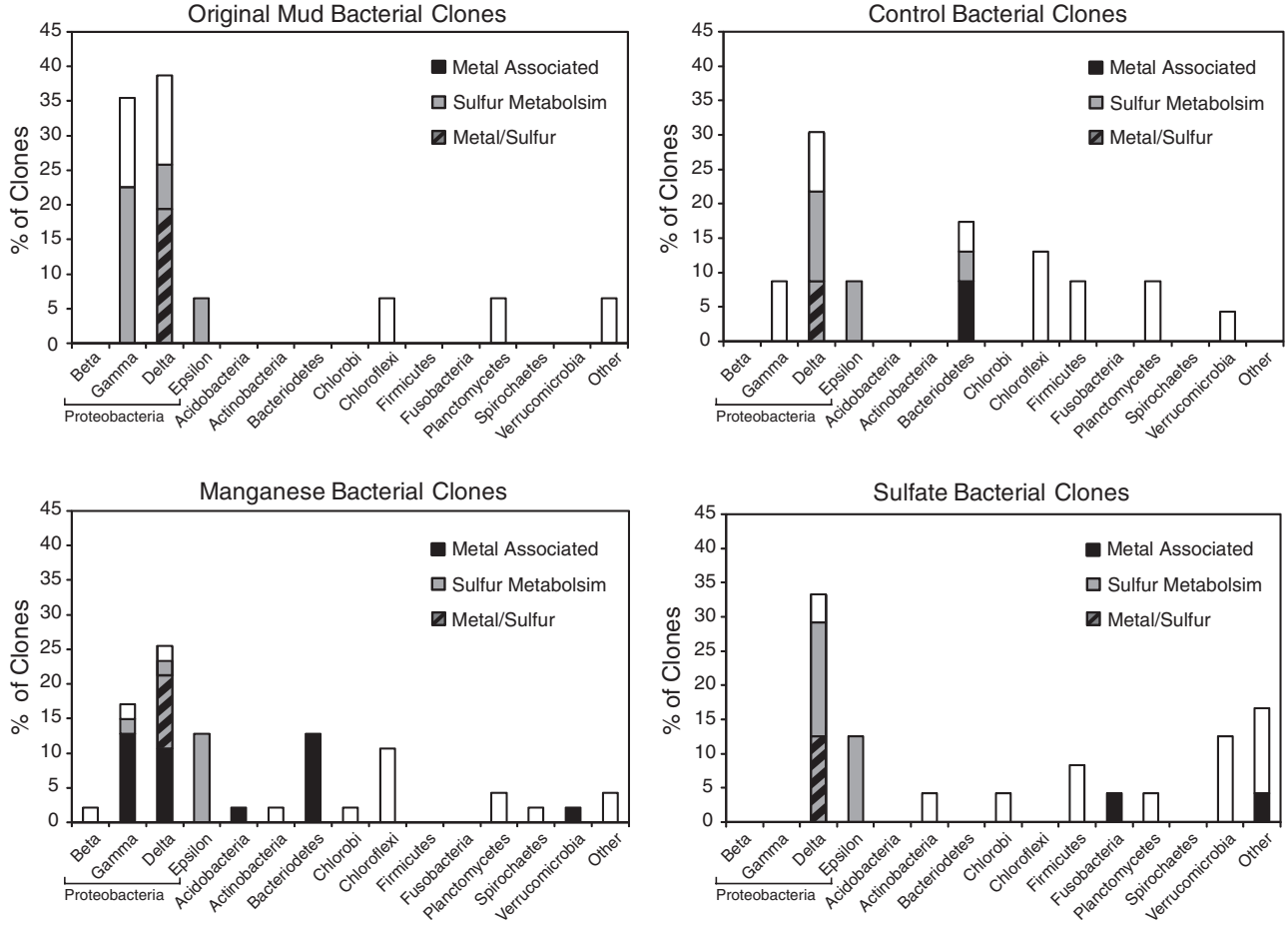

Fig. 3. Percent distribution of recovered bacterial clones based on 16S rRNA genes in the starting sediment (Other includes clades OP3 and Marine Group A), live control, manganese (Other includes clades Elusimicrobia and KSB3), and sulfate incubations (Other includes clades Marine Group A, KSB3, GN02, and TM6). Sulfur metabolism indicates phylotypes putatively involved in sulfur cycling. Metal associated represent phylotypes that are possible manganese reducers. Metal/Sulfur are the phylotypes that have the potential to partake in sulfur and/or metal cycling. The starting sediment was stored anaerobically for ~1 year before use and therefore does not reflect the proportions of bacteria when it was sampled.

Desulfobulbus (*36*) or ε-Proteobacteria, could be the underlying process observed, indirectly linking AOM to metal reduction. Although the shift in the bacterial community from known sulfate-reducing bacteria to putative metal-reducing microorganisms in the birnessite incubations supports the idea that the AOM is directly linked to metal reduction, the observed shift in microbial community could also be a result of the stimulation of heterotrophic metal reduction. If metal reduction is indirectly linked to AOM in marine sediments, then the realized energy gain for the microorganisms directly catalyzing AOM would be much lower than that suggested in Table 1. Regardless of mechanism, the stimulation of AOM with Mn and Fe has important implications for capacity of CH_4 oxidation.

It is estimated that AOM consumes most methane released in marine settings, equaling 5 to 20% of today's total global methane flux (*37*), making this process an important part of the global carbon cycle today. However, before Earth became oxygenated, growth of methanotrophs was limited by their ability to find electron acceptors. Based on the column-integrated photooxidation rates of 5 mg/cm^2/year of manganese and 200 mg/cm^2/year of iron (*38*), on the order of 10,000 Tg/year of methane could be oxidized during this time period by manganese- and iron-dependent AOM, irrespective of whether the processes directly link metal reduction to methane oxidation. Estimates of the methane flux to the atmosphere during the Proterozoic are on the order of 1,000 to 10,000 Tg/year (*39*), meaning that manganese- and iron-dependent AOM had the oxidative potential to oxidize the entire early Earth methane flux. Thus, manganese- and iron-dependent AOM could have been extremely important methane sinks, as well as energy sources, for the early biosphere.

References and Notes

1. K. F. Ettwig *et al.*, *Environ. Microbiol.* **10**, 3164 (2008).
2. A. Raghoebarsing *et al.*, *Nature* **440**, 918 (2006).
3. A. J. B. Zehnder, T. D. Brock, *Appl. Environ. Microbiol.* **39**, 194 (1980).
4. K. Nauhaus, T. Treude, A. A. Boetius, M. Krüger, *Environ. Microbiol.* **7**, 98 (2005).
5. S. D'Hondt *et al.*, *Science* **306**, 2216 (2004).
6. S. B. Joye *et al.*, *Chem. Geol.* **205**, 219 (2004).
7. J. R. Hein, R. A. Koski, *Geology* **15**, 722 (1987).
8. J. Reitner, J. Peckmann, A. Reimer, G. Schumann, V. Thiel, *Facies* **51**, 66 (2005).
9. S. W. Poulton, R. Raiswell, *Mar. Chem.* **72**, 17 (2000).
10. J.-M. Martin, M. Meybeck, *Mar. Chem.* **7**, 173 (1979).
11. There are minor contributions of manganese and iron from hydrothermal systems and aeolian input. See SOM text for further discussion.
12. R. A. Wheatcroft, C. K. Sommerfield, D. E. Drake, J. C. Borgeld, C. A. Nittrouer, *Geology* **25**, 163 (1997).
13. D. E. Canfield, B. Thamdrup, J. W. Hansen, *Geochim. Cosmochim. Acta* **57**, 3867 (1993).
14. Materials and methods are available as supporting material on *Science* Online.
15. J. J. Moran, C. H. House, K. H. Freeman, J. G. Ferry, *Archaea* **1**, 303 (2005).
16. J. J. Moran, C. H. House, B. Thomas, K. H. Freeman, *J. Geophys. Res.* **112**, G02011 (2007).
17. See relevant SOM text for discussion regarding dissolved manganese and iron concentrations.
18. B. Thamdrup, R. Rosselló-Mora, R. Amann, *Appl. Environ. Microbiol.* **66**, 2888 (2000).
19. V. J. Orphan, C. H. House, K. U. Hinrichs, K. D. McKeegen, E. F. DeLong, *Science* **293**, 484 (2001).
20. K. Knittel, T. Loesekann, A. Boetius, R. Kort, R. Amann, *Appl. Environ. Microbiol.* **71**, 467 (2005).
21. V. J. Orphan *et al.*, *Appl. Environ. Microbiol.* **67**, 1922 (2001).
22. V. J. Orphan, C. H. House, K.-U. Hinrichs, K. D. McKeegan, E. F. DeLong, *Proc. Natl. Acad. Sci. U.S.A.* **99**, 7663 (2002).
23. H. Niemann *et al.*, *Nature* **443**, 854 (2006).
24. A. Pernthaler *et al.*, *Proc. Natl. Acad. Sci. U.S.A.* **105**, 7052 (2008).
25. K. H. Nealson, D. Saffarini, *Annu. Rev. Microbiol.* **48**, 311 (1994).
26. B. M. Tebo, A. Y. Obraztsova, *FEMS Microbiol. Lett.* **162**, 193 (1998).
27. M. L. Coleman, D. B. Hedrick, D. R. Lovley, D. C. White, K. Pye, *Nature* **361**, 436 (1993).
28. D. E. Holmes *et al.*, *Microb. Ecol.* **48**, 178 (2004).
29. J. Reitner *et al.*, *Palaeogeogr. Palaeoclimatol. Palaeoecol.* **227**, 18 (2005).
30. D. C. Gillan, P. Pernet, *Biofouling* **23**, 1 (2007).
31. F. Gremion, A. Chatzinotas, H. Harms, *Environ. Microbiol.* **5**, 896 (2003).
32. R. J. Ellis, P. Morgan, A. J. Wheightman, J. C. Fry, *Appl. Environ. Microbiol.* **69**, 3223 (2003).
33. J. He, *Geomicrobiol. J.* **25**, 14 (2008).
34. R. C. Aller, P. D. Rude, *Geochim. Cosmochim. Acta* **52**, 751 (1988).
35. D. J. Burdige, K. H. Nealson, *Geomicrobiol. J.* **4**, 361 (1986).
36. D. R. Lovley, E. J. P. Phillips, *Appl. Environ. Microbiol.* **60**, 2394 (1994).
37. D. L. Valentine, W. S. Reeburgh, *Environ. Microbiol.* **2**, 477 (2000).
38. A. D. Anbar, H. D. Holland, *Geochim. Cosmochim. Acta* **56**, 2595 (1992).
39. A. A. Pavlov, M. T. Hurtgen, J. F. Kasting, M. A. Arthur, *Geology* **31**, 87 (2003).

40. We would like to thank M. Arthur for the use of his mass spectrometer, Z. Zhang and S. Goffredi for laboratory assistance, D. Walizer for technical assistance, and D. Jones for help with phylogenetics. We also thank the shipboard scientists, crew, and pilots of R/V *Atlantis* and R/V *Western Flyer*. Funding for this project has come from the National Science Foundation (MCB-0348492), National Aeronautics and Space Administration (NASA) Astrobiology Institute under NASA-Ames Cooperative Agreement NNA04CC06A, and the Penn State Biogeochemical Research Initiative for Education (BRIE) funded by NSF (IGERT) grant DGE-9972759. Sequences were submitted to GenBank and have accession numbers FJ264513 to FJ264602 and FJ264604 to FJ264884.

Supporting Online Material

www.sciencemag.org/cgi/content/full/325/5937/184/DC1
Materials and Methods
SOM Text
Figs. S1 to S3
References

18 December 2008; accepted 2 June 2009
10.1126/science.1169984

Consistency Between Satellite-Derived and Modeled Estimates of the Direct Aerosol Effect

Gunnar Myhre

In the Intergovernmental Panel on Climate Change Fourth Assessment Report, the direct aerosol effect is reported to have a radiative forcing estimate of –0.5 watt per square meter (W m^{-2}), offsetting the warming from CO_2 by almost one-third. The uncertainty, however, ranges from –0.9 to –0.1 W m^{-2}, which is largely due to differences between estimates from global aerosol models and observation-based estimates, with the latter tending to have stronger (more negative) radiative forcing. This study demonstrates consistency between a global aerosol model and adjustment to an observation-based method, producing a global and annual mean radiative forcing that is weaker than –0.5 W m^{-2}, with a best estimate of –0.3 W m^{-2}. The physical explanation for the earlier discrepancy is that the relative increase in anthropogenic black carbon (absorbing aerosols) is much larger than the overall increase in the anthropogenic abundance of aerosols.

The complex influence of atmospheric aerosols on the climate system and the influence of humans on aerosols are among the key uncertainties in the understanding of current climate change (*1*–*3*). The direct aerosol effect may have contributed to a cooling in the mid 20th century (*4*) and may have masked a considerable degree of current global warming (*5*), potentially leading to more rapid warming in the future because of stricter controls on aerosol emissions (*5*). In addition, the direct aerosol effect is probably responsible for a substantial part of the observed dimming and the later reversal to brightening (*6*) at many locations. The direct aerosol effect includes both scattering and absorption of solar light, and evaluating its magnitude is complicated by the fact that some atmospheric aerosols are predominately scattering, whereas others are mainly absorbing. The main anthropogenic scattering components are sulfate, nitrate, and organic carbon (OC), whereas black carbon (BC) absorbs solar radiation.

Previously, two approaches have been employed in the calculation of the total direct aerosol effect. The first approach uses global aerosol models to simulate the change in the aerosol abundance that is attributable to human activities and radiative transfer models to calculate the radiative forcing on the basis of simulations for pre-

Center for International Climate and Environmental Research–Oslo (CICERO), Post Office Box 1129 Blindern, N-0318 Oslo, Norway. E-mail: gunnar.myhre@cicero.uio.no

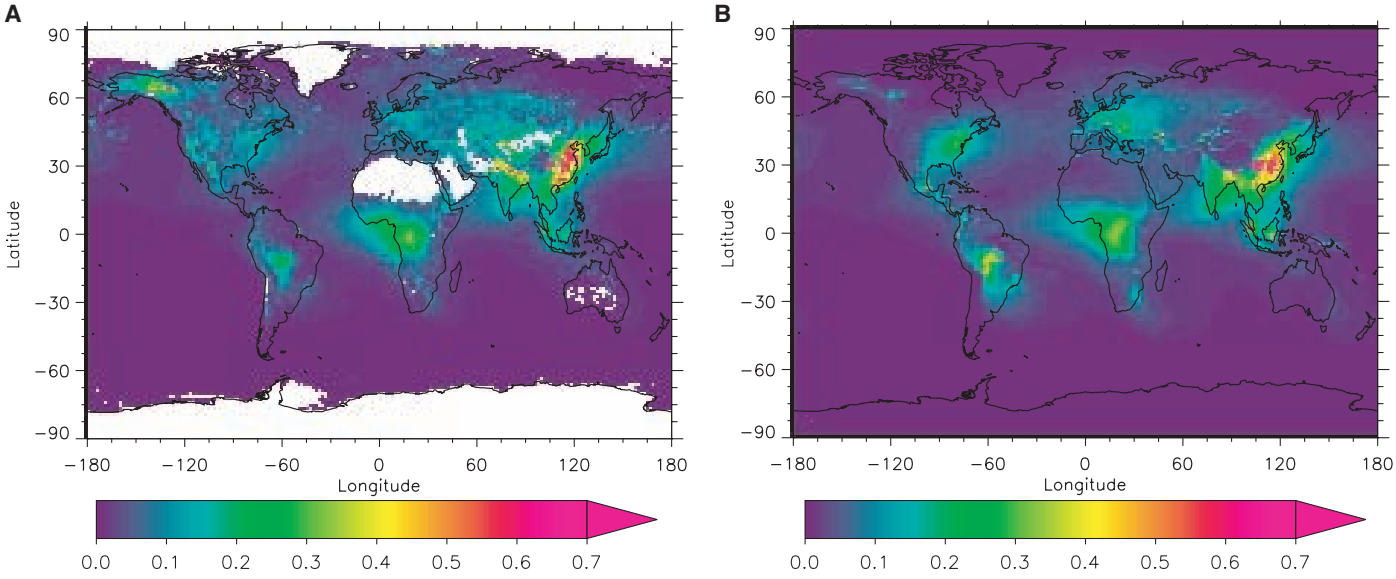

Fig. 1. Annual mean anthropogenic AOD from (**A**) the observation-based method and (**B**) the global aerosol model Oslo CTM2. The anthropogenic AOD in the observation-based method is derived from the total AOD from MODIS (shown for MODIS onboard Aqua) combined with the anthropogenic fraction of all types of aerosols from Oslo CTM2. Regions with missing MODIS data because of bright surfaces are shown in white. The aerosol species included in the derivation of modeled anthropogenic AOD are sulfate, nitrate, BC, and OC (primary and secondary).

industrial and present time (*7*). It has been known for some time that aerosol optical properties (especially the single scattering albedo) and the location of aerosols in relation to clouds strongly affect the radiative forcing of the direct aerosol effect (*8*–*11*). In the second approach, observational data have been used with some minor inputs from global aerosol models (*12*–*15*). The observation-based method has used satellite data of aerosol optical depth (AOD) in combination with either aerosol optical properties from ground-based sunphotometers from AERONET (Aerosol Robotic Network) (*12*, *16*) or observation-derived aerosol radiative efficiency (*14*, *15*). In the observation-based method, satellite retrieval constraints over land necessitate the use of information from global aerosol models in order to derive the change in AOD that is due to anthropogenic activity. The aerosol optical properties (in this respect, single scattering albedo and asymmetry factor) have been held constant between preindustrial and present time, and radiative forcing calculations have been performed with radiative transfer schemes (*12*, *16*) or the aerosol radiative efficiency has been assumed to be constant over the industrial era (*14*, *15*).

Recent analysis performed with the observation-based method by use of updated AODs from new satellite-retrieved MODIS (Moderate Resolution Imaging Spectroradiometer) data (collection 5 rather than collection 4) show a weakened radiative forcing, from –0.8 to –0.65 W m^{-2}. In addition, differences in observational coverage and the assumption that no anthropogenic aerosol existed before industrial times [defined as before 1750 (*1*)] could also explain some of the difference between a global aerosol model and the observational method (*16*). In the observation-based method of Bellouin *et al.* (*12*, *16*), it is also assumed that there is no radiative effect of the aerosols within cloudy-sky areas, whereas models diagnose differing signs and magnitudes of the cloudy-sky radiative forcing (*7*). Although the study of Bellouin *et al.* (*16*) contributes to an improved understanding of differences between model- and observation-based estimates of the direct aerosol effect, large differences remain and obstruct a better quantification of this important effect counteracting global warming.

In this study, I used both the estimates from a global aerosol model and from an observation-

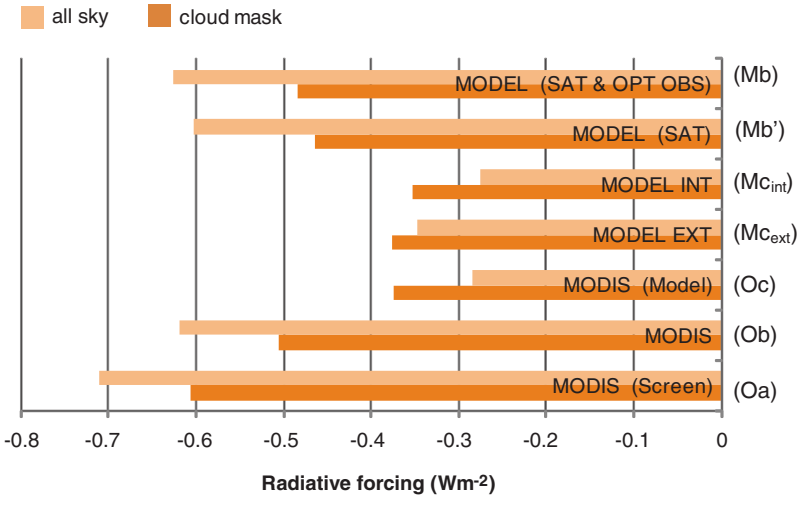

Fig. 2. Global and annual mean radiative forcing of the direct aerosol effect for observation-based method (O) and the global aerosol model Oslo CTM2 (M). The results for cloud mask do not take into account radiative effects of aerosols in cloudy regions, whereas all sky takes into account the direct aerosol effect both in cloudy and clear-sky conditions. The results denoted MODIS are from the observation-based method as described in (*21*). All the results for MODIS represent the mean of two calculations with satellite data from MODIS onboard Aqua and Terra. MODIS (Screen) (Oa) do not take into account the direct aerosol effect in regions of missing MODIS data, whereas MODIS (Ob) uses model information in regions with missing MODIS data. MODIS (Model) (Oc) uses modeled aerosol optical properties and its anthropogenic change. The model versions MODEL EXT (Mc_{ext}) and MODEL INT (Mc_{int}) represents two versions of the model, one with BC externally mixed and the other with hydrophilic BC internally mixed, respectively (*21*). MODEL (SAT) (Mb') use the observation-based approach with constant aerosol optical properties; otherwise, it is the same as MODEL Mc_{int}. MODEL (SAT & OBS OPT) (Mb) is the same as in the previous case, except that observed aerosol optical properties are used.

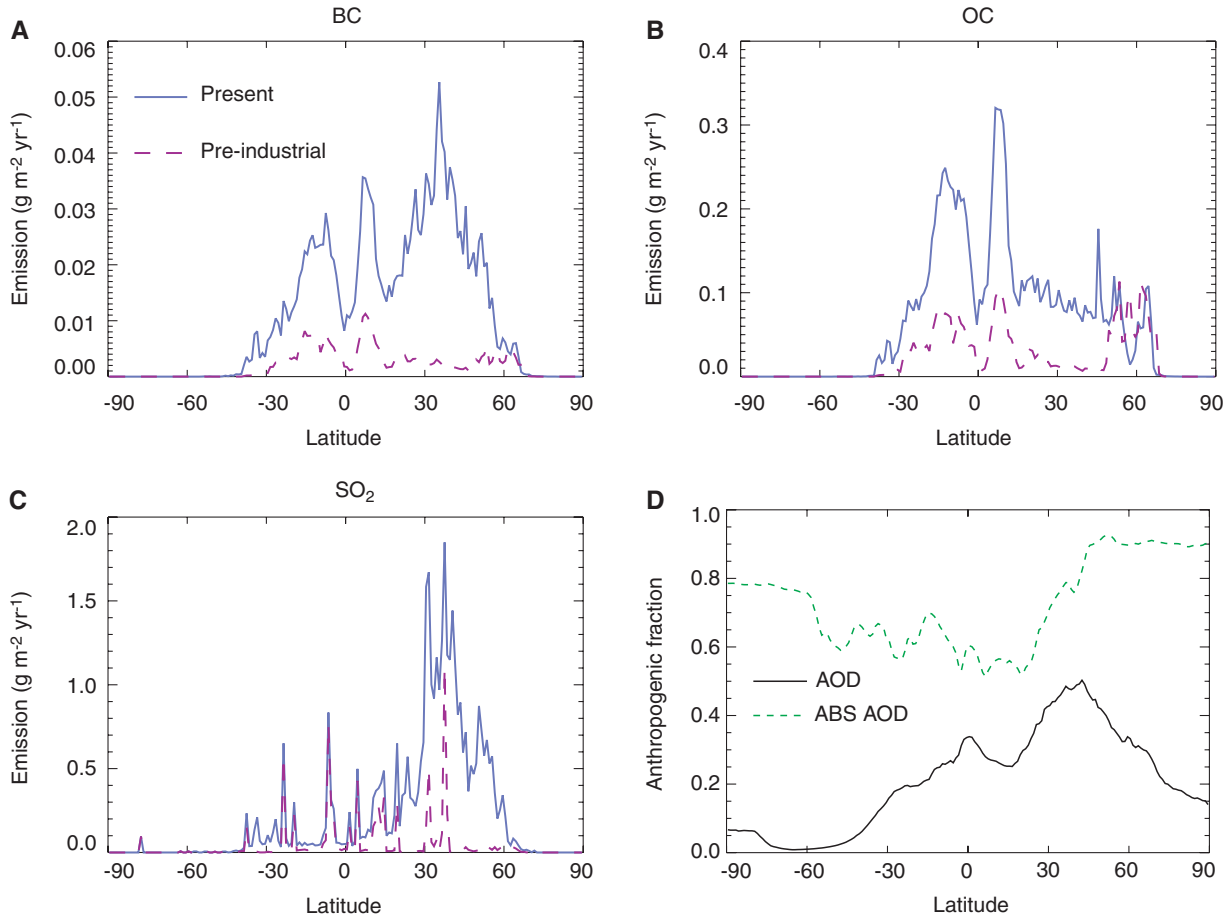

Fig. 3. Present time and preindustrial emissions of (**A**) BC, (**B**) primary OC, (**C**) SO_2, and (**D**) anthropogenic fraction of AOD (550 nm) and absorption AOD (ABS AOD) (550 nm). The anthropogenic fraction is shown as the ratio of the difference in AOD between 1750 and 2004 due to anthropogenic activity, to the total AOD (anthropogenic and natural).

Table 1. Radiative forcing (W m^{-2}) for the experiments shown in Fig. 2 and explained in the Fig. 2 caption for cloud mask and all sky.

	Cloud mask (W m^{-2})	All sky (W m^{-2})
MODEL (SAT & OPT OBS)	−0.48	−0.63
MODEL (SAT)	−0.46	−0.60
MODEL INT	−0.35	−0.28
MODEL EXT	−0.38	−0.35
MODIS (Model)	−0.37	−0.28
MODIS	−0.51	−0.62
MODIS (Screen)	−0.61	−0.71

based method in order to achieve consistency between these two methods, an important step toward quantification of the direct aerosol effect with the use of two independent approaches. The global aerosol model Oslo CTM2 is a state-of-the-art model that includes all the main atmospheric aerosol components (*17*, *18*). The observation-based method is based on satellite-retrieved AOD from MODIS (*19*) and aerosol optical properties from AERONET (*20*, *21*). Figure 1 shows that the anthropogenic AOD is quite similar in the observation-based method and the Oslo CTM2 model, with some regional differences. The standard MODIS aerosol retrieval is unable to retrieve data over surfaces with high reflectance. In Fig. 1, this can be seen over desert areas and snow- and ice-covered regions. The global and annual mean anthropogenic AOD is quite similar in the two approaches (*21*).

Because of the importance of clouds in the calculations of the direct aerosol effect, the radiative forcing is calculated for two cases: "cloud mask," in which the aerosol direct effect is assumed to be zero in the cloudy regions, such as in recent observation-based estimates (*12*, *16*), and "all sky," in which the radiative forcing in clear and cloudy regions is taken into account. The latter case is used as the radiative forcing in (*1*) so as to maintain consistency with the radiative forcing calculated for other forcing mechanisms. The radiative forcing is calculated as the change in the solar irradiance at the top of the atmosphere. Figure 2 and Table 1 show radiative forcing from the observation-based method (O indicates the observational estimates) and the model (M indicates the model estimates) for the cloud-mask and all-sky cases for the simulations (a) to (c), as described below. Using modeled aerosol fields in regions where MODIS is not able to retrieve aerosol information reduces the observational estimate of the cloud-mask forcing from ~–0.6 W m^{-2} (Oa) to –0.5 W m^{-2} (Ob). Furthermore, changing the preindustrial aerosol optical properties in the observation-based method so that they match the less absorbing preindustrial aerosols from the model (*21*) reduces the cloud-mask forcing to slightly weaker than –0.4 W m^{-2} (Oc). Thus, the observation-based method provides cloud-masked results (Oc) that are now statistically indistinguishable from the model results (Mc_{ext} and Mc_{int}).

Given the modeling framework, it is possible to also relax the modeling assumptions to those used in the observational methodology. Fixing the model aerosol optical properties for preindustrial

simulation to those modeled for the present time (Mb′) provides results for cloud-masked forcing that are very similar to the observation-based results (Ob). The final model simulation (Mb) uses aerosol optical properties for both present and preindustrial times that are fixed to those of the observations, and the results (Mb) are statistically indistinguishable from those from observations (Ob). Thus, it is here demonstrated that the differences in the cloud-masked forcing between the model and the observation-based method can be reconciled by including aerosols in regions without MODIS retrievals and including change in the aerosol optical properties from preindustrial to present time.

When considering all-sky simulations, the observation-based (Oa) and model-based (Mc_{ext} and Mc_{int}) data initially differed by approximately a factor of two. However, once the direct radiative forcing that was missing from satellite retrievals and the modeled change in the aerosol optical properties between preindustrial and present-day are accounted for (Oc), the results agree well with those from the model-based estimates (Mc_{ext} and Mc_{int}). Whereas the radiative forcing strengthens between the cloud-mask and all-sky cases for the observation-based results (Oa and Ob), the forcing weakens when modeled changes in the aerosol optical properties are taken into account (Oc). This is evident also in the model results, in which the model with internal mixture (Mc_{int}) has greater weakening from cloud-mask to all-sky than does the external mixing case (Mc_{ext}), in which the latter has a weaker aerosol absorption (*21*). This difference in the absorption may explain the difference in sign of the forcing in cloudy regions that varies among global aerosol models (*7*).

That aerosol optical properties, in particular the absorption, has changed so substantially between preindustrial and present times deserves some discussion. The main contributor to atmospheric aerosol absorption are BC aerosols and BC emissions, which have increased by more than a factor of six (*22*, *23*), whereas emissions of anthropogenic-influenced scattering aerosol components and their precursors have had a smaller increase with a factor of three to four (*23*). Figure 3 shows the preindustrial and present levels (representative for year 2000) of emissions of main anthropogenic aerosols and aerosol precursors. A substantial increase in the BC emission can be seen in Fig. 3, and fig. S3 shows that the increase in AOD for BC is also much stronger than for sulfate and OC. A consequence of the stronger increase in BC than other aerosol components is that the anthropogenic fraction of absorption AOD is much stronger than the increase in the anthropogenic fraction of total AOD, as shown in Fig. 3. The much stronger increase in the anthropogenic fraction of absorption AOD than total AOD will to some extent be model-dependent but will be robust because of the much stronger growth in the BC emissions than the growth in the rest of the aerosols and their precursors. This suggests that the global annual average single scattering albedo of the aerosols has been reduced because of human activity (*18*). The global mean annual average single scattering albedo computed in the model for all aerosols at 0.55 μm is 0.986 at preindustrial conditions and 0.970 at present-day conditions. Thus, aerosol in present times is approximately twice as absorbing as that in preindustrial conditions.

I find that change in the aerosol optical properties due to anthropogenic activity is a main reason for the difference between observation-based and model estimates of the radiative forcing. The agreement between these two methods, when similar aerosol optical properties are used in the calculations of the direct aerosol effect, allows to a much better extent a quantification of this radiative forcing mechanism. Thus, the bottom-up approach whereby anthropogenic aerosols and their precursors are modeled via emission, transportation, and deposition so as to estimate an aerosol optical depth and a radiative forcing is now in accordance with the top-down approach, in which satellite observations of aerosol optical depths are apportioned into anthropogenic fractions in order to derive a radiative forcing. The observation-based method of Chung *et al*. (*13*) relies much more on model information than the other observation-based studies (*12*, *14*–*16*) and has an anthropogenic change in the aerosol optical properties. Their resulting radiative forcing is weaker than other observation-based results but is in close agreement with the best estimate in this study. Thus, this study not only explains differences between model-based studies and observation-based studies but also within the group of observation-based studies. Although the observational and model methods for determining the direct radiative forcing indicate very close agreement in this study, it is acknowledged that the observational method relies on the model for determining the anthropogenic fraction, whereas other studies (*12*, *16*) attempt to use independent methods over ocean areas on the basis of the fine-mode fraction reported in the MODIS retrievals.

The previous disagreement between the two methods caused a disconcerting uncertainty that undermined our confidence in estimates of the direct aerosol effect. Understanding the differences between the two independent methods substantially enhances our confidence in the estimates of the direct radiative forcing of aerosols. The results in this study also show that the anthropogenically induced changes in the aerosol optical properties causes the earlier discrepancies, rather than the assumed aerosol optical properties in either the modeling or observational studies. This conclusion can be made because the results show very similar radiative forcing for modeled and observed aerosol optical properties. With this work, the uncertainty in the radiative forcing of the direct aerosol effect is substantially reduced, and the remaining uncertainty is probably related to the vertical profile of the aerosols and their location in relation to clouds. The differences among the global aerosol models in terms of the vertical profile of the aerosols are considerable (*24*, *25*), but results in this study show that the radiative forcing of the direct effect from the observation-based method has previously been too strong, and the forcing is weaker than –0.5 W m^{-2}. The best estimate from this study (–0.3 ± 0.2 W m^{-2}) suggests that the direct aerosol effect offsets only a modest 10% of the radiative forcing that is due to increases in well-mixed greenhouse-gas concentrations at their current concentrations.

Further, radiative forcing estimates of the direct aerosol effect must, at least partly, rely on global aerosol models, and pure estimates from observational data are currently not possible.

References and Notes

1. P. Forster *et al*., in *Climate Change 2007: The Physical Science Basis—Contribution of Working Group I to the Fourth Assessment Report of the Intergovernmental Panel on Climate Change*, S. Solomon *et al.*, Eds. (Cambridge Univ. Press, New York, 2007), pp. 129–134.
2. Y. J. Kaufman, D. Tanre, O. Boucher, *Nature* **419**, 215 (2002).
3. V. Ramanathan, P. J. Crutzen, J. T. Kiehl, D. Rosenfeld, *Science* **294**, 2119 (2001).
4. G. Myhre, A. Myhre, F. Stordal, *Atmos. Environ.* **35**, 2361 (2001).
5. V. Ramanathan, Y. Feng, *Proc. Natl. Acad. Sci. U.S.A.* **105**, 14245 (2008).
6. M. Wild *et al*., *Science* **308**, 847 (2005).
7. M. Schulz *et al*., *Atmos. Chem. Phys.* **6**, 5225 (2006).
8. J. Hansen, M. Sato, R. Ruedy, *J. Geophys. Res.* **102**, 6831 (1997).
9. J. M. Haywood, K. P. Shine, *Geophys. Res. Lett.* **22**, 603 (1995).
10. J. M. Haywood, D. L. Roberts, A. Slingo, J. M. Edwards, K. P. Shine, *J. Clim.* **10**, 1562 (1997).
11. G. Myhre, F. Stordal, K. Restad, I. S. A. Isaksen, *Tellus* **50**, 463 (1998).
12. N. Bellouin, O. Boucher, J. Haywood, M. S. Reddy, *Nature* **438**, 1138 (2005).
13. C. E. Chung, V. Ramanathan, D. Kim, I. A. Podgorny, *J. Geophys. Res.* **110**, D24207 (2005).
14. H. Yu *et al*., *Atmos. Chem. Phys.* **6**, 613 (2006).
15. J. Quaas, O. Boucher, N. Bellouin, S. Kinne, *J. Geophys. Res.* **113**, D05204 (2008).
16. N. Bellouin, A. Jones, J. Haywood, S. A. Christopher, *J. Geophys. Res.* **113**, D10205 (2008).
17. G. Myhre *et al*., *Tellus* **59**, 115 (2007).
18. G. Myhre *et al*., *Atmos. Chem. Phys.* **9**, 1365 (2009).
19. L. A. Remer *et al*., *J. Geophys. Res.* **113**, D14S07 (2008).
20. B. N. Holben *et al*., *Remote Sens. Environ.* **66**, 1 (1998).
21. Materials and methods are available as supporting material on *Science* Online.
22. T. C. Bond *et al*., *J. Geophys. Res.* **109**, D14203 (2004).
23. F. Dentener *et al*., *Atmos. Chem. Phys.* **6**, 4321 (2006).
24. J. P. Schwarz *et al*., *J. Geophys. Res.* **111**, D16207 (2006).
25. C. Textor *et al*., *Atmos. Chem. Phys.* **6**, 1777 (2006).

26. I highly appreciate the comments and valuable suggestions from J. Haywood in improving the manuscript. Comments and discussions with N. Bellouin, O. Boucher, and L. Nygaard are also appreciated. M. Johnsrud provided the observational data. I thank the principal investigators and their staffs for establishing and maintaining all of the AERONET sites used in this study. I also thank the Oslo CTM group. The research has been funded by the Norwegian Research Council.

Supporting Online Material

www.sciencemag.org/cgi/content/full/1174461/DC1
Materials and Methods
Table S1
Figs. S1 to S3
References

3 April 2009; accepted 22 May 2009
Published online 18 June 2009;
10.1126/science.1174461
Include this information when citing this paper.

Nonvolcanic Tremor Evolution and the San Simeon and Parkfield, California, Earthquakes

Robert M. Nadeau and Aurélie Guilhem

Nonvolcanic tremors occur adjacent to locked faults and may be closely related to the generation of earthquakes. Monitoring of the San Andreas Fault in the Parkfield, California, region revealed that after two strong earthquakes, tremor activity increased in a nearly dormant tremor zone, increased and became periodic in a previously active zone, and has remained elevated and periodic for over 4 years. Static shear- and Coulomb-stress increases of 6 to 14 kilopascals from these two earthquakes are coincident with sudden increases in tremor rates. The persistent changes in tremor suggest that stress is now accumulating more rapidly beneath this part of the San Andreas Fault, which ruptured in the moment magnitude 7.8 Ft. Tejon earthquake of 1857.

Nonvolcanic tremors (long-duration seismic events with no clear *P* or *S* waves) have generally been observed in transition zones between freely slipping and locked faults (*1*–*8*). In many of these locations, tremor activity increased with detectable transient fault zone deformation (slow-slip events) (*2*, *8*–*10*) or with dynamic stress changes produced by solid-earth and ocean tides and the surface waves of teleseismic (distant) earthquakes (*11*–*16*). These spatial and temporal associations suggest that tremor activity is closely related to the processes responsible for generating earthquakes. To investigate this possible relation, we analyzed tremor activity in the Parkfield region of California between 27 July 2001 and 21 February 2009. During this period, this region experienced two strong earthquakes: the moment magnitude (M_w) 6.5 San Simeon earthquake in 2003 (*17*) and the M_w 6.0 Parkfield earthquake in 2004 (*18*) (Fig. 1).

Borehole seismometer data from the High Resolution Seismic Network (HRSN) at Parkfield, California, recorded continuously at 20 Hz were used to detect 2198 tremors (12,547 min of cumulative activity) during our study period (*19*) (Fig. 2A). The tremor events lasted from 3 to nearly 21 min. Substantial activity also occurred below our detection threshold (*19*). Between 3 and 8 Hz, the average seismic energy released during the tremors was typically equivalent to an ~M_w 0.5 earthquake, and energies ranged over 1.5 M_w units among tremors not coincident with earthquakes. The frequency content of the tremors (based on 250-Hz sampled data) was also typically above background levels, between 1 and 15 Hz.

Continuous data from five seismographic networks (76 stations, fig. S1) were combined to locate the tremors by means of envelope cross-correlation techniques and a migrating grid search location program (*19*) (Fig. 1). Consistent with previous spatially or temporally limited studies (*3*, *12*, *14*, *20*), ~90% of the tremors were concentrated in a zone adjacent to the locked Cholame segment of the San Andreas Fault (SAF). An additional 5 to 10% were located ~65 km to the northwest along the SAF in the vicinity of Monarch Peak near Lonoak, California. Tremors in both zones occurred at depths between ~15 and 30 km: below the seismogenic zone (the upper ~15 km of Earth's crust, where most earthquakes occur) in the ductile lower crust and at or above the Mohorovicic discontinuity in this part of California.

A sudden increase in and subsequent decay of tremor activity (aftertremors) began immediately after the 2003 San Simeon and 2004 Parkfield earthquakes (Fig. 2A and fig. S2). Cumulatively, there was 140 min of tremor activity in the 45 days preceding the San Simeon event and 312 min of activity in the 45 days after that earthquake. An even larger increase in activity followed the Parkfield event: 850 min in the 45 days after Parkfield. In addition, approximately 3 weeks before the Parkfield earthquake, an unusually strong episode of activity (foretremor) lasting ~5 days also occurred (*19*) (Fig. 2A and fig. S2). During the 5-day episode, we detected 164 min of tremor, representing an over 10-fold rate increase as compared to the 45-day pre–San Simeon period. The peak daily activity during the episode was 82 min. The largest daily peak before the foreshock episode was 43 min, occurring 98 days after the San Simeon earthquake.

The decay of tremor activity after the Parkfield event continued until mid-2006, when annual activity rates had decreased to 150% of the rate for the year preceding the San Simeon earthquake. Since mid-2006, annual rates have generally increased, reaching ~181% of the pre–San Simeon level during the final year of our analysis (Fig. 2A).

Our data also show that zones relatively devoid of detectable tremor can transition into a state of long-term elevated activity as a result of perturbations from a nearby moderately strong earthquake. For example, before the Parkfield earthquake, tremor activity in the Monarch Peak tremor zone (Fig. 1) was low (14 tremors in ~3.2 years) (Fig. 2B). However, beginning ~10 days after the Parkfield event, activity in this zone increased substantially and has continued at an elevated rate (98 tremors in ~4.4 years) (Fig. 2B). The 10-day delay may reflect an anelastic redistribution of stress in the ductile lower crust.

After the Parkfield earthquake, persistent episodes of quasiperiodic tremor emerged along the SAF that are reminiscent of episodic tremor observed in some subduction zones (Fig. 2A) (*2*, *9*). However, unlike many subduction zone tremors, where the recurrence of dominant episodes is typically 6 months or longer and is accompanied by relatively low-amplitude inter-episode activity, the SAF episodes show progressively increasing recurrence intervals ranging from ~50 days (in 2005) to ~100 days (in 2008) and are accompanied by more energetic inter-episode activity (Fig. 2A). The SAF episodes have also typically

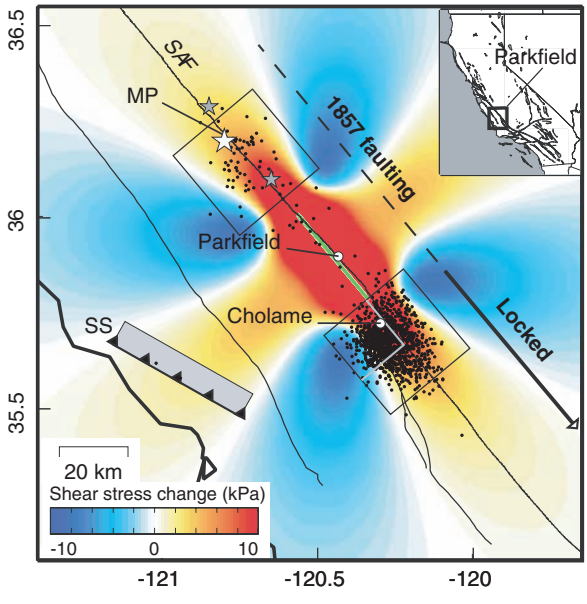

Fig. 1. Study region with 1250 well-located tremors (black dots). Thirty-kilometer-square boxes (black) define the Monarch Peak (MP) and Cholame tremor zones. Color contours give regional shear-stress change at 20 km depth from the Parkfield earthquake (green segment) along the SAF. The thrust-type San Simeon earthquake rupture is represented by the gray rectangle and line with triangles labeled SS. The currently locked Cholame segment is ~63 km long (solid portion of the arrow) and is believed capable of rupturing on its own in an ~M_w 7 earthquake. The gray lines within the Cholame box bound the west quadrant, where quasiperiodic episodes predominate. The white star indicates the epicenter and the gray stars the foreshocks of the 1857 Ft. Tejon earthquake (*30*, *31*).

Berkeley Seismological Laboratory, University of California, Berkeley, CA 94720, USA.

occurred as bursts of activity lasting ~3 to 10 days rather than 1 to 7 weeks, as is more common in subduction zones. These differences may, in part, be related to the tectonic environment or the much smaller dimensions of the SAF tremor zones.

The episodic tremors are not ubiquitous throughout the central part of the SAF. Rather, they seem to have been most persistent and regular in the western quadrant of the Cholame tremor zone, which is bounded by the SAF to the northeast and by the seismic-aseismic transition into the locked Cholame segment to the southeast (Figs. 1 and 2, B to D, and figs. S3 and S4). This localization of tremor behavior suggests that there are differences in the process generating tremor in different subregions of the SAF. It also supports the argument that tremor in the Cholame zone is distributed both normal to and along strike of the SAF at depth (figs. S3 to S5). Tremors in the Cholame zone are also spatially clustered, and >55% of the tremors are separated by ≤2 km from at least four other tremors and, in some cases, from as many as 35 other events. Precise relative locations of Cholame tremor activity with waveforms similar to those of a low-frequency earthquake showed that during a 24-hour period, the similar tremor formed a deep, near-linear, SAF-parallel structure within the Cholame zone at a depth of ~26 km (*20*). Taken together, the fault-normal distribution, clustering, and near-linear fault-parallel alignment of at least some tremor suggest that the SAF may broaden into several distinct subparallel zones as it extends into the ductile lower crust.

Static Coulomb- and shear-stress changes from the 2003 San Simeon and 2004 Parkfield earthquakes on planes aligned along the SAF at a depth of 20 km (*19*) (Fig. 1 and fig. S6) are small in the Cholame and Monarch Peak tremor zones (table S1), but both stress types increase with increases in tremor rates in the two zones. In the Cholame zone, modeled shear- and Coulomb-stress changes associated with the San Simeon earthquake are ~6 to 8 kPa, whereas those associated with the Parkfield event are ~9 to 14 kPa (table S1). In the Monarch Peak zone, shear- and Coulomb-stress changes from the San Simeon event, which failed to stimulate tremor, were negative (~ –4 to –9 kPa); however, stress changes from the Parkfield earthquake were positive (~6 to 9 kPa) and correspond to the postseismic activation in tremor activity in this zone (Fig. 2B). Static normal-stress changes from the earthquakes do not clearly correspond to the tremor rate changes in either zone (fig. S6 and table S1). This lack of correlation suggests that either normal-stress change did not play an important role in stimulating tremor or that other circumstances (such as the generally low change in normal stress as compared to that in shear stress, or offsetting signs of shear and normal stress; table S1) masked the effects of normal stress on tremor stimulation.

The static earthquake stress changes that stimulated the SAF tremors are roughly an order of magnitude smaller than those typically reported for the triggering of earthquakes (*21*). This suggests that tremors are a more sensitive indicator of stress change than are earthquakes. The small stress changes that stimulated the SAF tremor (~0.01 MPa or 1-10th of atmospheric pressure) are consistent with stress changes produced by solid-earth or ocean tides or the passage of surface waves from large teleseismic events that have stimulated tremor in subduction zones (*13*–*15*).

The periodic tremor and persistent elevated activity after the 2004 Parkfield earthquake (Fig. 2, A and B) are not consistent with expectations of exponentially decaying postseismic stress after an earthquake (*22*, *23*). It appears, therefore, that in the deep tremor zones, the SAF may have transitioned into a new state of stress and/or deformation. Models of faulting imply that steplike stress perturbations from nearby earthquakes or pore pressure changes during episodic fluid release could cause deformation styles to transition between steady-state, transient, and quasiperiodic (*7*). For such mechanisms to apply to the SAF, deep slow-slip events must be occurring and fluid pressures must be high in the tremor zones. Although deep slow slip associated with the SAF tremors has not been detected, slow-slip events with moment release equivalents as large as M_w 3 could occur in the tremor zones without being detected (*24*).

The lack of correlation between normal-stress and tremor rate changes from the San Simeon and Parkfield earthquakes may imply that effective normal stress is low and pore fluid pressure is high in the SAF zones. Recent studies of stimulation of tremor in the SAF by teleseismic events (*14*) and solid-earth tides (*16*) support this by showing that tremor rates correlate predominantly with variations in shear stress, even though normal-stress variations in some cases exceed shear-stress variations by roughly an order of magnitude (*16*). In subduction zones, the dehydration of subducting oceanic crust elevates fluid pressure (*4*). Although subduction no longer occurs along the SAF, two strong magnetic anomalies at Monarch Peak and Cholame (*25*) suggest that serpentinite bodies are present at depth, and these could be fluid sources (*26*) in the tremor zones. Alternatively, deep mantle–derived fluids might also play a role (*27*).

Because changes in SAF tremor activity have persisted for years beyond the last major quake in 2004, they could be signaling a shift in the process of deformation and stress accumulation beneath this portion of the SAF. The northwest tremor zone near Monarch Peak is an area of the SAF with anomalous structural complexity and low surface fault-creep rates (*28*). Two foreshocks (~M_w 6.1 and ~M_w 5.6) occurred in this area within 2 hours of the 1857 M_w 7.8 Ft. Tejon earthquake (*29*–*31*). Faulting from the 1857 event appears to have propagated from the Monarch Peak area southeastward along the SAF for ~350 km,

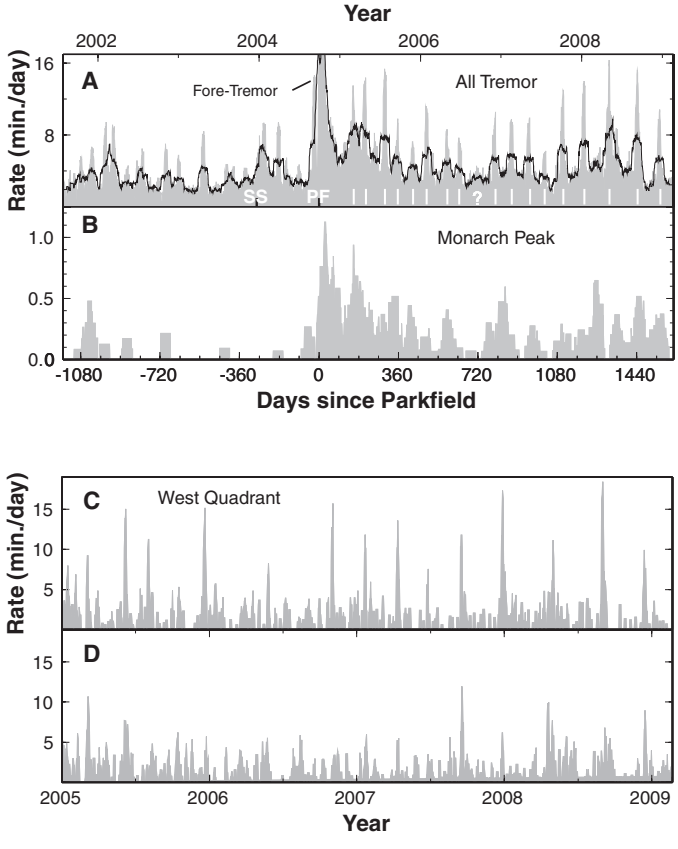

Fig. 2. Time histories of tremor activity. (**A**) Fifteen-day (gray) and 45-day (black) smoothed rate histories for all tremors in the study area. The times of the San Simeon and Parkfield earthquakes are indicated by SS and PF, respectively. Intense foretremor activity occurred ~3 weeks before PF. Fifteen- and 45-day peak values just after PF are 31.1 and 18.9 min/day, respectively. White bars are the interpreted times of quasiperiodic episodes. The question mark is the time of a weak or missing episode. (**B**) History of tremor in the Monarch Peak zone (45-day smoothed rate history). (**C**) History since 2005 of activity (5-day smoothed) in the western quadrant of the Cholame zone (Fig. 1 and figs. S3C and S4) (423 tremors; 2835 cumulative minutes of activity) showing strong episodic behavior. (**D**) Same as (C) for Cholame tremors outside the west quadrant (416 tremors; 2423 cumulative minutes), showing substantially less episodic behavior.

through Parkfield and the Cholame tremor zone (*31*) (Fig. 1). The rupture zone of the great 1857 event is composed of multiple fault segments (*32*), including the Cholame segment immediately southeast of the Cholame tremor zone. This segment is now fully locked. Its estimated mean recurrence time is between 85 and 142 years (*32*), and it last ruptured as part of the great 1857 event.

References and Notes

1. K. Obara, *Science* **296**, 1679 (2002).
2. G. Rogers, H. Dragert, *Science* **300**, 1942 (2003).
3. R. M. Nadeau, D. Dolenc, *Science* **307**, 389 (2005).
4. D. R. Shelly, G. C. Beroza, S. Ide, S. Nakamula, *Nature* **442**, 188 (2006).
5. M. R. Brudzinski, R. M. Allen, *Geology* **35**, 907 (2007).
6. S. Y. Schwartz, J. M. Rokosky, *Rev. Geophys.* **45**, RG3004 (2007).
7. Y. Liu, J. R. Rice, *J. Geophys. Res.* **112**, B09404 (2007).
8. J. S. Payero *et al.*, *Geophys. Res. Lett.* **35**, L07305 (2008).
9. H. Hirose, K. Obara, *Geophys. Res. Lett.* **33**, L17311 (2006).
10. Y. Hiramatsu, T. Watanabe, K. Obara, *Geophys. Res. Lett.* **35**, L13304 (2008).
11. M. Miyazawa, J. Mori, *Geophys. Res. Lett.* **33**, L05303 (2006).
12. J. Gomberg *et al.*, *Science* **321**, 1481 (2007); published online 22 November 2007 (10.1126/science.1149164).
13. J. L. Rubinstein, M. La Rocca, J. E. Vidale, K. C. Creager, A. G. Wech, *Science* **319**, 186 (2008); published online 22 November 2007 (10.1126/science.1150558).
14. Z. Peng *et al.*, *Geophys. Res. Lett.* **35**, L23305 (2008).
15. J. L. Rubinstein *et al.*, *J. Geophys. Res.* **114**, B00A01 (2009).
16. R. Nadeau, A. Thomas, R. Burgmann, *Eos* **89** (fall meeting suppl.), abstr. U33A-0053 (2008).
17. J. L. Hardebeck *et al.*, *Seismol. Res. Lett.* **75**, 155 (2004).
18. J. Langbein *et al.*, *Seismol. Res. Lett.* **76**, 10 (2005).
19. Materials and methods are available as supporting material on *Science* Online.
20. D. R. Shelly *et al.*, *Geophys. Res. Lett.* **36**, L01303 (2009).
21. G. C. P. King, R. S. Stein, J. Lin, *Bull. Seismol. Soc. Am.* **84**, 935 (1994).
22. J. C. Savage, J. Langbein, *J. Geophys. Res.* **113**, B10407 (2008).
23. F. Brenguier *et al.*, *Science* **321**, 1478 (2008).
24. M. J. S. Johnston, R. D. Borcherdt, A. T. Linde, M. T. Gladwin, *Bull. Seismol. Soc. Am.* **96**, S56 (2006).
25. A. Griscom, R. C. Jachens, *U.S. Geological Survey Professional Paper 1515*, R. E. Wallace, Ed. (U.S. Geological Survey, Washington, DC, 1990).
26. C. B. Raleigh, M. S. Paterson, *J. Geophys. Res.* **70**, 3965 (1965).
27. B. M. Kennedy, M. C. van Soest, *Science* **318**, 1433 (2007).
28. J. Rymer, M. Lisowski, R. O. Burford, *Bull. Seismol. Soc. Am.* **74**, 925 (1984).
29. K. Sieh, *Bull. Seismol. Soc. Am.* **68**, 1731 (1978).
30. A. J. Meltzner, D. J. Wald, *Bull. Seismol. Soc. Am.* **89**, 1109 (1999).
31. T. R. Toppozada, D. M. Branum, M. S. Reichle, C. L. Hallstrom, *Bull. Seismol. Soc. Am.* **92**, 2555 (2002).
32. Working Group on California Earthquake Probabilities, *U.S. Geol. Surv. Open File Rep. 2007-1437* (2008).

33. Supported by the U.S. Geological Survey through awards 06HQGR0167, 07HQAG0014, and 08HQGR0100, and by NSF through awards EAR-0537641 and EAR-0544730. Seismic data are archived at the Northern California Earthquake Data Center. Data processing was done at the University of California's Berkeley Seismological Laboratory. We thank R. Burgmann and D. S. Dreger for discussions. This is Berkeley Seismological Laboratory contribution 09-09.

Supporting Online Material

www.sciencemag.org/cgi/content/full/325/5937/191/DC1
Materials and Methods
Figs. S1 to S6
Table S1
References

27 March 2009; accepted 8 June 2009
10.1126/science.1174155

Evolution of the Turtle Body Plan by the Folding and Creation of New Muscle Connections

Hiroshi Nagashima,[1] Fumiaki Sugahara,[1,2] Masaki Takechi,[1] Rolf Ericsson,[1]* Yoshie Kawashima-Ohya,[1]† Yuichi Narita,[1]‡ Shigeru Kuratani[1]§

The turtle shell offers a fascinating case study of vertebrate evolution, based on the modification of a common body plan. The carapace is formed from ribs, which encapsulate the scapula; this stands in contrast to the typical amniote body plan and serves as a key to understanding turtle evolution. Comparative analyses of musculoskeletal development between the Chinese soft-shelled turtle and other amniotes revealed that initial turtle development conforms to the amniote pattern; however, during embryogenesis, lateral rib growth results in a shift of elements. In addition, some limb muscles establish new turtle-specific attachments associated with carapace formation. We propose that the evolutionary origin of the turtle body plan results from heterotopy based on folding and novel connectivities.

Turtles are characterized by their shell, and there have been various opinions as to the evolutionary origin of their unique body plan (*1*–*8*). One possible scenario suggests that acquisition of the osteoderms, the dermal skeletal elements, predated the bony shell (*6*), but other studies have emphasized the importance of more fundamental anatomical changes, especially those associated with the pectoral region, as the decisive factor in turtle evolution (*1*–*5*). The dorsal part of the turtle shell, or carapace, is derived from the ribs, and the scapula is found beneath the carapace, in contrast to the pattern of other amniotes in which the scapula is outside the rib cage (Fig. 1, A to E). Concomitant with the positional change of skeletal elements, the muscles connecting the trunk and scapula, the serratus anterior (AS) and levator scapulae–rhomboid muscle complex (LSR), also showed aberrant positions and connections in the adult turtle (Fig. 1, D and E, and fig. S1). This unusual topography led to the opinion that the turtle shell represents an evolutionary novelty (*1*–*5*). At first glance, this evolutionary shift cannot be resolved by gradual changes of shape and size while maintaining the basic architecture of the body, because an intermediate state is impossible. Thus, it was proposed that turtle evolution represents a radical, saltatory evolutionary change (*1*–*5*). This change has been ascribed to a developmental shift in the ribs, not of the scapula (*7*, *8*). However, the embryonic anatomy of the musculoskeletal system has not been analyzed sufficiently to identify the origin of the turtle-specific body plan.

To understand the developmental changes underlying the origin of the turtle *Bauplan*, we compared the development patterns in embryos of the Chinese soft-shelled turtle (*Pelodiscus sinensis*) and two other amniotes, the chicken (*Gallus gallus*) and the mouse (*Mus musculus*); three to four embryos were examined for each species and stage. As a specialized group of archosaurians, in which turtles are also included (*9*), avians have undergone specialization during evolution (SOM Text 1 and table S1); however, they are expected to exhibit an unaltered developmental pattern reflecting ancestral developmental programs that may have been lost or altered in turtles. Mammals, on the other hand, belong to synapsids, a lineage that diverged before archosaurians (*9*). Thus, the common developmental features shared by chicken and mouse are expected to represent the primitive state of amniotes. We focused on postorganogenetic periods of the embryos when the anatomical variations are thought to be becoming apparent (*10*), and the observations were based on comparative embryological methods.

We used *Sox9* expression as the marker for the skeletal precursor in the late pharyngula stage

[1]Laboratory for Evolutionary Morphology, RIKEN Center for Developmental Biology, 2-2-3 Minatojima-minami, Kobe 650-0047, Japan. [2]Graduate School of Science, Kobe University, Kobe 657-8501, Japan.

*Present address: Department of Biological Sciences, Macquarie University, 2109 Sydney, Australia.
†Present address: Laboratory of Immunology, Department of Health Pharmacy, Yokohama College of Pharmacy, 601 Matano-cho, Yokohama 245-0066, Japan.
‡Present address: Friedrich Miescher Institute for Biomedical Research, Maulbeerstrasse 66, CH-4058 Basel, Switzerland.
§To whom correspondence should be addressed. E-mail: saizo@cdb.riken.jp

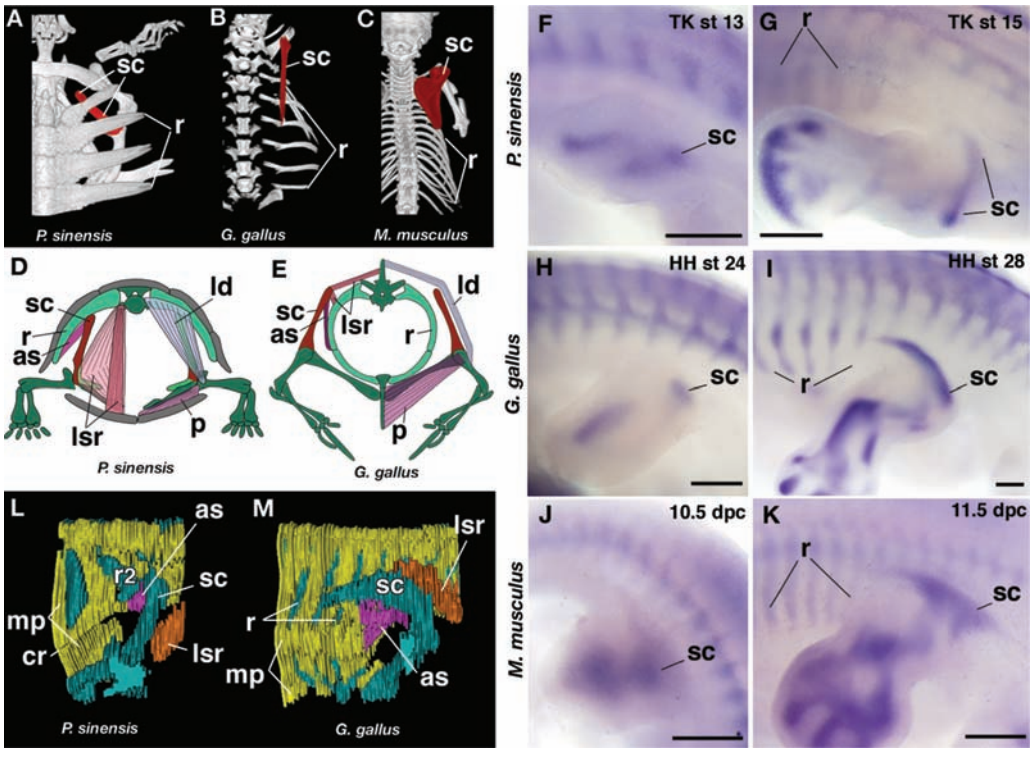

Fig. 1. Comparison of turtle, chicken, and mouse. (**A** to **C**) Dorsal views of computerized axial tomography scanned animals. (**D** and **E**) Comparison of deep (as, serratus anterior; lsr, levator scapulae and rhomboid complex) and superficial (ld, latissimus dorsi; p, pectoralis) muscles connecting the trunk and shoulder girdle/forelimb. (**F** to **K**) *Sox9* expression in stages 13 and 15 *P. sinensis*, stages 24 and 28 chicken, and embryonic day 10.5 and 11.5 mouse. (**L** and **M**) Three-dimensional reconstruction of the stage 16 *P. sinensis* and stage 30 chicken. Cartilages are blue, muscle plate (mp) yellow, AS muscle pink, and LSR muscle orange. Scale bar, 500 μm. cr, carapacial ridge; sc, scapula; r, ribs.

(Fig. 1, F to K) (*11*). In embryos of all three animals, the scapula anlage initially arose lateral to the body wall (somatopleure) into which the muscle plates had grown (Fig. 1, F to M). There were, however, subtle differences; the scapula blade in the stage 28 chicken and 11.5-day mouse began to grow posteriorly, lateral to the developing ribs (Fig. 1, I and K). The *P. sinensis* scapula anlage was located slightly anterior as compared to the chicken and mouse (Fig. 1G). Also, the ribs of *P. sinensis* embryo were comparatively shorter than those in chicken and mouse, in that they never invaded the body wall (*1*, *12*). Slightly later in development, the precursors of AS and LSR muscles also occupied mutually comparable positions in chicken and *P. sinensis*; the AS anlage was found on the ventroposterior aspect of the scapula, and the LSR on the dorsoanterior (Fig. 1, L and M, and movies S1 and S2).

The above data strongly suggested that the common musculoskeletal pattern observed in postpharyngula stage would already have been established in amniotes that gave rise to the turtles. In the chicken and mouse, this pattern is preserved with very little modification in the adult (Fig. 1M and fig. S1C). However, after this stage, the mechanism by which the turtle-specific body plan is generated became apparent. We observed that the second and more posterior ribs grew laterally and anteriorly over the scapula and the AS muscle by folding the dorsal part of the lateral body wall inward (Fig. 2, A to H, and movies S1 and S5). During this process, the same musculoskeletal connectivities were maintained, and as the second rib grew laterally and anteriorly, the AS anlage rotated in a ventral medial direction to assume its final position underneath the carapacial anlage (Fig. 2, A to J). The morphological change of the LSR muscles was less conspicuous (Fig. 3 and SOM Text 2). An analogous rib growth was observed in the pelvic region, and a similar folding was seen in the posterior part of the obliquus abdominis that spans between the posterior ribs and the pelvic girdle (SOM Text 3).

During the turtle-specific folding, ancestral connectivities were maintained between the ribs,

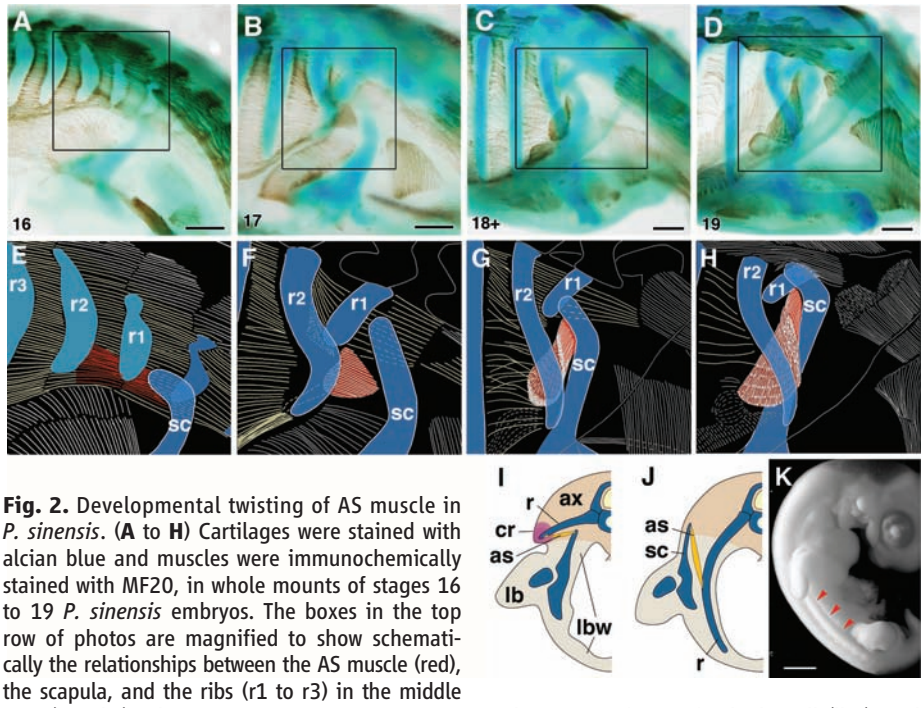

Fig. 2. Developmental twisting of AS muscle in *P. sinensis*. (**A** to **H**) Cartilages were stained with alcian blue and muscles were immunochemically stained with MF20, in whole mounts of stages 16 to 19 *P. sinensis* embryos. The boxes in the top row of photos are magnified to show schematically the relationships between the AS muscle (red), the scapula, and the ribs (r1 to r3) in the middle row. (**I** and **J**) Schematic transverse views to compare the topography of ribs, body wall (lbw), and forelimb bud (lb) with shoulder girdle between the embryos of turtles (I) and generalized amniotes (J). Generally, the amniote ribs grow ventrally into the lateral body wall, whereas in the turtle, they are arrested in the axial part (ax), growing toward the CR. (**K**) The CR (arrowheads) in stage 14 *P. sinensis* embryo. Scale bars, 500 μm for (A) to (D), 1 mm for (K).

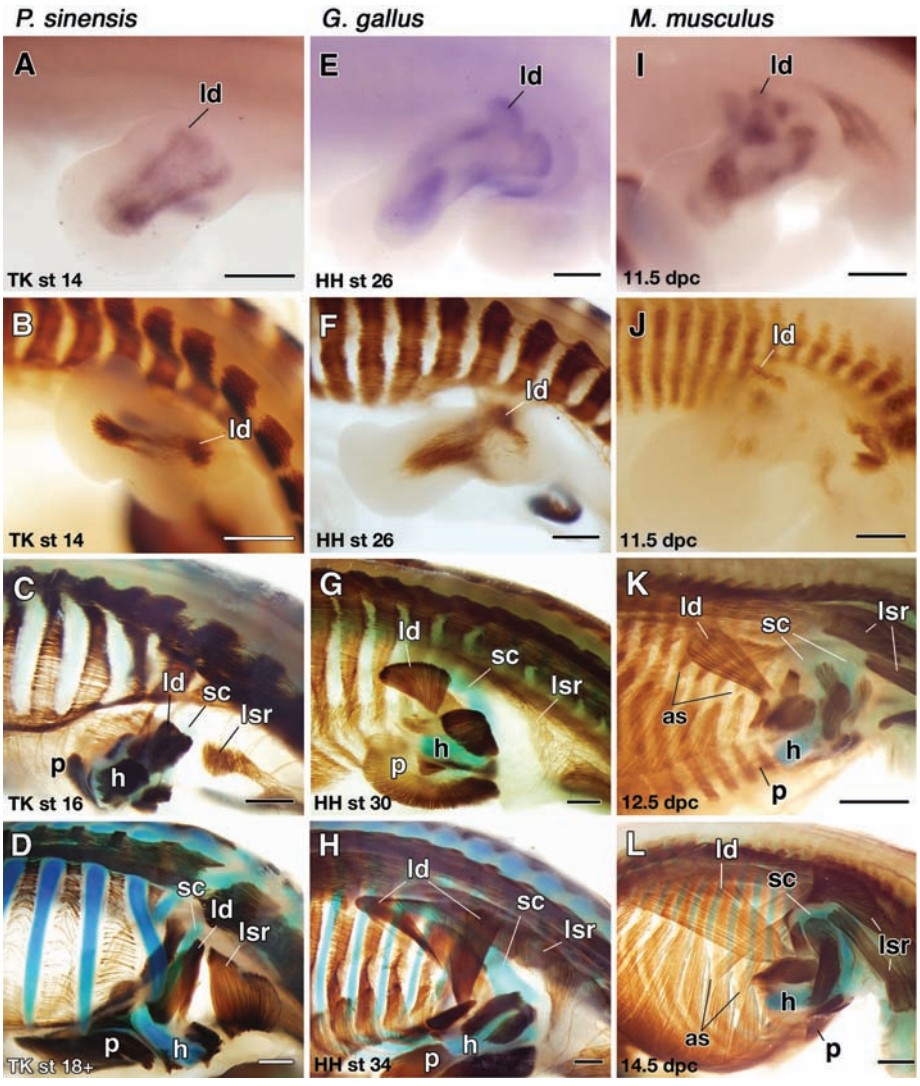

Fig. 3. Comparison of muscle development. (**A** to **D**) *P. sinensis* embryos, (**E** to **H**) chicken embryos, and (**I** to **L**) mouse embryos. (A, E, and I) Expression of *Lbx-1* in the right forelimb buds before muscle differentiation. *Lbx-1*–positive proximal cells represent latissimus dorsi muscle primordia. (B to D, F to H, and J to L) Immunostained embryos to show muscle and peripheral nerve development. Distal parts of the forelimb buds have been removed at the level of the humerus (h). Scale bar, 500 μm.

scapula, and AS and LSR muscles that arise as derivatives of the muscle plate (trunk muscles) (*13*) (Fig. 2, I and J). As shown in Fig. 2, the turtle scapula hung over the first rib, which does not extend or participate in carapace formation. Thus, in the turtle, the scapula arises primarily anterior to the ribs. Because the turtle ribs are confined to the axial domain (axial arrest of ribs), they can only grow laterally and anteriorly to cover the scapula dorsally, while the AS rotates to follow the rib (Fig. 2) (*12*). Still, this growth never altered the connectivities between the anatomical elements, and the positions of the folded muscle plate and rotated AS muscle indicate that the scapula was always morphologically outside the prospective rib cage that is indicated by the position of the muscle plate (movies S3 and S5). In other words, even though the turtle shell can be regarded as an evolutionary novelty, the changes accompanying its development are not so radical as to disrupt the morphological homologies of the above structures (*14*). Rather, the true novelty in turtles is in the axial arrest of the rib growth as well as in the folding at the hinge between the axis and body wall (Fig. 2, I and J).

During the same developmental period, some other muscles formed phylogenetically new connectivities. These muscles belong to the 'in-and-out muscles' primarily classified as limb muscles (*15*). In amniotes, they arise as *Lbx1*-positive, migrating muscle precursors (Fig. 3) (*16*), that is, these muscles invade the limb bud and grow out again to establish attachments onto the trunk. In all the amniote embryos observed, latissimus dorsi primordia came out of the forelimb buds to establish proximal connections (Fig. 3). In the turtle, the anlage grew dorsally and anteriorly to circumvent the carapace and to connect to the nuchal plate, which is the dermal skeleton that covers the cervicodorsal transition (Fig. 3, A to D, fig. S1B, and movie S3). The homologous muscles in the chicken and mouse grew more posteriorly to expand over the back, as in other amniotes (Fig. 3, E to L, fig. S1D, and movie S4). Similarly, pectoralis in *P. sinensis* attached to the dorsal aspect of the plastron, not the ventral aspect of the sternum as in other amniotes (fig. S2). These morphologically divergent attachments were specific to these in-and-out muscles in turtles. Thus, turtles appear to have used these muscles' flexibility in establishing new connections, particularly to invent novel morphological patterns specific to this taxon. Establishment of the turtle-specific new attachments was more conspicuous in the pectoral than in the pelvic region (SOM Text 3).

In summary, the turtle body plan can be explained by a combination of folding with conserved connectivities and the establishment of new connectivities. Therefore, morphological connectivities (i.e., morphological homologies) are partly conserved and partly disturbed. The latter may be regarded as a case of heterotopic shift that yielded novelty in the turtle, at the cost of some homologies (*17*, *18*), similar to the evolution of the gnathostome jaw (*19*).

As already reported, carapacial formation is based on the ribs attached to the vertebrae that are defined as dorsal (thoraco-lumbar) in terms of the conserved role of Hox (*20*, *21*). The growth of these ribs, however, is axially arrested by an unidentified mechanism and never invades the body wall (*12*). The latter situation results not only in ribs that grow over the scapula but also in the curious inward folding of the body wall. Along the folding line, the turtle-specific embryonic structure called the carapacial ridge (CR) (Fig. 1L and Fig. 2, I and K) develops through turtle-specific regulation of genes in the flank (*22*–*25*) and later grows anteriorly and posteriorly to form a circle that differentiates into the carapacial margin. The CR does not appear to induce the axial arrest of the ribs, as suggested previously (*2*, *26*), but rather functions in the flabellate expansion of the turtle ribs in late development (*12*), which characterizes the turtle-specific anatomy (Fig. 4). Although it remains to be determined which mechanism gives rise to the CR, it is likely that the CR is tightly linked to the axial arrest of the ribs in establishing the turtle body plan.

Such a developmental perspective is consistent with the morphology of the recently discovered oldest turtle, *Odontochelys*, which possessed a plastron but no carapace. It cannot be ruled out that the carapace of this animal merely underwent a secondary degeneration (*27*); however, if it really possessed the precarapacial dorsal ribs as reconstructed (*28*) (Fig. 4), the evolution of the turtle body plan would be consistent with the embryonic development of the modern turtle. At least, the dorsal ribs of *Odontochelys* appear to

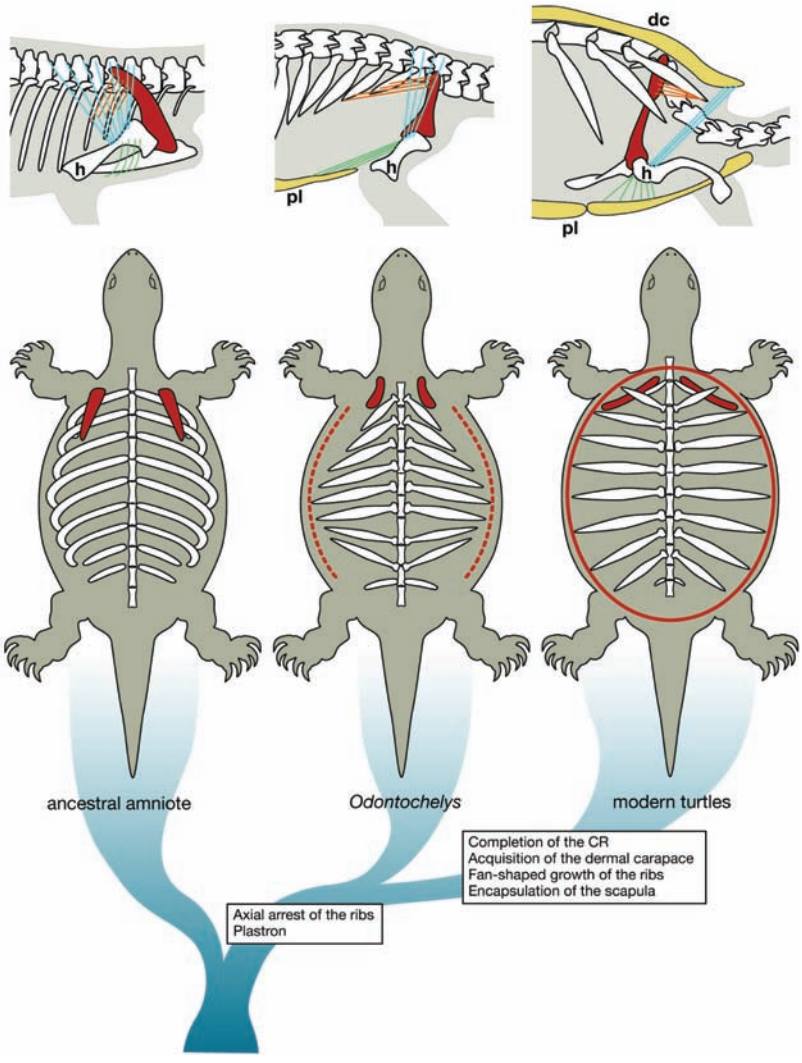

Fig. 4. Evolution of the turtle body plan. (**Top**) A hypothetical sequence of changes in musculoskeletal connectivities. The scapula is red, AS muscle orange, latissimus dorsi blue, and pectoralis green. In *Odontochelys*, the AS would have connected the scapula and distal tips of anterior ribs antero-posteriorly. The pectoralis would have connected the humerus and the plastron (pl). (**Bottom**) A phylogenetic consideration. In *Odontochelys*, the CR (red broken line) may have developed only temporarily and incompletely in the embryo. In the modern turtle, the CR (red solid line) forms a complete circle, inducing the fan-shaped growth of the ribs. dc, dermal carapace.

have already been arrested axially because they never bend strongly ventrally. As previously mentioned, this leads to the presumption that the CR-like ridge would have been acquired in the flank in their embryos (Fig. 4). However, it does not seem to have persisted and encircled the carapacial margin in later development as in the modern turtles, because the flabellate arrangement of the second to eighth ribs is not apparent in *Odontochelys*, that is, the tips of the ribs approximated to each other distally. Consistently, the anterior ribs grew posteriorly in the *Odontochelys*, the scapula remained anterior to the ribs, and the AS muscle would have been stretched to the anterior and posterior (Fig. 4, top), a pattern that is reminiscent of early *P. sinensis* embryos (Fig. 2, A and E).

Odontochelys reconstructed by Li *et al*. (*28*) resembles the embryonic modern turtles in some respects (Fig. 2, A and E, and Fig. 4), and this animal may represent an ancestral state. The *Odontochelys*-like, ancestral pattern is still retained in the first rib in modern turtles (Fig. 4, right). Although it remains to be seen whether latissimus dorsi of *Odontochelys* was shifted rostrally (Fig. 4, middle), its pectoralis would have established a new attachment to the dorsal aspect of the plastron (Fig. 4, middle). Thus, the developmental sequence of *P. sinensis* may not wholly recapitulate the suggested evolutionary sequence of turtles. Nevertheless, the above suggests that the dorsal arrest of ribs can now be assumed to have taken place by the common ancestor of *Odontochelys* and modern turtles (*28*), and in the latter, the completed CR would have allowed for emergence of the carapace (Fig. 4, bottom). The modern turtles have acquired their unique body plan by passing through an *Odontochelys*-like ancestral state during embryonic development. Our embryological study may help to explain the developmental changes involved in both the pre- and post-*Odontochelys* steps of turtle evolution, from an evolutionary developmental perspective.

References and Notes

1. A. C. Burke, *J. Morphol.* **199**, 363 (1989).
2. A. C. Burke, *Am. Zool.* **31**, 616 (1991).
3. B. K. Hall, *Evolutionary Developmental Biology* (Chapman & Hall, London, ed. 2, 1998).
4. S. F. Gilbert, G. A. Loredo, A. Brukman, A. C. Burke, *Evol. Dev.* **3**, 47 (2001).
5. O. Rieppel, *Bioessays* **23**, 987 (2001).
6. M. S. Lee, *Nature* **379**, 812 (1996).
7. H. Ruckes, *Ann. N. Y. Acad. Sci.* **31**, 81 (1929).
8. W. F. Walker Jr., *J. Morphol.* **80**, 195 (1947).
9. N. Iwabe *et al*., *Mol. Biol. Evol.* **22**, 810 (2005).
10. K. E. von Baer, *Entwicklungsgeschichte der Tiere: Beobachtung und Reflexion* (Born Träger, Konigsberg, 1828).
11. F. Pröls *et al*., *Dev. Biol.* **275**, 315 (2004).
12. H. Nagashima *et al*., *Development* **134**, 2219 (2007).
13. A. S. Romer, T. S. Parsons, *The Vertebrate Body* (Saunders, Philadelphia, 1977).
14. E. Geoffroy Saint-Hilaire, *Philosophie Anatomique*, tome premiere (J. B. Baillière, Paris, 1818).
15. D. J. R. Evans, P. Valasek, C. Schmidt, K. Patel, *Anat. Embryol.* **211**, 43 (2006).
16. L. E. Alvares *et al*., *Dev. Cell* **5**, 379 (2003).
17. G. B. Müller, G. P. Wagner, *Annu. Rev. Ecol. Syst.* **22**, 229 (1991).
18. E. Haeckel, *Jena Z. Natuwiss.* **9**, 402 (1875).
19. Y. Shigetani *et al*., *Science* **296**, 1316 (2002).
20. A. C. Burke, C. E. Nelson, B. A. Morgan, C. Tabin, *Development* **121**, 333 (1995).
21. Y. K. Ohya, S. Kuraku, S. Kuratani, *J. Exp. Zool.* **304B**, 107 (2005).
22. G. A. Loredo *et al*., *J. Exp. Zool.* **291B**, 274 (2001).
23. C. Vincent *et al*., *Dev. Genes Evol.* **213**, 464 (2003).
24. S. Kuraku, R. Usuda, S. Kuratani, *Evol. Dev.* **7**, 3 (2005).
25. J. E. Moustakas, *Evol. Dev.* **10**, 29 (2008).
26. J. Cebra-Thomas *et al*., *J. Exp. Zool.* **304B**, 558 (2005).
27. R. R. Reisz, J. J. Head, *Nature* **456**, 450 (2008).
28. C. Li *et al*., *Nature* **456**, 497 (2008).
29. We thank X.-C. Wu and C. Li for their valuable information on *Odontochelys* anatomy, R. Usuda for technical support, and R. Ladher, R. Hirayama, and D. Sipp for critical reading of the manuscript. The monoclonal antibodies (MF20 of D. A. Fischman, and 3A10 of T. M. Jessell and J. Dodd) were obtained from the Developmental Studies Hybridoma Bank, developed under the auspices of the National Institute of Child Health and Human Development and maintained by the University of Iowa, Department of Biological Sciences, Iowa City, IA 52242.

Supporting Online Material

www.sciencemag.org/cgi/content/full/325/5937/193/DC1
Materials and Methods
SOM Text
Figs. S1 and S2
Table S1
References
Movies S1 to S5

19 March 2009; accepted 26 May 2009
10.1126/science.1173826

Antigenic and Genetic Characteristics of Swine-Origin 2009 A(H1N1) Influenza Viruses Circulating in Humans

Rebecca J. Garten,[1]* C. Todd Davis,[1]* Colin A. Russell,[2,3] Bo Shu,[1] Stephen Lindstrom,[1] Amanda Balish,[1] Wendy M. Sessions,[1] Xiyan Xu,[1] Eugene Skepner,[2] Varough Deyde,[1] Margaret Okomo-Adhiambo,[1] Larisa Gubareva,[1] John Barnes,[1] Catherine B. Smith,[1] Shannon L. Emery,[1] Michael J. Hillman,[1] Pierre Rivailler,[1] James Smagala,[1] Miranda de Graaf,[2,4] David F. Burke,[2] Ron A. M. Fouchier,[4] Claudia Pappas,[1] Celia M. Alpuche-Aranda,[5] Hugo López-Gatell,[5] Hiram Olivera,[5] Irma López,[5] Christopher A. Myers,[6] Dennis Faix,[6] Patrick J. Blair,[6] Cindy Yu,[7] Kimberly M. Keene,[8] P. David Dotson Jr.,[9] David Boxrud,[10] Anthony R. Sambol,[11] Syed H. Abid,[12] Kirsten St. George,[13] Tammy Bannerman,[14] Amanda L. Moore,[15] David J. Stringer,[16] Patricia Blevins,[17] Gail J. Demmler-Harrison,[18] Michele Ginsberg,[19] Paula Kriner,[20] Steve Waterman,[21] Sandra Smole,[22] Hugo F. Guevara,[23] Edward A. Belongia,[24] Patricia A. Clark,[25] Sara T. Beatrice,[26] Ruben Donis,[1] Jacqueline Katz,[1] Lyn Finelli,[1] Carolyn B. Bridges,[1] Michael Shaw,[1] Daniel B. Jernigan,[1] Timothy M. Uyeki,[1] Derek J. Smith,[2,3,4]† Alexander I. Klimov,[1] Nancy J. Cox[1]†

Since its identification in April 2009, an A(H1N1) virus containing a unique combination of gene segments from both North American and Eurasian swine lineages has continued to circulate in humans. The lack of similarity between the 2009 A(H1N1) virus and its nearest relatives indicates that its gene segments have been circulating undetected for an extended period. Its low genetic diversity suggests that the introduction into humans was a single event or multiple events of similar viruses. Molecular markers predictive of adaptation to humans are not currently present in 2009 A(H1N1) viruses, suggesting that previously unrecognized molecular determinants could be responsible for the transmission among humans. Antigenically the viruses are homogeneous and similar to North American swine A(H1N1) viruses but distinct from seasonal human A(H1N1).

Influenza pandemics occur when an influenza virus with a hemagglutinin (*HA*), against which there is little or no existing immunity, emerges in the human population and efficiently transmits from human to human. The genomes of the last three pandemic influenza viruses (1918 H1N1, 1957 H2N2, and 1968 H3N2) all originated in whole or in part from nonhuman reservoirs, and the *HA* genes of all of the pandemic viruses ultimately originated from avian influenza viruses.

A(H1N1) influenza viruses were first isolated from swine in 1930 (*1*). They have been shown to be antigenically highly similar to a recently reconstructed human 1918 A(H1N1) virus (*2*) and likely share a common ancestor (*3*, *4*). From 1930 to the late 1990s, these "classical swine influenza" viruses circulated in swine and remained relatively antigenically stable (*5*, *6*).

In, or just before, 1998, the classical swine influenza viruses reassorted with a contemporary human A(H3N2) influenza virus and an American lineage avian influenza virus of an unknown subtype, resulting in the emergence of a triple reassortant H3N2 (rH3N2) swine virus in swine populations throughout North America (*7*–*9*). Shortly after the initial detection of the rH3N2 virus, subsequent reassortment between the rH3N2 virus and classical H1N1 swine virus is believed to have resulted in the generation of further triple reassortant swine A(H1N1) and A(H1N2) viruses (*6*). In addition to the detection of these triple reassortants in North American swine populations since the late 1990s, triple reassortant swine viruses of the North American lineage have also recently been detected in Asian swine populations (*10*–*12*). Since 1999, there has been antigenic divergence within the various triple reassortant H1 viruses, with as much as a 16-fold difference in hemagglutination inhibition (HI) assay titer from the pre-reassortment strains when measured with swine antisera (*6*), which if it were seen in human viruses would be sufficient antigenic change to require an update of the human seasonal influenza vaccine strain.

A(H1N1) viruses circulated in humans from 1918 until the A(H2N2) influenza pandemic of 1957. During this period there was substantial antigenic drift of A(H1N1) viruses in humans away from the 1918 virus (*2*, *13*). A(H1N1) influenza viruses from the early 1950s reemerged in humans in 1977 (*14*). From 1977 to 2009, there was substantial further antigenic evolution of the human A(H1N1) viruses that was sufficient to warrant eight updates of the H1 component of the influenza virus vaccine (*15*).

The relative antigenic stasis of classical H1N1 influenza viruses in swine until 1998 during the time when substantial antigenic drift of H1 in humans was observed has created a substantial antigenic gap between classical swine H1 and human seasonal H1 viruses. Thus, swine have become a reservoir of H1 viruses with the potential to cause major respiratory outbreaks or even a possible pandemic in humans.

In recent decades, both classical swine influenza and triple reassortant swine influenza viruses have occasionally been isolated from humans (*14*–*18*). Although these infections cause clinical disease, and occasionally hospitalizations and deaths, only limited human-to-human transmission has previously been documented.

In April 2009, a previously undescribed A(H1N1) influenza virus was isolated from humans in Mexico and the United States (*19*). As of 18 May 2009, there have been 8829 laboratory-confirmed cases in 40 countries, resulting in 74 deaths (*20*–*23*). Of the 2009 A(H1N1) viruses, we have sequenced full or partial genomes of 17 isolated in Mexico, and 59 from 12 states in the United States (table S1).

This 2009 A(H1N1) virus contains a combination of gene segments that previously has not been reported in swine or human influenza viruses in the United States or elsewhere. The *NA* and *M* gene segments are in the Eurasian swine genetic lineage (fig. S1, F and G). Viruses with *NA* and *M* gene segments in this lineage were originally derived from a wholly avian influenza virus and thought to have entered the Eurasian swine population in 1979 (*24*), continue to circulate throughout Eurasia (*25*), and have not been previously reported outside Eurasia. The *HA*, *NP*, and *NS* gene segments are in the classical swine lineage (fig. S1, D, E, and H). Viruses that seeded this lineage are thought to have entered swine around 1918 (*1*) and subsequently circulated in classical swine viruses and triple

[1]WHO Collaborating Center for Influenza, Centers for Disease Control and Prevention (CDC), Atlanta, GA 30333, USA. [2]Department of Zoology, University of Cambridge, Cambridge CB2 3EJ, UK. [3]Fogarty International Center, National Institutes of Health, Bethesda, MD 20892, USA. [4]Department of Virology, Erasmus Medical Center, 3000 CA Rotterdam, NL. [5]Instituto de Diagnóstico y Referencia Epidemiológicos (InDRE) Prolongación de Carpio, México, 11340 Mexico, DF. [6]Naval Health Research Center, San Diego, CA 92152, USA. [7]Arizona State Public Health Laboratory, Phoeniz, AZ 85007, USA. [8]Colorado Department of Public Health and Environment, Denver, CO 80230, USA. [9]Indiana State Department of Health Laboratories, Indianapolis, IN 46202, USA. [10]Public Health Laboratory, Minnesota Department of Health, St. Paul, MN 55164, USA. [11]Nebraska Public Health Laboratory, Omaha, NE 68198, USA. [12]Westchester County Department of Laboratories & Research Public Health Laboratories, Valhalla, NY 10595, USA. [13]Wadsworth Center, New York State Department of Health, Slingerlands, NY 12159, USA. [14]Ohio Department of Health Laboratory, Reynoldsburg, OH 43068, USA. [15]South Carolina Department of Health and Environmental Control, Columbia, SC 29223, USA. [16]Dallas County Health and Human Services, Dallas, TX 75207, USA. [17]San Antonio Metro Health District, Brooks City–Base, TX 78235, USA. [18]Diagnostic Virology Laboratory, Texas Children's Hospital, Houston, TX 77030, USA. [19]San Diego Public Health Laboratory, San Diego, CA 92186, USA. [20]Imperial County Public Health Department, El Centro, CA 92243, USA. [21]CDC Border Infectious Disease Surveillance Project, Atlanta, GA 30333, USA. [22]William A. Hinton State Laboratory Institute, Massachusetts Department of Public Health, Jamaica Plain, MA 02130, USA. [23]California Department of Public Health, Viral and Rickettsial Disease Laboratory, Richmond, CA 94804, USA. [24]Marshfield Clinic Research Foundation, Marshfield, WI 54449, USA. [25]Michigan Department of Community Health, Lansing, MI 48906, USA. [26]Public Health Laboratory, NYC Department of Health and Mental Hygiene, New York, NY 10016, USA.

*These authors contributed equally to this work.
†To whom correspondence should be addressed. E-mail: dsmith@zoo.cam.ac.uk (D.J.S.); njc1@cdc.gov (N.J.C.)

reassortant swine viruses (*26*). The *PB2* and *PA* gene segments are in the swine triple reassortant lineage (fig. S1, A and C). Viruses that seeded this lineage, originally of avian origin, entered swine in North America around 1998 (*9*). Finally, the *PB1* gene segment is in the swine triple reassortant lineage (fig. S1B). This lineage of *PB1* was seeded in swine from humans at the time of the North American swine triple reassortment events (*9*) and was itself seeded from birds around 1968 (*27*). Figure 1 summarizes these host and lineage origins for the gene segments of the 2009 A(H1N1) virus.

The *M* gene segment most closely related to the 2009 A(H1N1) viruses is from A/Hong Kong/1774/1999 (H3N2), which was isolated from a human case of swine influenza (*28*). A further human case of swine influenza, A/Thailand/271/2005, contains genes from both North American and Eurasian swine influenza lineages (*29*), indicating previous reassortment between these two swine virus lineages.

Given the history of reassortment events of swine influenza, it is likely that additional reassortant viruses have emerged but have not been sampled. The poor surveillance for swine influenza viruses and the observation that the closest

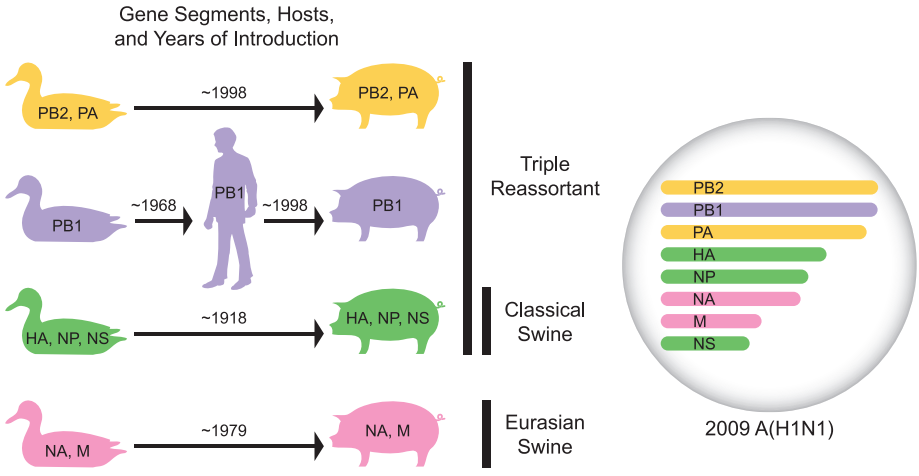

Fig. 1. Host and lineage origins for the gene segments of the 2009 A(H1N1) virus: *PB2*, polymerase basic 2; *PB1*, polymerase basic 1; *PA*, polymerase acidic; *HA*, hemagglutinin; *NP*, nucleoprotein; *NA*, neuraminidase; *M*, matrix gene; *NS*, nonstructural gene. Color of gene segment in circle indicates host. Determination of lineage is explained in the main text.

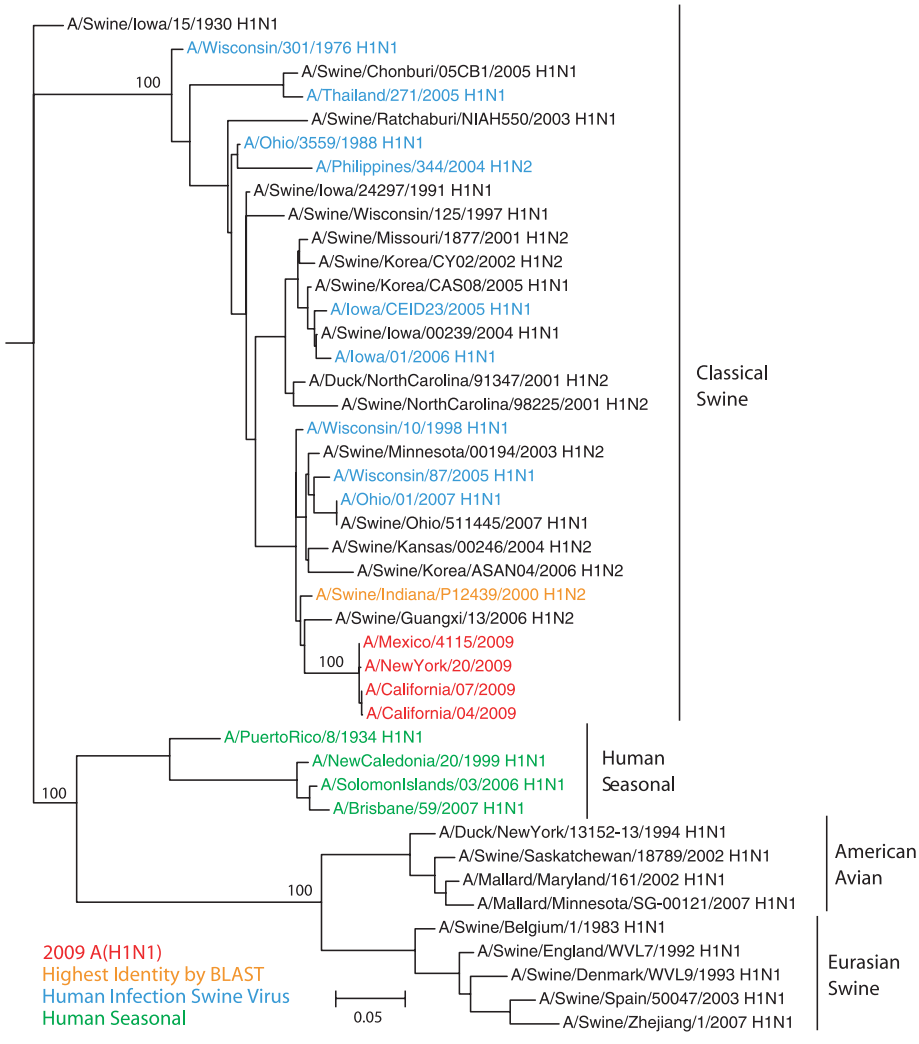

Fig. 2. A maximum likelihood phylogenetic tree for nucleotide sequences of the *HA* gene of selected influenza viruses. The selected viruses were chosen to be representative from among all available relevant sequences in GenBank: sequences that had both high and low divergence to avoid biasing the distribution of branch lengths; swine strains that had been isolated from humans and that had been isolated from swine; strains that were representative of the major gene lineages from different hosts; and the nearest BLAST relative to include the most closely related non-outbreak virus. Phylogenetic trees of a larger number of representative *HA* gene segments, and of all H1 *HA* swine gene segments, are shown in figs. S1D and S2D, respectively. Tree was inferred using PAUP* (version 4.0b10) (*40*), using GTR+I+Γ_4 (the general time-reversible model with the proportion of invariant sites and the gamma distribution of among-site rate variation with four categories estimated from the empirical data) as determined by ModelTest (*41*). Global optimization of the tree topology was performed by tree bisection-reconnection branch swapping. The robustness of individual nodes of the tree was assessed using a bootstrap resampling analysis (1000 replicates, with topologies inferred using the neighbor-joining method under the GTR+I+Γ_4 substitution model).

ancestral gene for each of the eight gene segments is of swine origin suggest that this virus might have been circulating undetected among swine herds somewhere in the world. Several scenarios exist, including reassortment in Asia or the Americas, for the events that have led to the genesis of the 2009 A(H1N1) virus. Where the reassortment event(s) most likely happened is currently unclear.

BLAST searches on GenBank (blastn using default settings) for each gene segment of the 2009 influenza A(H1N1) outbreak viruses showed that viruses with genes of highest nucleotide sequence identity were isolated, on average, 10 years ago (range 1992 to 2004), and top BLAST results for each gene segment had a sequence identity of 94 to 97% to the 2009 influenza A(H1N1) outbreak strains. This substantial divergence from previously sequenced strains is also shown by the long branch lengths to the current outbreak strains in the phylogenetic tree for each gene segment (Fig. 2 and fig. S1) (*30*). Though long, these branch lengths are not unusual for swine viruses; there are 52 other similar or longer branch lengths in the swine phylogenetic trees (fig. S2).

Within each gene segment, there is high (99.9%) identity among the outbreak viruses sequenced to date, suggesting that the cross-species introduction into humans was a single event or multiple events of genetically very similar viruses. Analysis across the genomes of the 2009 A(H1N1) viruses from Mexico and the United States to date found five minor genome variants: (i) the consensus sequence; (ii) T373I mutation in the *NP* paired with M581L mutation in the *PA*; (iii) amino acid substitutions of V106I and N247D in the *NA* (N2 numbering) paired with V100I in the *NP*; (iv) amino acid substitutions of S206T in the *HA1* (H3 numbering) clustering with both V106I and N247D in the *NA* (N2 numbering), V100I in the *NP*, and I123V in the *NS1*; and (v) amino acid substitutions of S91P and V323I (H3 numbering), together with S224P, in the *PA* (table S2) (*31*). The inclusion of isolates from Mexico or border states among all five genome variants reflects the likelihood that these early genome variants represent initial independent introductions into the United States from Mexico. Because of the short time interval since the 2009 A(H1N1) virus was first detected, it is not clear what effect, if any, these genome variations may have on viral characteristics such as transmissibility or pathogenesis.

Sequence analysis of the U.S. and Mexico isolates of the 2009 A(H1N1) viruses to date has not identified molecular features previously shown

Table 1. HI table of representative previous swine, and current outbreak, H1 influenza viruses. Complete HI tables of all outbreak strains tested to date are shown as tables S3 and S4. Swine viruses previously isolated from humans and sera raised to those viruses are shown in blue. 2009 A(H1N1) viruses and sera raised to them are shown in red.

HEMAGGLUTINATION INHIBITION REACTIONS OF INFLUENZA H1N1 SWINE LIKE VIRUSES(05/0709)

	REFERENCE FERRET ANTISERA									
STRAIN DESIGNATION	SW/IA/30	NJ/8/76	WI/10	SW/MN	OH/2	IL/9	CA/04	CA/05	DATE COLLECTED	PASSAGE
A/Swine/Iowa/1930	**320**	40	<10	20	<10	<10	<10	<10	Unknown	XEXE6
A/New Jersey/8/1976	80	**160**	10	40	<10	<10	<10	<10	Unknown	SpfE6
A/Wisconsin/10/1998	<10	2560	**1280**	640	5120	2560	640	2560	01/01/98	C3/C3E2
A/Swine/Minnesota/2002	40	640	640	**2560**	5120	2560	1280	5120	Unknown	SIVCX/C3
A/Ohio/2/2007	80	1280	640	2560	**5120**	5120	2560	5120	08/18/07	C1
A/Illinois/9/2007	80	1280	1280	2560	5120	**5120**	2560	5120	09/02/07	C1
A/California/04/2009	10	320	320	640	5120	640	**1280**	2560	04/02/09	C2
A/California/05/2009	40	320	320	1280	5120	1280	1280	**5120**	03/31/09	C2
TEST ANTIGENS										
A/California/06/2009	80	640	640	1280	5120	2560	1280	5120	04/17/09	M1/C1
A/California/07/2009	320	1280	1280	2560	5120	5120	2560	5120	04/10/09	C1
A/California/07/2009	80	640	320	1280	5120	1280	2560	5120	04/10/09	E2
A/California/08/2009	160	1280	640	2560	5120	2560	2560	5120	04/10/09	C1
A/California/08/2009	160	320	320	1280	5120	1280	2560	5120	04/10/09	E2
A/Kansas/2/2009	160	640	640	1280	5120	2560	2560	5120	04/25/09	C1
A/Kansas/3/2009	40	320	320	640	2560	640	1280	5120	04/25/09	C1
A/Ohio/07/2009	80	640	640	640	2560	1280	1280	5120	04/25/09	E2
A/Ohio/07/2009	80	640	320	640	5120	1280	1280	5120	04/25/09	C1
A/New York/18/2009	160	1280	640	2560	2560	2560	2560	5120	Unknown	E2
A/New York/20/2009	160	640	640	1280	5120	2560	5120	5120	Unknown	E2
A/New York/23/2009	160	640	320	1280	2560	1280	1280	5120	04/25/09	C1
A/New York/23/2009	80	640	640	1280	5120	1280	640	5120	04/25/09	E2
A/Texas/04/2009	20	160	160	640	1280	640	640	1280	04/15/09	X/C1
A/Texas/05/2009	320	1280	640	2560	5120	2560	2560	5120	04/16/09	X/C1
A/Texas/08/2009	40	320	320	640	5120	1280	1280	2560	04/25/09	E2
A/Texas/08/2009	40	320	320	640	2560	1280	1280	2560	04/25/09	C1
A/Indiana/9/2009	40	640	320	640	5120	1280	1280	2560	04/23/09	C1
A/Minnesota/02/2009	80	640	640	1280	5120	2560	2560	5120	Unknown	C1
A/Georgia/01/2009	80	640	320	640	5120	1280	1280	2560	04/28/09	E1
A/South Carolina/09/2009	80	640	640	1280	5120	2560	2560	5120	04/27/09	C1
A/Nebraska/02/2009	320	1280	1280	1280	5120	2560	2560	5120	Unknown	C1
A/Colorado/03/2009	320	640	640	1280	5120	2560	2560	5120	04/28/09	C1
A/Arizona/02/2009	160	640	640	1280	5120	1280	2560	2560	04/27/09	C1
A/Delaware/02/2009	160	640	640	1280	5120	1280	2560	5120	04/29/09	E1
A/Delaware/03/2009	320	1280	1280	2560	5120	2560	5120	5120	04/29/09	E1
A/Mexico/4486/2009	160	1280	1280	1280	5120	2560	2560	5120	04/15/09	C1
A/Mexico/4486/2009	160	1280	640	1280	2560	1280	2560	5120	04/15/09	E2
A/Mexico/4108/2009	320	1280	1280	2560	5120	2560	2560	5120	04/04/09	C1
A/Mexico/4108/2009	80	320	320	1280	5120	1280	1280	2560	04/04/09	E1
A/Mexico/3955/2009	160	640	640	2560	5120	2560	2560	5120	04/04/09	E2
A/Mexico/4486/2009	160	640	640	1280	5120	1280	1280	2560	04/15/09	C1/C1
A/Mexico/4516/2009	40	640	320	1280	2560	1280	2560	5120	04/17/09	C1/C1
A/Mexico/4603/2009	80	320	320	640	2560	1280	1280	2560	04/20/09	E2
A/Mexico/4603/2009	160	640	640	1280	5120	1280	1280	5120	04/20/09	C1/C1
A/Mexico/4627/2009	80	640	640	1280	2560	640	1280	5120	04/21/09	C1/C1
A/Mexico/4635/2009	160	640	640	1280	5120	2560	2560	5120	04/21/09	C1/C1
A/Mexico/4646/2009	160	640	320	1280	5120	1280	1280	5120	04/21/09	C1/C1

to confer increased transmissibility or virulence in studies of other influenza A viruses. The known receptor binding sites of the H1 *HA* protein are typical of many other classical swine H1N1 viruses recently isolated in North America. Although there are some mutations detected in the *HA* of the 2009 A(H1N1) viruses that differ from the classical swine consensus sequence, none of these were identified in known functionally important receptor binding sites. As expected, many of the 2009 A(H1N1) viruses contain amino acid substitutions at putative antigenic sites when compared with seasonal H1 *HA*; the effect of these substitutions is examined in the antigenic analysis below.

The 2009 A(H1N1) influenza viruses have the genetic marker (S31N in *M2*) for resistance to the adamantane antivirals and are sensitive to oseltamivir and zanamivir in functional assays (*22*, *32*). Adamantane resistance is a characteristic marker of the Eurasian swine lineage. Like the *M* gene segment, the closest available ancestor for the *NA* is also from a Eurasian swine virus. All further viruses tested to date (102 in total from Mexico and from 23 states of the United States) have the same pattern of resistance and sensitivity. Additionally, no genetic markers have been found in the *NA* that are known to decrease neuraminidase inhibitor sensitivities.

Many of the molecular markers predicted to be associated with adaptation to a human host or to the generation of a pandemic virus, as seen in 1918 H1N1 or highly pathogenic H5N1, are not present in the 2009 A(H1N1) viruses characterized here. All 2009 A(H1N1) viruses to date have a Glu at position 627 in the *PB2* protein, which is unexpected because all known human influenza viruses have a Lys at this position, whereas Glu^{627} is typical for avian influenza viruses. The *PB1-F2* protein has previously been associated with the increased pathogenicity of the 1918 virus and highly pathogenic H5N1 virus (*33*–*35*). However, the *PB1-F2* protein of the 2009 A(H1N1) viruses sequenced to date are truncated by the presence of a stop codon at position 12. The *NS1* protein is also truncated, by a stop codon at position 220, which creates a deletion of the PDZ ligand domain, a protein-protein recognition domain involved in a variety of cell-signaling pathways that have been implicated in the pathogenicity of 1918 H1N1 and highly pathogenic H5N1 viruses (*36*). Together these data suggest that other previously unrecognized molecular determinants are responsible for the ability of the 2009 A(H1N1) virus to replicate and transmit in humans.

Antibodies against the surface glycoprotein *HA* are of major importance for protection against infection, and the *HA* is the primary component of the currently licensed influenza virus vaccines. To determine the antigenic properties of the 2009 A(H1N1) viruses, 18 viruses isolated in Mexico and 38 isolated in the United States were characterized in HI assays using postinfection ferret antisera raised against a selection of swine H1 viruses, swine H1 viruses that have previously infected humans, 2009 A(H1N1) viruses, and representative viruses of the currently circulating seasonal human H1 and H3 viruses (Table 1, tables S3 and S4, and Fig. 3).

Antigenically, the 2009 A(H1N1) viruses are homogeneous, and among historical viruses, are antigenically most similar to classical swine A(H1N1) viruses, as well as to North American lineage triple reassortant A(H1N1) viruses that have circulated in swine over the past 10 years in the United States and that have occasionally infected humans during the same period (*18*). There have been only a few amino acid substitutions in the *HA* among the 2009 H1N1 viruses analyzed to date (table S5), and none of these amino acid changes appear to have an antigenic effect. The antigenic variation among the 2009 A (H1N1) viruses circulating in humans is currently less than that seen during a typical influenza season in humans (*37*, *38*).

Ferret postinfection antisera raised against the currently circulating seasonal human A(H1N1) viruses did not react with the 2009 A(H1N1) strains (Table 1). This lack of cross-reactivity does not, however, directly equate to a lack of cross-protection in humans between seasonal A(H1N1) and 2009 A(H1N1) viruses as humans have a more complex immune profile than the single infection used in ferrets for antigenic characterization. Tumpey *et al.* (*2*) showed a small boost of cross-reactive antibodies (measured by HI assay) to A/Swine/Iowa/1930 A(H1N1) in a proportion of human sera after vaccination with A/New Caledonia/20/1999 A(H1N1). Whether this boost would be protective, and the magnitude of the boost against the 2009 A(H1N1) viruses after vaccination with the current H1 component of the influenza virus vaccine, remain to be determined.

Circulation of an influenza A(H1N1) swine-origin virus in humans with an antigenically and genetically divergent *HA* and a previously unrecognized genetic composition is of concern to public health officials around the world. That this virus appears readily transmissible between humans is further cause for alarm. The evolutionary distances between the gene segments of this virus and its closest relatives indicate a lack of surveillance in swine populations that may harbor influenza viruses with pandemic potential. Worldwide monitoring of the antigenic and genetic properties of the 2009 A(H1N1) viruses continues for, among other reasons, detecting any changes and thus any necessity for selecting further vaccine candidates or changes in antiviral

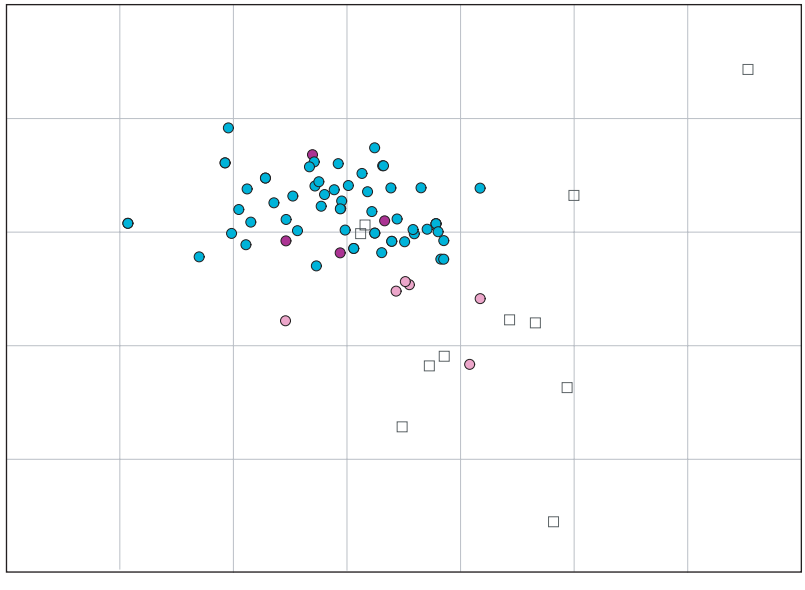

Fig. 3. Antigenic map of 71 early swine-origin 2009 A(H1N1) influenza viruses and 11 antisera. An antigenic map is a geometric representation of binding assay data, in this case the HI assay data in tables S3 and S4. In such a map, the relative positions of strains (colored circles) and antisera (uncolored squares) are adjusted such that the distances between strains and antisera in the map represent the corresponding HI measurements with the least error. Distance in the map thus represents antigenic distance, and the closer antigens are to each other in the map, the more similar they are antigenically (*38*). The color of a circle in the map indicates whether the strain is a 2009 A(H1N1) influenza virus (blue) or an A(H1) swine influenza virus isolated between 1998 and 2007 from either a swine (purple) or a human (pink) infected with a swine influenza virus. The vertical and horizontal axes both represent antigenic distance, and because only the relative positions of antigens and antisera can be determined, the orientation of the map within these axes is free (thus an antigenic map can be rotated in the same way that a geographic map can be rotated). The spacing between grid lines is one unit of antigenic distance—corresponding to a twofold dilution of antiserum in the HI assay. Two units correspond to fourfold dilution, three units to eightfold dilution, etc. A difference higher than fourfold in HI titer is usually considered to be sufficient to necessitate an update of the human seasonal influenza virus vaccine. Antigenic clusters of human seasonal influenza viruses typically have a radius of two antigenic units (fourfold in HI) (*38*) (see fig. S3 for a zoomable PDF of this antigenic map that additionally includes the names of each strain and antiserum).

recommendations. Ongoing full genome sequencing will monitor for the possibility of future reassortment events (*39*).

References and Notes

1. R. E. Shope, *J. Exp. Med.* **54**, 373 (1931).
2. T. M. Tumpey *et al.*, *Proc. Natl. Acad. Sci. U.S.A.* **101**, 3166 (2004).
3. O. T. Gorman *et al.*, *J. Virol.* **65**, 3704 (1991).
4. A. H. Reid, J. K. Taubenberger, *J. Gen. Virol.* **84**, 2285 (2003).
5. M. G. Sheerar, B. C. Easterday, V. S. Hinshaw, *J. Gen. Virol.* **70**, 3297 (1989).
6. A. L. Vincent *et al.*, *Vet. Microbiol.* **118**, 212 (2006).
7. A. I. Karasin *et al.*, *Virus Res.* **68**, 71 (2000).
8. R. J. Webby *et al.*, *J. Virol.* **74**, 8243 (2000).
9. N. N. Zhou *et al.*, *J. Virol.* **73**, 8851 (1999).
10. Y. Chen *et al.*, *Wei Sheng Wu Xue Bao* **48**, 466 (2008).
11. C. S. Lee *et al.*, *Virus Genes* **37**, 168 (2008).
12. D. S. Song *et al.*, *Virus Res.* **125**, 98 (2007).
13. E. D. Kilbourne *et al.*, *Proc. Natl. Acad. Sci. U.S.A.* **99**, 10748 (2002).
14. R. G. Webster, W. J. Bean, O. T. Gorman, T. M. Chambers, Y. Kawaoka, *Microbiol. Rev.* **56**, 152 (1992).
15. A. J. Hay, V. Gregory, A. R. Douglas, Y. P. Lin, *Philos. Trans. R. Soc. Lond. B Biol. Sci.* **356**, 1861 (2001).
16. A. P. Kendal, M. Goldfield, G. R. Noble, W. R. Dowdle, *J. Infect. Dis.* **136** (suppl.), S381 (1977).
17. K. P. Myers, C. W. Olsen, G. C. Gray, *Clin. Infect. Dis.* **44**, 1084 (2007).
18. V. Shinde *et al.*, *N. Engl. J. Med.* **360**, 2616 (2009).
19. *MMWR Morb. Mortal. Wkly. Rep.* **58**, 400 (2009).
20. *MMWR Morb. Mortal. Wkly. Rep.* **58**, 453 (2009).
21. CDC, *H1N1 Flu (Swine Flu)*, www.cdc.gov/h1n1flu/ (accessed 18 May 2009).
22. F. S. Dawood *et al.*, *N. Engl. J. Med.* **360**, 2605 (2009).
23. WHO, *Influenza A(H1N1)*, www.who.int/csr/disease/swineflu/en/index.html (accessed 18 May 2009).
24. M. Pensaert, K. Ottis, J. Vandeputte, M. M. Kaplan, P. A. Bachmann, *Bull. World Health Organ.* **59**, 75 (1981).
25. J. Maldonado *et al.*, *Vet. J.* **172**, 377 (2006).
26. C. W. Olsen, *Virus Res.* **85**, 199 (2002).
27. Y. Kawaoka, S. Krauss, R. G. Webster, *J. Virol.* **63**, 4603 (1989).
28. V. Gregory *et al.*, *J. Gen. Virol.* **82**, 1397 (2001).
29. N. Komadina *et al.*, *Virus Genes* **35**, 161 (2007).
30. Materials and methods are available as supporting material on *Science* Online.
31. Single-letter abbreviations for the amino acid residues are as follows: D, Asp; I, Ile; L, Leu; M, Met; N, Asn; P, Pro; S, Ser; T, Thr; and V, Val.
32. *MMWR Morb. Mortal. Wkly. Rep.* **58**, 433 (2009).
33. G. M. Conenello, D. Zamarin, L. A. Perrone, T. Tumpey, P. Palese, *PLoS Pathog.* **3**, 1414 (2007).
34. J. Steel, A. C. Lowen, S. Mubareka, P. Palese, *PLoS Pathog.* **5**, e1000252 (2009).
35. D. Zamarin, M. B. Ortigoza, P. Palese, *J. Virol.* **80**, 7976 (2006).
36. D. Jackson, M. J. Hossain, D. Hickman, D. R. Perez, R. A. Lamb, *Proc. Natl. Acad. Sci. U.S.A.* **105**, 4381 (2008).
37. C. A. Russell *et al.*, *Science* **320**, 340 (2008).
38. D. J. Smith *et al.*, *Science* **305**, 371 (2004).
39. Sequences will continue to be uploaded to the sequence databases [NCBI (National Center for Biotechnology Information) (www.ncbi.nlm.nih.gov/genomes/FLU/) and GISAID (Global Initiative on Sharing Avian Influenza Data) (http://gisaid.org)] as they are generated. See table S1 for a list of GenBank accession numbers. Antigenic data will be available at http://antigenic-cartography.org/.
40. D. L. Swofford, PAUP* (Sinauer, Sunderland, MA, 2003).
41. D. Posada, K. A. Crandall, *Bioinformatics* **14**, 817 (1998).

42. We thank the many individuals at the local, state, and national levels for their enormous contributions to the surveillance of the 2009 A(H1N1) virus; the entire CDC Influenza Division staff and emergency staff; the maintainers of the GISAID EpiFluDB and NCBI GenBank/IVR; and the members of the WHO Global Influenza Surveillance Network. The findings and conclusions of this report are those of the authors and do not necessarily represent the official position of the Centers for Disease Control and Prevention. R.A.M.F. was supported by National Institute of Allergy and Infectious Diseases under NIH contract HHSN266200700010C. E.S. was supported in part by the International Federation of Pharmaceutical Manufacturers and Associations through grant RG51953. C.A.R. was supported in part by a Research Fellowship from Clare College, Cambridge. D.J.S., C.A.R., E.S., and D.F.B. were supported by an NIH Director's Pioneer Award, part of the NIH roadmap for medical research, through grant DP1-OD000490-01; an FP7 grant, 223498 EMPERIE, from the European Union; and program grant RG P0050/2008 from the Human Frontier Science Program. GenBank accession numbers are listed in the Supporting Online Material.

Supporting Online Material

www.sciencemag.org/cgi/content/full/1176225/DC1
Figs. S1 to S3
Tables S1 to S6

12 May 2009; accepted 22 May 2009
Published online 22 May 2009;
10.1126/science.1176225
Include this information when citing this paper.

Caloric Restriction Delays Disease Onset and Mortality in Rhesus Monkeys

Ricki J. Colman,[1]* Rozalyn M. Anderson,[1] Sterling C. Johnson,[1,2,3] Erik K. Kastman,[2,3] Kristopher J. Kosmatka,[2,3] T. Mark Beasley,[4] David B. Allison,[4] Christina Cruzen,[1] Heather A. Simmons,[1] Joseph W. Kemnitz,[1,2,5] Richard Weindruch[1,2,3]*

Caloric restriction (CR), without malnutrition, delays aging and extends life span in diverse species; however, its effect on resistance to illness and mortality in primates has not been clearly established. We report findings of a 20-year longitudinal adult-onset CR study in rhesus monkeys aimed at filling this critical gap in aging research. In a population of rhesus macaques maintained at the Wisconsin National Primate Research Center, moderate CR lowered the incidence of aging-related deaths. At the time point reported, 50% of control fed animals survived as compared with 80% of the CR animals. Furthermore, CR delayed the onset of age-associated pathologies. Specifically, CR reduced the incidence of diabetes, cancer, cardiovascular disease, and brain atrophy. These data demonstrate that CR slows aging in a primate species.

Evidence that mammalian longevity could be increased emerged in 1935 in a rodent study showing that caloric restriction (CR), without malnutrition, extended average and maximum life span and delayed the onset of age-associated pathologies (*1*). It was not until the 1990s that CR became widely viewed as a scientific model that could provide insights into the retardation of the aging process (*2*) and thereby identify underlying mechanisms of aging (*3*). The inverse relationship between calorie intake and increase in life span in mice suggests a role for regulators of energy metabolism in the mechanism of CR. Accordingly, CR-induced metabolic reprogramming may be a key event in the mechanism of life span extension (*4*). Studies in yeast, worms, flies, and mice point to a role for nutrient-responsive signaling molecules, including SIRT1, mTOR, and PGC-1α, in aging and CR (*5*). The relevance of these findings for human aging depends on the conservation of the effects of CR on aging in primates.

The marked anatomical, physiological, and behavioral similarities between human and nonhuman primates make the latter particularly suited for providing insights into the biology of human aging. Although animals on CR appeared subjectively younger than controls (Fig. 1, A to D), we sought to determine whether they were biologically younger than controls. Two critical indicators of aging retardation are delays in mortality and in the onset of age-associated disease. The incidence of disease increases with age and is a fundamental contributor to mortality (*6*). Thus, we examined age-associated conditions most prevalent in humans, including diabetes, cancer, cardiovascular disease, and brain atrophy (*7*).

Our study was begun in 1989 at the Wisconsin National Primate Research Center (WNPRC) (*8*) (Fig. 2A). Rhesus macaques (*Macaca mulatta*) have an average life span of ~27 years in captivity and a maximal life span of ~40 years. All animals were adults (7 to 14 years old) when introduced into the study. Initially the study included 30 males, and the cohort was expanded in 1994 to include an additional 30 females and 16 males (*9*). These increased numbers improved statistical power, and the inclusion of females allowed us to monitor gender differences in the effects of CR. The animals were evenly matched and randomized to control or CR diets, taking into consideration baseline food intake, body weight, and age. Individualized food allotments were calculated based on daily food intake data that were collected for each animal over a

[1]Wisconsin National Primate Research Center, University of Wisconsin, Madison, WI 53715, USA. [2]Department of Medicine, University of Wisconsin, Madison, WI 53706, USA. [3]Geriatric Research, Education, and Clinical Center, William S. Middleton Memorial Veterans Hospital, Madison, WI 53705, USA. [4]Department of Biostatistics, University of Alabama at Birmingham, Birmingham, AL 35294, USA. [5]Department of Physiology, University of Wisconsin, Madison, WI 53706, USA.

*To whom correspondence should be addressed. E-mail: rcolman@primate.wisc.edu (R.J.C.); rhweindr@wisc.edu (R.W.)

3- to 6-month period. Once animals were assigned to either control or CR groups, each CR animal's individually determined baseline intake was reduced by 10% per month over a 3-month period to reach the desired 30% restriction.

Any animal that died underwent a complete necropsy by a board-certified pathologist (who was not told the animal's diet group), and the cause of death was determined. On this basis, we distinguished deaths due to age-related causes from those due to acute conditions probably unrelated to aging. Of the original 76 animals, 37% [14 out of 38 (14/38)] of the control animals died of age-related causes as compared to only 13% (5/38) of the CR group. Survival analysis (with a Cox regression) considering only age-related deaths revealed a statistically significant effect of CR in increasing survival ($P = 0.03$; Fig. 2B) with a hazard ratio (HR) of 3.0, indicating that at any point in time, the control animals had three times the rate of death from an age-related cause when compared to animals under CR. Seven control and 9 CR animals died of non–age-related causes, which included complications of anesthesia, gastric bloat, endometriosis, and injury. The effect of CR on overall mortality is in the predicted direction but is currently not statistically significant ($P = 0.16$; Fig. 2C).

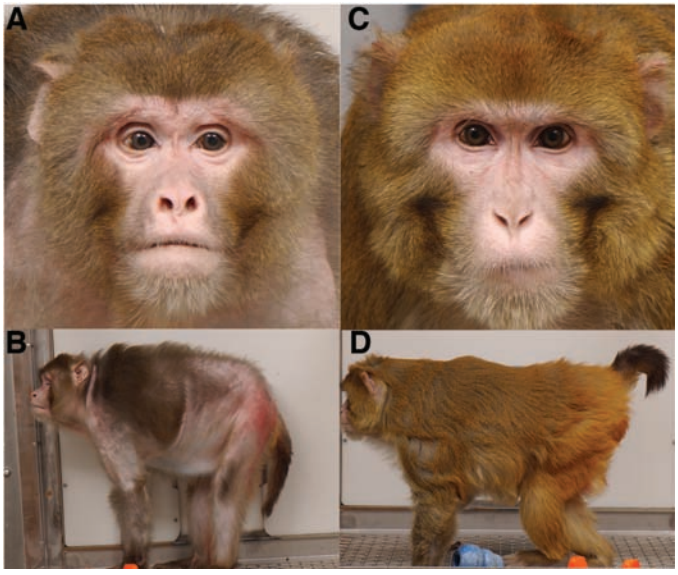

Fig. 1. Animal appearance in old age. (**A** and **B**) Photographs of a typical control animal at 27.6 years of age (about the average life span). (**C** and **D**) Photographs of an age-matched animal on CR.

Age-associated diseases in rhesus monkeys have been well documented for animals at the WNPRC and are similar to those observed in humans (*10*). The most prevalent of such diseases are diabetes, cancer, and cardiovascular disease. To determine the health and aging phenotype of each individual animal, we assessed food intake, body weight, body composition, serum chemistry, glucose regulation, energy expenditure, activity measurement, endocrine profiles, electrocardiogram, blood pressure, brain magnetic resonance imaging, and radiography. These measurements, and a minimum of twice-daily observation of the animals, allowed disease conditions to be identified early and treated appropriately.

The effects of CR on body composition and metabolic function were robust. Body weight

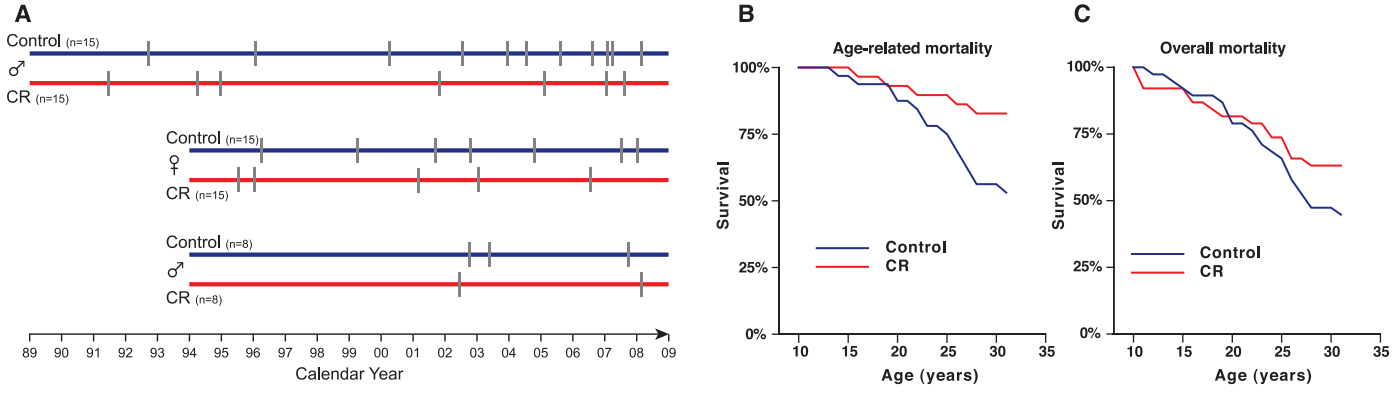

Fig. 2. Longitudinal study design and mortality curves. (**A**) Study design (initial group of 30 males and groups of 30 females and 16 males added in 1994). Hash marks represent deaths. (**B**) Age-related mortality. Animals that died from non–age-related causes are excluded. (**C**) Overall mortality. These curves depict data for animals that died from any cause.

Fig. 3. Effect of CR on age-associated disease. (**A**) Incidence of three major age-related conditions. Hash marks represent the age of diagnosis. Individual animals with multiple discrete diagnoses are represented multiple times. (**B**) Data represent the first occurrence of any age-related disease in each individual animal.

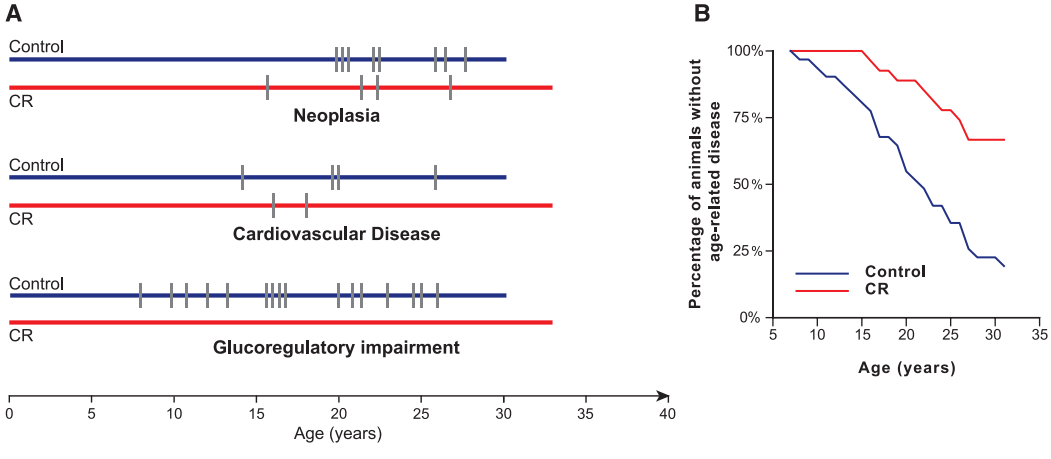

was reduced in animals on CR as compared to that of control animals, primarily due to a decrease in total body fat mass (*11*). The age-associated decline in muscle mass (sarcopenia) was also attenuated in animals exposed to CR (*12*). Dual-energy x-ray absorptiometry analysis of lean muscle mass throughout the study revealed the onset of sarcopenia at 15.5 years, with statistically significant maintenance of lean muscle mass in the animals on CR as compared to that of controls, which has been sustained in animals at old age.

Improvements in metabolic function conferred by CR, specifically insulin sensitivity, have been consistent and striking (*9*, *13*). We found that improved glucose homeostasis was maintained and that diabetes was prevented by CR. Of the initial 38 control animals, 5 progressed to diabetes and an additional 11 were classed as pre-diabetic. In contrast, all animals on CR (even those with compromised metabolic function at baseline) showed no impairment of glucose homeostasis (Fig. 3A). These data are consistent with CR providing long-term health benefits in protection against diabetes.

The incidence of cancer increases with age in rhesus monkeys, and intestinal adenocarcinoma is the most commonly diagnosed cancer in these animals (*14*). The methods used to detect and determine the type of cancer are described (*7*). The incidence of neoplasia was reduced by 50% in the animals undergoing CR as compared to that in controls (Fig. 3A). The most common form of neoplasia was gastrointestinal adenocarcinoma, which was identified in seven of the eight cases in the control animals and in two of the four cases in the animals on CR.

As it is in humans, cardiovascular disease is a prevalent age-associated disorder in rhesus monkeys. The methods used to diagnose cardiovascular disease are described (*7*). The most common diagnosis in living monkeys was leak of the mitral valve. The most frequently observed lesions at necropsy were valvular endocardiosis, cardiomyopathy, and myocardial fibrosis. The incidence of cardiovascular disease was reduced by 50% in the animals subjected to CR as compared to that in controls (Fig. 3A).

To assess the overall incidence of age-associated disease, we recorded the age at which animals experienced their first age-associated diagnosis. The diseases mentioned above and other clinical conditions, including diverticulosis and clinically relevant arthritis, were monitored. The effect of CR in reducing disease onset was statistically significant (P = 0.008, HR of 2.9). Age-related diseases were detected in control animals at about three times the rate they were detected in animals on CR (Fig. 3B). Animals on CR thus appear to be biologically younger than the normally fed animals.

Brain atrophy is a characteristic of human aging that is not accurately reproduced in smaller mammals (*15*). We therefore determined the regional effects of age, diet, and age by diet interactions on gray matter (GM) volume (*16*). There were several cortical regions (the bilateral frontal and temporal cortex) where decreases in volume with age were observed independent of diet (Fig. 4, A to C) (*17*). However, animals subjected to CR had statistically significant preservation of GM volume in subcortical regions (Fig. 4, D to F), including the caudate and putamen and the left insula. The examination of group differences in the slope of age-related GM atrophy (age by diet group interaction) reveals regions where CR significantly modified the aging effect (Fig. 4, G to I) in the midcingulate cortex, lateral temporal cortex bilaterally, and right dorsolateral frontal lobe, indicating relative preservation of volume with age in the CR group. Thus, CR reduced age-associated brain atrophy in key regions that subserve motor function and aspects of executive function.

Our data indicate that adult-onset moderate CR delays the onset of age-associated pathologies and promotes survival in a primate species. In two related nonhuman primate studies, the benefits of CR for health and longevity were less overt, possibly due to differences in study design (*18*, *19*). Given the obvious parallels between rhesus monkeys and humans, the beneficial effects of CR may also occur in humans. This prediction is supported by studies of people on long-term CR, who show fewer signs of cardiovascular aging (*20*). The effect of controlled long-term CR on maximal life span in humans may never be known, but our extended study will eventually provide such data on rhesus monkeys.

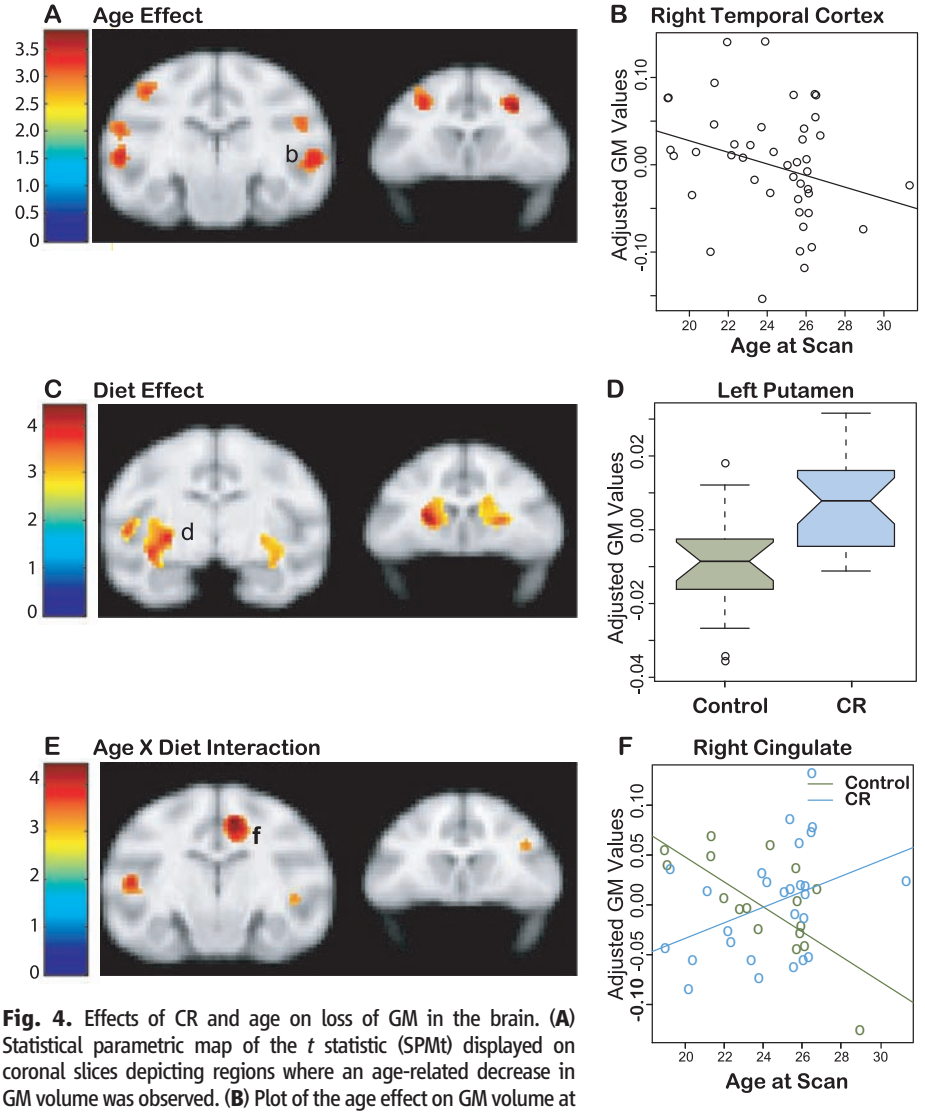

Fig. 4. Effects of CR and age on loss of GM in the brain. (**A**) Statistical parametric map of the *t* statistic (SPMt) displayed on coronal slices depicting regions where an age-related decrease in GM volume was observed. (**B**) Plot of the age effect on GM volume at the labeled location in (A). (**C**) SPMt indicating regions where CR monkeys exhibited preserved volume relative to controls. (**D**) Notched box plots for each group at the location labeled in (C) indicating the mean (center line); the 95% confidence interval (notches); and the 5th, 25th, 75th, and 95th percentiles (horizontal lines), representing the range of variability in the data. (**E**) SPMt depicting regions where the slope between GM volume and age differs as a function of group. (**F**) Scatter plot of the location labeled in (E). All comparisons included sex and total brain volume as covariates. The probability threshold for each *t* contrast was $P < 0.005$ (uncorrected). The color bars in (A), (C), and (E) represent the value of the *t* statistic. The left side of the brain is on the left in the images.

References and Notes

1. C. M. McCay, M. F. Crowell, L. A. Maynard, *Nutrition* **5**, 155 (1935).
2. R. H. Weindruch, R. L. Walford, *The Retardation of Aging and Disease by Dietary Restriction* (Charles C. Thomas, Springfield, IL, 1988).
3. B. K. Kennedy, K. K. Steffen, M. Kaeberlein, *Cell. Mol. Life Sci.* **64**, 1323 (2007).
4. R. M. Anderson, R. Weindruch, *Interdiscip. Top. Gerontol.* **35**, 18 (2007).
5. W. Mair, A. Dillin, *Annu. Rev. Biochem.* **77**, 727 (2008).
6. A. J. Vita, R. B. Terry, H. B. Hubert, J. F. Fries, *N. Engl. J. Med.* **338**, 1035 (1998).
7. Detailed information is supplied as supporting material on *Science* Online.
8. J. W. Kemnitz *et al.*, *J. Gerontol.* **48**, B17 (1993).
9. J. J. Ramsey *et al.*, *Exp. Gerontol.* **35**, 1131 (2000).
10. H. Uno, *Age (Omaha)* **20**, 1 (1997).
11. R. J. Colman, E. B. Roecker, J. J. Ramsey, J. W. Kemnitz, *Aging (Milano)* **10**, 83 (1998).
12. R. J. Colman, T. M. Beasley, D. B. Allison, R. Weindruch, *J. Gerontol. A Biol. Sci. Med. Sci.* **63**, 556 (2008).
13. T. A. Gresl *et al.*, *Am. J. Physiol. Endocrinol. Metab.* **281**, E757 (2001).
14. N. A. Rodriguez *et al.*, *J. Med. Primatol.* **31**, 74 (2002).
15. B. A. Yankner, T. Lu, P. Loerch, *Annu. Rev. Pathol.* **3**, 41 (2008).
16. C. D. Good *et al.*, *Neuroimage* **14**, 21 (2001).
17. G. E. Alexander *et al.*, *J. Neurosci.* **28**, 2710 (2008).
18. N. L. Bodkin, T. M. Alexander, H. K. Ortmeyer, E. Johnson, B. C. Hansen, *J. Gerontol. A Biol. Sci. Med. Sci.* **58**, 212 (2003).
19. J. A. Mattison, M. A. Lane, G. S. Roth, D. K. Ingram, *Exp. Gerontol.* **38**, 35 (2003).
20. J. O. Holloszy, L. Fontana, *Exp. Gerontol.* **42**, 709 (2007).

21. We acknowledge the excellent technical assistance provided by S. Baum, J. Christensen, J. A. Adriansjach, C. E. Armstrong, D. G. McLaren, C. Dizack, D. Shanmuganayagam, J. Root, and the Animal Care, Veterinary and Pathology Staff of the WNPRC. R.W. is a cofounder and member of the board of LifeGen Technologies, a company focused on nutritional genomics, including the impact of dietary interventions on the aging process. This work was supported by NIH grants P01 AG-11915 and P51 RR000167. This research was conducted in part at the WNPRC, which received support from Research Facilities Improvement Program grant numbers RR15459-01 and RR020141-01. This research was supported in part by facilities and resources at the William S. Middleton Memorial Veterans Hospital.

Supporting Online Material

www.sciencemag.org/cgi/content/full/325/5937/201/DC1
Materials and Methods
References

16 March 2009; accepted 1 June 2009
10.1126/science.1173635

Discovery of Swine as a Host for the *Reston ebolavirus*

Roger W. Barrette,[1] Samia A. Metwally,[1]* Jessica M. Rowland,[1] Lizhe Xu,[1] Sherif R. Zaki,[2] Stuart T. Nichol,[2] Pierre E. Rollin,[2] Jonathan S. Towner,[2] Wun-Ju Shieh,[2] Brigid Batten,[2] Tara K. Sealy,[2] Consuelo Carrillo,[1] Karen E. Moran,[1] Alexa J. Bracht,[1] Gregory A. Mayr,[1] Magdalena Sirios-Cruz,[3] Davinio P. Catbagan,[3] Elizabeth A. Lautner,[1] Thomas G. Ksiazek,[2]† William R. White,[1] Michael T. McIntosh[1]*

Since the discovery of the Marburg and Ebola species of filovirus, seemingly random, sporadic fatal outbreaks of disease in humans and nonhuman primates have given impetus to identification of host tropisms and potential reservoirs. Domestic swine in the Philippines, experiencing unusually severe outbreaks of porcine reproductive and respiratory disease syndrome, have now been discovered to host *Reston ebolavirus* (REBOV). Although REBOV is the only member of *Filoviridae* that has not been associated with disease in humans, its emergence in the human food chain is of concern. REBOV isolates were found to be more divergent from each other than from the original virus isolated in 1989, indicating polyphyletic origins and that REBOV has been circulating since, and possibly before, the initial discovery of REBOV in monkeys.

Filoviruses are associated with acute fatal hemorrhagic diseases of humans and/or nonhuman primates. The family consists of two genera: *Marburgvirus*, which comprises various strains of the *Lake Victoria marburgvirus* (MARV) discovered in 1967; and the antigenically distinct genus *Ebolavirus* discovered in 1976, which comprises five species including *Sudan ebolavirus* (SEBOV), *Zaire ebolavirus* (ZEBOV), *Ivory Coast ebolavirus* [also known as Cote d'Ivoire Ebola virus (CIEBOV)], *Bundibugyo ebolavirus* (BEBOV), and *Reston ebolavirus* (REBOV) (*1*). REBOV is the only member of the family thus far not associated with disease in humans (*2*).

Since the discovery of filoviruses more than 40 years ago, ostensibly random, sporadic, and fatal outbreaks of disease in primates have evoked interest in delineation of host tropisms, potential reservoirs for disease transmission, and persistence in nature (*3*). These lines of investigation have recently identified African fruit bats as potential reservoirs for ZEBOV (*4*, *5*) and MARV (*6*, *7*). Similar links to bats have been found for emerging infections in swine and humans involving paramyxoviruses and the severe acute respiratory syndrome (SARS) coronavirus (*8*, *9*).

Until now, REBOV has only been associated with disease in nonhuman primates (*2*, *10*). The virus was originally identified in 1989 in the United States from a shipment of cynomolgus monkeys (*Macaca fascicularis*) from the Philippines. Outbreaks of disease occurred in the United States in 1990 and 1996 and in Italy in 1992, which were traced back to a single facility in the Philippines (fig. S1) (*11*, *12*). Here, we report the identification of REBOV infection in domestic swine coinfected with porcine reproductive and respiratory syndrome virus (PRRSV) that were experiencing a severe respiratory disease syndrome.

In July 2008, the Philippine Department of Agriculture requested the assistance of the U.S.

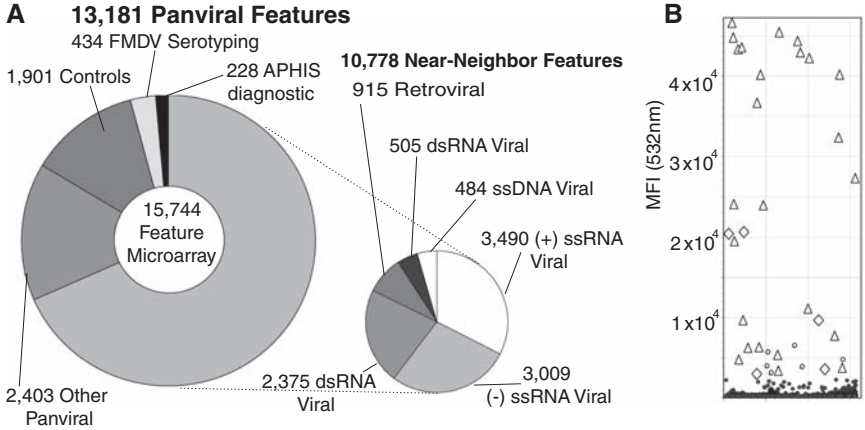

Fig. 1. Detection of REBOV in swine samples from the Philippines. (**A**) Composition of the panviral microarray used to detect REBOV. The microarray feature composition is summarized with reference to the number of unique features for identification of viral pathogens. FMDV, foot-and-mouth disease virus. (**B**) Microarray analysis of Vero cell culture of a swine lymph node from sample group A identified multiple positive features within the genus of Ebola viruses. These features corresponded primarily to sequences from REBOV with minimal reactivity toward SEBOV and ZEBOV. MFI, mean fluorescence intensity (△) Positive *Reston ebolavirus* spp. features; (◇) positive *Ebolavirus* genus features; (○) non-*Ebolavirus* features; and (●) negative features.

[1]Foreign Animal Disease Diagnostic Laboratory, National Veterinary Services Laboratories, Animal and Plant Health Inspection Services, United States Department of Agriculture, Plum Island Animal Disease Center, New York, NY 11944, USA. [2]Special Pathogens and Infectious Disease Pathology Branches, Centers for Disease Control and Prevention, Atlanta, GA 30333, USA. [3]Bureau of Animal Industry, Department of Agriculture, Quezon City 1101, Philippines.

*To whom correspondence should be addressed. E-mail michael.t.mcintosh@aphis.usda.gov (M.T.M.); samia.a.metwally@aphis.usda.gov (S.A.M.)

†Present address: Galveston National Lab, Department of Pathology, University of Texas Medical Branch, Galveston, TX 77550, USA.

Department of Agriculture (USDA), Animal and Plant Health Inspection Service (APHIS), Foreign Animal Disease Diagnostic Laboratory (FADDL), in the diagnostic investigation of recent multiple outbreaks of a respiratory and abortion disease syndrome in swine. Clinical signs resembled a highly pathogenic PRRSV infection, also referred to as "blue ear disease," which has recently been spreading through Asia (*13*–*15*). Sera and tissue samples were collected from five groups of swine at two commercial premises located in Pandi, Bulacan (sample group A); Manaoag, Pangasinan (sample groups C and E); and two inspection check points located in Sto. Nino, San Jose City, Nueva Ecija (sample group B) and Batangas (sample group D) (fig. S1). The diagnostic investigation at FADDL included diagnostics for African swine fever and classical swine fever, a directed investigation for the presence of PRRSV, and a more general search of other viral agents potentially contributing to the disease. Selected tissue samples from each group were tested and found negative for the presence of African swine fever, classical swine fever, swine vesicular disease, and foot-and-mouth disease. Consistent with a respiratory and reproductive disease syndrome, PRRSV was discovered. Sequence analysis of the *NSP2* gene revealed that it was most homologous to Chinese PRRSV isolates recently associated with blue ear disease in Asia. This determination was based on the presence of two unique deletions in the *NSP2* gene of the Philippines PRRSV isolate that are shared by recent Chinese PRRSV isolates associated with pathogenic PRRS in Asia (*14*, *16*). Simultaneously, a lymph node from group A, cultured in Vero cells, a monkey kidney cell line nonpermissive for PRRSV, revealed cytopathic effects indicating the presence of a virus other than PRRSV.

To resolve such unexplained cases, a panviral microarray has been developed that used a near-neighbor approach for the identification of taxonomically conserved viral protein microdomains. This tool consists of tens of thousands of conserved viral genetic signature sequences microscopically arrayed on a slide and is designed to capture extracted and amplified viral nucleic acid from a query sample (Fig. 1A). It is similar in concept and design to previously published pathogen microarrays, including a panmicrobial array named the GreeneChip (*17*, *18*) and the

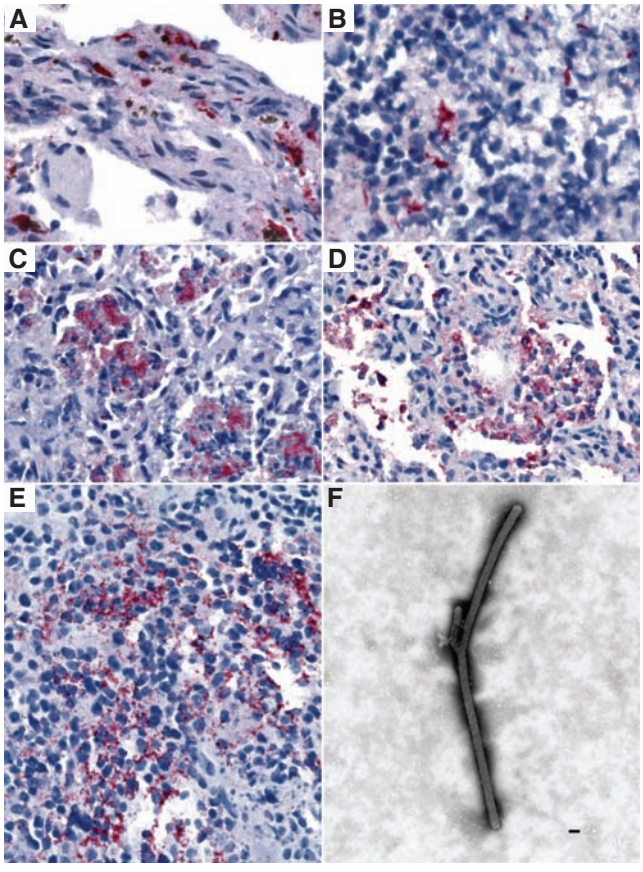

Fig. 2. Immunohistopathology of EBOV and PRRSV. (**A**) Lymph node capsule stained for EBOV antigens. (**B**) Lymph node tissue stained for EBOV antigens. (**C**) Lung tissue stained for EBOV antigens. (**D**) Lung tissue stained for PRRSV antigens. (**E**) Lymph node germinal center stained for PRRSV antigens. (A to E) Immunoalkaline phosphatase staining, naphthol fast red substrate with light hematoxylin counterstain. (**F**) Filovirus particle by negative-staining electron microscopy of the E6 Vero cell culture of the lymph node. Scale bar, 100 nm.

A

Nucleotide Similarity	Reston08-A	Reston08-C	Reston08-E	Reston96
Reston08-A				
Reston08-C	95.5%			
Reston08-E	96.9%	95.8%		
Reston96	97.7%	96.5%	98.70%	
Reston89	97.7%	96.9%	97.90%	98.80%

Amino acid changes		Reston08-A	Reston08-C	Reston08-E	Reston96
Reston08-A	5209 aa				
Reston08-C	5201 aa	193			
Reston08-E	5201 aa	122	193		
Reston96	5201 aa	98	171	64	
Reston89	5201 aa	105	148	92	61

B

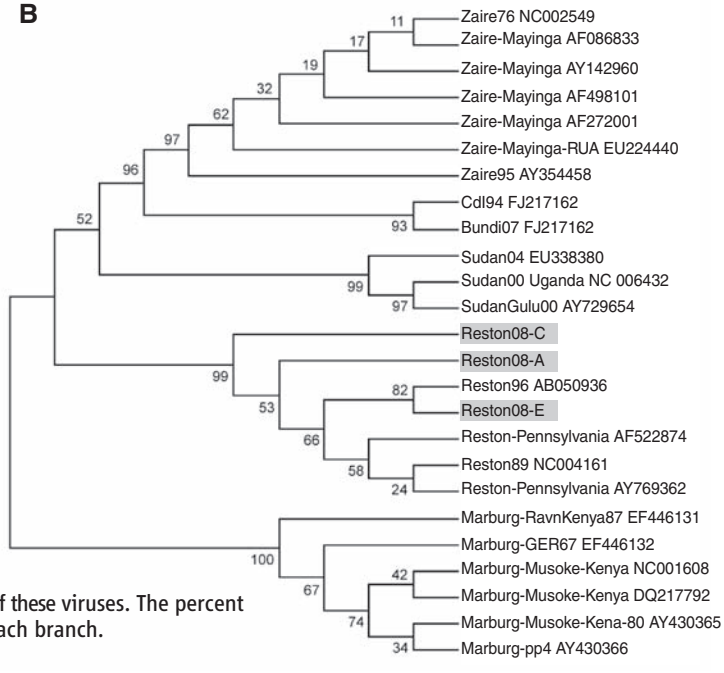

Fig. 3. Phylogeny of REBOV. (**A**) Full-length genomic sequences for Reston08-A, Reston08-C, and Reston08-E were experimentally determined, with the exception of the defined 5′ and 3′ termini, and aligned. Nucleotide similarity scores and the number of predicted amino acid changes between swine and monkey REBOV genomes are shown. (**B**) A consensus neighbor-joining tree drawn without distance topology illustrates the independent branching of the three 2008 Philippine swine viruses within the REBOV clade, demonstrating the divergence between each of these viruses. The percent branching out of 1000 random bootstrap iterations is indicated above each branch.

ViroChip used to characterize the SARS coronavirus (*19*).

To identify the unknown virus, the Vero cell culture was subjected to microarray analysis. Results revealed positive signals for 28 out of 28 distinct array features present in a 3.7-kb span of the REBOV *L* gene (Fig. 1B). By contrast, only 3 out of 30 and 2 out of 30 features were positive for the ZEBOV and SEBOV species, respectively. No other notable signals other than controls were positive (Fig. 1B). Because microarray results are sequence dependent, polymerase chain reaction (PCR) primers designed from the features themselves were used to PCR amplify and sequence the viral cDNA captured by the microarray slide. This sequence analysis confirmed that the captured viral sequences were more than 95% identical to the *L* gene of all previously sequenced REBOV isolates. Because REBOV is classified as a biological safety level 4 select agent, samples were transferred to the Special Pathogens Branch at the Centers for Disease Control and Prevention (CDC) (Atlanta, Georgia), and identification of REBOV was confirmed by Ebola-specific real-time reverse transcription (RT)–PCR analysis (table S1), antigen enzyme-linked immunosorbent assay, immunohistochemistry, and virus isolation in E6 Vero cell culture.

REBOV was only found in sample groups that also tested positive for PRRSV (table S1). Histopathological and immunohistochemical examination of lymph nodes from animals infected with REBOV and PRRSV from groups A and C showed different patterns of antigen localization and pathology (Fig. 2, A, B, and E). REBOV antigens were seen focally in lymphoid and lymph node capsule tissues with minimal necrosis (Fig. 2, A and B), whereas PRRSV antigens were seen in the germinal centers of lymphoid follicles displaying germinal cell hyperplasia and focal necrosis (Fig. 2E). Immunostaining of lung tissues for REBOV and PRRSV revealed localization of both viral antigens in areas displaying mixed inflammatory cells and sloughed necrotic debris in alveolar spaces consistent with interstitial pneumonia (Fig. 2, C and D). Negative-staining electron microscopy of the E6 Vero cell culture of the lymph node from the Bulacan site (group A) revealed filamentous virus particles and partially assembled intermediate particles characteristic of filoviruses (Fig. 2F). Serological studies on 13 swine sera from groups A, B, and D for the detection of antibodies to REBOV were negative. In contrast, antibodies to PRRSV were detected in swine sera from each of the tested sample groups A, B, and D.

RT-PCR revealed REBOV nucleic acid in animals from groups C and E, at the Pangasinan site, and from group A at the Bulacan site (fig. S1 and table S1). Samples from groups B and D did not test positive for REBOV or PRRSV; however, PCR revealed porcine circovirus type 2 (PCV-2) among samples from groups A, B, and D (table S1), and microarray analysis further revealed *Porcine teschovirus 1* from the SK6 porcine kidney cell culture of a tonsil from group D.

Viral genomes for REBOV identified from three samples—designated Reston08-A, Reston08-C, and Reston08-E—at two geographically distinct locations were ~18.9 kb in length and confirmed that the viruses were REBOV species (Fig. 3). The Reston08 viruses were significantly more divergent from each other (3.93% mean difference in nucleotide identity) than from the prototypical reference isolate from 1989 (2.5% mean difference in nucleotide identity), indicating polyphyletic origins of the REBOV infections in swine at both locations (Fig. 3A).

The lack of a phylogenetic clade, distinct from viruses in macaques, for the recent REBOV infections in swine (Fig. 3B) suggests that REBOV has been circulating since, and possibly before, the initial discovery of REBOV in monkeys exported from the Philippines in 1989. The isolation of REBOV from swine represents an extension in the known host tropism. The interisolate divergence of the three recent swine isolates is greater than that observed among the monkey isolates obtained from the single implicated primate export facility (Fig. 3A). Given the broader genetic diversity and geographic distribution of REBOV in swine, it is possible that REBOV spilled over to monkeys and swine from an as yet unidentified host. Bats have been implicated as reservoirs for other filoviruses, including ZEBOV and MARV, and may also represent a candidate reservoir for REBOV.

Of 141 tested individuals, we identified 6 individuals who worked on pig farms or with swine products that had positive serum immunoglobulin G (IgG) titers to REBOV, confirming the potential transmission from pigs to humans. The remaining 135 individuals tested negative for IgG titers to REBOV. Given the observed sequence divergence between the Reston08 viruses, a broader surveillance program is being planned. REBOV infection in domestic swine raises concern about the potential for emerging disease in humans and a wider range of livestock. However, as in previous REBOV incidents, there is no evidence of disease in humans despite the apparent occurrence of human infections evidenced by seropositive titers of REBOV-specific antibody.

The role of swine as either an incidental host or an integral part of the virus's transmission cycle has yet to be determined. Because evidence of coinfection with PRRSV, an arterivirus, was found with REBOV, we can speculate about a link between coinfection and disease in swine. This possibility is of interest in light of the atypical, highly pathogenic infections in swine by PRRSV that are currently spreading through Asia (*14*–*16*). Simian hemorrhagic fever virus, a well-known pathogen of captive primates and also an arterivirus of previously characterized pathogenicity, was identified in a coinfection of monkeys during the first detected outbreak of REBOV (*20*), although later studies clearly demonstrated the pathogenicity of REBOV as a single agent in experimentally infected monkeys (*21*).

There is concern that its passage through swine may allow REBOV to diverge and shift its potential for pathogenicity. Moreover, REBOV infections in swine highlight the need for investigations into the pathogenesis of REBOV in coinfections or in immunocompromised hosts. Through domestic and international interdisciplinary cooperation and collaboration, it is expected that future epidemiology and pathogenesis studies will shed light on the potential reservoirs, mode(s) of transmission, mechanisms of pathogenesis, prevalence of REBOV in nature, and its consequences for agricultural industries and trade.

References and Notes

1. J. S. Towner *et al.*, *PLoS Pathog.* **4**, e1000212 (2008).
2. S. Morikawa, M. Saijo, I. Kurane, *Comp. Immunol. Microbiol. Infect. Dis.* **30**, 391 (2007).
3. J. E. Strong *et al.*, *Proc. Natl. Acad. Sci. U.S.A.* **105**, 17982 (2008).
4. E. M. Leroy *et al.*, *Nature* **438**, 575 (2005).
5. R. Swanepoel *et al.*, *Emerg. Infect. Dis.* **2**, 321 (1996).
6. J. S. Towner *et al.*, *PLoS One* **2**, e764 (2007).
7. R. Swanepoel *et al.*, *Emerg. Infect. Dis.* **13**, 1847 (2007).
8. S. Wong, S. Lau, P. Woo, K. Y. Yuen, *Rev. Med. Virol.* **17**, 67 (2007).
9. W. Li *et al.*, *Science* **310**, 676 (2005).
10. P. E. Rollin *et al.*, *J. Infect. Dis.* **179** (Suppl. 1), S108 (1999).
11. M. E. Miranda *et al.*, *J. Infect. Dis.* **179** (Suppl. 1), S115 (1999).
12. C. J. Peters, J. W. LeDuc, *J. Infect. Dis.* **179** (Suppl. 1), ix (1999).
13. J. Han, Y. Wang, K. S. Faaberg, *Virus Res.* **122**, 175 (2006).
14. K. Tian *et al.*, *PLoS One* **2**, e526 (2007).
15. Y. Li *et al.*, *Vet. J.* **174**, 577 (2007).
16. Y. Li, X. Wang, P. Jiang, W. Chen, X. Wang, *Arch. Virol.* **153**, 1877 (2008).
17. G. Palacios *et al.*, *Emerg. Infect. Dis.* **13**, 73 (2007).
18. P. L. Quan *et al.*, *J. Clin. Microbiol.* **45**, 2359 (2007).
19. D. Wang *et al.*, *PLoS Biol.* **1**, E2 (2003).
20. P. B. Jahrling *et al.*, *Lancet* **335**, 502 (1990).
21. P. B. Jahrling *et al.*, *Arch. Virol. Suppl.* **11**, 115 (1996).

22. We thank members of the Diagnostic Services Section of FADDL (H. Petrowski, F. Mohamed, and M. Berninger), the CDC Special Pathogens Branch (D. Cannon, A. Comer, S. Dickerson, C. Manning, D. Miller, and Z. Reed), and the CDC Infectious Disease Pathology Branch (C. Paddock, P. Adem, and C. Goldsmith) for expert technical assistance. We are also grateful to P. Hauer (APHIS, USDA) for critical review of the manuscript and to T. Gomez and J. Willnow (USDA) for facilitating conversations between U.S. agencies and the Philippines. We thank G. Risatti for protocols for PRRSV RT-PCR. This work was funded by the USDA as part of an ongoing foreign animal disease diagnostic investigation. Support for microarray development and implementation is sponsored by the APHIS Science Fellows Program, USDA, and the Department of Homeland Security. R.W.B. is an award recipient of the APHIS Science Fellows Program. PRRSV *NSP2* sequences are available at GenBank (accession numbers FJ641193, FJ641194, and FJ641195), as are Reston08-A, Reston08-C, and Reston08-E sequences (accession numbers FJ621583, FJ621584, and FJ621585, respectively). Microarray data and analyses are available for download from NCBI Gene Expression Omnibus (accession GSE15687) at https://www.ncbi.nlm.nih.gov/geo/query/acc.cgi?acc=GSE15687. All authors declare that they have no competing interests.

Supporting Online Material

www.sciencemag.org/cgi/content/full/325/5937/204/DC1
Materials and Methods
Fig. S1
Table S1
References

24 February 2009; accepted 19 May 2009
10.1126/science.1172705

Induction of Synaptic Long-Term Potentiation After Opioid Withdrawal

Ruth Drdla,* Matthias Gassner,* Ewald Gingl, Jürgen Sandkühler†

μ-Opioid receptor (MOR) agonists represent the gold standard for the treatment of severe pain but may paradoxically also enhance pain sensitivity, that is, lead to opioid-induced hyperalgesia (OIH). We show that abrupt withdrawal from MOR agonists induces long-term potentiation (LTP) at the first synapse in pain pathways. Induction of opioid withdrawal LTP requires postsynaptic activation of heterotrimeric guanine nucleotide–binding proteins and *N*-methyl-D-aspartate receptors and a rise of postsynaptic calcium concentrations. In contrast, the acute depression by opioids is induced presynaptically at these synapses. Withdrawal LTP can be prevented by tapered withdrawal and shares pharmacology and signal transduction pathways with OIH. These findings provide a previously unrecognized target to selectively combat pro-nociceptive effects of opioids without compromising opioid analgesia.

Opioids are widely used by pain patients and by addicts. Abrupt withdrawal from acute opioid application may lead to opioid-induced hyperalgesia (OIH) that is also a key feature of the highly aversive withdrawal syndrome after prolonged opioid consumption (*1*). Several mechanisms have been proposed to underlie OIH (*2*–*7*). It has been suggested that opioid-induced and injury-induced hyperalgesia share underlying mechanisms (*8*, *9*). A synaptic model of injury-induced hyperalgesia is the long-term potentiation (LTP) at synapses between nociceptive C fibers and neurons in superficial spinal dorsal horn (*10*, *11*). It is an intriguing but as yet unproven hypothesis that opioids may not only modify (*12*, *13*) but also induce synaptic plasticity (*13*). We tested this hypothesis directly. We used a slice preparation from rat lumbar spinal dorsal horn with long dorsal roots attached. Whole-cell recordings were made from lamina I neurons with monosynaptic excitatory input from C fibers (*14*). Bath application of the MOR agonist D-(-)-2-amino-5-phosphonopentanoic acid (DAMGO) for 15 min induced a rapid, dose-dependent depression of C fiber–evoked excitatory postsynaptic currents (EPSCs) in all neurons tested without evidence of acute tolerance [inhibition was to 40 ± 7% (SEM) at 2 min of application and to 39 ± 7% at 15 min; Fig. 1, A and B]. Upon washout of DAMGO, responses became potentiated to 165 ± 17% of control 15 min after washout in 10 out of 14 neurons (Fig. 1, A and B). This opioid withdrawal LTP remained undiminished for the remaining recording periods of up to 100 min.

High doses of spinal morphine may lead to nonspecific OIH that is not mediated by opioid

Department of Neurophysiology, Center for Brain Research, Medical University of Vienna, Spitalgasse 4, 1090 Vienna, Austria.

*These authors contributed equally to this work.
†To whom correspondence should be addressed. E-mail: juergen.sandkuehler@meduniwien.ac.at

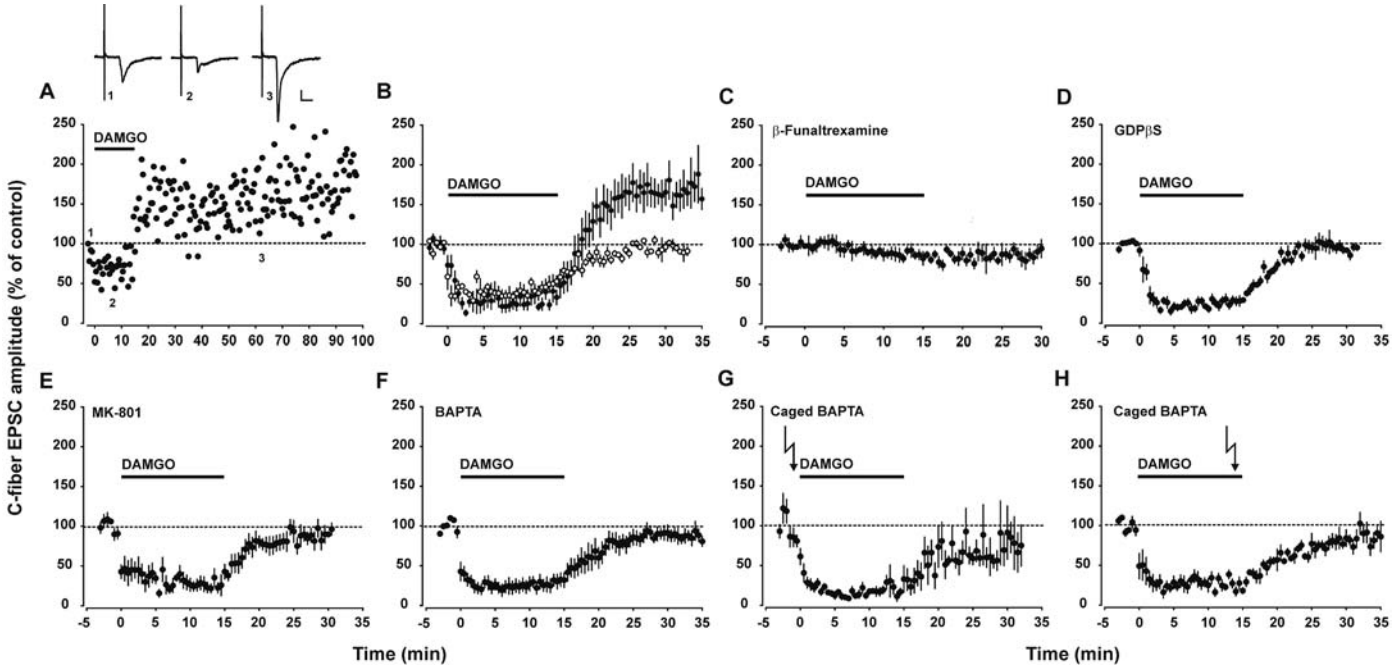

Fig. 1. LTP induction at synapses of afferent C fibers in vitro by acute application of MOR agonist DAMGO involves postsynaptic G protein coupling and NMDA receptor–dependent Ca^{2+} signaling. (**A**) Opioid withdrawal LTP in a spinal cord lamina I neuron. DAMGO (0.5 μM) was bath-applied for 15 min beginning at time 0 (black horizontal bar in all graphs). Amplitudes of individual C fiber–evoked EPSCs were normalized to predrug values and plotted versus time. The dotted lines in this and all other graphs indicate normalized EPSC amplitudes before DAMGO application. Insets show individual EPSC traces recorded at the indicated time points; calibration bars indicate 10 ms and 20 pA. (**B**) Average time courses of 10 neurons where DAMGO induced an acute synaptic depression ($P = 0.001$) and LTP upon washout ($P = 0.001$; solid circles) and four neurons in which DAMGO produced an acute depression only ($P = 1$; open circles). Error bars indicate 1 SEM. (**C**) Bath application of MOR antagonist β-funaltrexamine (25 μM) blocked both acute depression and LTP induction in all five neurons tested ($P = 0.011$). (**D**) Blocking postsynaptic G protein coupling with GDP-β-S added to the pipette solution (0.5 mM) blocked LTP induction in all five neurons tested without affecting acute synaptic depression ($P = 0.011$). (**E**) Blocking postsynaptic NMDA receptors with MK-801 added to the pipette solution abolished LTP induction in all five neurons tested ($P = 0.011$). (**F**) Preventing postsynaptic rise in $[Ca^{2+}]_i$ by Ca^{2+} chelator BAPTA added to the pipette solution fully blocked LTP induction but not acute synaptic depression in six out of seven neurons ($P = 0.024$). (**G**) Caged BAPTA was added to the pipette solution and released by flash photolysis (flash symbol) 1 min before DAMGO application. This blocked LTP induction in all five neurons tested ($P = 0.011$). (**H**) As in (G) but with flash photolysis 1 min before washout of DAMGO ($P = 0.011$).

receptors (*15*, *16*). We excluded any nonspecific effects by showing that acute depression and withdrawal LTP were both abolished by blockade of opioid receptors with naloxone (fig. S1) and by the MOR selective antagonist β-funaltrexamine (Fig. 1C). Any contribution of γ-aminobutyric acid type A ($GABA_A$) or glycine receptors, for example by disinhibition of synaptic strength (*17*, *18*) or block of LTP at inhibitory synapses (*12*), can be

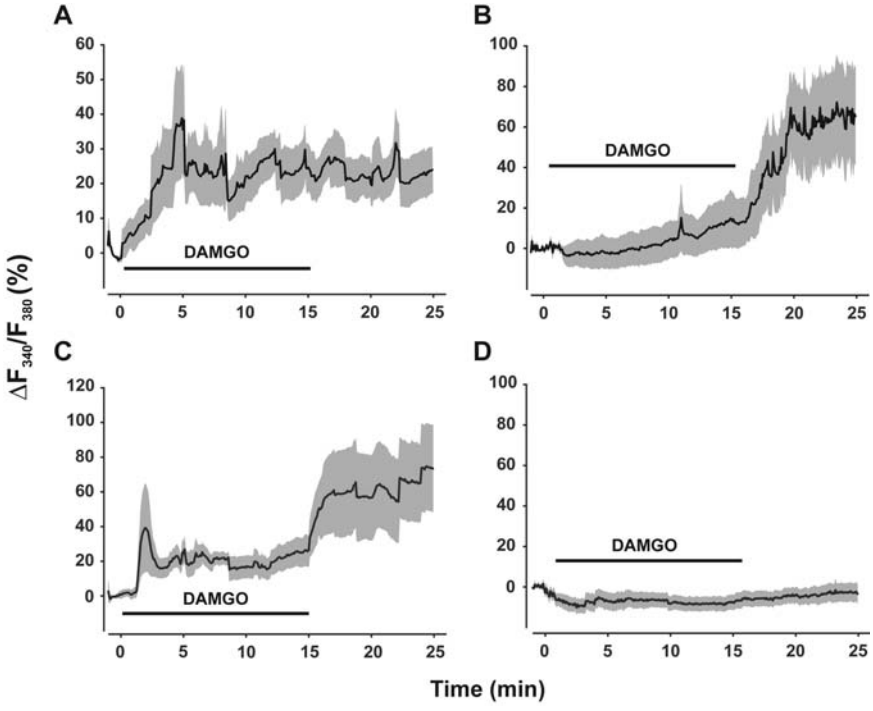

Fig. 2. Opioids induce Ca^{2+} rise in superficial spinal dorsal horn neurons in vitro during application and/or during washout. In transverse slices from lumbar spinal dorsal horn, lamina I neurons were filled with fura-2 pentapotassium salt through the patch pipette to measure Ca^{2+} gradients during bath application of DAMGO (horizontal bars) and upon washout. From a total of 35 superficial spinal dorsal horn neurons tested, 11 responded with an elevation of Ca^{2+} during DAMGO application (**A**), 8 neurons responded upon washout (**B**), 7 neurons displayed dual responses (**C**), and 9 neurons did not show any rise in Ca^{2+} (**D**). Solid lines represent mean values, and gray areas, one SEM.

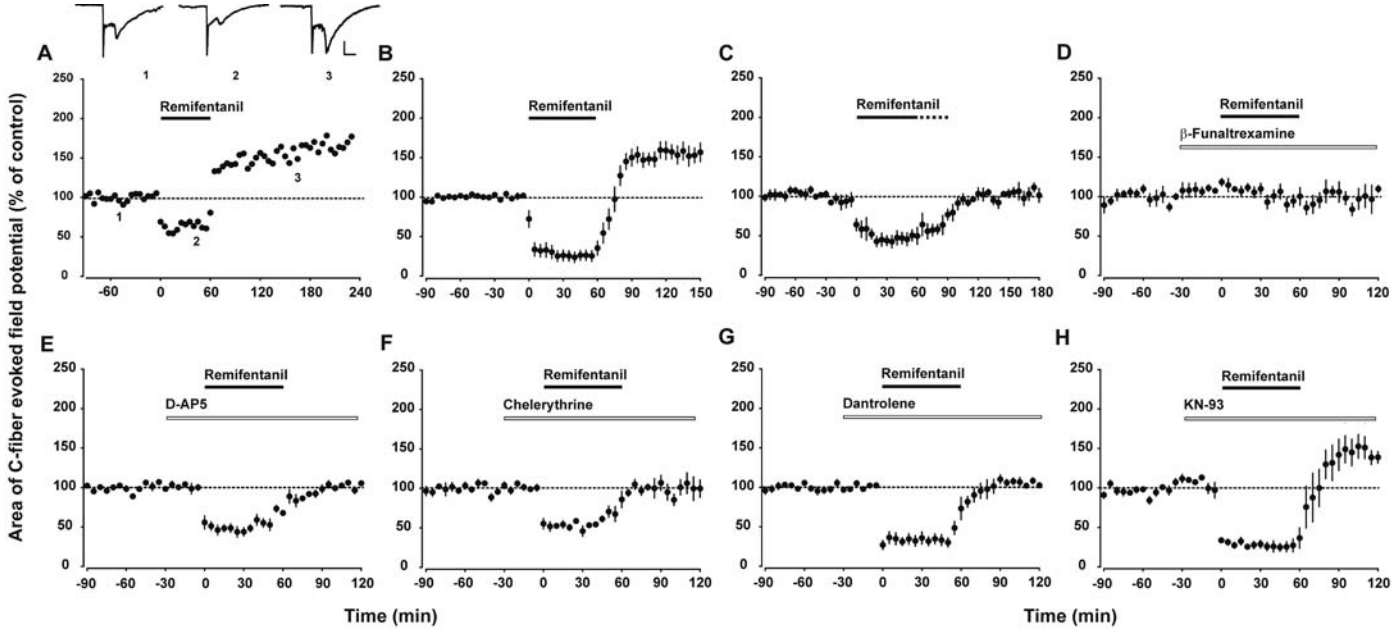

Fig. 3. Intravenous infusions of ultrashort-acting MOR agonist remifentanil induce LTP at C fiber synapses in vivo that involves activation of spinal NMDA receptors and PKC but not CaMKII. (**A**) Time course of area under the curve of individual C fiber–evoked field potentials in one rat. Values were normalized to predrug values (dotted line) and plotted versus time. In this and in all other graphs, remifentanil was injected as a bolus (30 $\mu g \cdot kg^{-1}$) followed by an infusion (450 $\mu g \cdot kg^{-1} \cdot hour^{-1}$ for 1 hour, black horizontal bars). Insets show individual traces of field potentials recorded at indicated time points. Calibration bars, 100 ms and 0.5 mV. (**B**) Averaged time course of C fiber–evoked field potentials recorded from 14 animals where withdrawal induced LTP ($P = 0.001$). Error bars indicate 1 SEM. (**C**) Tapered withdrawal (dotted line) from remifentanil over a period of 30 min prevented the potentiation of C fiber–evoked field potentials in all five animals tested ($P = 0.001$). (**D**) Spinal superfusion with β-funaltrexamine (250 μM, open horizontal bar) abolished acute depression and withdrawal LTP in all five animals tested ($P = 0.001$). (**E**) Topical application of NMDA receptor blocker D-AP5 (100 μM, open horizontal bar) blocked LTP induction ($P = 0.001$) but not acute synaptic depression by remifentanil ($P = 1$). (**F**) Spinal application of PKC inhibitor chelerythrine chloride (800 μM, open bar) blocked LTP induction ($P = 0.001$) but not synaptic depression by DAMGO ($P = 1$). (**G**) Spinal application of the ryanodine receptor blocker dantrolene (500 μM, open bar) blocked LTP induction ($P = 0.001$) but not acute depression by remifentanil ($P = 1$). (**H**) In contrast, spinal application of CaMKII blocker KN-93 at a concentration (400 μM, open bar) that blocks activity-dependent LTP in this in vivo model (*23*) failed to affect opioid withdrawal LTP ($P = 1$).

ruled out because experiments were done in the presence of bicuculline and strychnine.

Blockade of postsynaptic heterotrimeric guanine nucleotide–binding proteins (G proteins) with guanosine 5′-*O*-(2′-thiodiphosphate) (GDP-β-S) included in the pipette solution abolished opioid withdrawal LTP without affecting the acute depression of synaptic strength in C fibers (Fig. 1D). This suggests that withdrawal LTP requires postsynaptic G protein signaling. In contrast, the depressant effect of opioids is induced presynaptically at these synapses.

OIH and activity-dependent forms of LTP at C fiber synapses require activation of *N*-methyl-D-aspartate (NMDA) receptors (*8*, *10*). Blockade of postsynaptic NMDA receptors by MK-801 added to the pipette solution fully blocked opioid withdrawal LTP without affecting acute synaptic depression by DAMGO (Fig. 1E). Adding the Ca^{2+} chelator BAPTA [1,2-bis(2-aminophenoxy) ethane-*N*,*N*,*N*′,*N*′-tetraacetic acid] to the pipette solution had the same effect (Fig. 1F). OIH may develop during continuous chronic application of opioids or upon their withdrawal. The time point when opioids elevate intracellular calcium ion concentrations ($[Ca^{2+}]_i$) to cause LTP is, however, not known. We found that in individual lamina I neurons $[Ca^{2+}]_i$ may rise during acute opioid application (Fig. 2A), upon washout (Fig. 2B), or both (Fig. 2C). We next asked which of these different types of Ca^{2+} rise is essential for the induction of withdrawal LTP. We used a caged form of BAPTA to chelate Ca^{2+} ions in the postsynaptic neurons at defined time points by flash photolysis. When BAPTA was uncaged before DAMGO application, withdrawal LTP was prevented (Fig. 1G), confirming the previous experiment with BAPTA added to the pipette solution (Fig. 1F). Flash photolysis directly before the washout of DAMGO also fully blocked withdrawal LTP (Fig. 1H), indicating that a rise in postsynaptic $[Ca^{2+}]_i$ upon opioid withdrawal is essential for the induction of withdrawal LTP.

To evaluate whether opioid withdrawal LTP exists in the spinal cord of living animals with descending and segmental inhibitory systems intact, we next recorded C fiber–evoked field potentials in the superficial spinal dorsal horn of deeply anaesthetized adult rats (*11*). We used the ultrashort-acting MOR agonist remifentanil, which induces OIH in humans and in rodents. Intravenous injections of remifentanil caused a rapid depression of C fiber–evoked field potentials to 30 ± 8% within 5 min and to 33 ± 8% at 60 min, suggesting that no acute tolerance developed. Upon abrupt termination of the infusion, responses were potentiated in 14 out of 16 animals tested (Fig. 3, A and B). Mean potentiation was to 149 ± 1% of control (n = 14) at 120 to 150 min after the infusion and remained undiminished throughout the recording period of up to 4 hours (Fig. 3A). Boli only or shorter infusions (30 min) also led to withdrawal LTP but with lower incidence (fig. S2, A and B). Opioid withdrawal LTP was prevented when opioid infusion was tapered off over a period of 30 min (Fig. 3C). Application of vehicle only had no effect (fig. S2D). After intravenous remifentanil injection, opioid receptors in spinal cord mediated both the acute synaptic depression and the withdrawal LTP because spinal application of naloxone (fig. S2C) or β-funaltrexamine (Fig. 3D) blocked both effects. Blockade of NMDA receptors by spinal superfusion with the NMDA receptor antagonist [D-Ala^2, N-MePhe^4, Gly-ol]-enkephalin (D-AP5) also abolished withdrawal LTP in vivo but had no effect on the acute depression by systemic remifentanil (Fig. 3E). OIH apparently involves activation of protein kinase C (PKC) (*19*–*21*). Consistently, spinal application of PKC blocker chelerythrine abolished induction of withdrawal LTP without affecting the acute depression of synaptic strength (Fig. 3F).

Activity-dependent forms of LTP at C fiber synapses involve Ca^{2+} release from intracellular ryanodine receptor-sensitive Ca^{2+} stores and activation of calcium-calmodulin–dependent protein kinase II (CaMKII) (*11*, *22*, *23*). Blockade of ryanodine receptors by spinal superfusions with dantrolene blocked withdrawal LTP (Fig. 3G), whereas spinal application of CaMKII blocker KN-93 was ineffective (Fig. 3H). Thus, opioid withdrawal LTP requires a rise in postsynaptic Ca^{2+}, likely fueled by Ca^{2+} influx through NMDA receptor channels and by the release from intracellular stores. Interestingly, the CaMKII blocker had no effect, either on acute depression or on potentiation. Signaling pathways between opioid withdrawal LTP and activity-dependent forms of LTP thus overlap only partially.

It is not known whether opioids may also raise Ca^{2+} levels in spinal neurons in vivo. To test this directly, we used in vivo two-photon laser-scanning microscopy and assessed Ca^{2+} gradients in superficial dorsal horn neurons before, during, and after intravenous application of remifentanil. Of the 31 lamina I neurons tested, 15 responded with an elevation of Ca^{2+} concentration to the application of the opioid. In 6 neurons Ca^{2+} levels rose during drug application (Fig. 4A). In 9 other neurons, Ca^{2+} concentration remained constant during infusions but rose upon withdrawal from the opioid (Fig. 4B). One might thus speculate that these two patterns of Ca^{2+} rise consistently found in vivo and in vitro and involving distinct neuronal populations in superficial spinal dorsal horn may contribute to different forms of OIH. One that develops during continuous opioid application might contribute to opioid tolerance (*8*, *20*, *24*, *25*), and another one that may be part of the opioid withdrawal syndrome (*21*).

We have identified an activity-independent form of LTP that is induced by withdrawal from acute application of MOR agonists. This opioid withdrawal LTP shares signal transduction pathways with OIH. Opioid withdrawal- and activity-dependent forms of LTP (*11*, *22*) at C fiber synapses require activation of NMDA receptors, rise in postsynaptic Ca^{2+}, and activation of PKC. NMDA receptors have a PKC phosphorylation site, and phosphorylation removes the voltage-sensitive Mg^{2+} block (*26*). This may lead to NMDA receptor activation and Ca^{2+} influx at or near the resting membrane potential in the absence of any presynaptic activity, possibly by glial cell–derived glutamate (*27*) or elevated glutamate levels during opioid withdrawal (*28*).

OIH typically includes enhanced responsiveness to C fiber–mediated noxious mechanical and thermal stimuli (*1*). Collectively the published and present data suggest that opioid withdrawal LTP at synapses of nociceptive C fibers is a mechanism of OIH. We found that withdrawal LTP can be prevented by a tapered withdrawal regime and that it is mechanistically and spatially distinct from opioid-induced synaptic depression. This encourages hopes that OIH may be targeted specifically without interfering with powerful opioid analgesia.

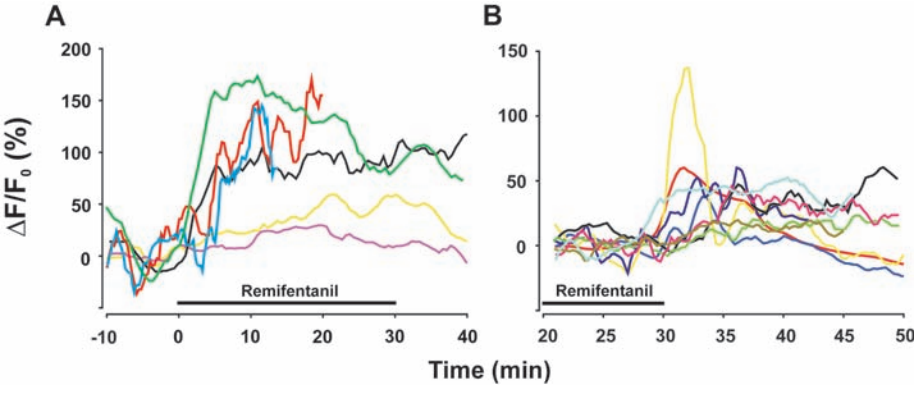

Fig. 4. In vivo imaging of Ca^{2+} gradients in superficial spinal dorsal horn neurons during application and upon washout of an opioid. A cardiopulmonary bypass was used to improve mechanical stability (*14*). Ca^{2+} gradients of a total of 31 neurons were monitored. (**A**) Six neurons responded with elevated Ca^{2+} levels during opioid application ($P < 0.001$). (**B**) Nine other neurons displayed Ca^{2+} rise upon washout ($P < 0.001$). Sixteen neurons did not respond with a significant change in $[Ca^{2+}]_i$ to opioid application. Each neuron is represented by a different color.

References and Notes

1. M. S. Angst, J. D. Clark, *Anesthesiology* **104**, 570 (2006).
2. F. Simonin *et al.*, *Proc. Natl. Acad. Sci. U.S.A.* **103**, 466 (2006).

3. H.-Y. Wang, E. Friedman, M. C. Olmstead, L. H. Burns, *Neuroscience* **135**, 247 (2005).
4. J. P. Fry, A. Herz, W. Zieglgänsberger, *Br. J. Pharmacol.* **68**, 585 (1980).
5. C. H. Brown, J. A. Russell, *Stress* **7**, 97 (2004).
6. L. R. Gardell *et al*., *J. Neurosci.* **22**, 6747 (2002).
7. T. W. Vanderah *et al*., *J. Neurosci.* **21**, 279 (2001).
8. D. J. Mayer, J. Mao, J. Holt, D. D. Price, *Proc. Natl. Acad. Sci. U.S.A.* **96**, 7731 (1999).
9. A. Vardanyan *et al*., *J. Pain* **10**, 243 (2008).
10. J. Sandkühler, *Physiol. Rev.* **89**, 707 (2009).
11. H. Ikeda *et al*., *Science* **312**, 1659 (2006).
12. F. S. Nugent, E. C. Penick, J. A. Kauer, *Nature* **446**, 1086 (2007).
13. J. T. Williams, M. J. Christie, O. Manzoni, *Physiol. Rev.* **81**, 299 (2001).
14. Materials and methods are available as supporting material on *Science* Online.
15. C. J. Woolf, *Brain Res.* **209**, 491 (1981).
16. T. L. Yaksh, G. J. Harty, B. M. Onofrio, *Anesthesiology* **64**, 590 (1986).
17. W. Zieglgänsberger, E. D. French, G. R. Siggins, F. E. Bloom, *Science* **205**, 415 (1979).
18. C. W. Vaughan, S. L. Ingram, M. A. Connor, M. J. Christie, *Nature* **390**, 611 (1997).
19. L. Chen, L.-Y. Huang, *Neuron* **7**, 319 (1991).
20. J. Mao, D. D. Price, D. J. Mayer, *J. Neurosci.* **14**, 2301 (1994).
21. S. M. Sweitzer *et al*., *Pain* **110**, 281 (2004).
22. H. Ikeda, B. Heinke, R. Ruscheweyh, J. Sandkühler, *Science* **299**, 1237 (2003).
23. R. Drdla, J. Sandkühler, *Mol. Pain* **4**, 18 (2008).
24. L. P. Vera-Portocarrero *et al*., *Pain* **129**, 35 (2007).
25. B. L. Kieffer, C. J. Evans, *Cell* **108**, 587 (2002).
26. L. Chen, L.-Y. Huang, *Nature* **356**, 521 (1992).
27. P. Sah, S. Hestrin, R. A. Nicoll, *Science* **246**, 815 (1989).
28. K. H. Jhamandas, M. Marsala, T. Ibuki, T. L. Yaksh, *J. Neurosci.* **16**, 2758 (1996).
29. Supported by grant no. P18129-B02 from the Austrian Science Fund (FWF).

Supporting Online Material

www.sciencemag.org/cgi/content/full/325/5937/207/DC1
Materials and Methods
Figs. S1 and S2
References

2 February 2009; accepted 12 May 2009
10.1126/science.1171759

A Functional Role for Adult Hippocampal Neurogenesis in Spatial Pattern Separation

C. D. Clelland,[1,2] M. Choi,[2] C. Romberg,[3] G. D. Clemenson Jr.,[1] A. Fragniere,[2] P. Tyers,[2] S. Jessberger,[4] L. M. Saksida,[3,5] R. A. Barker,[2,6]* F. H. Gage,[1]*† T. J. Bussey[3,5]*†

The dentate gyrus (DG) of the mammalian hippocampus is hypothesized to mediate pattern separation—the formation of distinct and orthogonal representations of mnemonic information—and also undergoes neurogenesis throughout life. How neurogenesis contributes to hippocampal function is largely unknown. Using adult mice in which hippocampal neurogenesis was ablated, we found specific impairments in spatial discrimination with two behavioral assays: (i) a spatial navigation radial arm maze task and (ii) a spatial, but non-navigable, task in the mouse touch screen. Mice with ablated neurogenesis were impaired when stimuli were presented with little spatial separation, but not when stimuli were more widely separated in space. Thus, newborn neurons may be necessary for normal pattern separation function in the DG of adult mice.

The dentate gyrus (DG) is thought to contribute to spatial or episodic memory by functioning as a pattern separator (*1*–*3*). Pattern separation is the formation of distinct representations of similar inputs (*4*). At the cellular level, pattern separation is achieved through the dispersion of cortical inputs from the entorhinal cortex onto a greater number of dentate granule cells (DGCs) with small place fields. By virtue of low firing rates (*5*) and sparse connectivity between DGCs and CA3 pyramidal cells (*6*), DGCs are particularly adapted to maintain and transmit orthogonalized information. This ability to pattern separate, or to differentially encode small or weak changes derived from increasingly similar or interfering inputs, is particularly important for the accuracy of memory encoding. Similarly, at the behavioral level, the ability to form and use memories derived from very similar stimuli that are closely presented in space and/or time depends on the ability to pattern separate incoming, and often complex, information (*1*, *7*, *8*). Lesions of the complete DG circuitry result in impaired pattern separation–dependent memory (*7*–*9*).

The DG is also one of two sites where neurogenesis is ongoing throughout life (*10*). Adult-born neurons integrate into DG circuitry (*11*–*13*) and are thought to play a role in learning and memory (*11*, *14*, *15*), but their contribution to hippocampal function remains unclear, in part because of the limited availability of behavioral assays probing this question.

We used low-dose x-irradiation (*16*) to focally ablate neurogenesis in the hippocampus of 8-week-old adult female C57Bl/6 mice (*17*, *18*), while sparing the rest of the brain, including the subventricular zone (Figs. 1, A to C and 2, A, G, and H, and figs. S1, A and B, S2, S3, and S4). To confirm that newborn neurons had been persistently ablated as well as to examine the extent of inflammation in the hippocampus after a 2-month recovery period post-irradiation, we analyzed the brains of irradiated (IR) and sham test mice (n = 5) that were killed the day behavioral testing commenced. IR test mice did not show differences in microglia numbers or morphology compared to sham controls (fig. S1, C and D), but they did show a statistically significant reduction in total numbers of both immature neurons and proliferating cells in the hippocampus (fig. S2, A to E).

Two months after irradiation, IR (n = 10) and sham (n = 9) mice were tested in a delayed nonmatching to place (DNMP) radial arm maze (RAM) task that we developed to test spatial pattern separation–dependent memory (Fig. 1). As we had hypothesized that deficits resulting from a knock-down of neurogenesis might be subtle, we purposely designed a challenging spatial task by using a large eight-arm RAM and ensuring the use of external spatial cues in forming spatial memories while eliminating odor as a facilitatory intramaze cue. The difficulty of this task was reflected in lower performance levels by sham mice compared with other RAM tasks (*19*). Mice were tested for the ability to select, from a choice of two arms, the arm location that had not been presented in a previous sample phase (DNMP) (Fig. 1E). During the sample phase, all arms except a start arm and the sample arm were blocked off. The mouse was permitted to visit the sample arm and retrieve a food pellet reward. To eliminate the ability of mice to use odor as a facilitatory intramaze cue, the RAM apparatus was rotated on wheels between sample and choice presentations, so that the locations of the start and sample arms, but not the arms themselves, were held constant during each trial. The rotation took ~20 s. During the choice phase, arms in the start and sample (unrewarded) locations and an additional correct (rewarded) location were open. Correct arms varied in distance from the sample arm by a spatial separation of two, three, or four arms (Fig. 1D). Mice that entered the correct (rewarded) arm were considered to have made correct choices. Mice that made incorrect choices (i.e., entered the sample/unrewarded arm) were allowed to self-correct. Mice went through four trials (sample plus choice phases) per day of pseudorandomly presented combinations of start plus sample plus correct arms for 15 consecutive days (60 trials total, 20 trials of each spatial separation) (*16*).

We analyzed pattern separation–dependent memory by testing whether mice could differentiate between locations that were presented closely in space [separation 2 (S2)] versus those that were

[1]Laboratory of Genetics, Salk Institute for Biological Studies, La Jolla, CA 92037, USA. [2]Centre for Brain Repair, University of Cambridge, Cambridge CB2 2PY, UK. [3]Department of Experimental Psychology, University of Cambridge, Cambridge CB2 3EB, UK. [4]Institute of Cell Biology, Department of Biology, ETH Zurich, Zurich, Switzerland. [5]Medical Research Council and Wellcome Trust Behavioral and Clinical Neuroscience Institute, University of Cambridge, Cambridge CB2 3EB, UK. [6]Department of Neurology, Addenbrooke's Hospital, Cambridge CB2 2QQ, UK.

*These authors contributed equally to this work.
†To whom correspondence should be addressed. E-mail: gage@salk.edu (F.H.G.); tjb1000@cam.ac.uk (T.J.B.)

more highly separated (S3 and S4). IR mice were selectively impaired at low separations (S2) but not at high separations (S3 and S4) [significant group × separation interaction, repeated measures analysis of variance (ANOVA): $F_{1,17} = 4.57$, $P = 0.047$; Bonferroni corrected t tests: S2: $t(17) = 2.55$, $P = 0.021$; S3+S4: $t(17) = 0.03$, $P = 0.974$] (Fig. 1F). These results suggest that adult hippocampal neurogenesis was not required to perform the task in which sample and correct arms were presented with a high degree of spatial separation (S3 and S4) but was required to correctly discriminate between choice and sample arms when presented in close spatial proximity.

To further examine whether loss of adult hippocampal neurogenesis results in global hippocampal deficits or specific pattern separation memory deficits, we tested a naive cohort of IR ($n = 10$) and sham ($n = 9$) mice on a challenging hippocampus-dependent spatial learning task and a two-choice spatial discrimination (pattern separation) task in the mouse touch screen (Fig. 2) (*16*). The mouse touch screen is useful in that all trials are directed by the mouse through an initiation process, and all testing is independent of the experimenter. The testing apparatus (Fig. 2B) consisted of a standard modular chamber fitted with an infrared touch screen, a pellet dispenser, a receptacle with light illumination and head entry detectors, and a tone generator. Mice were pretrained through several iterative stages to nose-touch stimuli on the screen to obtain a reward (*20*). Mice were then trained on a paired associates learning (PAL) object-in-place task (*21*) that tests the ability to correctly associate three objects (flower, plane, and spider) with their correct spatial locations on the screen (left, middle, and right, respectively) (Fig. 2C). Mice were only rewarded when they identified the correct object in its correct location during a choice between two objects: one object in its correct spatial location and one object in one of two incorrect locations. Mice were given 36 trials per day plus correction trials over 55 days. Both IR and sham mice learned the task at the same rate (repeated measures ANOVA, $F_{53,742} = 0.18$, $P = 0.671$) (Fig. 2D). The demonstration that the performance of IR mice was not different from that of sham mice on this hippocampus-dependent spatial task indicates that mice without neurogenesis are still capable of acquiring, at a normal rate, a complex task involving spatial information on the touch screen.

These IR and sham mice were next tested for spatial discrimination ability in the touch screen with the use of a hippocampus-dependent two-choice spatial discrimination paradigm (*22*) (Fig. 2E). Briefly, mice were required to choose the correct spatial location between two illuminated boxes in two out of five possible locations until a criterion (seven out of eight consecutive touches) was reached. Once the criterion was met, the correct and incorrect locations automatically switched. Similar to the DNMP task in the RAM, pattern separation was tested by varying the distance between choice locations. Lit choice boxes were either far apart [separated by three unlit spaces (high separation, S4; Fig. 2E)] or close together [separated by one unlit space (low separation, S2; Fig. 2E)]. Spatial separations were held constant during each testing session per day but were varied across testing days.

In agreement with our findings using the RAM, IR mice were significantly impaired at low (S2) but not high (S4) separations during acquisition [significant group × separation interaction, repeated measures ANOVA, average trial to criterion: $F_{1,17} = 6.04$, $P = 0.025$; Bonferroni corrected t tests: S2: $t(17) = 2.54$, $P = 0.020$; S4: $t(17) = 0.63$, $P = 0.540$] (Fig. 2F). Ablating neurogenesis with the use of focal x-irradiation induces impairments consistent with a deficit in pattern separation in two independent tasks carried out in two very different testing situations. This impairment appears to be specific, as IR mice were capable of learning difficult object-place associations (PAL) at the same rate and to the same performance level as sham mice. Furthermore, the spatial memory deficits observed were similar in both the navigable RAM and non-navigable touch screen.

Given concerns regarding potential off-target effects due to focal x-irradiation, despite the long recovery period, we employed a second independent method to knock down neurogenesis, with the use of lentiviral expression of dominant negative Wnt (dnWnt) protein, and then tested these mice on the same RAM protocol (Fig. 3 and fig. S5A) used in the first experiment described above. We used the previously described lentiviral vectors expressing cytomegalovirus-driven dnWnt followed by an internal ribosomal entry site (IRES)–green fluorescent protein (GFP) from the same vector or a control vector expressing only GFP (GFPcon) (*16*, *23*).

Inhibition of Wnt signaling locally in the DG reduces the number of newborn neurons without affecting progenitor proliferation in other brain regions (*23*, *24*). Eight-week-old C57Bl/6 female mice received bilateral stereotaxic injections of 1 μl of either dnWnt-expressing lentivirus ($n = 16$) or GFPcon lentivirus ($n = 15$) into the DG, resulting in a significant reduction in proliferating cells and neurogenesis (Fig. 3, A and B, and fig. S5). Behavioral testing in the RAM commenced 2 months after viral injection. Similar to the pattern separation deficit observed in IR mice, dnWnt mice were impaired at low (S2) but not high (S3 and S4) separations compared with GFPcon mice [significant group × separation interaction, repeated measures ANOVA: $F_{1,24} = 4.51$, $P = 0.044$;

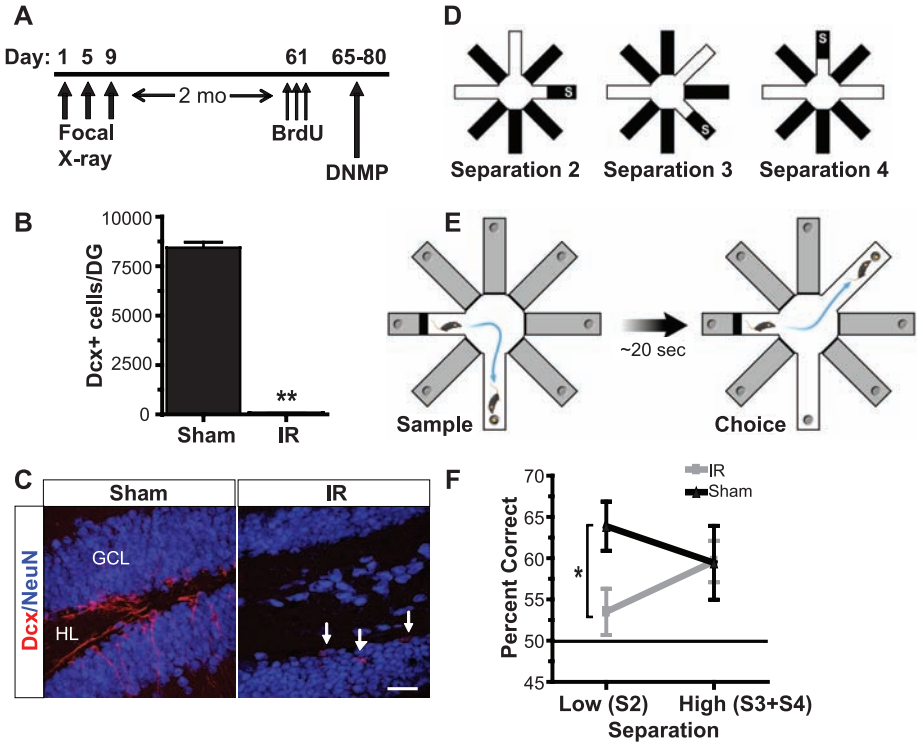

Fig. 1. Mice with ablated neurogenesis due to focal x-irradiation show impaired spatial memory for similar, but not distinct, spatial locations in the radial arm maze. (**A**) Mice were irradiated 2 months before behavioral testing. (**B** and **C**) Irradiation significantly reduced the total numbers of immature Dcx+ cells in IR mice [white arrows at right in (C)] compared with sham controls [(C), left] [independent samples t test, $t(17) = 29.82$, $P < 0.001$]. GCL, granule cell layer; HL, hilus. (**D**) Pattern separation was tested using a DNMP protocol in the RAM by varying the distance between sample and correct arms: S2, low; S3 and S4, high (S, start arm). (**E**) Each trial consisted of a sample phase (left) and a choice phase (right). The mouse had to nonmatch to the new location. (**F**) IR mice were impaired at low (S2) but not high (S3 and S4) separations in the DNMP task. The horizontal black line represents chance. Error bars indicate SEM. Scale bars, 25 μm. $^{**}P < 0.01$; $^{*}P < 0.05$.

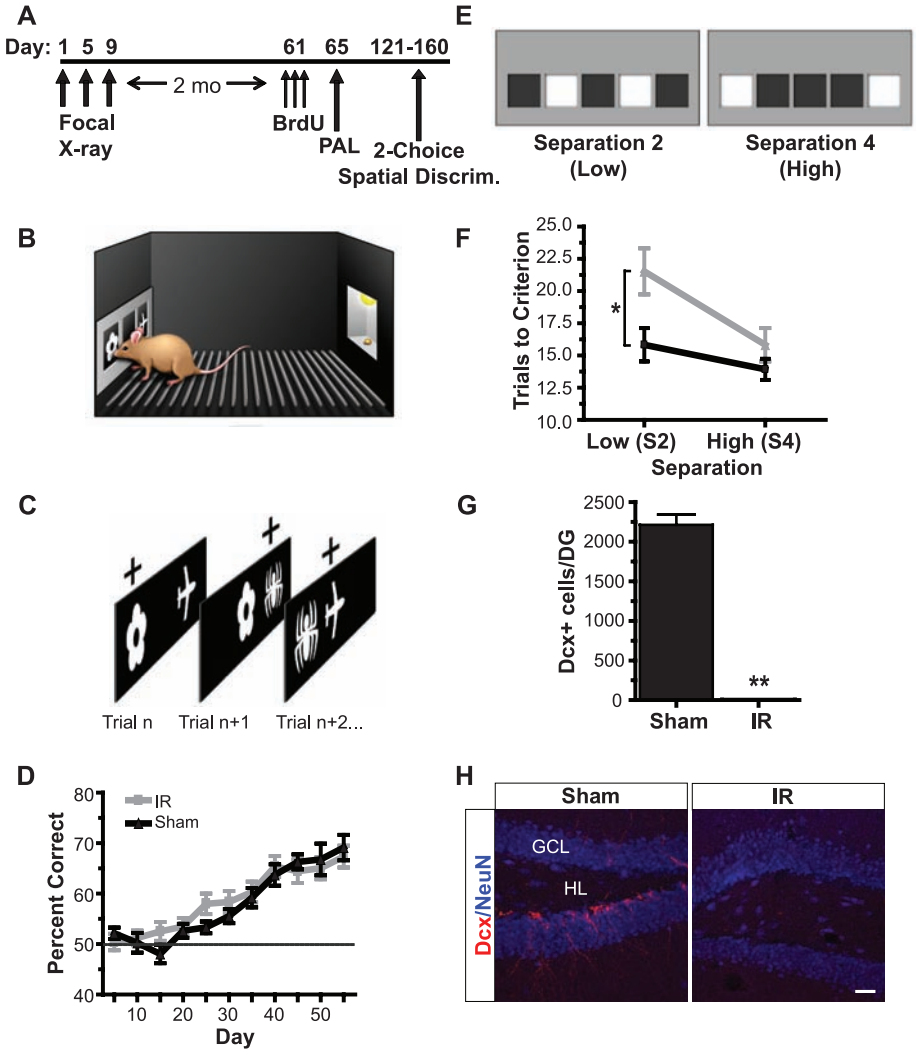

Fig. 2. Mice with ablated neurogenesis due to focal x-irradiation show impaired spatial discrimination for similar but not distinct spatial locations, but not impaired associative object-in-place memory, in the mouse touch screen. Mice were irradiated 2 months before behavioral testing as in (**A**). After pretraining for 7 to 10 days in which mice learned to nose-touch stimuli on the infrared touch screen (**B**) to obtain a reward, mice were trained on an associative object-in-place task (PAL) (**C**). For example, as in the left panel of (C), mice had to choose a flower at left as a correct association over the incorrect association of a plane at right to obtain a reward. (**D**) IR mice learned the PAL task at the same rate as sham controls (horizontal black line represents chance). (**E**) Mice were then tested on a two-choice spatial discrimination task in which they had to respond to the correct location [e.g., left illuminated box of left screen in (E)] until a criterion of seven out of eight consecutive correct touches was recorded before reversing to the previously incorrect location [e.g., right illuminated box of left screen in (E)]. Mice were tested on either the low (S2, left screen) or high (S4, right screen) separation, as depicted in (E) during each testing day. (**F**) IR mice exhibited significantly impaired performance at low (S2) but not high (S4) separations during acquisition of this task, consistent with a pattern separation deficit similar to that observed in the first experiment (Fig. 1). (**G** and **H**) Irradiation significantly reduced the total numbers of immature Dcx+ cells in IR mice [right in (H)] compared with sham controls [left in (H)] [independent samples *t* test, $t(17) = 18.14$, $P < 0.001$]. Error bars indicate SEM. Scale bars, 50 μm. $^{**}P < 0.01$; $^{*}P < 0.05$.

Bonferroni corrected *t* tests: S2: $t(24) = 3.02$, $P = 0.006$; S3 and S4: $t(24) = 0.46$, $P = 0.926$] (Fig. 3C). Thus, mice with decreased neurogenesis due to expression of the dnWnt protein are impaired at spatial pattern separation or the ability to correctly distinguish rewarded from nonrewarded spatial locations only when stimuli to be discriminated are presented closely in space.

This study provides experimental evidence of a role for newborn neurons in the adult DG in spatial discrimination, consistent with a role in spatial pattern separation. We used two independent strategies to ablate neurogenesis, and the observed deficits were similar in two very distinct testing contexts. Mice with ablated neurogenesis showed a selective impairment specific to memory performance depending on pattern separation but were not impaired at the hippocampus-dependent PAL task, indicating that mice were able to learn complex associations in which space was a component.

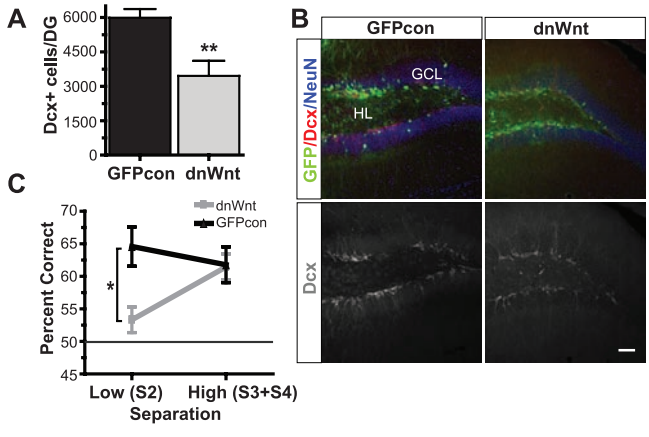

Fig. 3. Mice with decreased neurogenesis due to targeted lentiviral expression of dnWnt show impaired spatial memory for similar, but not distinct, spatial locations in the radial arm maze in a similar pattern to that seen in irradiated mice. (**A** and **B**) dnWnt expression [right in (B)] significantly reduced the total numbers of immature Dcx+ cells in dnWnt mice (A) compared with GFP controls [left in (B)] [independent samples *t* test: $t(24) = 3.47$, $P = 0.002$]. Single channel images depicting Dcx+ cells are shown below triple channel images in (B). (**C**) Pattern separation was tested using a DNMP as in Fig. 1. dnWnt mice were impaired at low (S2) but not high (S3 and S4) separations in the DNMP task. The horizontal black line represents chance. Error bars indicate SEM. Scale bars, 50 μm. $^{**}P < 0.01$; $^{*}P < 0.05$.

Previous studies involving rodent lesions of either the dorsal hippocampus (*22*) or the DG (*7*–*9*) suggest that regions outside of the DG are responsible for disambiguating memories derived from spatially distinct inputs (comparable to the large separations used in this study). In addition, it has been suggested that recruitment of independent cell populations in the CA3 alone, presumably via direct input from the entorhinal cortex (*25*), may be sufficient to disambiguate memories for more distinct spatial inputs (*1*, *26*, *27*) or make associations between objects and space (*28*). In this

context, it is interesting to note that the impairments after ablation of neurogenesis described here are parameter-sensitive (i.e., specific to conditions with a high premium on pattern separation), which may help to explain the variable and sometimes contradictory results from other neurogenesis-ablation studies in which this parameter was not explicitly considered (*18*, *24*, *29*, *30*).

dnWNT mice with a ~50% decrease in neurogenesis had a similar pattern of impairment to that seen in the IR group in which neurogenesis was almost completely ablated, suggesting that there may be a critical threshold for the amount of neurogenesis that is behaviorally relevant. A level-dependent requirement of adult neurogenesis for hippocampus-dependent learning has also been reported in rats (*24*). In addition, our RAM task may be sufficiently challenging that even partial manipulation of newborn neuron numbers is adequate to impair performance.

The DG has been shown to be important for pattern separation, and our results show that adult neurogenesis appears to be important for the ability of the DG to perform that function optimally. It remains to be investigated whether immature neurons contribute to pattern separation directly or whether they contribute in more complex ways to a circuit necessary for normal DG function, as suggested by recent modeling studies (*31*), and whether the function of immature neurons is distinct from that of mature granule cells.

References and Notes

1. J. K. Leutgeb, S. Leutgeb, M.-B. Moser, E. I. Moser, *Science* **315**, 961 (2007).
2. T. Nakashiba, J. Z. Young, T. J. McHugh, D. L. Buhl, S. Tonegawa, *Science* **319**, 1260 (2008); published online 24 January 2008 (10.1126/science.1151120).
3. A. Bakker, C. B. Kirwan, M. Miller, C. E. L. Stark, *Science* **319**, 1640 (2008).
4. D. Marr, *Philos. Trans. R. Soc. London Ser. B Biol. Sci.* **262**, 23 (1971).
5. M. W. Jung, B. L. McNaughton, *Hippocampus* **3**, 165 (1993).
6. D. G. Amaral, N. Ishizuka, B. Claiborne, *Prog. Brain Res.* **83**, 1 (1990).
7. P. E. Gilbert, R. P. Kesner, I. Lee, *Hippocampus* **11**, 626 (2001).
8. P. E. Gilbert, R. P. Kesner, W. E. DeCoteau, *J. Neurosci.* **18**, 804 (1998).
9. M. R. Hunsaker, R. P. Kesner, *Hippocampus* **18**, 955 (2008).
10. C. Zhao, W. Deng, F. H. Gage, *Cell* **132**, 645 (2008).
11. H. van Praag *et al.*, *Nature* **415**, 1030 (2002).
12. N. Toni *et al.*, *Nat. Neurosci.* **11**, 901 (2008).
13. S. Jessberger, G. Kempermann, *Eur. J. Neurosci.* **18**, 2707 (2003).
14. H. van Praag, B. R. Christie, T. J. Sejnowski, F. H. Gage, *Proc. Natl. Acad. Sci. U.S.A.* **96**, 13427 (1999).
15. E. Gould, A. Beylin, P. Tanapat, A. Reeves, T. J. Shors, *Nat. Neurosci.* **2**, 260 (1999).
16. Materials and methods are available as supporting material on *Science* Online.
17. L. Santarelli *et al.*, *Science* **301**, 805 (2003).
18. J. S. Snyder, N. S. Hong, R. J. McDonald, J. M. Wojtowicz, *Neuroscience* **130**, 843 (2005).
19. D. Bernstein *et al.*, *Pharmacol. Biochem. Behav.* **22**, 301 (1985).
20. A. J. Morton, E. Skillings, T. J. Bussey, L. M. Saksida, *Nat. Methods* **3**, 767 (2006).
21. J. C. Talpos, B. D. Winters, R. Dias, L. M. Saksida, T. J. Bussey, *Psychopharmacology (Berlin)* **205**, 157 (2009).
22. S. M. McTighe, A. C. Mar, C. Romberg, T. J. Bussey, L. M. Saksida, *Neuroreport* **20**, 881 (2009).
23. D. C. Lie *et al.*, *Nature* **437**, 1370 (2005).
24. S. Jessberger *et al.*, *Learn. Mem.* **16**, 147 (2009).
25. M. Fyhn, T. Hafting, A. Treves, M. B. Moser, E. I. Moser, *Nature* **446**, 190 (2007).
26. S. Leutgeb *et al.*, *Science* **309**, 619 (2005).
27. A. Vazdarjanova, J. F. Guzowski, *J. Neurosci.* **24**, 6489 (2004).
28. P. E. Gilbert, R. P. Kesner, *Behav. Neurosci.* **117**, 1385 (2003).
29. C. L. Zhang, Y. Zou, W. He, F. H. Gage, R. M. Evans, *Nature* **451**, 1004 (2008).
30. J. M. Wojtowicz, M. L. Askew, G. Winocur, *Eur. J. Neurosci.* **27**, 1494 (2008).
31. J. B. Aimone, J. Wiles, F. H. Gage, *Neuron* **61**, 187 (2009).

32. We thank M. J. Armstrong and J. B. Aimone for useful input and discussions, M. L. Gage for editorial comments, and J. Simon for assistance with figures. This work was funded in part by James S. McDonnell, Lookout, and Mather's Foundations; the Kavli Institute for Brain and Mind; and NIH (grant NS-050217) (F.H.G.), and also by the NIHR Biomedical Research Centre Award to the University of Cambridge and generous donations from patients and families to the Huntington's and Parkinson's Disease Research Clinics at the Brain Repair Centre, University of Cambridge (R.A.B.). This work was also supported in part by MaxNetAging and NCCR Neural Plasticity and Repair Grants (S.J.) and Marshall's and Jack Kent Cooke Foundation scholarships (C.D.C.).

Supporting Online Material

www.sciencemag.org/cgi/content/full/325/5937/210/DC1
Materials and Methods
Figs. S1 to S5
References

9 March 2009; accepted 26 May 2009
10.1126/science.1173215

IRAP Identifies an Endosomal Compartment Required for MHC Class I Cross-Presentation

Loredana Saveanu,[1] Oliver Carroll,[1] Mirjana Weimershaus,[1] Pierre Guermonprez,[2] Elke Firat,[3] Vivian Lindo,[4] Fiona Greer,[4] Jean Davoust,[1] Roland Kratzer,[1] Susanna R. Keller,[5]* Gabriele Niedermann,[3]* Peter van Endert[1]†

Major histocompatibility complex (MHC) class I molecules present peptides, produced through cytosolic proteasomal degradation of cellular proteins, to cytotoxic T lymphocytes. In dendritic cells, the peptides can also be derived from internalized antigens through a process known as cross-presentation. The cellular compartments involved in cross-presentation remain poorly defined. We found a role for peptide trimming by insulin-regulated aminopeptidase (IRAP) in cross-presentation. In human dendritic cells, IRAP was localized to a Rab14$^+$ endosomal storage compartment in which it interacted with MHC class I molecules. IRAP deficiency compromised cross-presentation in vitro and in vivo but did not affect endogenous presentation. We propose the existence of two pathways for proteasome-dependent cross-presentation in which final peptide trimming involves IRAP in endosomes and involves the related aminopeptidases in the endoplasmic reticulum.

Peptide ligands for MHC class I molecules are produced by intracellular proteases (*1*). Initial antigen degradation by cytosolic proteasome complexes is frequently followed by N-terminal peptide trimming, which can occur in the cytosol and by endoplasmic reticulum (ER) aminopeptidases (ERAPs) (*2*). Peptides are transported into the ER by the transporter associated with antigen processing (TAP) for loading of newly synthesized MHC class I molecules. Loading of MHC class I molecules with internalized, cross-presented antigens in dendritic cells (DCs) is thought to play an important role in priming of CD8$^+$ T cell responses to pathogens and tumors, as well as in immune tolerance to self.

While screening crude microsome lysates for peptidases involved in N-terminal trimming of human leukocyte antigen (HLA) class I ligands, we identified insulin-regulated aminopeptidase (IRAP). IRAP was detected as an interferon γ (IFN-γ)–induced activity trimming a fluorogenic Leu–aminomethyl coumarin (AMC) substrate in anion exchange chromatography (Fig. 1A) (*3*). The peak containing IRAP also trimmed a precursor of the HLA-A2–restricted epitope SLYNTVATL (*4*, *5*). IRAP is a ubiquitous zinc-dependent aminopeptidase closely related to ERAP1 and ERAP2 (*6*). IRAP localizes to regulated endosomal storage compartments in adipocytes and muscle cells together with the glucose transporter Glut4; these compartments are termed Glut4 storage vesicles (GSVs) (*7*). Signaling through the insulin or immunoglobulin E (IgE) receptors induces rapid translocation of ~50% of IRAP to the cell surface (*7*, *8*). The function of the compartment storing IRAP in other cell types, such as DCs, remains unknown.

To evaluate whether IRAP qualifies as a trimming aminopeptidase, we tested its sub-

[1]INSERM, U580, 75015 Paris, France; Université Paris Descartes, Faculté de Médecine René Descartes, 75015 Paris, France. [2]INSERM, U653, 75006 Paris, France; Institut Curie, Centre de Recherche, 75006 Paris, France. [3]Clinic for Radiotherapy, University Hospital of Freiburg, 79106 Freiburg, Germany. [4]M-SCAN Ltd., Wokingham, Berkshire RG41 2TZ, UK. [5]Division of Endocrinology, Department of Internal Medicine, University of Virginia, Charlottesville, VA 22908, USA.

*These authors contributed equally to this work.
†To whom correspondence should be addressed. E-mail: peter.van-endert@inserm.fr

strate specificity and interaction with MHC class I molecules. Human IRAP displayed a broader specificity toward fluorogenic substrates than did its ER-resident relatives (Fig. 1B). IRAP also efficiently converted the 15-nucleotide oligomer epitope precursor K15I to the minimal epitope G9I, which in the ER requires the concerted action of ERAP1 and ERAP2 (*4*) (Fig. 1C). The amount of IRAP eluted was doubled by IFN-γ incubation of HeLa cells (Fig. 1A), although IRAP mRNA levels were not (fig. S1). Because IRAP eluted in a fraction also containing MHC class I molecules (Fig. 1A), increased recovery of IRAP activity could have resulted from its association with IFN-γ–induced MHC molecules. A fraction of cellular IRAP was coprecipitated with HLA class I molecules from bone marrow–derived DCs (BMDCs) (Fig. 1D), compatible with a role for IRAP in MHC class I antigen presentation.

Because IRAP resides in endocytic vesicles (*7*), we considered that it may be involved in the MHC class I cross-presentation of exogenous antigens internalized by DCs through phagocytosis or receptor-mediated endocytosis (*9*). Although cross-presented antigens are believed to be processed mainly by factors also involved in the endogenous pathway, such as TAP, Sec61, or ERAP1 (*10*), the intracellular routes mediating the junction between the endocytic pathway and the ER have been difficult to decipher (*9*). In human myeloid DCs and murine BMDCs, ~25% of IRAP colocalized with HLA class I molecules (Fig. 1E and fig. S2), whereas no colocalization was observed with endolysosomal proteins (HLA class II and Lamp-1). In the absence of DC phagocytosis, we could not detect colocalization with three ER-resident proteins: KDEL receptor, ERAP1, and TAP2. This was not due to a failure of antibodies to recognize ER-resident IRAP, because strong colocalization with two ER markers of a hemagglutinin (HA)–tagged IRAP variant carrying a KDEL sequence was readily detectable, whereas ER colocalization was completely absent for HA-tagged IRAP lacking a KDEL sequence (fig. S3). Thus, newly synthesized IRAP molecules must exit rapidly from the ER. However, IRAP showed considerable colocalization with syntaxin 6 (STX6; 51%), a Q-SNARE (soluble *N*-ethylmaleimide–sensitive factor attachment) known to stain GSVs (*11*). IRAP colocalized most strongly (76%) with Rab14, which may play a role in preventing phagosome fusion with lysosomes in macrophages (*12*, *13*). Similar data were obtained in murine BMDCs (fig. S4), where IRAP also showed considerable colocalization with the mannose receptor (MR) (57%), reported to mediate efficient cross-presentation of soluble antigen (*14*).

During phagocytosis, IRAP was strongly enriched in purified early phagosomes but not in late phagosomes, whereas ERAP was not enriched in phagosomes (Fig. 2A), consistent with a recent proteomics analysis of phagosomes (*15*). In DCs phagocytosing yeast cells, IRAP colocalized preferentially with MHC class I molecules

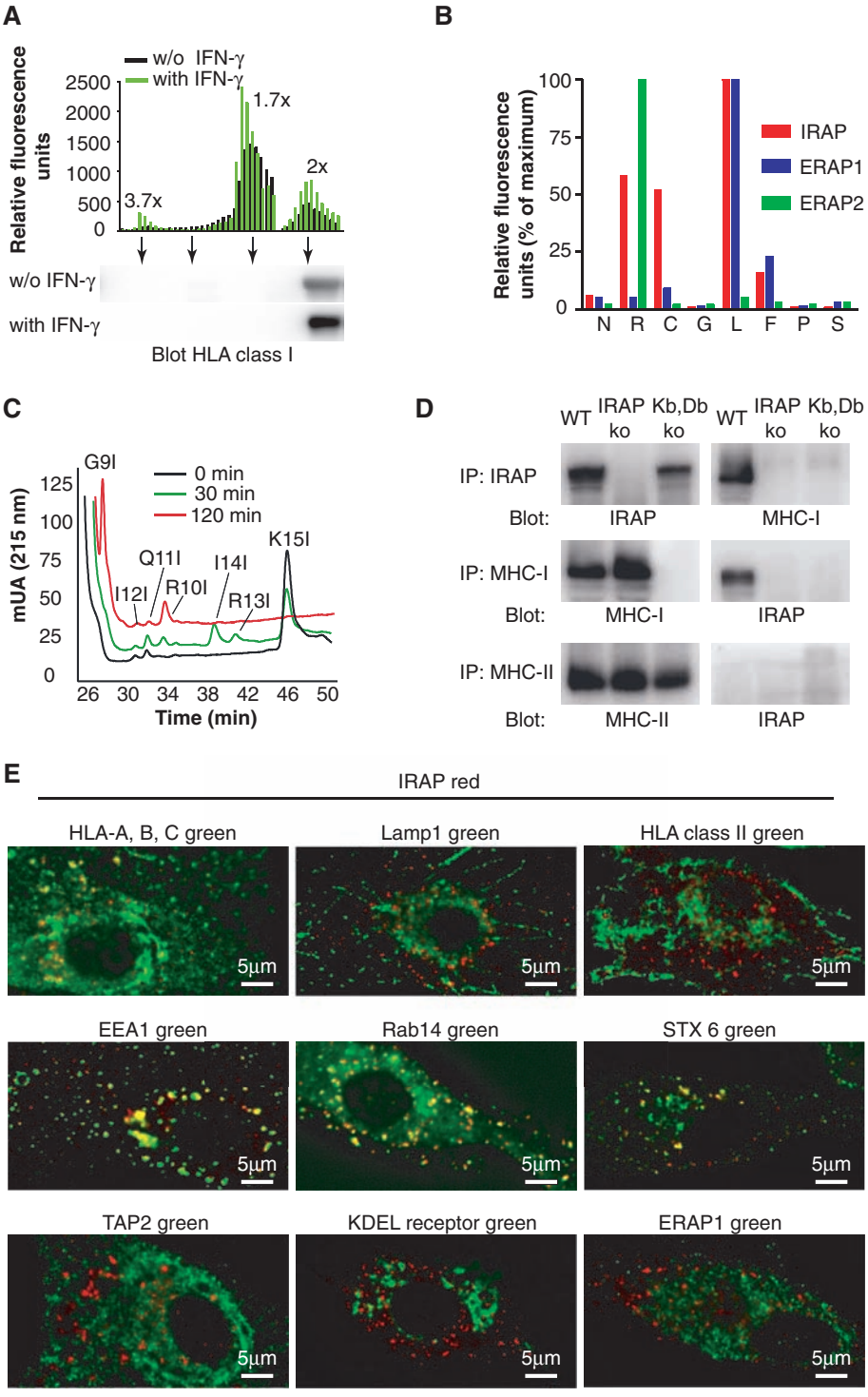

Fig. 1. Identification of an MHC class I–associated aminopeptidase. (**A**) Hydrolysis of Leu-AMC by fractionated crude microsomal proteins from untreated or IFN-γ–treated HeLa cells. Numbers above peaks indicate relative induction of Leu-AMC hydrolysis by IFN-γ incubation. MHC class I was detected exclusively in peak 4 by immunoblot analysis; ERAP1 and ERAP2 elute exclusively in peak 1 under identical chromatographic conditions (*4*). (**B**) Recombinant human IRAP, ERAP1, and ERAP2 were tested for aminoacyl-AMC hydrolysis. For each enzyme, results are expressed as percent of maximum hydrolysis set at 100. (**C**) Peptide K15I (KIRIQRGPGRAFVTI) (*5*) was digested with recombinant IRAP. Degradation products are designated by the N-terminal residue followed by peptide length and C-terminal residue. (**D**) IRAP, MHC class I, and MHC class II molecules were immunoprecipitated (IP) from BMDCs lysed with a mild detergent. Precipitates were split at a ratio of 1:9 for detection of directly precipitated and coprecipitated proteins, and analyzed by immunoblot as indicated. Control DCs were from $K^bD^b\beta_2m$ knockout (ko), HLA-B7 transgenic mice; WT, wild type. (**E**) Subcellular localization of IRAP (red) in human myeloid DCs.

internalized from the surface in vesicles adjacent to phagosomes, or in phagosomal membranes (Fig. 2, B and C, and fig. S5). Internalized MHC class I molecules could not be detected in late Lamp1$^+$ phagosomes (fig. S5). ERAP did not colocalize with internalized MHC class I molecules (<0.5%; Fig. 2B). This suggests that internalized MHC class I molecules may traffic together with IRAP from phagosomes to GSV-

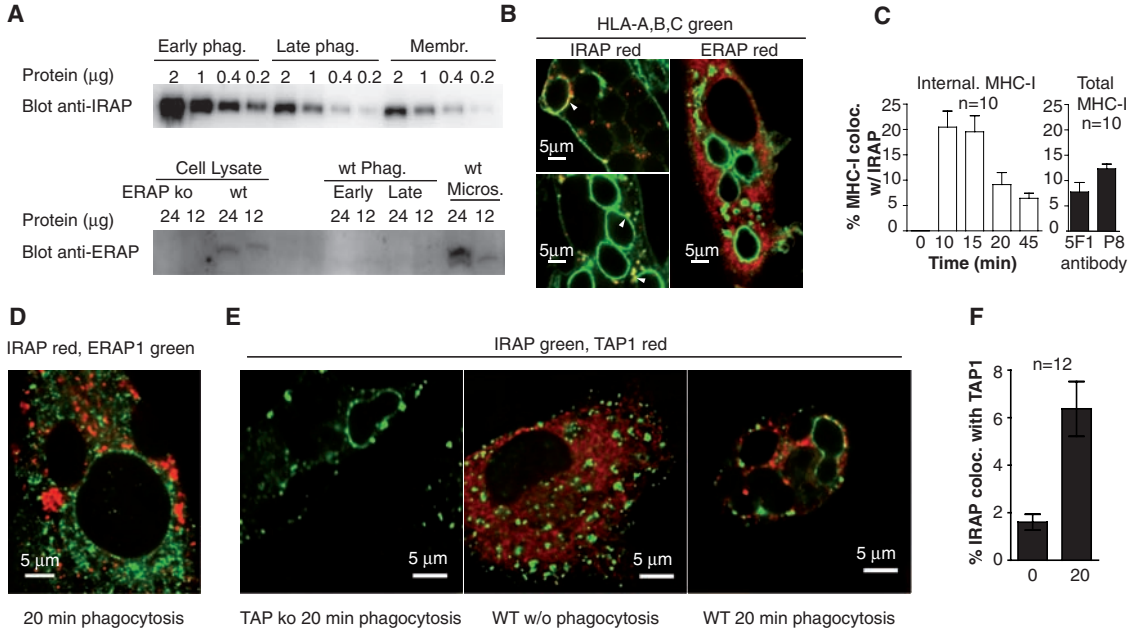

Fig. 2. IRAP, but not ERAP, is recruited to phagosomes. (**A**) Serial dilutions of membranes from early (20 min) and late (2 hours) BMDC phagosomes were examined for IRAP and ERAP by immunoblot. Total cellular proteins or membrane proteins, and crude microsomes served as controls. One of two (ERAP blot) or four (IRAP blot) similar experiments is shown. (**B**) Human myeloid DCs were stained after 20 min of yeast cell phagocytosis for IRAP, ERAP, and HLA-A, B, and C. (**C**) BMDCs were stained for cell surface K^b molecules, fed yeast cells, and analyzed for colocalization of IRAP with K^b after different intervals. The right panel shows the percent colocalization (mean ± SD) of total cellular MHC class I with IRAP after 15 min. (**D**) Human myeloid DCs were stained for IRAP and ERAP. (**E**) Murine BMDCs, before or 20 min after phagocytosis of yeast cells, were stained with antibodies to IRAP and mouse TAP1. (**F**) The percentage of IRAP colocalizing with TAP1 was calculated using correlation maps.

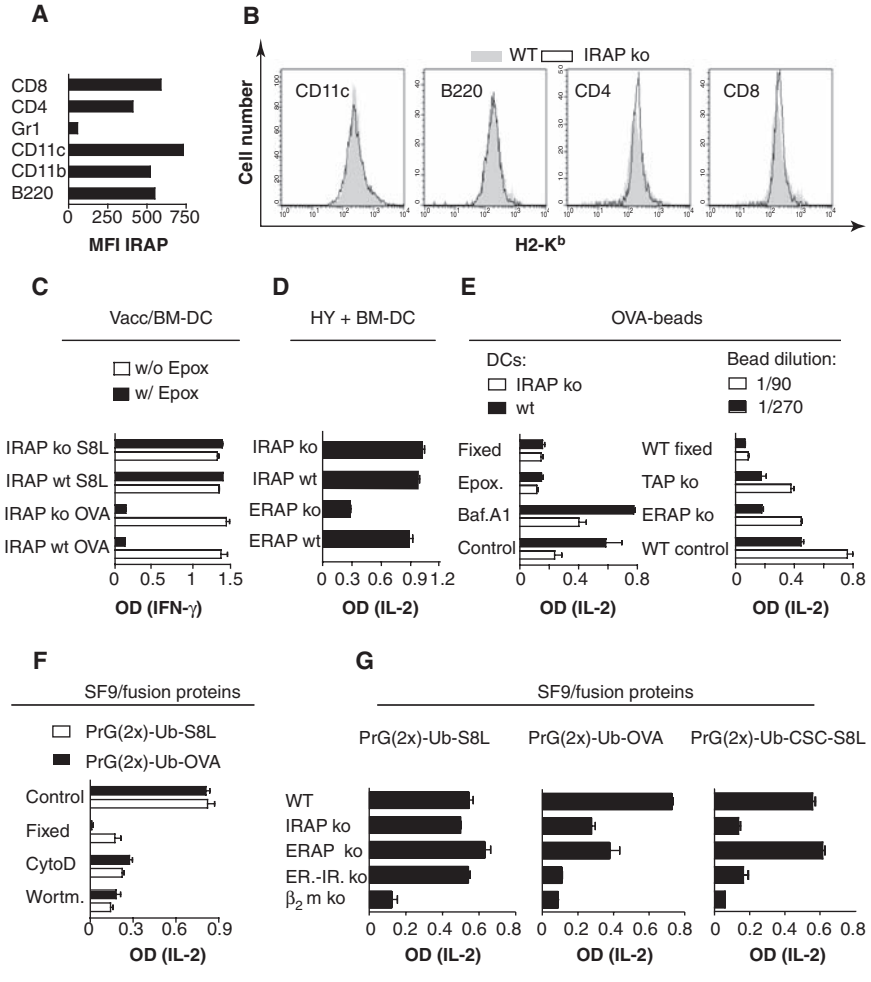

Fig. 3. IRAP is required for cross-presentation in vitro. (**A**) Fluorescence-activated cell sorter analysis of intracellular IRAP expression in mouse splenocyte subpopulations. (**B**) Expression of H2-K^b on splenic DCs ($CD11c^+$), B cells ($B220^+$), helper ($CD4^+$), and killer ($CD8^+$) T cells. (**C**) Generation of S8L in the endogenous pathway by vaccinia-infected DCs. The response of OT-I effector T cells was measured by IFN-γ enzyme-linked immunosorbent assay. Epox, epoxomicin (proteasome inhibitor); wt, wild type. (**D**) Endogenous presentation of the SMCY male antigen by DCs to HY $CD8^+$ T cells. (**E**) In vitro cross-priming of OT-I cells by DCs incubated with OVA-coated beads. Baf.A1, bafilomycin A1. (**F**) In vitro cross-priming of OT-I cells with necrotic insect cells containing fusion proteins. CytoD, cytochalasin D; Wortm., wortmannin. (**G**) DCs were incubated with necrotic insect cells expressing fusion proteins comprising OVA, S8L, or S8L with an N-terminal CSC extension. The experiments shown correspond to one of two [(A), (D), (F), and (G)], three [(C) and (E)], or five (B) experiments. Means + SD are shown in (C) to (G). Splenic DCs were used in (E), BMDCs in all others.

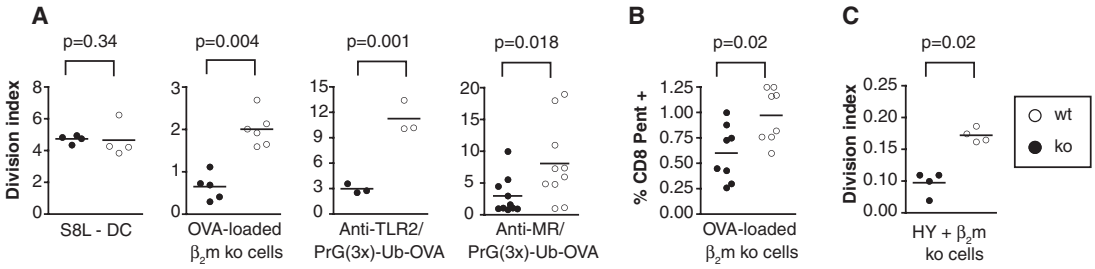

Fig. 4. IRAP deficiency compromises in vivo cross-priming. (**A**) Mice were injected with CFSE-labeled OT-I cells, followed 24 hours later by injection of antigen. Three days later, OT-I proliferation (expressed as divisions per precursor OT-I cell) was examined by flow cytometry. Antigens were S8L-pulsed BMDCs, β_2m knockout splenocytes electroporated with OVA, or OVA fusion proteins targeted for internalization through TLR2 or the MR. (**B**) Mice were injected with OVA-loaded β_2m knockout splenocytes. Ten days later, priming of endogenous $CD8^+$ T cells was measured by staining with a K^b/S8L pentamer. (**C**) SV129 mice were injected with CFSE-labeled HY T cells, followed 24 hours later by injection of male MHC-unmatched (Balb/c) splenocytes.

like vesicles before phagosome fusion with lysosomes takes place. DC activation by pathogen compounds induces TAP recruitment to MR^+ endosomes (*14*). Phagocytic DC activity did not increase IRAP colocalization with ERAP (Fig. 2D). In contrast, colocalization of IRAP with TAP increased from <2% in resting murine BMDCs to 6.5% (Fig. 2, E and F). Thus, ER-phagosome or endosome fusion events may selectively deliver TAP but not ERAP1 to $IRAP^+$ vesicles.

To examine a potential role of IRAP in antigen presentation, we studied previously generated IRAP knockout mice (*8*, *16*). Deficiency for IRAP, which is normally expressed by all mouse splenocyte subpopulations except granulocytes (Fig. 3A), did not affect MHC class I expression by splenic lymphocytes including $CD11c^{hi}$ DCs (Fig. 3B), which also matured normally upon LPS stimulation (fig. S6). BMDCs from IRAP knockout mice expressing full-length ovalbumin (OVA) or the preprocessed K^b-restricted OVA epitope S8L (SIINFEKL, $OVA_{257\text{-}64}$), or pulsed with the synthetic epitope, presented epitope S8L normally to specific OT-I $CD8^+$ T cells (*17*) (Fig. 3C and fig. S7). Thus, production of epitope S8L in the endogenous processing pathway is proteasome-dependent (Fig. 3C) and ERAP-dependent (*18*), but does not require IRAP. Endogenous presentation of the male antigen SMCY (*19*) also required expression of ERAP but not IRAP by DCs (Fig. 3D). These results provide strong evidence against involvement of IRAP in the endogenous MHC class I processing pathway.

To study the impact of IRAP deficiency on cross-presentation, we first examined the presentation of OVA-coated beads to OT-I cells. The efficiency of bead phagocytosis by BMDCs was not affected by IRAP deficiency (fig. S8). Cross-presentation of beads was abolished by two proteasome inhibitors but was not affected, or even increased, by two inhibitors of lysosomal proteases (Fig. 3E and fig. S9). Cross-presentation also was compromised by TAP deficiency (Fig. 3E). Thus, OVA internalized by phagocytosis was shuttled into the pathway involving antigen degradation in the cytosol, but not into the vacuolar pathway involving acid lysosomal proteases (*20*, *21*). Cross-presentation of particulate OVA was reduced by ERAP deficiency (Fig. 3E) (*18*, *22*). IRAP deficiency resulted in an at least equal reduction of presentation by 50 to 70% (Fig. 3E). This result suggests that precursors of epitope S8L could be trimmed both by an ER aminopeptidase and an endosomal aminopeptidase.

Next, we studied cross-presentation of necrotic insect cells expressing fusion proteins consisting of two or three Ig-binding domains derived from protein G (PrG), ubiquitin (Ub), and OVA or S8L. In the cytosol, OVA or S8L antigen is expected to be removed from these proteins by deubiquitinating enzymes. Cross-priming of OT-I cells required actin and phosphatidylinositol 3-kinase–dependent uptake of antigenic material by live DCs, demonstrating the absence of free peptide in the material (Fig. 3F). Generation of S8L from a phagocytosed fusion protein containing the preprocessed epitope not requiring trimming was not compromised in IRAP or ERAP single- or double-deficient DCs (Fig. 3G). However, absence of IRAP or ERAP reduced generation of S8L from a fusion protein containing full-length OVA. Absence of both peptidases had an additive effect (Fig. 3G), which suggests that the two enzymes may act in independent pathways. S8L generation from a precursor peptide extended by a sequence adapted to the cleavage specificity of IRAP but not ERAP [PrG(2x)-Ub-CSC-S8L] was reduced by >75% in IRAP-deficient DCs but was not affected by ERAP deficiency (Fig. 3G). Thus, IRAP acts as an epitope-trimming peptidase in an endosomal compartment.

Finally, we examined cross-priming of carboxyfluorescein succinimidyl ester (CFSE)–labeled, adoptively transferred naïve OT-I T cells in vivo (Fig. 4). IRAP deficiency did not affect recovery from lymph nodes and spleens of transferred OT-I cells (fig. S10), nor did it alter proliferation of transferred OT-I cells in response to S8L-pulsed DCs (Fig. 4A). In contrast, cross-presentation of cell-associated OVA was reduced (Fig. 4A and fig. S11). Next, we immunoaffinity-purified the fusion protein PrG(3x)-Ub-OVA and targeted it in vivo to cells expressing Toll-like receptor 2 (TLR2) or the MR via binding of its PrG domains to specific antibodies. IRAP deficiency resulted in reduced cross-presentation of receptor-targeted fusion protein (Fig. 4A and fig. S11). Moreover, IRAP deficiency reduced cross-priming of endogenous $CD8^+$ T cells by cell-associated OVA, as revealed by analysis of splenocytes from primed mice with K^b/S8L pentamers (Fig. 4B). Cross-presentation of a second antigen, cell-associated SMCY male antigen, was also compromised in IRAP knockout mice (Fig. 4C).

Our findings indicate that the final proteolytic trimming of cross-presented antigens can occur in an endosomal DC compartment sharing several markers associated with regulated endosomal storage vesicles. Recruitment of Rab14 may reduce routing of antigens into an acid lysosomal environment known to be detrimental for cross-presentation (*23*). Physical association of IRAP with abundant, presumably internalized class I molecules may favor a direct linkage between peptide trimming and MHC class I loading. Cross-presentation of antigens processed in an IRAP-dependent manner required active proteasome but not lysosomal proteases, which suggests that this pathway implicates cytosolic antigen degradation followed by peptide transport into $IRAP^+$ endosomes by TAP recruited upon phagocytosis. However, considering the relatively efficient TAP-independent cross-presentation of S8L (Fig. 3E), the existence of a pathway implicating IRAP together with an alternative endosomal peptide transporter, or together with a role for the proteasome unrelated to antigen degradation, cannot be ruled out entirely.

We found that both IRAP and ERAP are implicated in cross-presentation. Considering the functional redundancy and the complete absence of colocalization between the enzymes, the existence of two parallel proteasome-dependent cross-presentation pathways is the most plausible explanation (fig. S12). According to our model, MHC class I molecules can be loaded with cross-presented peptides in three intracellular compartments: endosomes, ER, and lysosomes/vacuoles.

References and Notes

1. N. Shastri, S. Cardinaud, S. R. Schwab, T. Serwold, J. Kunisawa, *Immunol. Rev.* **207**, 31 (2005).
2. L. Saveanu, O. Carroll, Y. Hassainya, P. van Endert, *Immunol. Rev.* **207**, 42 (2005).
3. See supporting material on *Science* Online.
4. L. Saveanu *et al.*, *Nat. Immunol.* **6**, 689 (2005).
5. Single-letter abbreviations for amino acid residues: A, Ala; C, Cys; D, Asp; E, Glu; F, Phe; G, Gly; H, His; I, Ile; K, Lys; L, Leu; M, Met; N, Asn; P, Pro; Q, Gln; R, Arg; S, Ser; T, Thr; V, Val; W, Trp; Y, Tyr.
6. M. Tsujimoto, A. Hattori, *Biochim. Biophys. Acta* **1751**, 9 (2005).
7. S. R. Keller, *Front. Biosci.* **8**, s410 (2003).

8. M. G. Wallis, M. F. Lankford, S. R. Keller, *Am. J. Physiol.* **293**, E1092 (2007).
9. N. Monu, E. S. Trombetta, *Curr. Opin. Immunol.* **19**, 66 (2007).
10. A. L. Ackerman, A. Giodini, P. Cresswell, *Immunity* **25**, 607 (2006).
11. A. M. Shewan *et al.*, *Mol. Biol. Cell* **14**, 973 (2003).
12. C. Kuijl *et al.*, *Nature* **450**, 725 (2007).
13. G. B. Kyei *et al.*, *EMBO J.* **25**, 5250 (2006).
14. S. Burgdorf, C. Scholz, A. Kautz, R. Tampe, C. Kurts, *Nat. Immunol.* **9**, 558 (2008).
15. L. D. Rogers, L. J. Foster, *Proc. Natl. Acad. Sci. U.S.A.* **104**, 18520 (2007).
16. S. R. Keller, A. C. Davis, K. B. Clairmont, *J. Biol. Chem.* **277**, 17677 (2002).
17. K. A. Hogquist *et al.*, *Cell* **76**, 17 (1994).
18. E. Firat *et al.*, *J. Immunol.* **178**, 2241 (2007).
19. P. Kisielow, H. Bluthmann, U. D. Staerz, M. Steinmetz, H. von Boehmer, *Nature* **333**, 742 (1988).
20. L. Ramachandra *et al.*, *Immunol. Rev.* **168**, 217 (1999).
21. L. Shen, L. J. Sigal, M. Boes, K. L. Rock, *Immunity* **21**, 155 (2004).
22. J. Yan *et al.*, *J. Exp. Med.* **203**, 647 (2006).
23. A. Savina *et al.*, *Cell* **126**, 205 (2006).

24. We thank Metabolex Inc. for an anti-IRAP serum, N. Shastri for an anti-ERAP serum, B. Rocha for HY mice, O. Lantz for TAP knockout mice, L. Chatenoud for OT-II mice, B. Fouquet and N. Merzougui for technical help, and A. M. Lennon-Dumesnil for critical reading of the manuscript. Supported by grant PROTARVAC of the European Commission (P.v.E., F.G., G.N.), by INSERM fellowships (O.C., R.K.), and by grants from the Deutsche Forschungsgemeinschaft and from the Medical Faculty of the University of Freiburg (G.N.).

Supporting Online Material

www.sciencemag.org/cgi/content/full/1172845/DC1
Materials and Methods
Figs. S1 to S12
References

27 February 2009; accepted 22 May 2009
Published online 4 June 2009;
10.1126/science.1172845
Include this information when citing this paper.

Hematopoietic Cytokines Can Instruct Lineage Choice

Michael A. Rieger, Philipp S. Hoppe, Benjamin M. Smejkal, Andrea C. Eitelhuber, Timm Schroeder*

The constant regeneration of the blood system during hematopoiesis requires tightly controlled lineage decisions of hematopoietic progenitor cells (HPCs). Because of technical limitations, differentiation of individual HPCs could not previously be analyzed continuously. It was therefore disputed whether cell-extrinsic cytokines can instruct HPC lineage choice or only allow survival of cells that are already lineage-restricted. Here, we used bioimaging approaches that allow the continuous long-term observation of individual differentiating mouse HPCs. We demonstrate that the physiological cytokines, macrophage colony-stimulating factor and granulocyte colony-stimulating factor, can instruct hematopoietic lineage choice.

All blood cells are generated from progenitor cells with more than one lineage potential (hematopoietic progenitor cells, HPCs). Hematopoiesis depends on tightly controlled lineage choice. Cytokines are necessary and sufficient for the production of specific mature blood cell types (*1*). However, despite decades of research, it is disputed whether cytokines instruct HPCs to differentiate into a specific lineage (*2*). Alternatively, cytokines may simply allow the survival or proliferation of cells that had already independently decided for this lineage. The cytokines' function would then only be to select the right cell types from a pool of already lineage-restricted cells (*3*). Cell-intrinsic transcription factors (*4*–*7*) and activation of ectopically expressed cytokine receptors (*8*–*10*) were shown to instruct lineage decisions. However, because of technical limitations, the instructive action of cytokines acting physiologically on unmanipulated HPCs could not be demonstrated (*1*, *11*). As illustrated in fig. S1 (*12*), the discontinuous analysis of HPCs does not allow conclusive answers (*13*): In order to exclude the selective model, the exact kinship, lineage commitment, and cell death of all individual cells in HPC colonies must be identified (*14*, *15*). Prior analyses had not continuously followed all individual cells in constantly mixing HPC cultures long enough and with sufficient resolution. The selective model is currently favored in the literature (*11*, *16*).

Using bioimaging approaches that allowed continuous long-term observation at the single-cell level (*17*) (fig. S2 and movies S1 to S4), we analyzed cultures of murine granulocyte-macrophage progenitors (GMPs) (*18*) (fig. S3) in the presence of only macrophage- or granulocyte colony-stimulating factor (M- or G-CSF). Single-cell tracking showed that GMPs functionally respond to both cytokines with high cloning efficiency (figs. S4 and S5). Culture in only M- or G-CSF leads almost exclusively to mature monocytic (M) or neutrophil granulocytic (G) cells, respectively (fig. S6). We utilized LysM::GFP mice (*19*), expressing enhanced green fluorescent protein (GFP) from the *lysozymeM* gene locus as an early molecular reporter for unilineage commitment. Whereas only extremely weak LysozymeM::GFP expression (LysM::GFP$^-$) is found in undifferentiated GMPs, LysM::GFP is drastically up-regulated (LysM::GFP$^+$) upon differentiation (*19*–*21*) (figs. S2B and S7 to S9 and movie S5). LysM::GFP$^+$ cells have lost their colony-forming potential (Fig. 1, A and B, and fig. S9) and are unilineage-restricted to either the M or G lineage (Fig. 1, A and C).

This approach allows detection of cell death and unilineage commitment of all cells in GMP cultures. We continuously observed hundreds of GMPs and all of their progeny throughout development into only M- or G-committed cells in the presence of only M- or G-CSF (375 pedigrees for M-CSF, 318 for G-CSF) (figs. S10 and S11). Colonies without cell death can be explained in two ways: (i) the colony-initiating cell was a bipotent GMP, and with the absence of selective cell deaths, it must have differentiated exclusively into the lineage supported by the present cytokine, or (ii) the colony-initiating cell was already unilineage-restricted to this lineage (Fig. 2A). We determined that the original GMP population contained a maximum of 23 ± 6% and 53 ± 7% potentially unilineage-restricted M and G cells, respectively (fig. S3).

Quantifying the frequency of GMP pedigrees without cell death in single-cytokine conditions allowed us to identify the lineage-instructive effect of M- and G-CSF. In 88 ± 2% (M-CSF) and

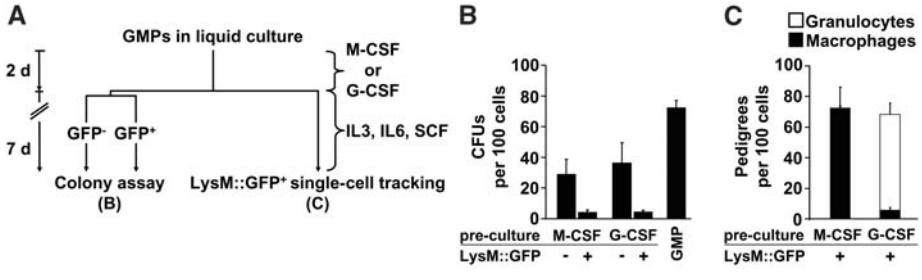

Fig. 1. LysM::GFP is a marker for unilineage-restricted G or M cells. (**A**) Experimental procedure. (**B** and **C**) LysM::GFP$^+$ cells derived from GMPs cultured with only M- or G-CSF for 48 hours have lost colony-forming potential (B) and are unilineage-restricted (C). Means ± SD of 50 pedigrees per condition and experiment (n = 3). CFU, colony-forming unit; IL, interleukin; SCF, stem cell factor.

Institute of Stem Cell Research, Helmholtz Zentrum München—German Research Center for Environmental Health, Neuherberg-Munich, Germany.

*To whom correspondence should be addressed. E-mail: timm.schroeder@helmholtz-muenchen.de

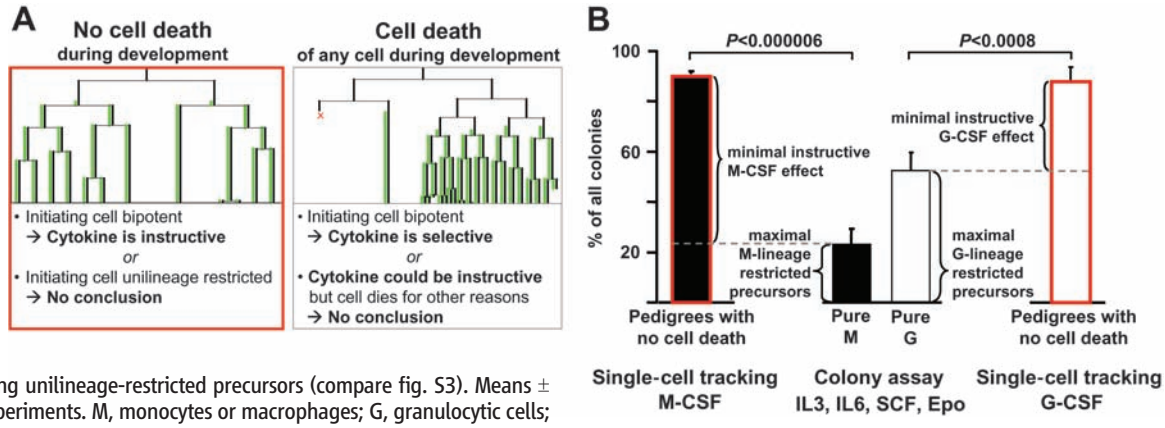

Fig. 2. M-CSF and G-CSF instruct lineage choice in GMPs. (**A**) Pedigrees were grouped according to the existence of cell death events. Green lines illustrate LysM::GFP expression. (**B**) The frequency of colonies without cell death until development into only M cells (black bars) or G cells (white bars) cannot be explained by contaminating unilineage-restricted precursors (compare fig. S3). Means ± SD, three independent experiments. M, monocytes or macrophages; G, granulocytic cells; Epo, erythropoietin.

87 ± 6% (G-CSF) of pedigrees leading exclusively to M and G cells, respectively, no cell death occurred (Fig. 2B). These percentages far exceed those of colonies that could have been generated from unilineage-restricted precursors potentially contaminating the GMP population that we used ($P < 0.000006$ and $P < 0.0008$ for M- and G-CSF, respectively). M- and G-CSF therefore instructed at least 65% and 34% of bipotent GMPs to differentiate into the M and G lineage, respectively (Fig. 2, A and B). Moreover, depending on the cytokines present, around 90% of the identical GMP population differentiates exclusively into different lineages, which demonstrates that these GMPs are bipotent. Thus, our assumption of maximally 23% (M) and 53% (G) contaminating unilineage-restricted progenitors in the starting GMP population is too conservative, and both cytokines instruct most GMPs into alternative lineages. In addition, we show that M- and G-CSF not only instruct lineage choice of differentiating cells, but also induce or accelerate differentiation: The onset of LysM::GFP expression in GMP progeny was accelerated by both M-CSF ($P < 0.00000026$) and G-CSF ($P < 0.000012$) (fig. S12).

Previous studies had postulated an exclusive selective effect of cytokines (*22*–*28*). In those studies, however, cytokine receptors were ectopically expressed in mutated progenitor cell lines or inappropriate cell types with molecular composition different from that of primary progenitors physiologically responding to those cytokines (*24*, *26*). Studies with mice either lacking cytokine receptors (*22*, *25*) or expressing chimeric cytokine receptors (*23*, *27*, *28*) demonstrated the interchangeability of cytokine receptor–derived signals for the generation (survival, proliferation, or lineage choice) of specific lineages. However, compensatory effects of other cytokines specifically for lineage choice could not be excluded. Our study shows that M- and G-CSF can instruct the lineage choice of genetically unmanipulated GMPs that physiologically respond to these cytokines (fig. S1). This demonstrates that signal transduction pathways of cell-extrinsic cytokines can influence the intracellular lineage commitment machinery (*29*). The technology described here for cell fate analysis will be useful for identifying these signaling pathways and for analyzing complex cellular systems in which a few individual cells (such as stem cells) control tissue development, homeostasis, and repair.

References and Notes

1. D. Metcalf, *Blood* **111**, 485 (2008).
2. D. Metcalf, *Blood* **92**, 345 (1998).
3. T. Enver, C. M. Heyworth, T. M. Dexter, *Blood* **92**, 348 (1998).
4. A. Dakic *et al.*, *J. Exp. Med.* **201**, 1487 (2005).
5. H. Iwasaki *et al.*, *Immunity* **19**, 451 (2003).
6. C. V. Laiosa, M. Stadtfeld, T. Graf, *Annu. Rev. Immunol.* **24**, 705 (2006).
7. F. Rosenbauer *et al.*, *Nat. Genet.* **38**, 27 (2006).
8. J. Iwasaki-Arai, H. Iwasaki, T. Miyamoto, S. Watanabe, K. Akashi, *J. Exp. Med.* **197**, 1311 (2003).
9. M. Kondo *et al.*, *Nature* **407**, 383 (2000).
10. A. G. King, M. Kondo, D. C. Scherer, I. L. Weissman, *Proc. Natl. Acad. Sci. U.S.A.* **99**, 4508 (2002).
11. L. Robb, *Oncogene* **26**, 6715 (2007).
12. Materials and methods are available as supporting material on *Science* Online.
13. T. Schroeder, *Nature* **453**, 345 (2008).
14. D. Metcalf, A. W. Burgess, *J. Cell. Physiol.* **111**, 275 (1982).
15. T. Suda, J. Suda, M. Ogawa, *Proc. Natl. Acad. Sci. U.S.A.* **81**, 2520 (1984).
16. A. B. Cantor, S. H. Orkin, *Curr. Opin. Genet. Dev.* **11**, 513 (2001).
17. H. M. Eilken, S. Nishikawa, T. Schroeder, *Nature* **457**, 896 (2009).
18. K. Akashi, D. Traver, T. Miyamoto, I. L. Weissman, *Nature* **404**, 193 (2000).
19. N. Faust, F. Varas, L. M. Kelly, S. Heck, T. Graf, *Blood* **96**, 719 (2000).
20. M. Stadtfeld, F. Varas, T. Graf, *Methods Mol. Med.* **105**, 395 (2005).
21. M. Ye *et al.*, *Immunity* **19**, 689 (2003).
22. X. M. Dai *et al.*, *Blood* **99**, 111 (2002).
23. M. A. Goldsmith *et al.*, *Proc. Natl. Acad. Sci. U.S.A.* **95**, 7006 (1998).
24. T. Kinashi *et al.*, *J. Exp. Med.* **173**, 1267 (1991).
25. F. Liu, H. Y. Wu, R. Wesselschmidt, T. Kornaga, D. C. Link, *Immunity* **5**, 491 (1996).
26. G. A. McArthur, L. R. Rohrschneider, G. R. Johnson, *Blood* **83**, 972 (1994).
27. C. L. Semerad, J. Poursine-Laurent, F. Liu, D. C. Link, *Immunity* **11**, 153 (1999).
28. R. Stoffel *et al.*, *Proc. Natl. Acad. Sci. U.S.A.* **96**, 698 (1999).
29. F. J. Pixley, E. R. Stanley, *Trends Cell Biol.* **14**, 628 (2004).

30. We thank T. Graf for the LysM::GFP mice; A. Roth, C. Raithel, and K. Azadov for technical assistance; and B. Schauberger for programming contributions. This study was supported by the Deutsche Forschungsgemeinschaft. Authors' contributions: M.A.R. designed and performed experiments, discussed results, and wrote the paper with T.S.; P.S.H., B.M.S., and A.C.E. performed experiments and commented on the manuscript; and T.S. developed the time-lapse imaging and cell-tracking technology, advanced it with all the authors, and designed the study.

Supporting Online Material

www.sciencemag.org/cgi/content/full/325/5937/217/DC1
Materials and Methods
Figs. S1 to S12
References
Movies S1 to S5

27 January 2009; accepted 20 May 2009
10.1126/science.1171461

Plasmid Preparation Kits

Plasmid Plus Kits provide convenient, large-scale plasmid preparation. The design and unique binding chemistry of the spin columns allow a simple bind-wash-elute procedure based on a novel chemistry. The procedure can be performed in 20 minutes for the midi/maxi preps and 40 to 50 minutes for mega/giga preps. The plasmid DNA is highly concentrated and ready for use in subsequent applications without further ethanol preparation. The binding chemistry of the Plasmid Plus spin columns ensures that highly pure plasmid DNA is obtained every time. The plasmid DNA is free of contaminants such as RNA, proteins, and genomic DNA.

Qiagen
For information 240-686-7686
www.qiagen.com

Pipette

The E-Man Hybrid is a new generation pipette that offers high performance, durability, and ergonomics. It combines the simplicity of a manual pipette with innovative real-time sensing technology and allows for real-time monitoring of the position of the piston and the amount of liquid dispensed. Good-manufacturing-practice functions include saved calibration and service alerts. It is designed to fulfill the most stringent regulatory requirements. Precision is increased by a visual alert that indicates inadequately executed pipetting of samples. Its ergonomic design includes great feel and light weight.
Mettler Toledo
For information 800-472-4646
www.mt.com/mt/filters/E-man

Chilled Reagent Reservoir Holders

CoolTroughs are new chilled reusable reservoir holders designed to improve the integrity of reagents and extend working time at 0° to 5°C. Manufactured with nontoxic gel encased in heavy duty polyvinyl chloride, CoolTrough reagent reservoir holders chill or freeze quickly and provide consistent cooling without the contamination risks or inconvenience of ice baths. They come with disposable 100-ml polypropylene liners, making it easy and convenient to change or replenish reagents without the use of additional cooling devices.
Porvair Sciences
For information +44-1372-824290
www.porvairsciences.com

Electrophoresis System

The Enduro Gel XL system is a compact system for separation of nucleic acids in agarose gels. The system includes a programmable power supply, gel running tank, and a complete gel casting set for quick gel preparation. No expensive consumables, such as precast gels and special buffers, are required. The power supply features a large, digital LCD and allows precise control of voltage, current, and run time. The power supply and gel running tank simply connect side by side, eliminating the typical red and black wire leads and saving bench space. Gel casting accessories allow easy preparation of miniature (6 cm by 6 cm), medium (6 cm by 12.5 cm), and large (12 cm by 12.5 cm) gels with various sample well volumes and spacing. The system is suitable for a wide range of applications from quick screening of a few samples to screening up to 96 polymerase chain reaction samples. All gel trays are ultraviolet-transparent for transillumination.
Labnet International
For information 888-522-6381
www.labnetlink.com

PCR Detection System

The CFX384 real-time polymerase chain reaction (PCR) detection system with CFX Manager software, Security Edition, can be used to ensure compliance with US Food and Drug Administration regulations for secure handling of electronic records. The system performs high throughput, real-time PCR in a 384-well format conveniently and flexibly. It provides superior performance in uniformity, dynamic range of detection, and multiplexing capabilities. Researchers can run it as a stand-alone system without a computer or run up to four instruments from one computer. Featuring the Bio-Rad C1000 thermal cycler as the base thermal cycler instrument, the CFX384 incorporates innovative optical technologies and software to deliver sensitive, reliable detection for applications including absolute quantitation, genetic variation analysis, and gene expression. The system reads each well individually with high sensitivity and no cross-talk. Multiple data acquisition modes are available to tailor runs to suit any application.
Bio-Rad Laboratories
For information 800-424-6723
www.bio-rad.com

Bar-coded Storage Tubes

Robotics-friendly MatriTubes are laser-etched two-dimensional (2D) tubes in 96-well and 384-well formats. They have a well volume of 35 µl and are supplied with permanent 2D bar codes on the base to track individual samples securely. They are manufactured of high-grade, clarified polypropylene. They can maintain sample integrity with cap and foil sealing options.
Matrical Bioscience
For information 509-343-6225
www.matrical.com

Electronically submit your new product description or product literature information! Go to **www.sciencemag.org/products/newproducts.dtl** for more information.

Newly offered instrumentation, apparatus, and laboratory materials of interest to researchers in all disciplines in academic, industrial, and governmental organizations are featured in this space. Emphasis is given to purpose, chief characteristics, and availabilty of products and materials. Endorsement by *Science* or AAAS of any products or materials mentioned is not implied. Additional information may be obtained from the manufacturer or supplier.

RUPRECHT-KARLS-
UNIVERSITÄT
HEIDELBERG

The **Medical Faculty Mannheim of the University of Heidelberg** is seeking - immediately effective – applications for the new position of a

W3 endowed Chair „Efficiency Analysis in Diagnostics“

This Chair is situated within Health Economics and Outcome Research and shall conduct systematic research on the impact of innovative strategies in diagnostic pathways and therapy stratification within the setting of academic high-end medicine with a special focus on in-vitro diagnostics. Specific aim is the evidence-based further development of efficient conduct and usage of health care resources in medical decision-making.

The endowed Chair shall contribute new global scientific cognitions in Health Economics and Outcome Research, thus strengthen the emerging “European Metropolitan Region Rhine-Neckar” and generate a highly visible profile in questions regarding process-oriented diagnostic strategies far beyond regional context. The holder of this position is expected to actively strengthen interdisciplinary academic activities in Health Technology Assessment at the Medical Faculty Mannheim and faculties located within said Metropolitan Region, respectively. The cooperation with the faculties for Economics at the University of Mannheim is strongly encouraged.

Within the Medical Faculty Mannheim, the endowed Chair is situated at the Institute for Clinical Chemistry (Dir.: Univ.-Prof. Dr. M. Neumaier). Within the Medical School´s teaching activities, the Chair is expected to have a strong commitment to the education of Medical Undergraduates in aspects of Health Economics.

The Faculty is looking for a dynamic personality with an outstanding research profile and pronounced capabilities for the medical-interdisciplinary dialogue. The applicant should have excellent skills in the areas of Outcome assessment in Health Care systems and in Health Economics. He/She should be capable of initiating and organizing interdisciplinary studies and should have previous experience in their preparation, planning and monitoring. The applicant is expected to propose recommendations and validate interdisciplinary diagnostic approaches in the context of theoretical models of medical decision-making. The endowed Chair for “Efficiency Analysis in Diagnostics” will occupy a pioneering role in Germany and shall be given to an innovative researcher committed to excellence in research.

The endowed position is available initially for 5 years with a 5 years extension in case of successful scientific peer review. Upon successful evaluation at closure of the endowment, the position will receive tenure. Candidates must have finished their academic education with an MD or MD/PhD degree, habilitation or equivalent degrees of qualification in research. An additional degree in Economics is welcome.

The Medical Faculty Mannheim of the University of Heidelberg hires on the basis of merit and is committed to employment equity. At equal aptitude, women and handicapped individuals (please specify your status when applying) will be given priority.

The deadline for applications is 6 weeks following the publication of this announcement. Applications including a scientific and professional curriculum vitae and appropriate documents, a listing of teaching experiences, a publication list (with no more than 5 reprints of the past 5 years) and the cumulative impact factor should be addressed to the **Dean of the Medical Faculty Mannheim of the University of Heidelberg, Univ.-Prof. Dr. Dr. h.c. Klaus van Ackern, University Medicine Mannheim,Theodor-Kutzer-Ufer 1-3, D-68135 Mannheim**.

NRF RESEARCH FELLOWSHIP

The Singapore National Research Foundation (NRF) invites brilliant, young researchers who are ready for their first independent research appointments to apply for the prestigious NRF Research Fellowship Awards.

- ✓ **Are you among the best in your research field?**
- ✓ **Are you ready to lead your first independent research team?**
- ✓ **Join the ranks of the elite NRF Research Fellows!**

Apply now if you have a PhD from a top university and work at the forefront of research in your field. A prior post-doctoral stint at a world renowned university or research organisation would be a significant advantage.

The NRF Research Fellowship provides:

- Complete freedom and independence to pursue your research direction in Singapore
- A 3-year research grant of up to US$1.5 million
- A competitive salary
- The opportunity for joint appointments at the host university or research institution
- Freedom to select the host institution in Singapore

The NRF Research Fellowship is open to all talented scientists and researchers under the age of 40 years at the date of application, and within 10 years post-PhD. We welcome research in all disciplines of science and technology.

Please apply online at the following web-link before **6 September 2009**:

https://rita.nrf.gov.sg/NRF_RF_2009

Shortlisted candidates will be invited to Singapore to present their research work, meet local researchers and identify potential collaborators and host research organisations. Final selection for the awards will be made by the NRF Scientific Advisory Board co-chaired by Dr. Curtis Carlson (President & CEO of SRI International) and Prof. Ulrich Suter (Emeritus Professor, ETH Zurich).

For further queries, please email **karen_tan@nrf.gov.sg**

About the National Research Foundation

The NRF supports the Research, Innovation and Enterprise Council chaired by the Prime Minister to provide a coherent strategic overview of R&D policies and direction in Singapore. It manages a S$5 billion National Research Fund to develop R&D as a key driver in transforming Singapore into a knowledge and innovation based economy.

Singapore National Research Foundation
100 High Street, #03-02, The Treasury
Singapore 179434
Tel: +65-63329010
Website: www.nrf.gov.sg

ambitious?

Schering-Plough Corporation is an innovation-driven, science-centered global health care company with leading prescription, animal health and consumer health care products. Our Translational Medicine Research Center in Singapore focuses on translating the vast progress in fundamental biomedical research into benefits for patients. The Center is comprised of a Translational Research Laboratory and a Translational Medicine Unit. We are looking for individuals who are enthusiastic and passionate about research for the following positions.

Associate Director, Immunological Biomarker Development

Will be responsible for planning, developing and managing the "immuno" laboratory section of our TRL facility.

Requirements: *Ph.D. in Biochemistry or relevant equivalent discipline, a minimum of 10 years hands-on experience with developing and validation of immunological assays and excellent knowledge of immuno diagnostic technologies, preferably also of immuno histochemistry technologies.*

Ph.D. Scientist, PET/SPECT Radiotracer Evaluation

Will work to establish PET/SPECT tracer evaluation capabilities, providing scientific leadership as well as manage a team of scientists involved in the evaluation of novel radiotracers with a specific application to innovative drug discovery research programs.

Requirements: *Ph.D. in Pharmacology, Neuroscience or a related Life Science discipline and a minimum of five years experience in techniques such as quantitative receptor autoradiography, in vivo radioligand binding or non-invasive imaging techniques such as PET or SPECT imaging.*

PhD Group Leader, PET/SPECT Radiochemistry

Will provide scientific leadership and manage a team of scientists involved in the development of novel synthesis routes to label novel small molecules for evaluation as part of Schering-Plough Research Institute (SPRI) drug discovery research programs.

Requirements: *Ph.D. in PET/SPECT Radiochemistry or related discipline with more than 5 years post PhD experience and a proven track record in PET radiochemistry.*

Ph.D. Scientist, Magnetic Resonance Imaging (MRI)

Will be primarily responsible for management of a team involved in the development of innovative preclinical translational MRI-based approaches to investigate drug action and disease management to ensure the success of our drug discovery programs.

Requirements: *PhD in MR physics, biology or related field and a minimum three years experience in the area of preclinical MRI, including specific hands-on experience in the application of small-bore MRI to biologically-relevant questions (preferably in neuroscience, oncology or a related discipline.)*

Ph.D. Scientist/Group Leader, Protein Biochemistry

Will be responsible for providing proteins, peptides and antibodies required for biomarker assay development and proteomics activities, through combination of in-house protein expression capabilities and external resources.

Requirements: *Ph.D. in Protein Biochemistry or related discipline with more than 5 years post PhD experience and a proven track record in protein expression, purification and analytics.*

PhD Scientist, LC-MS/Mass Spec. Proteomics-Metabolomics

Will coordinate and execute mass spectrometry, as part of Proteomics/Metabolomics while focusing on LC-MS/MS for biomarker discovery and protein analytics and MRM MS for peptide biomarker validation and assay development.

Requirements: *Ph.D. in Analytical Chemistry, Biomolecular mass spectrometry or related field with a minimum of 3 years post PhD experience.*

PhD Scientist/Group Leader, Cell-based Assays

Will be responsible for forming and coordinating the group as part of the Immunological Assays section, including include development and execution of cellular immunological biomarker assays, based on FACS and High Content analyses.

Requirements: *Ph.D in Immunology or a related Life Science discipline with a minimum of 5 years post PhD experience and a proven track record in Immunological cell-based assay development.*

Associate Director, Pharmacology

Will head the Pharmacology Section, with responsibility for leading this Section as part of the Translational Research Laboratory (TRL).

Requirements: *MD or Ph.D. in Pharmacology or related Life Science discipline with a minimum of 10 years post PhD experience with proven track record in pharmacological research.*

Schering-Plough

To apply, please visit www.schering-plough.com/sciencejobs. We value the diversity of our global workforce. We are an equal opportunity employer.

Director
Information, Technology and Systems Division

Enjoy challenging work and make important contributions to the Nation

The Institute for Defense Analyses (IDA) a not-for-profit corporation that operates three Federally Funded Research Development Centers (FFRDCs), two serving the Department of Defense and one serving the Office of Science and Technology Policy in the Executive Office of the President, is seeking highly qualified candidates to direct it's Information, Technology and Systems Division. Focusing on assuring the security of our nation by creating sponsor-sustainable advantages in cyberspace, division researchers:

- Analyze enterprise information capabilities supporting national security missions;
- Examine advanced technologies and concepts for emerging cyber capabilities; and
- Assess ways to improve cyber operations and information warfare capabilities.

IDA offers competitive salary, an excellent benefits package and a superior professional working environment. The selected individual will be subject to a security investigation and must meet the requirements for access to classified information. U.S. citizenship is required. IDA is proud to be an equal opportunity employer.

Interested candidates are encouraged to visit IDA's career website for more information and to apply: **www.ida.org**.

IDA

INSTITUTE FOR DEFENSE ANALYSES

Grant for Postdoctoral Positions in Sweden

This grant enables researchers with doctorates (PhDs or equivalent) to work at Swedish higher education institutions or research establishments. The programme spans up to two years. Research areas: Natural Sciences, Engineering Sciences, Medicine, Humanities, Social Sciences and Educational Sciences.

Call for applications opens early July. Submission deadline is August 27, 2009.

Further information at www.vr.se

Vetenskapsrådet

Postdoctoral Scholars for MERIT Program, a newly funded NIH IRACDA program

University of Alabama at Birmingham **MERIT** Program is seeking individuals who are interested in outstanding teaching and research experiences during their postdoctoral training. The MERIT Program will provide opportunities for research experience at UAB and teaching experience at minority serving institutions, including Miles and Stillman Colleges, located near UAB.

MERIT Fellows are supported for three years at NRSA rates beginning at $37,368; are provided health insurance at no charge, a yearly travel allowance to professional meetings and yearly research or training allowance.

Applicants to the **MERIT** Program must be PhD candidates or recent PhD graduates (within the past year) and a US citizen or non-citizen national; individuals with comparable degrees, including MD and DVM, are also eligible.

Application materials as well as other information are available by clicking on the **MERIT** logo at the Office of Postdoctoral Education website, **www.postdocs.uab.edu**.

Women and persons from diverse backgrounds, including underrepresented racial and ethnic groups, individuals with disabilities, and individuals from disadvantaged backgrounds, are encouraged to apply.

MILES STILLMAN MERIT UAB

Weill Cornell Medical College

EXPERIMENTAL PATHOLOGY FACULTY POSITIONS

The Department of Pathology and Laboratory Medicine of the Weill Cornell Medical College invites applications for faculty positions in experimental pathology. Candidates are expected to develop and maintain productive, independent, externally funded research programs in basic mechanisms of human disease which fall within the broad areas of molecular oncology and cancer genetics.

Candidates may hold an MD, a PhD, or combined MD and PhD degrees but must possess a sufficient amount of post-doctoral research training to develop an independent research program. Teaching responsibilities will include graduate and medical students.

The Department offers a supportive intellectual environment in which several mid-level and senior scientists direct well-funded independent research programs in molecular oncology, immunobiology, and vascular biology. Modern research laboratory facilities, excellent core facilities, and competitive start-up packages are available.

Interested applicants should submit a curriculum vitae, representative recent publications, and a brief description of past scientific accomplishments, future research plans, and career objectives, as well as the names of three individuals familiar with the applicant and the applicant's research program. Applications will be accepted until all positions are filled. Please submit via email to **rubinma@med.cornell.edu** or to:

Dr. Mark A. Rubin
Vice Chairman for Experimental Pathology
Department of Pathology and Laboratory Medicine
Weill Cornell Medical College
1300 York Avenue, Box #69
New York, New York 10065

Weill Cornell Medical College is an Equal Opportunity/Affirmative Action Employer. Women and minority candidates are encouraged to apply.

King Abdullah University of Science and Technology KAUST

PROVOST and EXECUTIVE VICE PRESIDENT FOR ACADEMIC AFFAIRS
King Abdullah University of Science and Technology (KAUST)
Saudi Arabia

King Abdullah University of Science and Technology (KAUST) is being established as a private graduate research university in Saudi Arabia. KAUST (**http://www.kaust.edu.sa**) aims to be a world-renowned research university harnessing science and technology to take on the regional and global challenges of the 21st century through bold research and innovative education and their transformative potential. To build an open, enabling environment for teaching and research unfettered by disciplinary boundaries, KAUST has adopted a matrix structure of Academic Divisions and Research Centers. KAUST has also built up an extensive network of partnerships with leading research universities and corporations around the world.

With one of the largest university endowments in the world, KAUST is a merit-based institution governed by an independent international Board of Trustees. The environmentally friendly campus with state-of-the-art research facilities is built on 36 sq kilometers on the shores of the Red Sea near Jeddah, Saudi Arabia. Opening its doors to students in September 2009, KAUST's pioneer class of 350 students, 25% of whom are female, come from about 60 countries. At maturity, KAUST will enroll 2,000 students in MSc and PhD programs. The medium of instruction is English.

Provost and Executive Vice President for Academic Affairs

The Provost and Executive Vice President for Academic Affairs ("Provost") is a faculty member and reports directly to the President. As KAUST's chief academic officer, the Provost has overall responsibility for KAUS T's academic and research programs, Academic Divisions, and Research Centers, as well as student admissions, affairs and life.

Working closely with the President, other officers, and senior administrators of the University, the Provost plays a key role in developing and implementing the University's vision and strategic plan. The Provost provides academic leadership and acts for the University's President in his/her absence. The Provost works closely with the Academic Division Chairs and Research Center Directors to establish academic and research priorities and to allocate resources in support of the University's research and academic missions. Together with the Academic Division Chairs, the Provost oversees faculty development, including the recruitment, appraisal, promotion, and retention process. The Office of the Provost also coordinates curriculum development across the degree programs offered by Academic Divisions.

The Provost works in partnership with the Executive Vice President for Administration and the Senior Vice President for Research and Economic Development. The Provost's direct reports include the Associate Provost for Faculty Affairs, Academic Division Chairs, Research Center Directors, Assistant Provosts for Research, for Student Affairs and for Student Life, Director of the KAUST Library, and Director for Academic Budget and Planning.

Contact Information
Korn/Ferry International, which is assisting with this search, invites confidential inquiries, nominations and applications. All communications will be held in absolute confidence. Nominations should include nominee contact information. Applications should include a CV and letter explaining interest and relevant experience. The position is available beginning September 2009.

Korn/Ferry International
John Kuhnle, Managing Director-Global Education Practice
Elizabeth Dycus, Senior Consultant
802/765-4543
KAUSTprovost@kornferry.com

Tenure Track Faculty Positions (Assistant/Associate Professor)

The Department of Biochemistry and Molecular Biology at the Medical College of Georgia invites applications for two tenure track positions (ACH48042 and ACH058693) at the levels of Assistant Professor or Associate Professor. The positions are available effective October 1, 2009. A Ph.D. or M.D. degree with appropriate post-doctoral or academic experience is required. Research areas of interest for new recruits include stem cell biology, epigenetics and cancer genetics, cancer invasion and metastasis, and inflammatory bowel disease. Other areas of cancer biology (angiogenesis, tumor microenvironment, tumor immunology) will also be considered. Faculty members are expected to participate in teaching medical students and graduate students, but extramurally funded research will be the primary focus and responsibility for these new positions. Successful candidates are expected to have extramural funding (Associate Professor) or be ready to apply for extramural funding (Assistant Professor). The new positions come with substantial laboratory space and highly competitive start-up package. Successful candidates will also be appointed as adjunct members in the MCG Cancer Center and will have access to several state-of-the-art core facilities available at the Cancer Center.

Interested individuals should send their Curriculum Vitae, statement of research interests, and names of references to: **Dorothy Tuan, Ph. D., Faculty Search Committee Chair, Department of Biochemistry and Molecular Biology, Medical College of Georgia, Augusta, GA 30912-2100**. Candidates can also email the application to **Ida Walker** (E-mail: **iwalker@mcg.edu**).

The Medical College of Georgia is an AA/EEO/Equal Access/ADA Employer and a Tobacco-Free Institution.

ORNL Neutron Sciences
Scientific Computing

The Neutron Sciences Directorate at Oak Ridge National Laboratory (ORNL) invites applications for the positions of Scientific Computing Researcher and Scientific Computing Associate. With the world's highest flux reactor-based neutron source (the High Flux Isotope Reactor) and the world's most intense pulsed accelerator-based neutron source (the Spallation Neutron Source), ORNL has become the world's foremost center for neutron science. Research at these facilities will encompass the physical, chemical, materials, biological, and medical sciences and will provide opportunities for up to 2000 researchers each year from industry, research facilities, and universities all over the world.

For more information about these positions and to apply online visit: https://www2.orau.gov/ORNL_POST

- **Scientific Computing Researcher—ORNL09-94-NSSD**
  Qualifications: Successful candidate must have a Ph.D. in physics, computer science, computer engineering, or other engineering or scientific discipline with demonstrated experience developing analysis related software which others have used. (Please see online posting for more details.)
- **Scientific Computing Associate—ORNL09-93-NSSD**
  Qualifications: Successful candidate must have a minimum of a Masters Degree in physics, computer science, computer engineering, or other engineering or scientific discipline with demonstrated experience developing analysis related software. (Please see online posting for more details.)

To learn more about Neutron Sciences at ORNL visit http://neutrons.ornl.gov

This appointment is offered through the ORNL Postgraduate Research Participation Program and is administered by the Oak Ridge Institute for Science and Education (ORISE).

Huazhong Agricultural University Recruits Professors

Huazhong Agricultural University (HZAU) is a National Key university of the "211project" and celebrated its 110th anniversary in 2008, located at Wuhan City of Hubei province. The beautiful campus is one of the largest in China (4.9 km^2), surrounded by natural lakes.

Now we seek candidates under 55 years old for multiple positions of full-time professors in the following fields: Crop Cultivation and Farming System, Crop Genetics and Breeding, Pomology, Vegetable Science, Microbiology, Biochemistry and Molecular Biology, Aquaculture Science, Animal Genetics, Breeding and Reproduction Science, Agriculture Economics, etc.

Depending on the candidates' qualification and experience, we will provide each candidate 2,000,000-10,000,000 RMB research running fund, 100,000-1,000,000 RMB one-off living allowance, annual salary referring to income earned abroad and domestic purchasing power, research assistants and lab space. We will offer a new on-campus apartment of 150 m^2, campus job for spouse and school/kindergarten for children.

We welcome sincere candidates to visit our university. We will provide roundtrip traveling expenses for visitors who contact us in advance.

Additionally, the university is also interested in excellent doctors with overseas education/research experience for the above positions that will be provided favorable treatment and conditions. Qualified candidates can directly contact the Department of Personnel of Huazhong Agricultural University: Contactor: **Miss Deng** or **Mr. Jiang**, E-mail: **rcjlzx@mail.hzau.edu.cn**; Phone Number: **86-27-87280957**.

Related Web Site: **http://www.hzau.edu.cn**

Postdoctoral Positions

MAINE MEDICAL CENTER RESEARCH INSTITUTE

Several postdoctoral positions are available at the Maine Medical Center Research Institute (MMCRI) for individuals with a Ph.D. or M.D. degree with a commitment to a research career in vascular biology, stem and progenitor cell biology, or bone and metabolic disorders. Qualified candidates will have demonstrated experience in molecular and cellular biology and/or mouse models of human diseases. Successful applicants will have access to state-of-the-art laboratories and Core facilities. Salary and a comprehensive benefits package are nationally competitive.

To apply online, go to: **www.mmc.jobs.** For additional information on available positions in specific laboratories, please visit our website: **http://www.mmcri.org/admin/postdoc.html.**

www.mmcri.org

Maine Medical Center
MaineHealth

centered around you

Ce–M–M–

Research Center for Molecular Medicine
of the Austrian Academy of Sciences

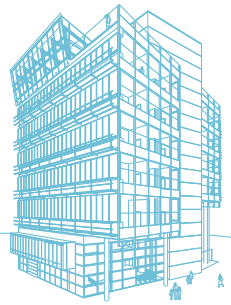

Principal Investigators

to start during 2010/2011 in the new purpose-made research building in the middle of Vienna's medicalcampus

To complement and strengthen the current faculty, CeMM is looking for outstanding individuals who work on an exciting problem of molecular medicine preferably but not exclusively pertaining to Innate Immunity, Infection Biology, Inflammation, Hematopoiesis, Hematological Malignancies, Blood and Vascular Disorders in general. Approaches that we are particularly interested in are: Systems Biology, Bioinformatics, Genomics, Epigenetics, Metabolomics, Chemical Biology, High-Content Screening, Single-Cell Technologies, Drug Imaging Technologies, Cell Imaging Tissue Repair and Stem Cell Biology. We also have a focus on kinases, ubiquitination, epigenetics and molecular intervention approaches with the potential for therapeutic development.

We are looking for MD and/or PhD scientists for their first independent appointment or early in their independent careers to apply their expertise close to a clinical setting in a stimulating research environment. Initial appointments are for five years but are expected to be extended after reviewing for an additional term of three years, subject to review by the Scientific Advisory Board. Required are an MD or PhD degree, scientific quality and originality, a track record of achievements as well as a collaborative and interdisciplinary mindset. Applications should be in English and contain a CV, publication list, names and address of three references, a short summary of research interests and objectives. Please also summarize in one paragraph what you believe your single greatest research achievement has been so far and why.

Please send all documents in English to:
Anita Ender, aender@cemm.oeaw.ac.at
Deadline: August 15, 2009

CeMM, the Research Center for Molecular Medicine is an international, independent and interdisciplinary research institution of the Austrian Academy of Sciences located at the Campus of the Vienna General Hospital and Medical University of Vienna (MUV). For more information about CeMM and about these positions please visit our website: **www.cemm.at**

St. Jude Children's Research Hospital
ALSAC • Danny Thomas, Founder
Finding cures. Saving children.

FACULTY POSITIONS
DEPARTMENT OF HEMATOLOGY

The Department of Hematology, at St. Jude Children's Research Hospital, is seeking to fill two faculty positions at the level of ASSISTANT and/or ASSOCIATE MEMBER. We are specifically seeking applicants whose research program is or will be focused on laboratory-based research in Hematology. Candidates with interests in erythropoiesis, stem cell biology, iron metabolism, or other areas in molecular hematopoiesis are encouraged to apply. Research plans that are either basic or translational science will be considered. An MD, PhD, or a combined degree is required.

The Hematology Department currently consists of nine faculty members who are engaged in clinical and laboratory research in sickle cell disease, thalassemia, gene therapy for blood disorders, hemophilia disorders, and various aspects of molecular hematopoiesis.

St. Jude offers a rich academic environment for laboratory-based research in Hematology with state-of-the-art resources for genomics, molecular bioinformatics, genetic animal models, cell and animal imaging, cell sorting and flow cytometry. We also have an active Sickle Cell Center, a GMP-manufacturing facility, and other strong clinical resources. Numerous opportunities exist for interdisciplinary academic collaborations, both within the Department of Hematology and within the institution.

Interested individuals should send their CV and a brief description of their research plans to:

Brian Sorrentino, MD • Chair, Search Committee
Chair, Hematology Faculty Search Committee
Department of Hematology
St. Jude Children's Research Hospital
262 Danny Thomas Place – MS #341
Memphis, TN 38105-3678
E-mail: Brian.sorrentino@stjude.org
Ph: (901) 595-2727

St. Jude is an Equal Opportunity Employer and a Drug-Free Workplace.
Candidates receiving offers of employment will be subject to pre-employment drug testing and background checks.

Federal law requires all employers to verify the identity and employment eligibility of all persons hired to work in the United States.
To support this mandate, St. Jude Children's Research Hospital participates in E-Verify.

www.stjude.org

University of Glasgow

Faculty of Physical Sciences

Department of Physics & Astronomy

Professor of Solid State Physics

A Professorial appointment is available for a candidate who will provide scientific leadership in the Solid State Physics group, and conduct world class research on aspects of condensed matter or materials physics. Current research strengths in the Solid State Physics group are in nanoscale physics and associated technology and in electron microscopy. Both experimental physicists, and theoretical physicists with interests in working closely with the experimental programme, will be considered. You will also play a key role, with colleagues, in developing and implementing departmental strategy in research and teaching. Should a candidate of appropriate stature and reputation present themselves, they will be appointed to the Chair of Natural Philosophy at the University.

For further information on the post please contact Professor Andrew Long (hod@physics.gla.ac.uk).

Apply online at www.glasgow.ac.uk/jobs

If you are unable to apply online please contact us on 0044 141 330 3898 for an application pack, quoting Ref 00029-5.

Closing date 31 August 2009.

Interviews are anticipated to be held on 5th and 6th October 2009.

The University is committed to equality of opportunity in employment.

The University of Glasgow is a registered Scottish charity, number SC004401.

www.glasgow.ac.uk

Medical College of Wisconsin/ Children's Hospital of Wisconsin

Pediatric Endocrinology

The Section of Endocrinology within the Department of Pediatrics at the Medical College of Wisconsin, in conjunction with the Children's Hospital of Wisconsin, Children's Research Institute is seeking candidates for faculty positions within the Max McGee National Research Center for Juvenile Diabetes. The Center is closely affiliated with the high-volume Diabetes Clinic at Children's Hospital of Wisconsin as well as the Human and Molecular Genetics Center at The Medical College of Wisconsin. We focus on using state-of-the-art analysis platforms to better understand the pathogenesis of type 1 diabetes, with a strong emphasis on translational research. Opportunities for collaborative research with clinical and basic scientists within the section, as well as with other faculty within the Medical College of Wisconsin, are excellent. Children's Hospital of Wisconsin is a large and successful freestanding children's hospital that was recently ranked #3 in the nation by *Parents* magazine. Metro-Milwaukee is a lakeshore community of 1.5 million located 90 miles north of Chicago.

Candidates should have training, experience, and active research programs within the field of immunology related to type 1 diabetes or the field of pancreatic beta cell biology. We are seeking highly productive candidates with successful track records in the procurement of extramural funding and participation in collaborative research programs. Eligible candidates are expected to hold a Ph.D. or M.D./Ph.D. (or equivalent), and proven excellence and productivity in research. Highly competitive start-up packages will be provided to facilitate program development. Please submit resumes to:

Martin J. Hessner, Ph.D., Associate Professor
Medical College of Wisconsin
Department of Pediatrics
8701 Watertown Plank Road, Milwaukee, WI 53226
e-mail: **mhessner@mcw.edu**, Fax: 414-456-4496
Or apply online: **www.mcw.edu/careers**

EEO/AA M/F/D/V

Children's Hospital and Health System™ MEDICAL COLLEGE OF WISCONSIN

Children's Specialty Group™

Ohio Research Scholar
Biobased Emergent Materials

The Ohio State University's (OSU) College of Food, Agricultural, and Environmental Sciences, Ohio Agricultural Research and Development Center (OARDC) invites applications from outstanding scientists and engineers who have established programs of preeminence for an endowed chair in Biobased Emergent Materials. The successful candidate will focus on biological, chemical, and/or physical processes to create novel polymeric systems applied to biobased materials development. This Ohio Research Scholar position is one of several newly created endowed chairs that are part of a multi-university, statewide initiative formed to create a research cluster of excellence in technology-enabling and emergent materials. The cluster is a cross-disciplinary collaboration between The Ohio State University, University of Dayton, and The University of Akron (UA) together with coordinated industrial support. For more information on this and related positions please visit: **http://orsp.osu.edu**.

Based on the OSU/OARDC Wooster campus, the successful candidate will collaborate with all facets of the emergent materials research cluster programs associated with OSU and other Ohio universities. He/She will hold a joint appointment in the Dept. of Horticultural and Crop Science and the Department of Food, Agricultural and Biological Engineering with the potential for an adjunct appointment with UA's College of Polymer Science and Polymer Engineering. This collaboration will link OSU and UA to create innovative and novel materials and processes, and to train a new generation of scientists and engineers for the emerging global biobased economy.

Review of applications will begin **August 1, 2009** and continue until the position is filled.

The Ohio State University is an Equal Opportunity, Affirmative Action Employer. Women, minorities, veterans, and individuals with disabilities are encouraged to apply.

OPPORTUNITIES FOR SCIENTISTS OF INDIAN ORIGIN

GOVERNMENT OF INDIA
MINISTRY OF SCIENCE & TECHNOLOGY
DEPARTMENT OF BIOTECHNOLOGY
RAMALINGASWAMI FELLOWSHIP

Applications are invited for "Ramalingaswami Fellowship", a re-entry scheme of the Department of Biotechnology, Ministry of Science & Technology, Govt. of India.

Objective

1. The scheme is aimed at bringing back scientists of Indian origin working out side the country in various fields of Biotechnology, including agriculture, health sciences, bio-engineering, energy, environment, bioinformatics and all other related areas, and who are desirous of pursing R&D in an Indian institution.

Eligibility

2. The applicant should possess a higher degree or equivalent, such as PhD, MD etc with an outstanding track record reflected in publications and other recognitions.
3. Only candidates of Indian origin working oversease are eligible to apply. Those who have already returned to India and are working in India are not eligible.

About the fellowship

4. Each awardee selected will receive fellowship amount of Rs. 75,000/ pm consolidated and a contingency grant of Rs. 5,00000 / year for purchase of consumables, minor equipment, international and domestic travel, engaging manpower and other contingent expenditure to be incurred in connection with the implementation of the project. However, institute / university where applicant proposes to work can consider giving the necessary benefits like (HRA/housing, medical, leave travel and other benefits) as applicable to regular faculty.

1. In case an awardee during the tenure of the fellowship finds a suitable position at any research institute/ university, he or she can take up the job in that case he / she will have to opt for either fellowship or salary. However, she / he can continue taking contingency grant with the prior approval of the department.
2. Ramalingaswami Fellows could take up fellowship at any of the scientific institutes / university in the country. However application should be duly forwarded by the competent authority of the host Institute.

Duration

The duration of the fellowship will be for a period of five years extendable by another 5 years on a fresh appraisal.

The applications may be sent as per Proforma duly forwarded by the competent authority to **Dr. Meenakshi Munshi, Joint Director, Department of Biotechnology, Block-2, 7th Floor, CGO Complex, Lodhi Road, New Delhi -110 003, Email :- meenakshi29@dbt.nic.in latest by 31st July, 2009.** The other details regarding the proforma may be seen at **www.dbtindia.nic.in.**

Opening positions of Shanghai ChemPartner

Shanghai ChemPartner is one of leading service providers in China, focusing on custom synthesis, medicinal chemistry, biology, DMPK, Tox, chemical process development, and manufacturing. There are over 1,000 scientists in the company located in Shanghai Zhangjiang Hi-Tech Park. With a strong financial performance and healthy investment, the company has embraced its fast growth in recent years. To keep up with the growing demands for R&D outsourcing, we are looking for experienced candidates who thrive in a fast paced research organization.

1. Head of Quantitative Biology group
Qualifications: A Ph.D. in biological science (biochemistry, cell biology, etc) with a minimum 3 ~ 6 years of drug discovery experience in pharmaceutical or biotech industries is preferred. Strong hands-on skills in several of the following areas: in vitro kinase assay, biochemical assays and cell-based assays (in-cell kinase assay, cytotoxicity, proliferation, apoptosis, immunophenotyping, ELISA, and radio isotope assays). The candidate shall be familiar with data processing and other scientific software (Excel, Prizm, etc) with solid project managerial skills.

2. Head of Protein Science group
Qualifications: Ph.D. in biochemistry or other life sciences with at least 3-5 years industry experience. The candidate should have thorough understanding and solid hands-on experience in protein engineering, expression, refolding, purification, characterization and assay development. Knowledge of protein drug development is a plus.

3. Scientist, Oncology
Qualifications: Master or Ph.D. in Biological or Medical Sciences with research experience in one of the following biological effect areas: growth factor/survival, angiogenesis, cell cycle control and cell signaling pathway. The candidate should have cancer research experience in an industrial setting. Experience in in vitro and/or in vivo models for solid tumors and applying these models for small molecule studies is essential. Good understanding on key issues of oncology and how to apply it for drug discovery and development

4. Senior Scientist, Cell Biology
Qualifications: Master Degrees or Ph.D. in biomedical science, cell biology, pharmacology or related disciplines. Hands-on experience in cell culture and cell based assay are essential with experience in cell biology research a must. The candidate should have experience in experimental design, trouble shooting, data interpretation and statistical analysis. A strong work ethic, excellent oral and written communication skills are essential. Understanding of drug discovery and development process is desired but not required.

5. Senior Research Fellow, In Vitro Biology and Assay Technology
Qualifications: A Ph.D. with 8 or more years in industry research experience, in the area of HTS, assay development in drug discovery and development is essential. An extensive understanding of assay technology, HTS, drug discovery and development process. Track record of managing drug discovery programs. Demonstrated ability to provide technical and administrative leadership and motivate teams in drug discover research environment. Proven ability to work collaboratively.

6. Senior Leader, Bioanalytical Sciences and GLP Compliance
Qualifications: Ph.D. in Bioanalytical Chemistry, Analytical Chemistry, Biochemistry or related discipline. 10 or more years of pharmaceutical industry experience in a DMPK Department or GLP Bioanalytical Lab. Provide scientific leadership and technical expertise for LC/MS/MS assay development, validation, sample analysis and trouble shooting for preclinical and clinical samples of small molecules and their metabolite(s). Desire and ability to work in a matrix environment to ensure client timelines and needs are met.

7. Senior Research Fellow in Neuroscience
Qualificatons: A Ph.D. in Pharmacology or other biomedical sciences with at least 8-years' industry experience in neuroscience is preferred. The ideal candidate should have hands-on experience in assay development for GPCR or ion channel targets, and program leading experience in areas such as pain, neurodegeneration, or anxiety/depression. An excellent oral as well as written communication skill is essential.

For more information about us, please to to: **www.chempartner.cn** or **www.shangpharma.com**. Discover your future with us by sending your CV to **recruitment@chempartner.cn**.

AWI Stiftung Alfred-Wegener-Institut für Polar- und Meeresforschung in der Helmholtz-Gemeinschaft
HELMHOLTZ GEMEINSCHAFT

Within the forthcoming BMBF joint project "Biological Impacts of Ocean Acidification (BIOACID)", starting by September 15th, 2009 - funding provided, the Departments of Bio-, Geo- and Climate sciences seek applications for

- several **PhD-student positions** (TVöD-Bund 13/2),
- **1 Post-Doc** (TV-L 13),
- **1 Technical assistant (aquaculture)** (TVöD-VKA)

The world oceans take up one third of the anthropogenic carbon dioxide (CO_2), causing pH and the carbonate saturation to decline. A reliable prediction of the response of marine organisms (phyto- and zooplankton, invertebrates, fishes and their life stages) and systems to such changes requires a detailed understanding of the underlying mechanisms as well as long-term studies under controlled conditions. BIOACID intends to carry out interdisciplinary studies of development, growth and activity performance, and of the mechanisms of acid-base and ion regulation incl. calcification. The scope of the work is complemented by molecular analyses, by modelling and the study of synergistic effects of ocean acidification and other environmental factors, with the goal to reach predictability of future responses of marine organisms and ecosystems.

Detailed descriptions of each position and of the specific requirements are available on the AWI homepage under Open Positions (http://www.awi.de/en/news/open_positions/bremerhaven_helgoland_sylt).

PhD studentships are three years fixed-term positions that provide the opportunity to attain a PhD degree. The PhD students will be enrolled in the Helmholtz Graduate School for Polar and Marine Research "POLMAR" (www.polmar.awi.de). The work will be carried out in close cooperation with national and international partners and require highly motivated and independent candidates, with a positive attitude to working in an interdisciplinary team.

Severely disabled applicants with high technical and personal suitability will be preferentially selected, please see our notification on our homepage under job offers / jobs. AWI specifically encourages female candidates to apply with a view towards increasing the proportion of female scientists. AWI supports balanced work-life career development via a variety of alternatives.

AWI supports balanced work-life career development via a variety of alternatives.

Applications, including the usual documents (cover letter, curriculum vitae, copies of scientific degrees, and the names and contact information of two references), with reference number should be sent by **July 30th 2009** to: Alfred-Wegener-Institute for Polar- and Marine Research, Personnel Department, P.O. Box 12 01 61, 27515 Bremerhaven / Germany (http://www.awi.de)

University of California
Berkeley, California

DIRECTOR

Lawrence Berkeley National Laboratory

The President and the Regents of the University of California invite nominations and applications for the position of Director of the Lawrence Berkeley National Laboratory (Berkeley Lab), which is a multidisciplinary laboratory managed by the University of California (UC) for the U.S. Department of Energy (DOE) Office of Science. The appointment will be effective upon selection, or at such later time as is mutually agreeable to the appointee and the University.

The Director is responsible for the overall operation and strategic direction of the Laboratory, which conducts a major national multidisciplinary program of research and development. The Director leads the development and integration of the Laboratory's scientific vision, goals, and objectives. The position provides leadership to laboratory management and serves as the highest level management liaison with UC, DOE, and other public and private agencies. Within University policy, the Director exercises broad delegated powers in the overall leadership and administration of the Laboratory's programs and operations, including the definition of their technical aspects, the negotiation of their size and content, and the execution of these programs with the highest quality. In addition, the Director ensures a sustained strong workforce, which presently includes approximately 3,700 staff members plus an additional 3,200 guest researchers. The Director must maintain a robust infrastructure and an integrated safety management program. The Director is also responsible for ensuring that the DOE national user facilities hosted by the Laboratory are managed cost-efficiently and provide the level of service and scientific utility required by the world's leading researchers.

Candidates should have demonstrated success in leading and managing large scientific programs or complex organizations and should have a distinguished record of scientific and technical accomplishments. Strong leadership skills are required, including the ability to gain the confidence of key leaders, scientists, and operations staff, and the ability to develop strategic relationships and partnerships with key constituents. The ideal candidate should have demonstrated management responsibility in a mission-oriented, research and development institution. Significant management experience is needed to ensure that support functions achieve compliance with all applicable Federal, State, and UC policies. Other required competencies and capabilities may be identified through the candidate selection process.

Berkeley Lab, established in 1931, is located on a 200-acre site in the hills above the UC Berkeley campus and has an annual budget in excess of $600 million. There are 14 scientific divisions whose members perform unclassified basic and applied research across a broad spectrum of program areas. The Lab hosts five DOE national user facilities, and leads or participates in numerous national and regional collaborations. Eleven scientists associated with Berkeley Lab have won the Nobel Prize and 55 Nobel Laureates were trained or had significant collaborations at the Laboratory. Thirteen Berkeley Lab scientists have won the National Medal of Science, and 61 are members of the National Academy of Sciences. More than 250 researchers hold joint faculty appointments with UC Berkeley, and there are 350 postdoctoral fellows and 450 graduate and undergraduate students.

Applications, accompanied by current resumes, and nominations may be sent to:

University of California
Office of the President
Attn: LBNL Search
1111 Broadway Street, Suite 1450
Oakland, CA 94607-4081
or email: directorsearch@ucop.edu

The position will remain Open Until Filled but applicants are encouraged to submit resume and statement of interest to the above address by no later than August 31, 2009 to be given full consideration. Salary is commensurate with experience. In conformance with applicable law and policy, the University is an affirmative action/equal opportunity employer.

Junior Faculty, Tenure-Track Physician-Scientist in Cancer and Stem Cell Research

Opportunity: A funded junior faculty tenure-track MD or MD/PhD physician-scientist translational investigator position (Asst or early Assoc Prof) is available to study microRNA genetic and epigenetic regulation of normal and leukemic stem cells. The mentor's laboratory research focuses on the cell and molecular biology of hematopoietic stem-progenitor cells and their malignant counterparts, with multiple projects designed to determine the cellular function and molecular mechanism of action of selected stem cell-expressed microRNAs in primary stem-progenitor cells (*Proc Natl Acad Sci* **104:**2750, 2007 or *J Immunol* **180:**5645, 2008), human embryonic stem cells (*Blood* **206:**860, 2005 or *Cell Stem Cell* **1:**461, 2008) and leukemia cells (*Blood* **108:**1223, 2006). Translational goals are to manipulate genes regulating early steps in blood formation to increase human hematopoietic stem cell numbers and function, and to identify gene targets for novel leukemia therapies.

Initial appointment for 3 years, with salary and research startup support and 80% protected research time. Appointment in the University of Maryland Greenebaum Cancer Center (headed by **Dr. Kevin Cullen**), the Center for Stem Cell Research and Regenerative Medicine (headed by **Dr. Curt Civin**) and appropriate basic science and clinical academic departments. Extensive opportunities to team with interactive laboratories in state-of-the-art facilities. Prior junior faculty mentees have made cutting-edge discoveries and become distinguished physician-scientists.

Qualifications: Postdoctoral fellow, junior, or mid-career investigator; faculty experience preferred. Doctoral/postdoctoral research background including experience with microRNA, hematopoiesis, or embryonic stem cells and many techniques of current molecular and cell biology. Active laboratory-based research and patient-oriented responsibilities in or directly related to cancer, with potential to move findings from basic to clinical. Medical oncologist and/or hematologist preferred and will be a member of the Cancer Center's Hematologic Malignancies Program (headed by **Dr. Maria Baer**), but other clinical disciplines will also be considered. Ability to work independently and creatively, as well as to collaborate productively. Prior U.S. citizen or resident with valid visa at the time of appointment.

Contacts: Interested applicants should email CV, brief description of research background and interests and personal references to:

Curt I. Civin, MD
Associate Dean for Research,
University of Maryland School of Medicine
Director, Center for Stem Cell Biology and Regenerative Medicine
Professor of Pediatrics
Email: ccivin@som.umaryland.edu
AND
Maria Baer, MD
Director, Hematologic Malignancies Program
University of Maryland Greeenebaum Cancer Center
Professor of Medicine
Email: mbaer@umm.edu

The University of Maryland, Baltimore encourages women and members of minority groups to apply and is an AA/EEO/ADA Employer.

Gene-Environment Interaction

Faculty Position

The University of Texas School of Public Health (UTSPH) invites applications for a full-time tenure-track faculty position at the Associate or Full Professor level with an emphasis in human gene-environment interaction. The position is based in the Division of Environmental and Occupational Health Sciences. With 150 faculty and 1100 students, the UTSPH is located in the renowned Texas Medical Center, the largest medical center in the world. Houston, the nation's fourth largest city, is a vibrant multi-cultural center, and a world leader in healthcare, petroleum, energy and international commerce and shipping.

The selected candidate will be an accomplished scientist who will be expected to establish an extramurally-funded program of independent and collaborative research, contribute to the educational mission of the School through teaching and advising master's and doctoral students, and perform community service. The research environment in the Texas Medical Center provides unparalleled opportunities to collaborate with interdisciplinary researchers, including the UTSPH Human Genetics Center and the Brown Foundation Institute of Molecular Medicine for the Prevention of Human Diseases within The University of Texas Health Science Center at Houston.

Qualifications include: (1) earned doctorate in an appropriate discipline; (2) demonstrated research proficiency in human gene-environment interaction; (3) commitment to excellence in teaching and advising graduate students; (4) track record of external funding and peer-reviewed publications; (5) excellent written and oral communication skills.

This position will be available September 1, 2009. Review of applications will begin immediately and continue until the position is filled. Academic rank will be determined by the qualifications of the candidate. Candidates should submit a letter of interest, C.V. and contact information for three professional references to: **Lawrence Whitehead, PhD, EOHS.Search@uth.tmc.edu, or mail to Lawrence Whitehead, PhD, Chair, Gene-Environment Interaction Search Committee, Division of Environmental and Occupational Health Sciences, The University of Texas School of Public Health, 1200 Herman Pressler, Suite W-1016, Houston, Texas 77030.**

The University of Texas Health Science Center at Houston is an EO/AA employer. M/F/D/V. Minorities and women are strongly encouraged to apply. This is a security-sensitive position and thereby subject to Texas Education code §51.215. A background check will be required for the final candidate.

The University of Texas
School of Public Health at Houston

Max Planck Institute for Molecular Biomedicine

MAX-PLANCK-GESELLSCHAFT

The Max Planck Society Announces

4 Independent Junior Research Groups

in the Area of

Stem Cells and Human Degenerative Disease

As a result of the joint effort of the Max Planck Society, the Ministry for Innovation, Science, Research and Technology of the State of North Rhine-Westphalia and the Medical Faculty of the University of Münster to foster stem cell research for the study of human degenerative disease, the Max Planck Institute for Molecular Biomedicine (www.mpi-muenster.mpg.de) has openings for four Independent Junior Research Groups. The group leader position as well as modern laboratory space is guaranteed for five years (W2; equivalent to associate professor level), he or she is entitled to funding for a research group. The institute runs an International PhD Program (IMPRS) and has strong links to the University of Münster.

The Max Planck Institute with its network (such as the Lead Discovery Center and the Chemical Genomics Centre of the Max Planck Society located in nearby Dortmund), offers an ideal interdisciplinary research environment for scientists interested in developing in vitro models of human degenerative disease and in studying the underlying pathophysiological processes at a molecular and metabolic level. We would also like to encourage scientists specializing on bioinformatics and interested in developing models for normal and pathophysiological processes to apply.

The Max Planck Society seeks to increase the number of women in those areas where they are underrepresented and therefore explicitly encourages women to apply. The Max Planck Society is also committed to employing more handicapped individuals and especially encourages them to apply.

Application requirements are detailed on www.mprg.mpg.de

Further information can be obtained through Hans Schöler - Managing Director - Max Planck Institute for Molecular Biomedicine.
Email: office@mpi-muenster.mpg.de

Please send your application until August 24, 2009. The selected candidates will be invited to Münster to participate in a symposium (October 19 and 20, 2009).

CUA

Director, Biotechnology Graduate Program

The Biology Department at The Catholic University of America has an opening for the Director of its new Biotechnology Program. The successful candidate will teach graduate courses, develop collaborations with biotechnology industry, and maintain an externally sponsored research program in an area of biotechnology. This is a tenure track position at the rank of Associate Professor but exceptionally qualified candidates may be considered for a higher rank. The biology department has a strong research emphasis in cell and molecular biology and offers undergraduate and graduate programs including the PhD (**http://biology.cua.edu/**). We seek candidates who have a strong track record of research accomplishments, extensive experience in the biotechnology industry and a passion to develop an exciting new program. Please send CV, a statement of career interests, and three letters of reference by **August 31, 2009** to **Dr. Venigalla Rao, Chair of Search Committee, Department of Biology, The Catholic University of America, 620 Michigan Ave NE, Washington, DC 20064**; e-mail: **rao@cua.edu**.

The Catholic University of America was founded in the name of the Catholic Church as a national university and center of research and scholarship. Regardless of their religious affiliation, all faculty are expected to respect and support the University's mission. CUA is an Affirmative Action/Equal Opportunity Employer, EOE/AA/V/D/M/F.

Quantitative Fisheries Ecologist and Large Mammal Ecologist

The Department of Fisheries, Wildlife, and Conservation Biology invites applications for two tenure track, Assistant Professor positions: a Large Mammal Ecologist with a focus on landscape scale habitat relationships and a Quantitative Fisheries Ecologist. Successful candidates will: (1) develop an externally funded and nationally recognized research program in their field; (2) contribute to undergraduate and graduate education as required by the department; (3) advise undergraduate, graduate and post-doctoral students; (4) participate in faculty governance and service in the department, college and university; and (5) interact with government agencies. A Ph.D. or international equivalent is required.

For further information and to apply online, go to **https://employment.umn.edu**; search for Requisition #161573 for Large Mammal Ecologist position or #161318 for Quantitative Fisheries Ecologist position.

Review of applications will start on 1 September 2009; position is open until filled. Direct questions about the position and application process to Nancy Rothman, **rothm005@umn.edu**.

The University of Minnesota is committed to the policy that all persons shall have equal access to its programs, facilities and employment without regard to race, color, creed, religion, national origin, sex, age, marital status, disability, public assistance status, veteran status, or sexual orientation.

University of Minnesota

POSITIONS OPEN

GeoVax Vaccines Serving Humanity

MEDICAL DIRECTOR
AIDS Vaccine Development

GeoVax, Inc., a biotechnology company based in Atlanta, Georgia, is seeking candidates for Medical Director of its HIV/AIDS vaccine program. GeoVax's candidate vaccines are currently in phase 2a trials through the HIV Vaccine Trials Network and are in preparation for entering therapeutic trials. The Medical Director will report to the Director of Research and Development and be responsible for key areas including: clinical trials liaison (FDA/NIH-HIV Trials Networks/other), clinical trials protocol development, testing coordination, preparation and presentation of clinical trial results. The Medical Director will interface with the research and development and quality control teams and their vaccine development and testing programs.

Qualifications and experience: M.D. or M.D.-Ph.D with interest in vaccine development; five to 10 years of experience with HIV/AIDS; document development experience (clinical trial protocols, manuscript preparation, grant writing); outstanding verbal and written communication skills; wet laboratory experience with human immunology desirable.

Interested candidates should submit curriculum vitae, a brief statement of HIV/AIDS and vaccine-related interests and accomplishments, and the names of three references to:

Human Resources
GeoVax Labs, Inc.
1256 Briarcliff Road N.E.
Atlanta, GA 30306
E-mail: hr@geovax.com
Telephone: 404-727-0971
Fax: 404-712-9357

GeoVax, Inc., is an Equal Opportunity/Affirmative Action Employer.

TENURE-TRACK FACULTY POSITIONS
Flathead Lake Biological Station
The University of Montana

AQUATIC BIOGEOCHEMIST

Flathead Lake Biological Station (FLBS) invites applications for a tenure-track position in biogeochemistry of river and lake ecosystems. Statement of rationale for the application, with emphasis on ability to obtain research funding, and vita listing three references, must be sent electronically to **e-mail: biogeo@flbs.umt.edu.**

CONSERVATION ECOLOGIST

FLBS invites applications for a tenure-track position in conservation ecology in a landscape genetics context. Statement of rationale for the application, with emphasis on ability to obtain research funding, and vita listing three references, must be sent electronically to **e-mail: consecology@flbs.umt.edu.**

Both positions are full time at FLBS on the east shore of Flathead Lake near Polson, Montana, with half-time salary for teaching and service and remaining annual salary derived from research funding. Specifically looking for individuals that want to work in the transdisciplinary environment fostered at FLBS; more information at **website: http://www.umt.edu/flbs.** A Ph.D. and postdoctoral research experience required. Screening will begin August 4, 2009, and will continue until a suitable applicant is hired.

Affirmative Action/Equal Opportunity Employer/ADA/Veterans Preference Employer.

POSITIONS OPEN

POSTDOCTORAL POSITION

The Department of Biological Sciences at Wichita State University, a comprehensive university in a metropolitan Kansas setting, seeks applicants for a Postdoctoral position. This position is an unclassified 12-month appointment and is funded through a five-year NIH grant.

The project involves defining the mechanism(s) responsible for the significantly greater biological activity of a novel follicle-stimulating hormone (FSH) variant, which possesses only a subunit glycans as compared with the classic four-glycan form. Applicant must have a Ph.D. degree with appropriate training in contemporary cell and molecular biology or glycoprotein biochemistry. Experience with reproductive biology is preferred.

For additional information and requirements and to apply, go to **e-mail: www.hrepartners.com.**

Offers of employment are contingent upon completion of a satisfactory criminal background check as required by Board of Regents policy.

POSTDOCTORAL POSITION is available to study the molecular pathogenesis of the Lyme disease spirochete, *Borrelia burgdorferi*. Available projects ask how *B. burgdorferi* adapts to arthropod and mammalian hosts and establishes persistent infection. Applicants must have a Ph.D. in microbiology, molecular biology, or biochemistry as well as publications in peer-reviewed journals. Experience with mouse experimental models is a plus. To apply, send curriculum vitae and the e-mail addresses for three references to: **Dr. Jon Skare, e-mail: jskare@medicine.tamhsc.edu.** *The Texas A&M Health Science Center is an Affirmative Action/Equal Opportunity Employer.*

PRINCIPAL SCIENTIST, Bioengineering/Biomaterials: Southwest Research Institute, San Antonio, Texas. Develop new bone and tissue scaffold platforms, manage technical projects and personnel, conduct and support programs in biomaterial and bioengineering applications. Requires a Ph.D. in bioengineering, biochemistry, or chemical engineering or applied biosciences with at least five to eight years of related experience in industry/academia after postdoctoral training. Job title to be matched to experience. For more information or to apply: **website: http://www.swri.jobs. Job code 01-01392.**

MARKETPLACE

Call for Papers

Submit your research now to be one of the first to be considered for publication in the **inaugural issue** of *Science Translational Medicine!*

Science Translational Medicine, to be published online weekly beginning in the fourth quarter 2009, focuses on the conversion of basic biomedical research into practical applications, thus bridging the research-to-application gap.

The editors of ***Science Translational Medicine*** are accepting manuscripts for review in the following areas:
cancer, cardiovascular disease, metabolism/diabetes/obesity, neuroscience/neurology/psychiatry, immunology/vaccines, infectious diseases, policy, behavior, bioengineering, physics, chemical genomics/drug discovery, imaging, applied physical sciences, medical nanotechnology, drug delivery, biomarkers, gene therapy/regenerative medicine, toxicology and pharmacokinetics, data mining, cell culture, animal, and human studies, medical informatics, and other interdisciplinary approaches to medicine.

Review the information for authors at http://sciencemag.org/marketing/stm/papers.dtl

Recommend a subscription to your library: www.sciencemag.org/cgi/recommend_subscription

Submit your research at www.submit2scitranslmed.org

For more information, contact Editor Katrina Kelner, Ph.D. at scitranslmededitors@aaas.org

Science Translational Medicine
AAAS

Integrating Medicine and Science

www.ScienceTranslationalMedicine.org

R&D Systems Bioactive Proteins

High quality proteins aren't a luxury, they are a necessity.

WHAT'S THE RISK? ✓ Missed opportunities ✓ Non-specific results ✓ Experiments that can't be repeated ✓ Weeks or months of wasted time

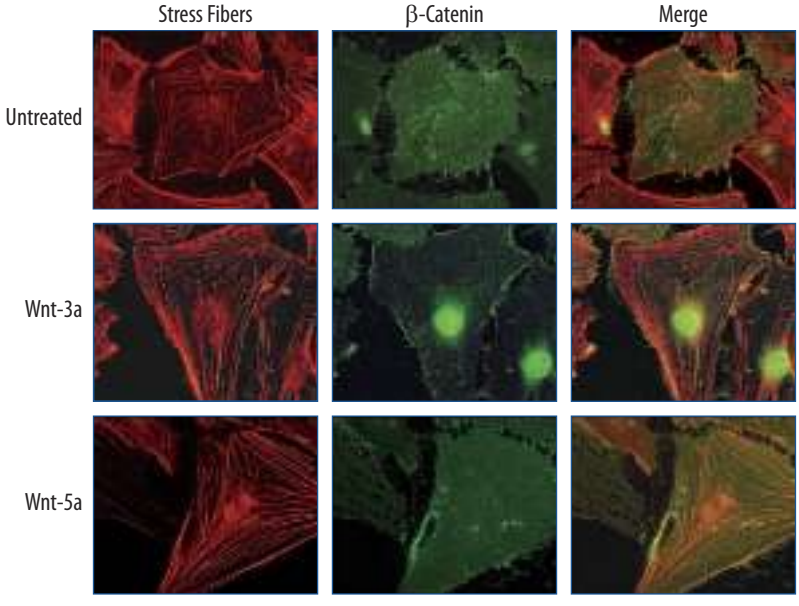

R&D Systems recombinant mouse Wnt-3a (Catalog # 1324-WN) and Wnt-5a (Catalog # 645-WN) promote stress fiber formation in NIH-3T3 cells, while only Wnt-3a promotes nuclear β-Catenin accumulation. Please visit our website for information about our new high purity human Wnt-3a (Catalog # 5036-WNP). *Images Courtesy of Dr. Raymond Habas, Robert Wood Johnson School of Medicine.*

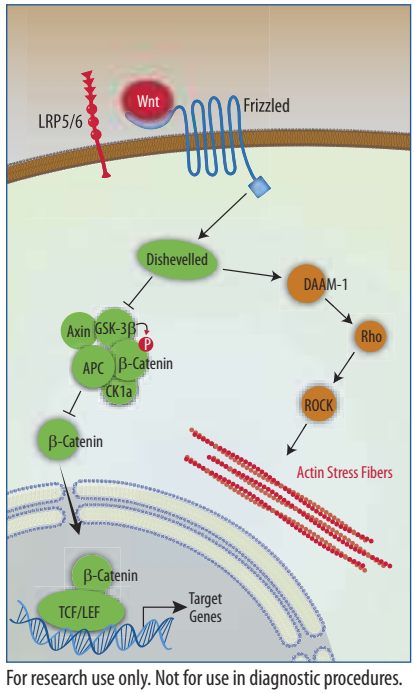

For research use only. Not for use in diagnostic procedures.

R&D Systems has spent almost 25 years building its reputation as a source for high quality proteins.

Every stage of protein development takes place in R&D Systems' laboratories, from cloning of the gene, to protein purification and testing for bioactivity. Because we control all aspects of protein manufacturing, R&D Systems can better control the quality of our products and the technical assistance we offer. Please visit our website at **www.RnDSystems.com/go/Proteins** for more information.

Cancer Development Endocrinology Glycobiology Immunology Neuroscience Proteases Signal Transduction Stem Cells

R&D Systems Tools for Cell Biology Research™

USA & Canada **R&D Systems, Inc.** Tel: (800) 343-7475 info@RnDSystems.com
Europe **R&D Systems Europe, Ltd.** Tel: +44 (0)1235 529449 info@RnDSystems.co.uk
China **R&D Systems China Co., Ltd.** Tel: (800) 988-1270 info@RnDSystemsChina.com.cn

Selection expanding weekly—visit **www.RnDSystems.com/go/request** to sign up for weekly new product updates.

R&D SYSTEMS®